ON THE FRACTURE TOUGHNESS AND STABLE CRACK GROWTH IN
SHAPE MEMORY ALLOYS UNDER COMBINED THERMOMECHANICAL
LOADING

A Dissertation

by

SAMEER SANJAY JAPE

Submitted to the Office of Graduate and Professional Studies of
Texas A&M University
in partial fulfillment of the requirements for the degree of

DOCTOR OF PHILOSOPHY

Chair of Committee,   Dimitris C. Lagoudas
Committee Members,   Amine Benzerga
                     Ibrahim Karaman
                     Jay Walton
Head of Department,   Rodney Bowersox

May   2017

Major Subject: Aerospace Engineering

ABSTRACT

Advanced multifunctional materials such as shape memory alloys (SMAs) offer unprecedented improvement over conventional materials when utilized as high power output solid-state actuators in a plethora of engineering applications, viz. aerospace, automotive, oil and gas exploration, etc., replacing complex multi-component assemblies with compact single-piece adaptive components. These potential applications stem from the material's ability to produce large recoverable actuation strains when subjected to combined thermomechanical loads, via a diffusionless solid-to-solid phase transition between high-temperature cubic austenite and low-temperature monoclinic martensite crystalline phases. To ensure reliable design, functioning and durability of SMA-based actuators, it is imperative to develop a thorough scientific knowledge base and understanding about their fracture properties i.e. crack-initiation and growth during thermal actuation, vis-a-vis the phase transformation metrics (i.e. transformation strains, hysteresis, and temperatures, critical stresses for phase transformation, etc.) and microstructural features (grain size, precipitates, and texture). Systematic experimental and analytical investigation of SMA fracture response based on known theories and methodologies is posed with significant challenges due to the inherent complexity in SMA thermomechanical constitutive response arising out of the shape memory and pseudoelastic effects, martensite detwinning and variant reorientation, thermomechanical coupling, and transformation induced plasticity (TRIP). In this study, a numerical analysis is presented that addresses the fundamental need to study fracture in SMAs in the presence of aforementioned complexities. Finite element modeling with an energetics based fracture toughness criterion and SMA thermomechanical behavior with nonlinearities from

thermomechanical coupling and TRIP was conducted. A specific analysis of a prototype boundary value fracture problem yielded results similar to those obtained experimentally, viz. stable crack growth with transformation toughening, dependence of failure cycle on bias load and catastrophic failure during cooling, and are explained using classical fracture mechanics theories. Influence of TRIP as a monotonically accumulating irrecoverable plastic strain on the crack-tip mechanical fields in case of stationary and advancing cracks is also investigated using the same computational tools. Thermomechanical coupling in shape memory alloys, which is an important factor when utilized as solid-state actuators manifests itself through the generation and absorption of latent of transformation and leads to non-uniform temperature distribution. The effect of this coupling vis-a-vis the mechanics of static and advancing cracks is also analyzed using the energetics based approach.

DEDICATION

To my parents,

My mother, who gave me the strength to follow my dreams and work hard towards fulfilling them, and my father, who instilled in me a sense of wonder and curiosity towards the world around.

ACKNOWLEDGEMENTS

I would like to take this opportunity to thank all the people who have contributed to the successful completion of this thesis.

First and foremost, I would like to thank my advisors Prof. Dimitris C. Lagoudas and Dr. Theocharis Baxevanis for accepting me as part of this research endeavor. Prof. Lagoudas, who is one of the best teachers that I have had the pleasure of learning from, taught me the essentials of critical thinking and scientific research throughout my PhD experience and helped me develop a appreciation for SMAs and their mechanics. Through our meetings and discussions, I was able to develop the ability ask important and broad scientific questions, study their impact on real-world technology and scrutinize my own results. Prof. Lagoudas also gave me important lessons on how to communicate my thoughts and ideas to my peers and seniors in an effective and succinct manner. Dr. Baxevanis taught me the foundations of fracture mechanics, material behavior, numerical analysis and helped me see the overall picture of a difficult and elusive scientific problem that we were tackling. His invaluable advice about proper technical writing also helped me develop my own way of conveying ideas and results through writing.

I would also like to express gratitude to my mentors and teachers who were part of the committee. Prof. Benzerga's teaching and guidance with regards to mechanics and failure of metals proved to be an invaluable factor in the understanding of my research. His support and constructive criticism has proved to be an important contribution to the success of this work. Prof. Jay Walton, a great mentor and teacher, with his profound knowledge of mathematical continuum mechanics and fracture, gave precious inputs and advice from time to time. Prof. Karaman, through our

regular research meetings taught me the experimental and hands-on side of the complexities of SMA behavior. His unique perspective from an experimental background and his guidance with regards to relating theory with experiments proved to be indispensable in successful completion of this thesis.

I would also like to acknowledge the help and support of my friends and colleagues in our research group. A special thanks to Dr. Alex Solomou, Dr. Edwin Peraza-Hernandez and Dr. Majid Tabesh. Alex was influential in providing the necessary UMAT code that made a major part of the research possible. I appreciate Majid for helping me with some of the important ideas and concepts about SMAs early on in my research. Edwin's inputs were especially helpful in discussions and questions I had regarding the SMA UMAT. My colleague Rob Wheeler's research on actuation fatigue of SMAs also proved to be crucial in the numerical modeling in my own research. I also wholeheartedly thank all my colleagues in the research for providing a friendly, inquisitive and fun-filled work environment.

I thank my family, my mother Sugandha, my father Sanjay and my brother Vaibhav, who stood by me and believed in me all these years and gave their unconditional love and support. Finally, I would to thank all my colleagues, fellow students, professors and staff at the aerospace engineering department at Texas A& University for creating a positive and nurturing educational environment. Graduate school at Texas A&M has been the most rewarding and unforgettable experience of my life, and I wholeheartedly thank all the people who made it possible.

CONTRIBUTORS AND FUNDING SOURCES

NOMENCLATURE

SMA	Shape memory alloys
TRIP	Transformation induced plasticity
E_A	Elastic modulus of Austenite
E_M	Elastic modulus of Martensite
ν_A	Poisson's ratio of austenite phase
ν_M	Poisson's ratio of martensite phase
σ_{ij}	Cartesian components of the stress tensor
σ_s	Stress required for start of martensite detwinning
σ_f	Stress required for finish of martensite detwinning
C_M	Forward transformation slopes in the stress-temperature phase diagram
C_A	Reverse transformation slopes in the stress-temperature phase diagram
σ_∞	Uniaxial tensile stress at infinity
M_s	Martensitic start temperature
M_f	Martensitic finish temperature
A_s	Austenitic start temperature
A_f	Austenitic finish temperature
M_d	Temperature above which austenite plastically deforms without forward transformation
$\boldsymbol{\epsilon^t}$	Transformation strain tensor
ξ	Martensite volume fraction
g^t	Transformation hardening energy

T_0	Reference temperature
$\boldsymbol{S}$	Fourth-order effective compliance tensor
α	Second order effective thermal expansion tensor
c	Effective specific heat
s_0	Effective specific entropy at the reference state
u_0	Effective specific internal energy at the reference state
f_ξ	Transformation hardening function
ϵ_{ij}^t	Cartesian components of the transformation strain tensor
S_{ijkl}^A	Components of the austenite compliance tensor
S_{ijkl}^M	Components of the martensite compliance tensor
π^{fwd}	Thermodynamic driving forces for forward transformation
π^{rev}	Thermodynamic driving forces for reverse transformation
f^{fwd}	Transformation hardening behavior during forward phase transformation
f^{rev}	Transformation hardening behavior during reverse phase transformation
ρ	Density
Δ	Difference in property between the martensitic and the austenitic states
α_i	Coefficients that assume real number values
ϵ_{ij}^p	Cartesian components of the plastic strain tensor
v_α	Poisson ratio of the current phase

E_α	Elastic modulus of the current phase
δ_{ij}	Kronecker's delta
Λ_{ij}	Components of the direction tensor
s_{ij}	Stress deviator components
$\bar{\sigma}$	Equivalent stress (von Mises)
σ_m	Mean normal stress
H^{sat}	Transformation strain at saturation
Φ	Transformation surface
M^{0s}	Initial martensite start temperature
β_{ij}	Components of the back stress
D_i^b	Coefficients associated with the back stress
D_i^d	Coefficients associated with the drag stress
C_1^p, C_2^p	Parameters that govern the saturation value of plastic strain
ζ^d	Accumulated detwinned martensitic volume fraction
H^{max}	Maximum attainable transformation strain at all stress levels
$E_{\gamma\delta}^t$	Transformation and plastic strain in circular spots in the vicinity of the crack tip
β	Angle between the crack line and line connecting crack tip and the circular spots
dK_I	Enhancement in crack-tip stress intensity due to eigenstrains in the vicinity of crack tip
G_I	Crack-tip energy release rate due to thermal variations

G_∞	Crack-tip energy release rate due to mechanical loading alone
G_{crit}	Critical crack-tip energy release rate
K_{crit}	Critical stress intensity factor
T	Stress triaxiality ratio
K_{IC}	Critical stress intensity factor for crack initiation
SIM	Stress-induced martensite
CT	Compact tensile specimen
LEFM	Linear elastic fracture mechanics
VCCT	Virtual Crack Closure Technique
SE(B)	Single edge notched bend specimen

TABLE OF CONTENTS

LIST OF FIGURES

xx

LIST OF TABLES

1. INTRODUCTION

1.1 Shape Memory Alloy Behavior and Applications

Shape memory alloys (SMA) are a class of inter-metallic alloys that have the capability to recover large, apparently permanent strains when subjected to specific thermal or mechanical loading conditions. Reversible, diffusionless solid-to-solid phase transformation between the material's austenite and martensite phases is the key physical mechanism behind this phenomenon. A representative phase diagram with the applied stress as ordinate and temperature as abscissa, is used to demonstrate the different equilibrium phases of a typical SMA with a fixed composition (Figure 1.1). The low temperature-low symmetry crystalline phase of martensite (which can be B19'-monoclinic, tetragonal, or orthorhombic with respect to its crystal structure) typically exists in a twinned or *self-accommodated* form at low applied stresses and undergoes detwinning in the presence of enough bias stress (σ_s, σ_f as shown in the phase diagram), resulting in a dominant martensite variant and macroscopic strain [62, 87, 37, 83]. At high temperature, the SMA exists in a highly symmetric B2-cubic crystalline phase of austenite. Both austenite and martensite phases represent the preferential equilibrium state of the same metallic alloy with a fixed material composition. Moreover, transition between the austenite and martensite phases (which is triggered by stress or temperature or a combination of both) does not occur by movement of atoms but by a diffusionless shear lattice distortion. At high enough temperature, SMAs can undergo shape-change due to purely mechanical loading under isothermal conditions resulting in a reversible martensitic transformation from austenite to martensite. This property is termed as *pseudoelasticity*. On the other hand, when an SMA is under a constant mechanical load (or

no load, in some special cases), temperature change can cause reversible martensitic transformation; a property termed as *shape memory effect* ([62]). The parent cubic austenite phase transforms to the martensite phase upon cooling (forward transformation), through the martensitic-start(M_s) martensitic finish(M_f) temperature interval, whereas martensite transforms back into the austenite state through the austenitic-start(A_s)austenitic finish(A_f) temperature interval (Figure 1.1), which are dependent on alloy composition, material processing, and applied stress levels. At any intermediate temperatures between M_s and M_f or A_s and A_f, the SMA exists as a two phase mixture of austenite and martensite.

SMA actuators (typically, in the shape of wires, springs or thin films) take advantage of these properties and are capable of performing significant amount of mechanical work when subjected to relatively small temperature changes. The work output per unit volume of SMA actuators exceeds that of other electromagnetic or thermal actuators (such as piezoelectric or thermopneumatic) (Figure 1.2), and are therefore a desirable alternative when large actuation forces are required in a small volume and thermodynamic efficiency is not essential [108, 80]. Some notable engineering applications that make use of SMA actuators have been in the aerospace industry [43, 31, 44], such as, the Smart Wing program by a collaboration of DARPA [61], AFRL, and Northrop Grumman that made use of SMAs as wire tendons to actuate hinge-less ailerons and as torque tubes to initiate span-wise wing twist of a scaled-down F-18 aircraft wing, NASA's Smart Aircraft and Marine Propulsion System demonstration (SAMPSON) that employed a complex system of SMA wire/rod bundles to change the geometry of an F-15 engine inlet and also the shape of the inlet lip through actuation [43, 102], and the Boeing variable geometry chevron to reduce aircraft engine noise levels during take off and landing and thereby increase engine performance [45, 44].
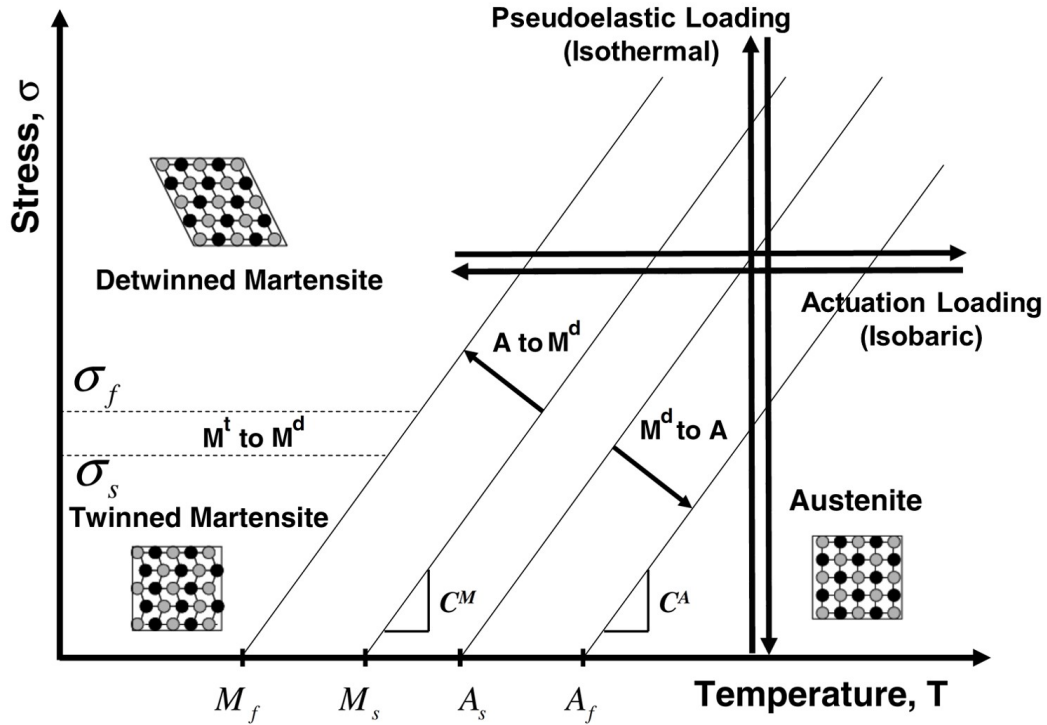
Figure 1.1: Representative stress-temperature phase diagram of an SMA showing the low-temperature monoclinic martensite (twinned or self-accommodated and detwinned) and high-temperature cubic austenite crystalline phases; stress-induced isothermal *pseudoelastic* loading path and temperature-induced isobaric *actuation* loading path are shown, along with the relevant transformation and detwinning stresses and temperatures (from Figure 1.7 of [62], © 2008 Springer US, with permission of Springer-Verlag US, DOI:10.1007/978-0-387-47685-8)

During their life-cycle, SMA actuators are typically subjected to hundreds of thousands of themomechanical loading cycles. Cracks form in SMA actuators owing to thermally-induced transformation fatigue (Figure 1.4) and effective use of SMA-based actuators requires an understanding of their fracture and actuation-fatigue-crack-growth properties. Following their development in the 1960s, SMAs (particularly NiTi) were a popular choice for applications pertaining to biomedical devices owing to their biocompatibility and biofunctionality. Development of a wide array of

3
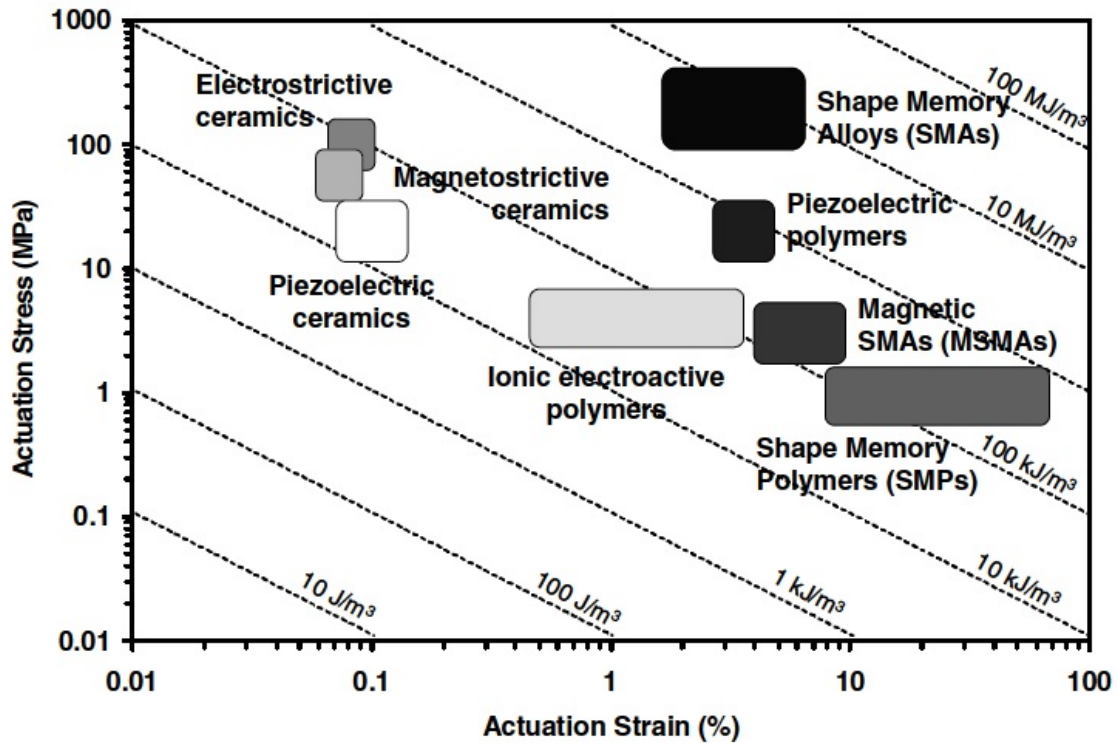
Figure 1.2: Actuation energy density diagram indicating typical ranges of actuation stress, actuation strain, and the actuation energy densities of different active materials that exhibit direct coupling. SMAs show relatively higher actuation energy density compared to other smart materials (from Figure 1.1 of [62], © 2008 Springer US, with permission of Springer-Verlag US, DOI:10.1007/978-0-387-47685-8).

SMA-based biomedical devices such as cardiovascular stents and filters, orthodontic arch-wires and braces, dental drills, orthopedic spacers, porous SMA bone implants, and surgical instruments [62] was carried out over the last half-century. These applications necessitated a large volume of scientific and engineering research on mechanical fatigue of SMAs. Owing to the small sizes of biomedical devices, fracture mechanics of SMAs, especially under thermomechanical loading conditions, largely remained unexplored by the scientific community. However, in today's technological
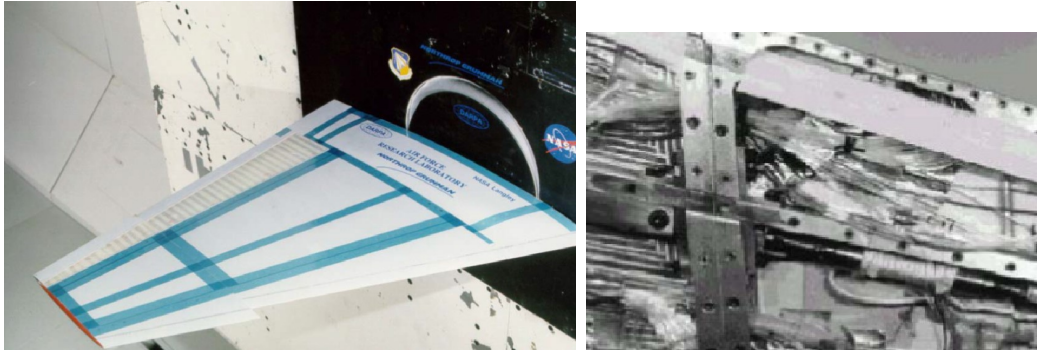
<center>(a)　　　　　　　　　　　　　　　(b)</center>

Figure 1.3: (a) Total view of the SMART Wing model (b) Cut away view of the SMA torque tubes; as installed in the model during Phase 1 of the SMART Wing project (from Figure 1.20 of [62], © 2008 Springer US, with permission of Springer-Verlag US, DOI:10.1007/978-0-387-47685-8).

landscape, there is a growing importance of SMAs for commercial applications involving high power output solid state actuators in non-biomedical applications such as aeronautics, energy conversion and storage, and automotives. Typically large sizes of SMA actuators call for the application of concepts from fracture mechanics to thermomechanical loading in SMAs. As such, the reliable and safe design of SMA actuators requires us to understand the effect of crack initiation and growth in SMAs under combined thermomechanical loading, on the overall thermomechanical behavior and load bearing capacity of shape memory alloys.

<center>1.2　　Fracture of SMAs: Background and Literature Review</center>

Vast literature has been produced that addresses the phenomenology and modeling approaches when it comes to SMA thermomechanical behavior and mechanical fatigue over the past half century, but limited attention has been devoted to careful and systematic usage of fracture mechanics tools, both experimental and theoretical, applied to SMAs. The main reason behind this stems from the fact that a bulk of

<center>5</center>
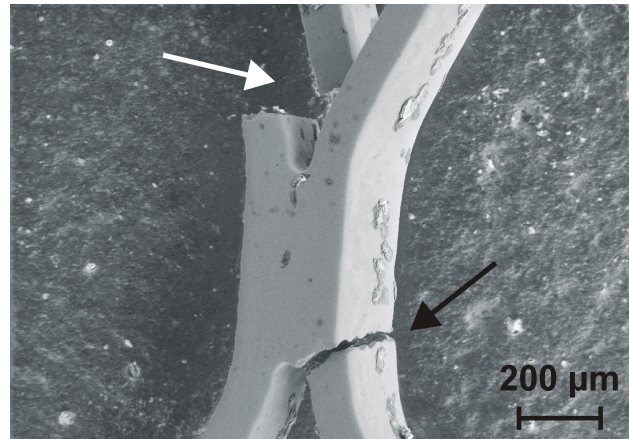
(a)
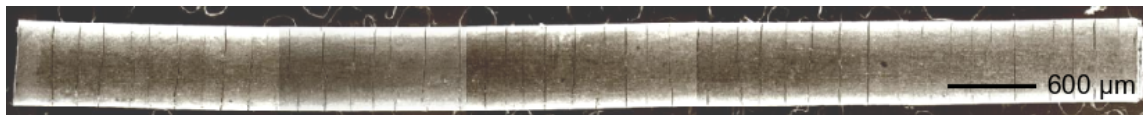
(b)

(c)

Figure 1.4: (a) Optical picture of a fractured NiTi SMA stent (from Figure 7 of [36], © 2008 Elsevier, with permission of Elsevier, http://dx.doi.org/10.1016/j.msea.2007.04.129)(b) Surface crack development for TiNiCu SMA wire actuator undergoing complete transformation cycles (from Figure 5 of [64], © 2006 Springer Netherlands, with permission of Springer, DOI: 10.1007/1-4020-4972-2-650) (c) Optical picture of 50.2%Ni NiTi compact tension specimen fractured in mode-I tension (Source: "Fracture Mechanics of NiTi SMAs", Gollerthan, S. and Eggeler, G., International Conference on Martensitic Transformations, Santa Fe, New Mexico, 2008)

SMA applications since their induction into engineering usage has been in the broad area of biomedical devices (e.g. cardiovascular stents, dental appliances, orthopedic implants, etc.). In biomedical devices the physical size of the SMA components, usually utilized for their pseudoelastic response, is generally small [89, 110, 32]. As a result, flaw sizes are typically large compared to the overall component dimensions and nucleation of a macroscopic crack is generally followed by immediate and catastrophic material failure [8]. Hence, characterization of fracture toughness and the study of mechanics or kinetics of crack growth in SMAs was considered redundant, and the main objective was to design components that could withstand crack nucleation. Fracture toughness characterization and fracture mechanics becomes relevant when size of the specimen or component is large enough to sustain stable crack growth before catastrophic failure occurs and some amount of residual material functionality is still intact.

Recently, SMAs are becoming more mainstream for potential applications as high energy output solid-state actuators in various engineering fields like aerospace, oil and gas, automotive, etc. These applications will require SMAs to not only replace complex mechanical assemblies of several interconnected components with a single SMA component but also produce larger actuation output in a small envelope volume, compared to traditional electromagnetic actuators. Consequently, relatively larger sized SMA components as solid-state actuators will be inducted into engineering devices in the near future, and will have to undergo hundred of thousands of thermomechanical cycles throughout their service life. Optimum functionality and performance of these SMA actuators in order to reduce actuator weight and cost of operation will thus require the systematic application of fracture mechanics and toughness characterization methods to analyze crack growth and failure in SMA material under various thermomechanical loading paths. As a starting point, a brief

literature review of the existing experimental and theoretical research on fracture of SMAs under purely mechanical loading is given.

1.2.1 Quasi-static isothermal mechanical loading

The limited data available related to theoretical and experimental scientific research on fracture of SMAs over the past two decades has been largely dedicated to addressing the problem of fracture and crack growth in SMAs subjected to quasi-static mechanical loading under isothermal conditions [13, 76, 77, 38, 113, 96, 71, 29, 28, 27, 42]. It has been observed that fracture of SMAs under these conditions bears important similarities with fracture of other dissipative systems, such as conventional elastic-plastic materials. Static and advancing cracks in SMAs under pseudoelastic loading and their effect on mechanical strength have been studied to analyze the structural life of SMAs under mechanical and functional fatigue with the help of experimentation as well as analytical and/or semi-empirical models. Nonetheless, fracture behavior of SMAs also shows notable characteristics that are different from traditional metals and alloys, owing to the complex nonlinear behavior of SMAs

1.2.1.1 Experimental studies on fracture of SMAs

Robertson et. al. [96] and Gall et. al. [41] have reported crack tip stress-induced phase transformation or stress induced martensite (SIM) in NiTi polycrystalline alloys under pseudoelastic loading (Figure 1.5). Crack tip SIM has also been reported in single crystalline NiTi alloys by Creuziger et. al. ([27]), with two different crystallographic orientations tested, as shown in Figure 1.7 and in Cu-based single crystalline SMAs [70, 113]. In situ synchrotron X-ray microdiffraction was used by Robertson et. al. [96] in order to examine local strains and dynamic phase transformation at a growing crack tip under mechanical loading and the effects of phase transformation (its size and shape) and austenite orientation at the crack tip
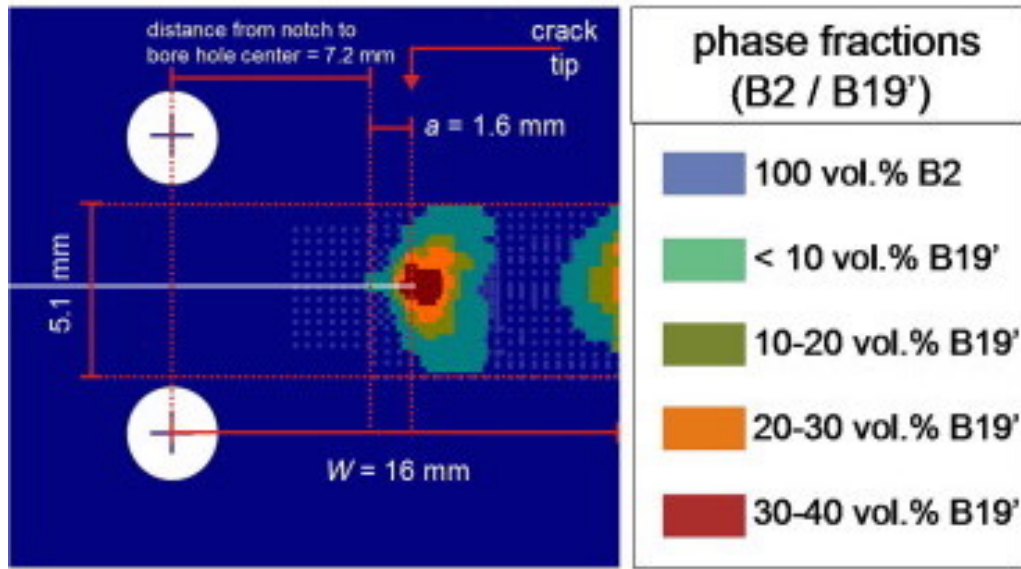
Figure 1.5: Phase fractions of the austenite B2 and martensite B19' structures for the two transformation zones in a pseudoelastic NiTi SMA CT specimen obtained by in situ synchrotron measurements at high stress intensity (from Figure 7(a) of [41], © 2009 Elsevier, with permission of Elsevier, http://dx.doi.org/10.1016/j.actamat.2008.10.055).

on micromechanics of crack propagation were studied. Fully transformed region at the crack tip was surrounded by partially transformed and untransformed austenite, and stress relaxation after crack growth was seen to cause reverse phase transformation and strain reversals in the crack wake [28]. Transformation zone under plane strain, similar to crack tip plasticity, was thought to be suppressed as compared to that under plane stress, due to higher material constraint and presence of hydrostatic stresses ahead of the crack tip.
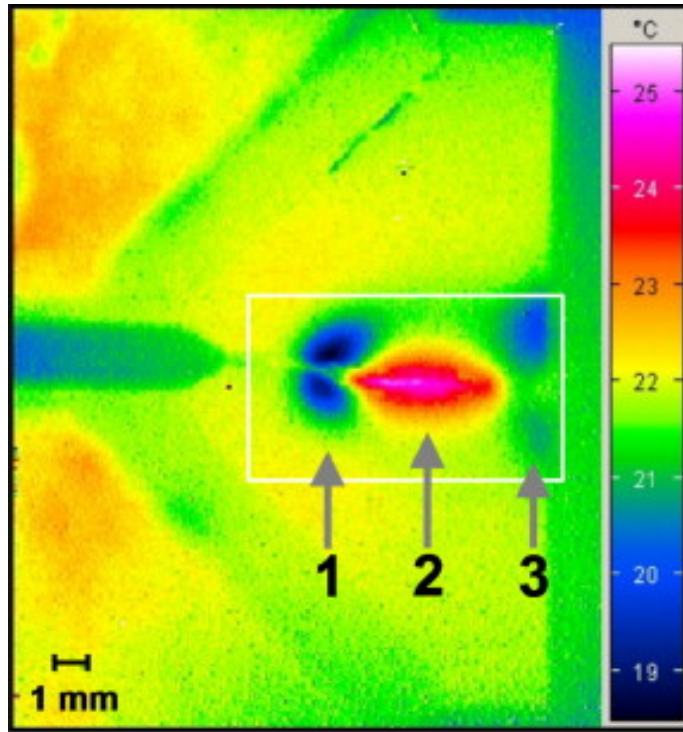
Figure 1.6: Thermographic image obtained during in situ dynamic loading of a pseudoelastic NiTi SMA CT specimen providing direct physical evidence for the back-transformation of stress-induced martensite in the wake of the advancing crack tip. The three arrows indicate the crack tip position prior to crack propagation (arrow 1), the actual crack position (arrow 2) and a region ahead of the crack tip (arrow 3) (from Figure 3 of [42], © 2009 Elsevier, with permission of Elsevier, http://dx.doi.org/10.1016/j.actamat.2009.08.015).

Gollerthan et. al. [41] later performed mechanical and microstructural experiments on miniature CT specimens of Nickel rich NiTi SMAs and showed the existence of stress induced martensite at the crack tip. In situ synchrotron measurements showed separate austenite B2 and martensite B19' structures under pseudoelastic loading with martensite at the crack tip surrounded by region of partial transformation and austenite (Figure 1.5), and stress relaxation due to phase transformation was also observed. In-situ synchrotron X-ray diffraction (XRD) measurements were

10

also used by [29] to create 2D maps of elastic strain and texture near the crack tip in martensitic NiTi compact tension specimens and showed phase transformation and detwinning at the crack tip. Young et. al. [122], later confirmed using synchrotron X-ray diffraction that reversible phase transformation between the austenite B2 structure and the stress-induced B19' martensite structure occurs in front of the crack tip due to loading and that upon unloading, reverse transformation from B19' to B2 occurs behind the crack tip.

Earlier experimental investigations by Gall et. al. [38] studied fracture mechanisms in polycrystalline $Ni_{50.8\%}Ti$ SMAs with Ni_4Ti_3 precipitates with three different precipitate sizes, 50nm, 150nm and 400nm. Scanning electron microscope (SEM) fractographic images depicted cleavage fracture along the 100 and 110 crystallographic planes with distinct rivermarks in the micrographs as well as void nucleation, growth and coalescence from the second phase particles, and the two mechanisms were seen to act simultaneously. Size of the Ni_4Ti_3 precipitates and concentration of Ni in the matrix was seen to govern the dominance of one mechanism over another. Cleavage fracture was seen prominent in semi-coherent precipitates (50-150 nm) whereas ductile tearing was common with incoherent (400nm) precipitates. Early estimates of fracture toughness values of NiTi SMAs were provided by Holtz. et. al. where the authors investigated fatigue threshold behavior of NiTi compact tensile (CT) specimens by comparing K-values of stable martensite phase vs. stress induced austenite-martensite phase and provided a fracture toughness versus temperature plot.
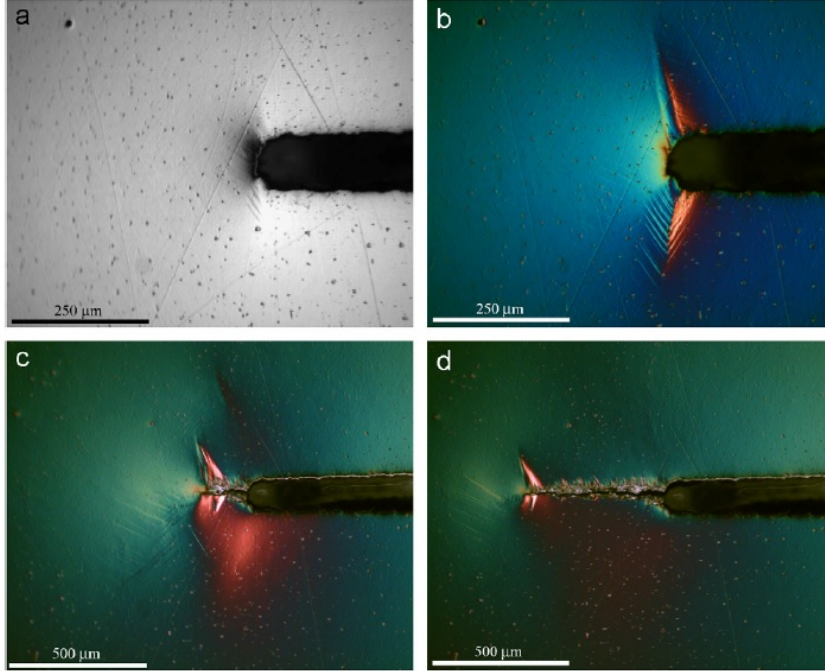
Figure 1.7: Progression of transformation and crack propagation of single crystal NiTi [111]. (a) Transformation prior to loading. (b) Growth of "microtransformation" of martensite ahead of the notch tip. (c) Growth of transformation zone, with martensite plates both ahead and to the side of the notch. (d) Immediately prior to fracture, a significant amount of out of plane deformation has occurred ahead of the notch, as indicated by the bright region (from Figure 4 of [27], © 2008 Elsevier, with permission of Elsevier, http://dx.doi.org/10.1016/j.jmps.2008.04.002).

Fracture toughness, an engineering parameter used to describe the resistance of a material to fracture in presence of a crack like flaw and an applied loading, of NiTi SMAs has been reported in literature in the form of crack resistance R-curve, where dependence of fracture toughness with increasing sub-critical crack length is plotted [49, 112, 96, 40, 41]. Most of the experimental work has been done under conditions that are not plane-strain where the specimen thickness was not enough to determine the asymptotic thickness dependent value of fracture toughness, which

Void nucleation, growth, and
coalescence from Ti$_3$Ni$_4$ precipitates

Cleavage
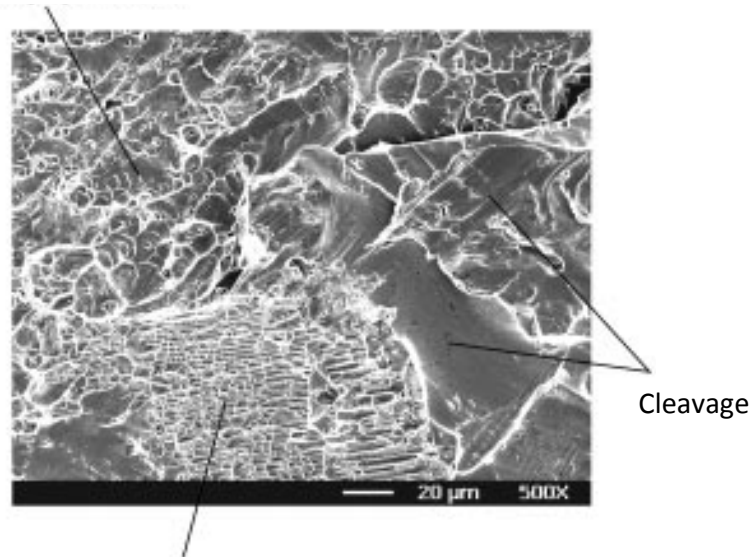
Void nucleation, growth, and
coalescence from fractured Ti-C
inclusions

Figure 1.8: Representative SEM image from a crystal aged 1.5 h @ 823 K and loaded along the [148] direction, demonstrating the three different fracture mechanisms observed in the precipitated NiTi (from Figure 7 of [38], © 2001 Elsevier, with permission of Elsevier, DOI: 10.1023/A:1011069204123)

results in the plane strain fracture toughness of the specimen [98]. Holtz et. al. generated fracture toughness data from fatigue crack growth study conducted at varying temperatures of a Nitinol plate, where the toughness was plotted as a function of temperature and hence the corresponding stable phase (martensite, austenite or mixed). Increasing toughness with temperature was reported and was linked to different fracture mechanisms dominating the fracture processes.

Vaidyanathan et al. [112], Gollerthan et al. [41], and Robertson and Ritchie [96] independently measured critical stress intensity factor K_{IC} values as fracture tough-

ness measures and calculated approximately $30MPa.m^{1/2}$ value for pseudoelastic NiTi above austenitic-start temperature A_f and below M_d (Figure 1.10 and Figure 1.11). Usage of LEFM and critical stress intensity factor K_{IC} as fracture toughness parameter places stricter restrictions on the test specimens thickness. However, in normal operating temperatures between A_f and M_d, stress induced phase transformation and detwinning in SMAs substantially suppresses crack tip plasticity, leading to some relaxation on specimen thickness for Linear elastic fracture mechanics (LEFM) analysis. Another methodology is the usage of critical J-integral as fracture criterion for toughness characterization to further relax the restrictions on specimen sizes. Fracture toughness in terms of crack resistance "R"-curve data for thin-walled Nitinol pseudoelastic tube tested at high temperature $378°C$ in air, showed dependence of crack-initiation toughness values on the crack propagation direction within the tube [97]. Finally, the phenomenon of stable crack *growth* under monotonically increasing load or displacement conditions, as shown in Figure 1.11, has been reported in the form of fracture resistance *R-curves* and is attributed to transformation toughening [41, 95]. Fracture toughening associated with crack advance and stable crack growth is attributed to dissipated energy at the crack tip supplied by external loading and resulting from the hysteretic stress–strain excursions experienced by material elements close to the tip.

In another important observation, Gollerthan et. al. [41] noted that the crack tips of martensitic and pseudoelastic NiTi CT specimens under SEM at varying load levels as shown in Figure 1.12. SEM micrographs show the absence of typical feature of crack tip blunting and crack tips appear to stay sharp under increasing loading. Crack tip blunting, which is strongly associated with dislocation emissions and resulting microscopic deformations at a scale smaller than martensite/austenite variants at the crack tip, was thus concluded to be not responsible for the nonlin-

14
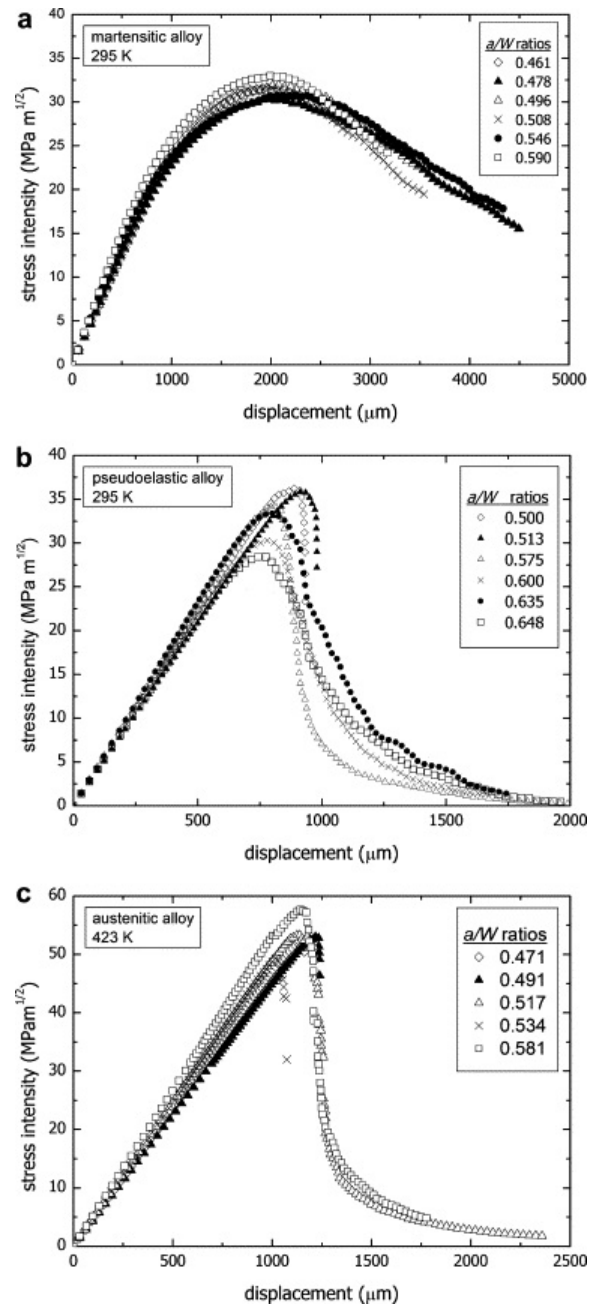
Figure 1.9: Stress intensity (K^*) vs. displacement curves of the (a) martensitic NiTi SMA at 295 K, (b) pseudoelastic NiTi SMA at 295 K and (c) austenitic NiTi SMA at 423 K (temperature above M_d) with varying dimension ratios. (from Figure 9 of [41], © 2009 Elsevier, with permission of Elsevier, http://dx.doi.org/10.1016/j.actamat.2008.10.055).

15
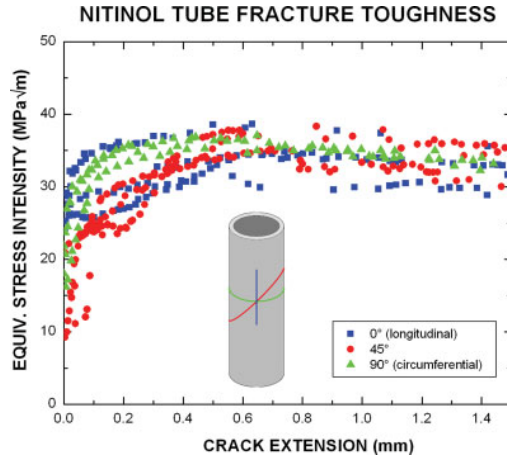
Figure 1.10: Fracture toughness in terms of crack-resistance (R-curve) data for thin-walled superelastic Nitinol tube tested in 378°C air. Crack-initiation toughness values were significantly lower than those at steady-state, and depended strongly on crack-propagation direction within the tube (from Figure 2 of [97], © 2007 Wiley, with permission of Wiley Periodicals, Inc., DOI: 10.1002/jbm.b.30840)
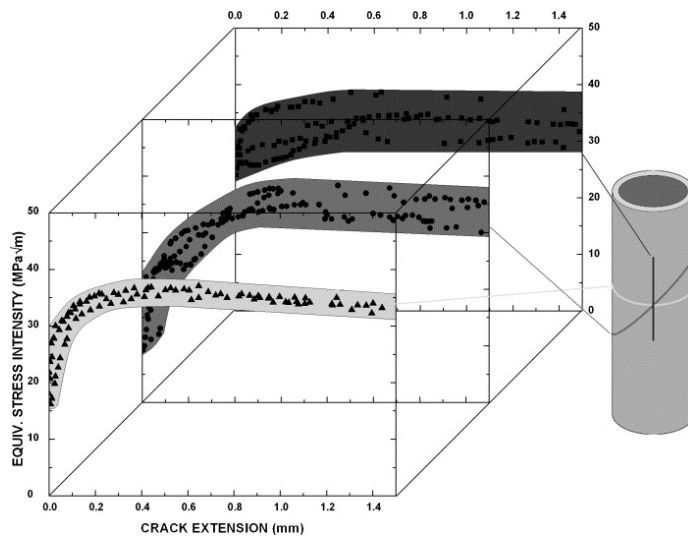
Figure 1.11: Fracture toughness in terms of crack-resistance (R-curve) data for thin-walled superelastic Nitinol tube (from Figure 9 of [95], © 2007 Elsevier, with permission of Elsevier, http://dx.doi.org/10.1016/j.biomaterials.2006.09.034)

16

ear behavior of the stress-intensity vs displacement shown in Figure 1.10. Microscopic crack growth events were also observed in both martensitic and pseudoelastic NiTi prior to reaching maximum stress intensity factor, but the associated crack extensions were small ($5\mu m$) compared to the dominant crack and their effect on deviation of the stress intensity factor-vs-displacement behavior from linearity was considered to be negligible. Infrared (IR) thermography also revealed temperature gradients on the material's surface which indicate heat flows associated with forward phase transformation (increase in temperature due to exothermic nature of forward transformation) and reverse phase transformation (decrease in temperature due to endothermic nature of reverse transformation) (Figure 1.6).

Thus, given the unique material behavior of SMAs, high local stresses at geometric discontinuities and crack-tips cause microstructural changes giving rise to stress-induced martensite transformation (SIM) and martensitic reorientation at the crack tip, and reverse martensitic transformation due to unloading in the wake of a growing crack (Figure 1.5). It has also been shown that SIM plays a key role in dictating fracture properties such as crack initiation fracture toughness and crack-growth resistance in SMAs. The crack-tip stress-induced phase transformation/detwinning is primarily responsible for the phenomenon of stable crack growth observed in single crystalline [70, 27] and polycrystalline SMAs. [95] were the only ones presented evidence of stable crack growth in NiTi in the form of rising R curve in polycrystalline SMAs. [42] provided direct physical evidence for the back-transformation of stress-induced martensite expected to occur due to unloading in the material regions left behind the advancing crack tip. Stress induced transformation and martensite detwinning thus seems to be the dominant mechanism causing the aforementioned nonlinear behavior; plasticity due to dislocation slip at the crack tip is suppressed whereas microcrack assisted deformation is negligible.
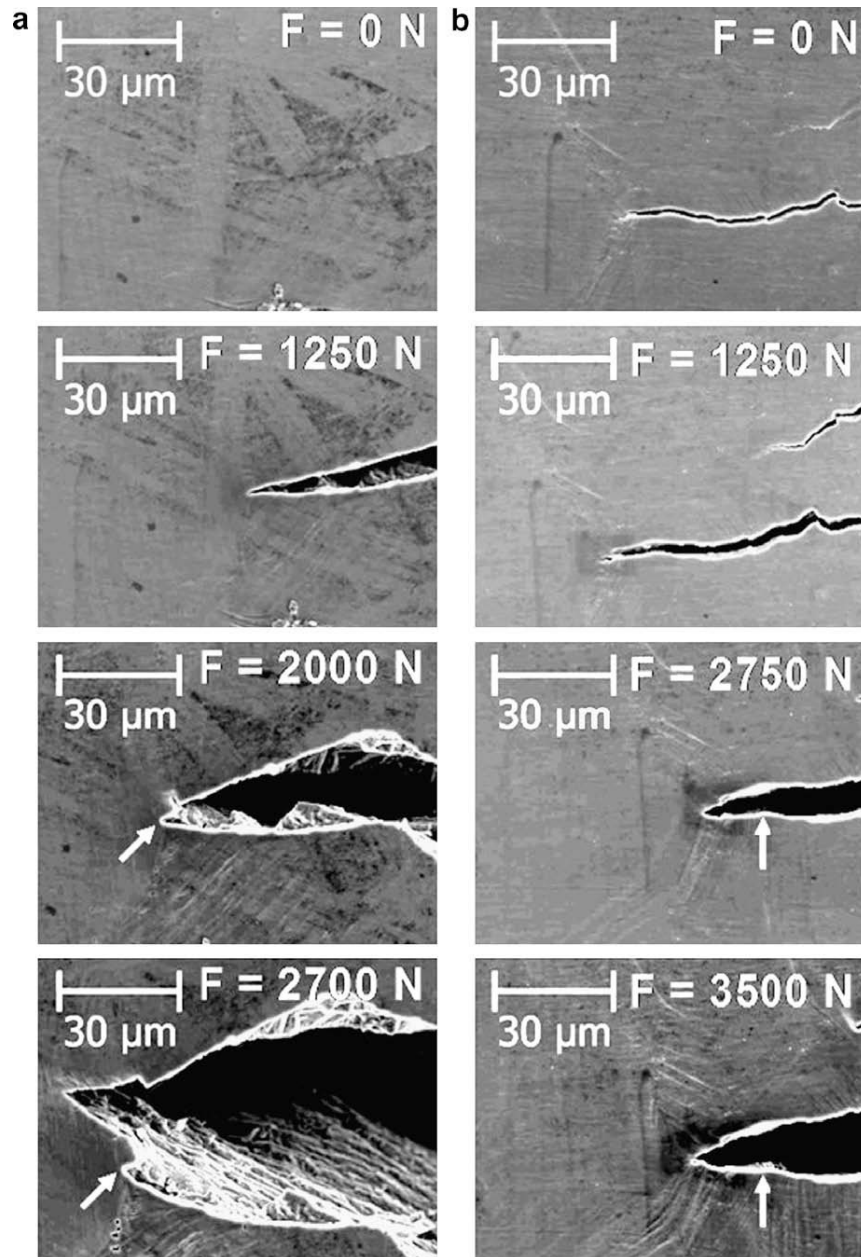
Figure 1.12: Scanning electron micrographs of (a) martensitic and (b) pseudoelastic NiTi SMAs at applied loads of 0N, 1250N, 2000N and 2700N and 0N, 1250N, 2750N and 3500N, respectively, during an in situ fracture experiment (from Figure 11 of [41], © 2009 Elsevier, with permission of Elsevier, http://dx.doi.org/10.1016/j.actamat.2008.10.055)

1.2.1.2   Modeling of SMA fracture response

Analytical and numerical modeling of SMA fracture under quasi-static mechanical loading and isothermal conditions have been developed for the past two decades to analyze static [13, 114, 116, 73, 74, 75, 72, 67, 66] and growing cracks [119, 120, 118]. Finite element calculations have demonstrated that the loading experienced in material regions close to a stationary crack tip in pseudoelastic SMAs is *nearly* proportional [6] and the stress-induced phase transformation results in a slight increase of the driving force for crack growth [7, 12, 10]. Crack-tip stress-induced phase transformation is primarily responsible for the phenomenon of stable crack *growth* under monotonically increasing load or displacement conditions. Analytical approaches were used to determine the size of stress-induced phase transformation zone under mode I utilizing Irwin's correction of LEFM, that accounts for the stress redistribution due to transformation around the crack tip. [73, 74, 75, 72] excluded plastic yielding of martensite under loading, while [116] included plasticity in their model for NiMnGa ferromagnetic shape memory alloys (FSMAs), but assumed a linear stress distribution in the region of elastically-deformed, fully-transformed martensite close to the crack tip. In their analysis, [73, 74, 75, 72] used the "small-scale transformation" condition where the fracture process zone in an SMA was vanishingly small, analogous to the small-scale yielding condition in classical elasto-plastic metals when transformation stress was compared with corresponding yield stress, in order to properly apply Irwin's modified criterion. Based on their analysis, it was concluded that austenitic stress intensity factor was always greater than linear elastic fracture mechanics predictions, while the martensitic stress intensity factor was always smaller, due to the mismatch between Young's moduli of martensite and austenite, thus leading to a toughening effect arising from phase transformation.

19
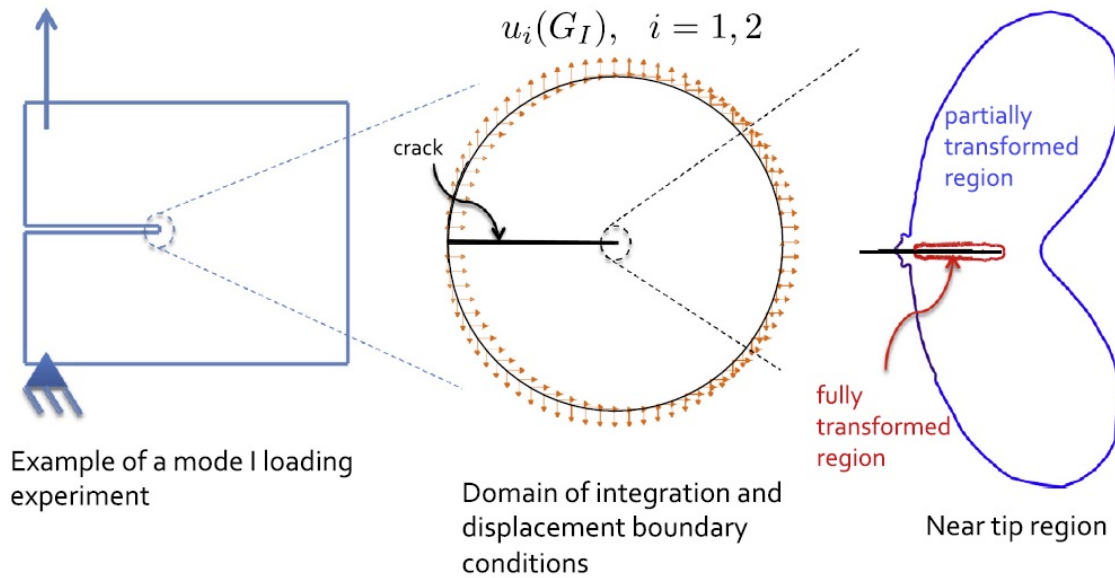
Figure 1.13: Boundary value problem for finite element analysis of mode-I crack growth in SMAs under mechanical loading and under the small-scale transformation condition (from Figure 2 of [12], © 2013 Elsevier, with permission of Elsevier, http://dx.doi.org/10.1016/j.ijplas.2013.04.007)

Later, [7] introduced an analytical model that incorporated plasticity alongside phase transformation in a formulation proposed by Dugdale for conventional elastic-plastic materials under plane stress conditions, and concluded that plasticity was suppressed by phase transformation, when comparing an SMA with plastic dissipation and an equivalent elasto-plastic material with yield stress equal to transformation stress of the SMA.

Yi et. al. [119, 120] numerically investigated the fracture toughening mechanism in SMAs under mode I and mixed mode loading conditions loading. They used the analysis of Their analyses followed closely that of [78] and [22], where transformation toughening in quasi-brittle zirconia based ceramics was investigated using modified LEFM theory together with the Eshelby equivalent inclusion method, to
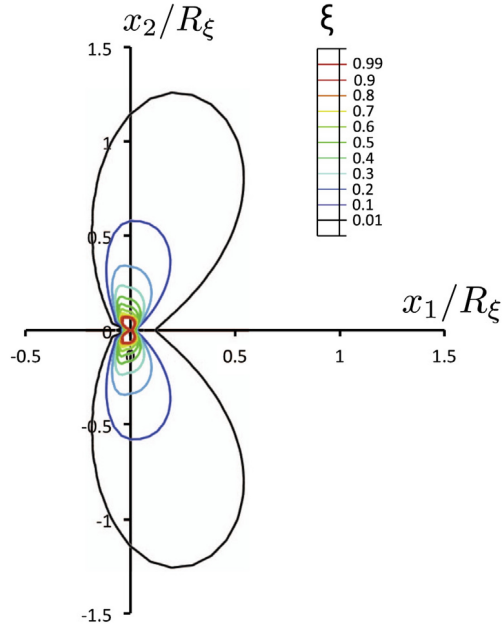
(a) Static crack (at initiation of crack prop-
agation)
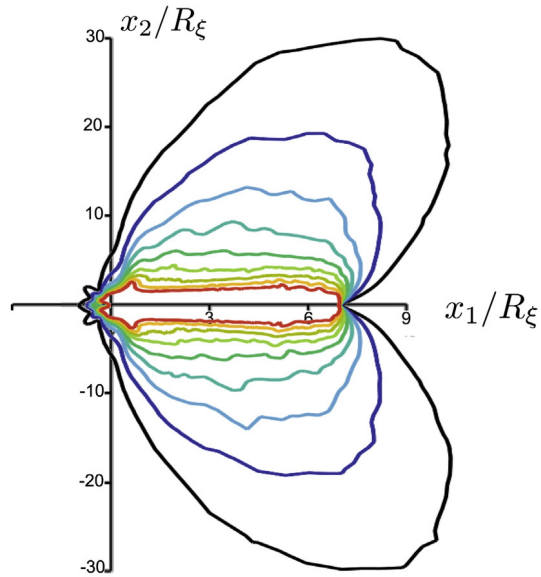
(b) Growing crack (close to nominally steady state
conditions).

Figure 1.14: Contours of martensite volume fraction in the vicinity of the crack tip
taken from finite element analysis of mode-I crack growth in SMAs, plotted with
normalized axes (from Figure 5 of [12], © 2013 Elsevier, with permission of Elsevier,
http://dx.doi.org/10.1016/j.ijplas.2013.04.007)

21

obtain crack resistance R-curves. They found that stress induced transformation at the crack tip increases the toughness for a growing crack and decreases the crack tip intensity. Freed and Banks-Sills [35] developed a cohesive zone model to analyze the effects of stress induced martensite on crack growth resistance in SMAs, as well as to simulate the effects of reverse transformation in the wake of the crack which occurs during crack propagation, and found that reverse phase transformation significantly reduces the toughness enhancement associated with forward transformation. Their analysis was similar to that of [109], who used finite element framework to examine the effect of reverse phase transformation on the crack growth resistance of SMAs during crack propagation under small scale transformation conditions. It is important to note that [35] was only valid for proportional loading conditions and both works referenced above assume that a finite pre-determined level of transformation strain is instantaneously accumulated once a level of stress is attained at a material point, i.e. no partial transformation allowed. Later, [12] modeled quasi-static stable crack growth in SMAs for plane strain, mode I loading using finite element method and VCCT under nominally isothermal loading paths for temperatures below the austenitic-start temperature. Small scale transformation conditions were assumed and transformation toughening behavior associated with crack advance was measured using ratio of the far-field energy release rate to the crack-tip energy release rate. The observed increased fracture toughness was associated with closure stresses acting on the crack tip due to transformed material left behind in the wake of the advancing crack tip.

As a first attempt to understand the fracture behavior of SMAs under actuation, [11] numerically investigated the effect of thermo-mechanically-induced global phase transformation on the driving force for crack growth of a static crack in an infinite center-cracked SMA plate under plane-strain mode-I constant applied loading. The

22

analysis was carried out using Abaqus unified FEA suite and the thermo-mechanical loading path used in the analysis was an idealization of typical loading paths that utilize SMAs as actuators subjected to constant external mechanical loading under temperature variations, and is referred to as isobaric. Previous experimental work has shown that most SMAs undergo brittle fracture with very little energy being dissipated in formation of a plastic zone at the crack tip. As such, the driving force for crack growth was identified by a single variable, *viz.* the crack-tip energy release rate, which was calculated using the Virtual Crack Growth Technique (VCCT). Two zones of transformation were observed ahead of the static crack tip: a fully transformed martensitic region, where the incremental material response is linear elastic, surrounded by a region of partially transformed material. During cooling, a significant increase in the crack-tip energy release rate, almost an order of magnitude compared to that due to purely mechanical loading, was also observed, suggesting the occurrence of crack growth during cooling of the specimen. A detailed review of this numerical work has been given in Section 2.

1.3 Fracture of SMAs Under Combined Thermomechanical Loading: Recent Experiments

In recent experimental findings at Texas A&M University [1], an intriguing fracture behavior of SMAs under thermal actuation was observed. When fatigue pre-cracked compact tensile (CT) specimens of binary $Ni_{50}Ti_{50}$ (at.%) were subjected to a constant tensile load and then thermally cycled, stable crack growth and ultimate failure was observed during *cooling* of the specimens. Failure due to unstable crack growth was observed for constant applied tensile loads much lower, as low as 25%, than the isothermal tensile strength of the specimen in purely martensitic phase when tested

---

[1]The experiments were performed at Texas A&M University and will be published elsewhere.

under constant tensile load at room temperature conditions.
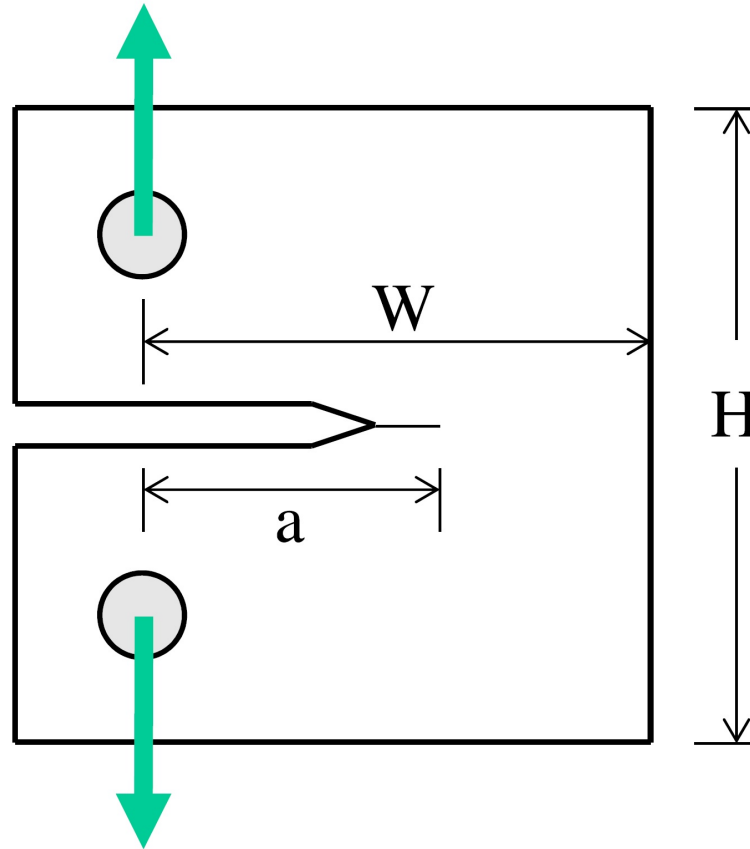
Figure 1.15: Sketch of ASTM standard compact tensile (CT) SMA specimen used for the fracture toughness tests. Fatigue loading is initially carried out on the specimen with a machined notch to generate a small fatigue pre-crack. Tensile loading is applied through loading pins as shown. In the above geometry, W = 20 mm and a = 6mm, and thickness B = 3 - 3.5 mm (from Figure 1a of [123], © 2012 Elsevier, with permission of Elsevier, http://dx.doi.org/10.1016/j.engfracmech.2012.02.001).

A sketch representing the typical geometry and dimensions of an ASTM standard CT specimen is shown in Figure 1.15. The planar dimensions were 20-25 mm and thicknesses ranged from 3-3.5 mm. CT specimens with a machined notch were initially subjected to mechanical fatigue loading to generate fatigue pre-cracks approximately 6mm in length. The phase transition temperatures for this SMA material are

$M_f = 58^oC$, $M_s = 67^oC$, $A_s = 94^oC$, and $A_f = 106^oC$. Two sets of fracture tough-ness tests were initially carried out to calculate the martensitic and pseudoelastic fracture toughness of SMA: (1) Mechanical loading until failure using load control of SMA under room temperature conditions when the material is purely martensitic (room temperature). The corresponding force vs. displacement or toughness curves of martensite are shown in blue in Figure 1.16 and (2) mechanical loading until failure of SMA at high temperature (170°) when the material is purely austenitic, shown in red (Figure 1.16). Corresponding critical stress intensity factor K_{IC}, when the force reaches maximum value and crack starts to grow, are calculated for both these cases are shown in Figure 1.16. $K_{IC} = 38.39 MPa\sqrt{m}$ was calculated for the room temperature test, and a fraction of this K_{IC}, viz. $75\%(K_{IC} = 30 MPa\sqrt{m})$, $37.5\%(K_{IC} = 15 MPa\sqrt{m})$, and $25\%(K_{IC} = 10 MPa\sqrt{m})$, and the corresponding load level was utilized as a constant bias load for the following actuation fracture toughness tests.

In the following actuation fracture toughness tests, CT specimens were fatigue pre-cracked with crack lengths in the range of 2mm from the notch root. Specimens were then placed inside a thermal chamber equipped with an induction heater (Roy 1500, Fluxeon, CA) with PID temperature controller Euroterm 2204, and a liquid nitrogen input for convective cooling to allow for PID-controlled temperature tests. Six thermocouples were placed on the specimen at different distances from the gage section and were used for temperature measurements. The loading/actuation path was as follows: the specimens were first held at zero load and heated to 150^oC, a temperature well above the material's austenite finish temperature to minimize forward transformation during loading, and then isothermally loaded to a certain tensile load levels (loads equivalent to a fraction of the critical K_{IC} of martensite, as discussed before).
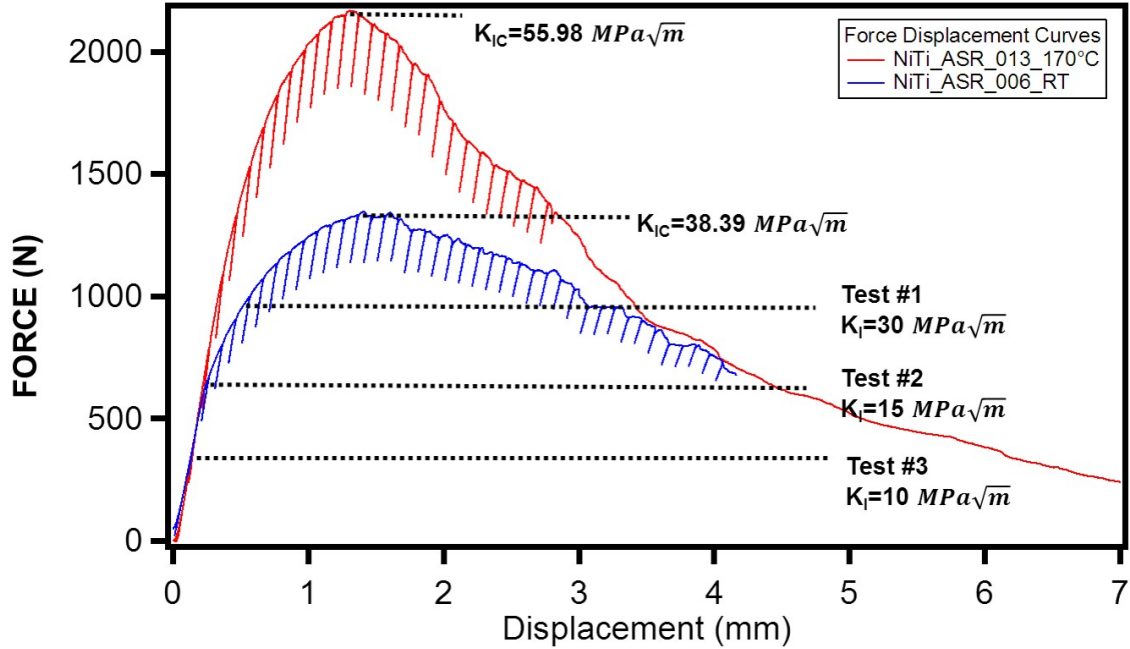
Figure 1.16: Force (N) vs. displacement (mm) curves showing the fracture toughness of SMAs at two different temperature: room temperature where the material is in martensite state (blue) and 170° where the material is in austenite state (red). Critical stress intensity factor K_{IC} for the corresponding load values for these two cases was calculated and a fraction of that K_{IC} was used as constant load for actuation fracture tests (Courtesy: Ceylan Hayrettin ("Experimental Evidence on Stable Crack Growth in Shape Memory Alloys during Thermal Cycles under Stress", C. Hayrettin, S. Jape, T. Baxevanis, I. Karaman, S.U. Ozguc, D. C. Lagoudas (In preparation))).

Maintaining a constant tensile load, the specimens were now cooled at a rate of 10^oC/min and forward transformation was induced. Digital Image Correlation (DIC) was used to measure strains on the specimen surface and strain field images from the DIC showed significantly high strains near crack-tip area during the cooling. For the case with high initial bias load, $viz.$ $K_{IC} = 75\%$, the DIC strain fields are first shown. As temperature was lowered further below martensite start temperature, higher strains were observed near the crack tip and eventually stable crack growth was observed as shown (Fig. 1.17). The crack was seen to grow to about 11mm from

6mm in total length (when measured from load line to the crack tip location), the average temperature wass around 71°C and the load dropped to about 1400N from initial constant load level of 1810N. Stable crack growth was seen through cooling cycle until steady state was reached and the crack grew uncontrollably, leading to catastrophic failure.

Time (s)	Force (N)	Temperature (°C)	Crack_Length (mm)	Stress Intensity Factor K (MPa√m)
325.414	1408.25	71.3 ± 3.06	11.7039849	53.45376157
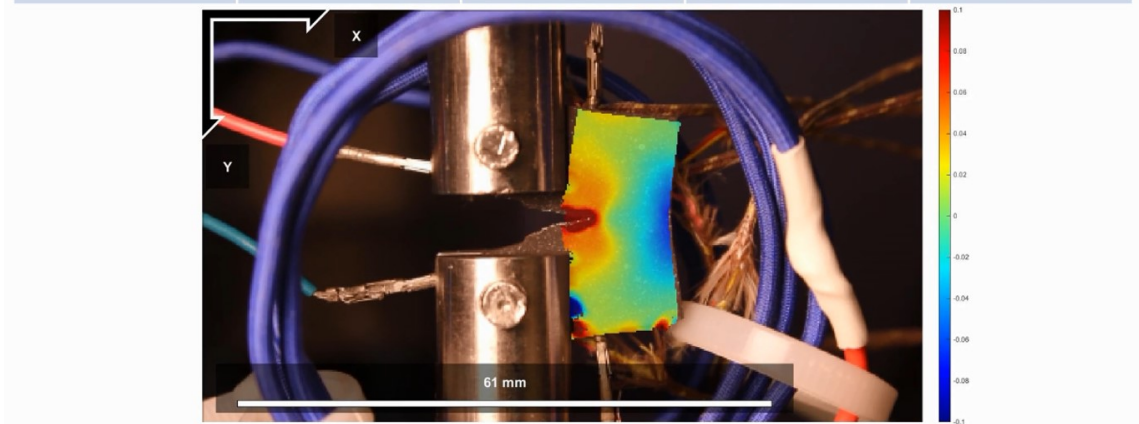
Figure 1.17: Strain in the direction of the tensile applied loading (vertical to the axes of the notches and tensile load being 75% of the isothermal strength at room temperature) during stable crack growth due to cooling and before the formation of an unstable crack (Courtesy: Ceylan Hayrettin ("Experimental Evidence on Stable Crack Growth in Shape Memory Alloys during Thermal Cycles under Stress", C. Hayrettin, S. Jape, T. Baxevanis, I. Karaman, S.U. Ozguc, D. C. Lagoudas (In preparation))).

With different initial bias loads ($K_{IC} = 75\%, 37.5\%, 25\%$), for a higher bias load ($\approx$1800N), crack growth is triggered at $\approx$ 74°C, in the first cooling cycle and sta-

ble crack growth is observed as temperature is decreased from $\approx 74^oC$ to $\approx 71^oC$. The crack grows from 6mm initial length to about 14mm, before steady state crack growth occurs and leads to catastrophic failure. In the second case, for a lower initial bias load, crack growth is triggered during cooling and a small amount of crack growth occurs. However crack growth is arrested in the first cooling cycle and the specimen transforms into martensite. During the second cooling cycle, crack grows to a limited extent before it is again arrested and transformation in completed without catastrophic failure is reached. The crack thus grows incrementally through multiple thermal cycles. Finally, after 7 thermal cycles, the specimen cannot sustain any additional crack growth and final failure is observed when the crack has grown to approximately twice its original length.

These experiments depict an interesting fracture behavior of SMAs when subjected to constant mechanical loading and boundaries but varying thermal conditions. With reduction in temperature due to cooling, other traditional metals display a typical thermal contraction, which is supposed to act as a limitation on crack growth. SMAs on the contrary, display a tendency for crack growth when temperature is reduced, owing to their nonlinear thermomechanical properties. In this research work, an attempt to understand this particular fracture behavior and its relationship with SMA material properties and other nonlinear phenomena, using finite element analysis and fracture mechanics, is undertaken.

1.4   Outline

This dissertation is organized in the following major sections: Section 2 describes formulation of the boundary value problem and solution methodology using finite element analysis for global thermo-mechanically induced phase transformation in an infinite center cracked SMA specimen. Stationary and advancing cracks are studied

28

and the effect of phase transformation parameters, applied bias loads, boundary conditions and crack configurations is presented. In Section 3, the aforementioned finite element analysis is extended to a plane strain infinite-medium center-cracked polycrystalline SMA material system with TRIP, subjected to constant remote loading and varying uniform temperature. Modified SMA material constitutive law, which incorporates additional internal variables related to the magnitude of irreversible TRIP strain into the classical SMA constitutive model is used. Numerical studies delve into the details of mechanical fields close to the stationary and moving crack tips using strain energy release rate as a single fracture toughness parameter and its dependence on the magnitude and orientation of accumulated plastic strains is studied. Section 4, details the effects of thermomechanical coupling originating from the generation/absorption of latent heat during phase transformation on near-tip fields in static and advancing cracks. Strong thermomechanical coupling exists in SMAs and is investigated by incorporating a material subroutine that includes coupling for the prototype infinite medium center-cracked SMA under actuation loading, and varying cooling/heating rates are applied. Finally, Section 5 is devoted to listing key findings of this work along with conclusions drawn from the obtained numerical results. Future work, which relates to connecting computational models to experimental fracture toughness calculations, incorporating SMA material phenomena such as martensite reorientation, finite strains and utilization of two-parameter fracture toughness theories, and modified crystal plasticity based SMA model in order to capture microstructural reasons behind fracture, to produce more accurate predictions, is described.

2. STABLE CRACK GROWTH AND TRANSFORMATION TOUGHENING DURING THERMAL ACTUATION OF SHAPE MEMORY ALLOYS*

2.1 Introduction

Shape memory alloys (SMAs) are a special class of inter-metallic alloys that can recover large, seemingly permanent, strains – an order of magnitude greater than those in traditional alloys – when subjected to appropriate thermomechanical inputs. A reversible, diffusionless, solid-to-solid, phase transformation between the material's high-temperature, high-symmetry austenite and low-temperature, low-symmetry martensite crystalline phases is the physical mechanism behind this phenomenon. Two key behaviors result from this transformation – the *shape memory effect* (SME) and *pseudoelasticity*. The former refers to the ability of the material to recover transformation strains via heating from a deformed shape in martensite to a remembered, austenitic one while the latter is associated with the large, hysteretic stress–strain excursions experienced by SMAs at a sufficiently high temperature [62].

Since their discovery in the 1960s, SMAs have been predominantly used in pseudoelastic biomedical devices (such as endovascular stents, dental appliances, orthopedic implants and surgical instruments) [101, 32, 110, 89]. However, in today's technological landscape, there is a growing importance of SMAs for commercial applications involving high power output solid state actuators in non-biomedical applications such as aeronautics and transportation. Solid-state SMA actuators are capable of performing significant amount of mechanical work when subjected to temperature changes, usually via joule heating. The work output per unit volume

---

*Portions of this section are reprinted or adapted from [58] S. Jape, T. Baxevanis, and D.C. Lagoudas, Stable Crack Growth During Thermal Actuation of Shape Memory Alloys. Shape Memory and Superelasticity, Volume 2, Issue 1, 104113, 2016. Copyright © 2016 by Springer. Reproduced with permission. doi:10.1007/s40830-015-0046-8

of SMA-based actuators exceeds that of other electromagnetic or thermal actuators (such as piezoelectric or thermo-pneumatic) and are therefore a desirable alternative when large actuation forces and a small volume are required and thermodynamic efficiency is not important [43, 62, 108, 80]. Some of the notable engineering applications that make use of SMA actuators in the aerospace industry, are the Smart Wing Program by a collaboration of DARPA, AFRL, and Northrop Grumman [61], NASA's Smart Aircraft and Marine Propulsion System demonstration (SAMPSON) [102], and the Boeing variable geometry chevron [62].

Reliable and safe design of SMA actuators requires understanding of the fracture properties of SMAs and the potential impact of macroscopic cracks on their functional and structural response. Owing to their unique thermomechanical properties, fracture response of SMAs is more complex than that of traditional structural metals and metallic alloys due to the reversibility of phase transformation, detwinning and reorientation of martensitic variants, the possibility of dislocation and transformation-induced plasticity, and the strong thermomechanical coupling [8]. Although there is a considerable body of theoretical and experimental work dedicated to address the problem of fracture and crack growth in SMAs subjected to mechanical loading at *nominally isothermal* conditions [109, 13, 119, 38, 118, 35, 29, 28, 27, 41, 30, 73, 74, 66, 7, 6, 12, 10, 9, 46, 3], there is a dearth of literature related to the fracture behavior of SMAs under combined *thermomechanical* loading. As recently observed, pre-cracked NiTi SMA specimens may fail during cooling, under a constant applied tensile load that is lower than the isothermal strength at the beginning of cooling. Failure by the formation of an unstable crack during cooling was observed for bias load levels as low as 37% of the isothermal bias load needed for failure at the beginning of cooling. This is an intriguing response that from an energetic point of view may seem in disagreement with the general view of dissipa-

tive processes resulting in an enhancement of fracture toughness. As a first attempt to understand this characteristic SMA response, Baxevanis *et al.* [11, 8] numerically investigated the effect of thermomechanically-induced phase transformation on the driving force for crack growth in an infinite center-cracked SMA plate during thermal cycling under plane-strain, mode-I, constant applied loading. This thermomechanical loading path (referred to as *isobaric*) is an idealization of typical loading paths that utilize SMAs as actuators. Motivated by experimental [38, 41] and analytical findings [6, 12], the authors argued that in most SMA material systems the length scale of the nonlinear deformation zone surrounding the crack tip should be small enough to ensure the validity of (i) an analysis of the fracture response of SMAs on the basis of a constitutive law that does not account for plastic deformation, and (ii) a single parameter for characterizing the fracture toughness of martensite forming at the crack tip, *i.e.*, the crack-tip energy release rate. A significant increase in the crack-tip energy release rate was found during cooling, almost an order of magnitude greater than that due to the isothermal mechanical loading applied before cooling. Thus, it is plausible that the crack-tip energy release rate may reach the material specific critical value during cooling under a constant mechanical load and initiate crack growth, in accordance with the experimentally observed response described above.

In this paper, the authors build upon the aforementioned work and investigate crack growth in SMAs under thermal actuation for the same prototype problem of infinite center-cracked SMA plate under plane-strain, mode-I, constant applied loading. Specifically, it is examined whether the interplay between the increase in driving force for crack growth due to large scale phase transformation and the shielding effect of the transformed material left in the wake of growing crack results in stable crack growth. Moreover, the near-tip mechanical fields and fracture toughness

32

are investigated and their sensitivity to phase transformation metrics and bias load levels is reported.

The paper is organized as follows. In Section 2.2, the constitutive material model used to simulate the thermomechanical behavior of SMAs is briefly reviewed. In Section 2.3, the boundary value problem is formulated and the solution methodology using the finite element method and VCCT is outlined. In Section 2.4, first, a brief review of the key results reported in [11, 8] is presented to draw a connection between those results that refer to static cracks and the crack growth results discussed in detail later on in the same section. Finally, some of the key findings of this work are summarized and concluded in Section 2.5.

2.2   Material Model

The proposed model relies on the unified model for polycrystalline SMAs proposed by Boyd and Lagoudas [18, 19, 63]. It is developed within the framework of continuum thermodynamics and adopts the classical rate-independent small-strain flow theory for the evolution equations of the transformation strains. In this model, the Gibbs energy is selected as the thermodynamic potential instead of the Helmholtz free energy, because it is customary to define thermomechanical loading path for SMAs in the stress-temperature space. Note that the Gibbs free energy, G, is a function of the independent state variables stress, $\boldsymbol{\sigma}$, and temperature, T, which can be more suitable when comparing numerical results with experimental, and the state variables, ξ and ε. The explicit form of the Gibbs free energy is given by Boyd and Lagoudas [18, 19], and Qidwai and Lagoudas [90]

$$G(\boldsymbol{\sigma}, T, \boldsymbol{\varepsilon}^t, \xi) = -\frac{1}{2\rho}\boldsymbol{\sigma} : \boldsymbol{S} : \boldsymbol{\sigma} - \frac{1}{\rho}\boldsymbol{\sigma} : [\boldsymbol{\alpha}(T - T_0) + \boldsymbol{\varepsilon}^t]$$

$$+ c\left[(T - T_0) - T\ln\left(\frac{T}{T_0}\right)\right] - s_0 T + u_0 + \frac{1}{\rho}f(\xi), \quad (2.1)$$

where T_0 is a reference temperature. The material parameters $\boldsymbol{S}$, $\boldsymbol{\alpha}$, c, s_0, and u_0 are the fourth-order effective compliance tensor, the second-order effective thermal expansion tensor, the effective specific heat, the effective specific entropy at the reference state, and the effective specific internal energy at the reference state, respectively. The function $f(\xi)$ is a transformation hardening function and will be defined in the following sections.

Within the context of isotropic elastic response, the increments of the strain tensor components, $d\varepsilon_{ij}$, are given as

$$d\varepsilon_{ij} = S_{ijkl}d\sigma_{kl} + dS_{ijkl}\sigma_{kl} + d\varepsilon_{ij}^t, \quad (2.2)$$

where σ_{ij}, ε_{ij}^t are the Cartesian components of the stress tensor and of the transformation strain tensor, respectively, and S_{ijkl} are the components of the 'current' compliance tensor. The thermoelastic strains are an order of magnitude smaller than the transformations strains, and thus neglected. Throughout this paper, standard Einstein notation is used with summation over repeated indices assumed. The 'current' compliance tensor varies with the martensite volume fraction ξ as $S_{ijkl} = (1 - \xi)S_{ijkl}^A + \xi S_{ijkl}^M$, where S_{ijkl}^A and S_{ijkl}^M are the components of the compliance tensor of austenite and martensite, respectively. The assumption of elastic isotropy for both the austenitic and martensitic phases reads as $S_{ijkl}^\alpha = \frac{1+\nu_\alpha}{2E_\alpha}(\delta_{il}\delta_{jk} + \delta_{ik}\delta_{jl}) - \frac{\nu_\alpha}{E_\alpha}\delta_{ij}\delta_{kl}$, where the index α stands for A in the case of

austenite and for M in the case of martensite. E_α, ν_α denote the Young's modulus and Poisson's ratio of the two phases, respectively, and δ_{ij} is Kronecker's delta. The above approximation of the 'current' compliance tensor is considered sufficient although more accurate approximations on the basis, for example, of the self-consistent or Mori-Tanaka methods, could be used instead. Other effective properties of the SMA material can also be expressed in terms of the corresponding properties of austenite and martensite and the martensite volume fraction as: $\alpha_{ij} = (1 - \xi)\alpha_{ij}^A + \xi\alpha_{ij}^M$, $c = (1 - \xi)c^A + \xi c^M$, $s_0 = (1 - \xi)s_0^A + \xi s_0^M$, $u_0 = (1 - \xi)u_0^A + \xi u_0^M$.

An evolution equation of the transformation strain is defined so that it is related to the evolution of martensite volume fraction ξ,

$$d\varepsilon_{ij}^t = \Lambda_{ij}d\xi, \quad \Lambda_{ij} = \begin{cases} \Lambda_{ij}^{fwd}, \ d\xi > 0, \\ \\ \Lambda_{ij}^{rev}, \ d\xi < 0, \end{cases} \tag{2.3}$$

where, Λ_{ij}, the components of the direction tensor, are defined as

$$\Lambda_{ij}^{fwd} = \frac{3}{2}\frac{H^{cur}}{\bar{\sigma}}s_{ij}, \quad \Lambda_{ij}^{rev} = \frac{\varepsilon_{ij}^t}{\xi}. \tag{2.4}$$

Here, H^{cur} is the uniaxial transformation strain magnitude for complete transformation, $\bar{\sigma} = \sqrt{\frac{3}{2}s_{ij}s_{ij}}$ is the Mises equivalent stress and $s_{ij} = \sigma_{ij} - \sigma_{kk}\delta_{ij}/3$ are the stress deviator components. During forward transformation, the transformation strain is oriented by the direction of the deviatoric stress, which motivates the selected J_2 form of the direction tensor. During reverse phase transformation, it is assumed that the direction and magnitude of the transformation strain recovery is governed by the average orientation of the martensite at transformation reversal (the cessation of forward transformation, be it partial or full). This definition allows to return to

a zero transformation strain for every state with a null martensite volume fraction. H^{cur} is a function of the stress state since most SMA materials do not exhibit a constant maximum attainable transformation strain at all stress levels. A saturated value of maximum attainable transformation strain, H_{sat}, is reached at a high stress level, which is dependent on the SMA material as well as the processing conditions for a polycrystalline material, resulting in different crystallographic and morphological textures, for example. Following this observation, the maximum transformation strain H^{cur} is represented by the following decaying exponential function

$$H^{cur}(\bar{\sigma}) = H_{sat}\left(1 - e^{-k\bar{\sigma}}\right),\tag{2.5}$$

where the parameter k controls the rate at which H^{cur} exponentially evolves from 0 to H_{sat}.

During transformation, the stress tensor components should remain on the transformation surface

$$\Phi = 0, \quad \Phi = \begin{cases} \Phi^{fwd} = \pi^{fwd} - Y_0, \ d\xi > 0, \\\\ \Phi^{rev} = -\pi^{rev} - Y_0, \ d\xi < 0, \end{cases}\tag{2.6}$$

with π^{fwd}, π^{rev} being the thermodynamic driving forces for forward and reverse transformation, respectively, and Y_0 is the critical value of the thermodynamic force to both initiate and sustain forward and reverse phase transformation. The thermodynamic driving force for forward transformation is written as

$$\pi^{fwd} = \sigma_{ij}\Lambda_{ij}^{fwd} + \frac{1}{2}\Delta S_{ijkl}\sigma_{ij}\sigma_{kl} + \rho\Delta s_0 T - \rho\Delta u_0 - f^{fwd},\tag{2.7}$$

36

where

$$f^{fwd} = \frac{1}{2}\alpha_1 \left[1 + \xi^{n_1} - (1 - \xi)^{n_2}\right] + \alpha_3, \tag{2.8}$$

and for reverse transformation

$$\pi^{rev} = \sigma_{ij}\Lambda_{ij}^{rev} + \frac{1}{2}\Delta S_{ijkl}\sigma_{ij}\sigma_{kl} + \rho\Delta s_0 T - \rho\Delta u_0 - f^{rev}, \tag{2.9}$$

where

$$f^{rev} = \frac{1}{2}\alpha_2 \left[1 + \xi^{n_3} - (1 - \xi)^{n_4}\right] - \alpha_3. \tag{2.10}$$

f^{fwd} and f^{rev} are functions describing the transformation hardening behavior during forward and reverse phase transformation, respectively. s_0 and u_0 are the specific entropy and internal energy, respectively, ρ is the density, Δ denotes the difference in property between the martensitic and the austenitic states, α_i ($i = 1, 2, 3$) and n_i ($i = 1, 2, 3, 4$) are coefficients that assume real number values.

Given these constitutive relations the following model parameters must be calibrated: (i) the elastic parameters of martensite and austenite, (ii) parameters contained in the functional form of the maximum transformation strain $H^{cur}(\bar{\sigma})$, and (iii) six model parameters ($\rho\Delta s_0$, $\rho\Delta u_0$, α_1, α_2, α_3, Y_0) that are characteristic of the martensitic transformation. The common material properties that are used to calibrate the model are E_A, E_M, ν_A, ν_M, H_{sat}, M_s, M_f, A_s, A_f, C_M, and C_A. M_s, M_f, A_s and A_f are the martensitic-start, martensitic-finish, austenitic-start and austenitic-finish temperatures at zero load, respectively, and C_M and C_A are the forward and reverse transformation slopes in the stress–temperature phase diagram, respectively (Figure 2.1). The elastic constants can be calculated directly from isothermal stress–strain curves where loads are applied at temperatures outside the transformation regions. The parameters for $H^{cur}(\bar{\sigma})$ can be calibrated directly
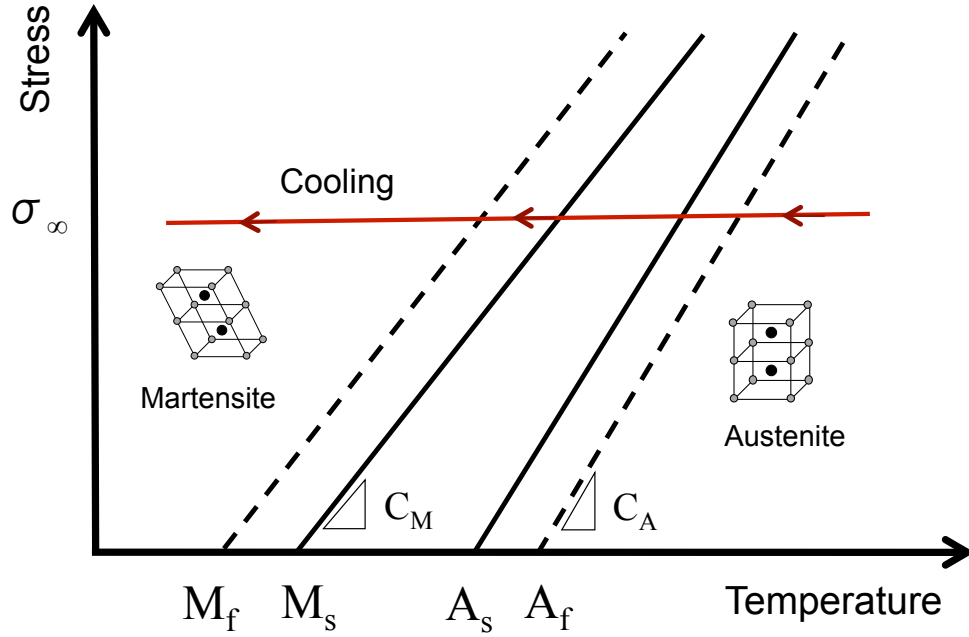
Figure 2.1: Stress–temperature phase diagram. Cooling at constant applied load.

from isobaric material testing, where the value of k in particular is chosen to best fit the experimental trend. The remaining six parameters are calibrated by considering the conditions under which forward transformation begins and ends in the stress–temperature space [62]. The exponents n_i $(i = 1, 2, 3, 4)$ do not have an associated material property but are directly chosen to best fit the two corners of the forward transformation plots.

2.3 Problem Formulation

In this section, the boundary value problem of mode-I crack growth in an infinite center-cracked SMA plate subjected to thermal cycling under plane strain constant applied loading is described.

The SMA plate is subjected to far-field in-plane uniform uniaxial tensile load,

in the direction normal the crack line as shown in Fig. 3.3. The load is applied at a nominal temperature higher than the austenitic-finish temperature, A_f, and a region of transformed material is formed near the crack tip. Small scale transformation conditions prevail, according to which the size of the transformation zone is small compared to the crack length $2a$, by applying a load resulting in uniaxial tensile stress at infinity, σ_∞, that is sufficiently smaller than the stress required for initiation of martensitic transformation, σ^{M_s}, at the given temperature. Maintaining the tensile load at the boundary constant, the entire cracked SMA specimen is then subjected to thermal cycling, *i.e.*, alternate cooling and heating between the high temperature at which the mechanical load is applied and a low temperature that is smaller than M_f (to ensure that the bulk of the specimen completely transforms between pure austenite and martensite). The cooling and heating rates are assumed to be sufficiently slow with respect to the time rate of heat transfer by conduction in order to discard any effects of local temperature gradients arising from latent heat of phase transformation and to maintain a uniform temperature field throughout the specimen.

Due to symmetry of the problem, the analysis is restricted to one quarter of the plate. A system of co-ordinates (x_1, x_2) is chosen such that the origin lies at the center of the crack and the x_1-axis is extending along the line of the crack while the x_2-axis is aligned in the direction of loading. A finite element mesh of 8-node, isoparametric quadrilateral elements is constructed in ABAQUS to represent the center-cracked SMA specimen with a finer mesh density in the crack growth path in front of the the crack-tip. The VCCT capability of ABAQUS, which is an extension of the classical crack-closure technique based on Irwin's crack closure integral [54, 99, 60, 115], is employed to calculate the crack-tip energy release rate.

Within this model for fracture of SMAs, dimensional analysis and manipulation
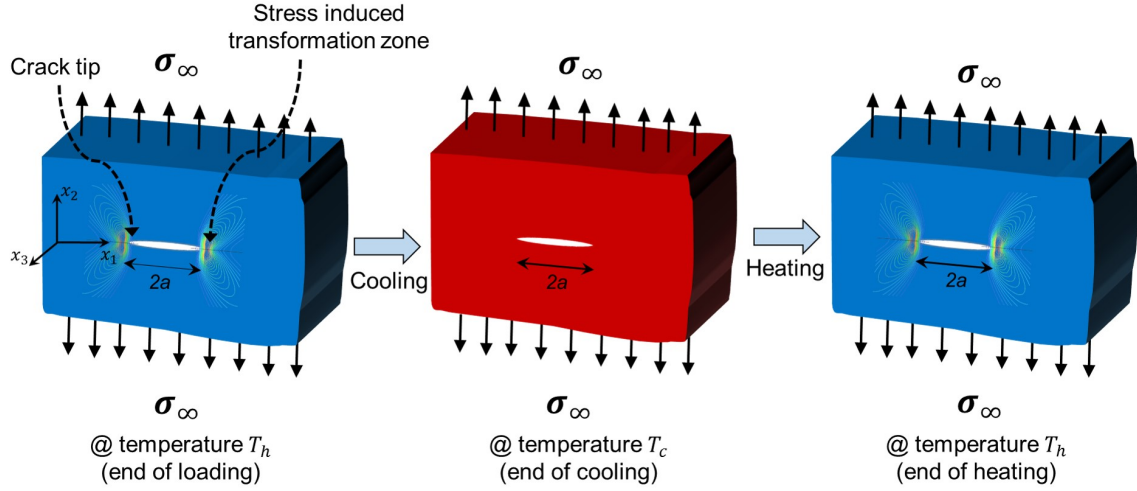
Figure 2.2: Boundary value problem for an infinite center-cracked SMA plate in initial austenite phase subjected to a constant far-field uniaxial tensile loading and thermal cycling. Martensite regions are shown in red color and austenite ones in blue.

of the constitutive law dictate that the normalized stresses, $\sigma_{ij}/\sigma_\infty$, strains, ε_{ij}/H_{sat}, and temperature, $C_M(T - M_s)/\sigma_\infty$ will be dependent on the following dimensionless parameters:

$$\frac{E_A H_{sat}}{\sigma_\infty}, \; k\sigma_\infty, \; \frac{C_M(A_s - M_s)}{\sigma_\infty}, \; \frac{C_M(A_f - A_s)}{\sigma_\infty}, \; \frac{C_M(M_s - M_f)}{\sigma_\infty}, \; \frac{C_M}{C_A},$$

$$\frac{E_M}{E_A}, \; \nu_M, \frac{\nu_M}{\nu_A}, \tag{2.11}$$

which, under the convention of tensile stresses being positive, are subject to the following inequalities

$$\frac{C_M(A_f - A_s)}{\sigma_\infty} \geq 0 \quad \text{and} \quad \frac{C_M(M_s - M_f)}{\sigma_\infty} \geq 0,$$

since $M_f \leq M_s$, $A_s \leq A_f$. Note that, in what follows, the Poisson's ratios of the two phases are assumed equal, *i.e.*, $\nu_A = \nu_M = \nu$, which is the case for most SMA material systems.
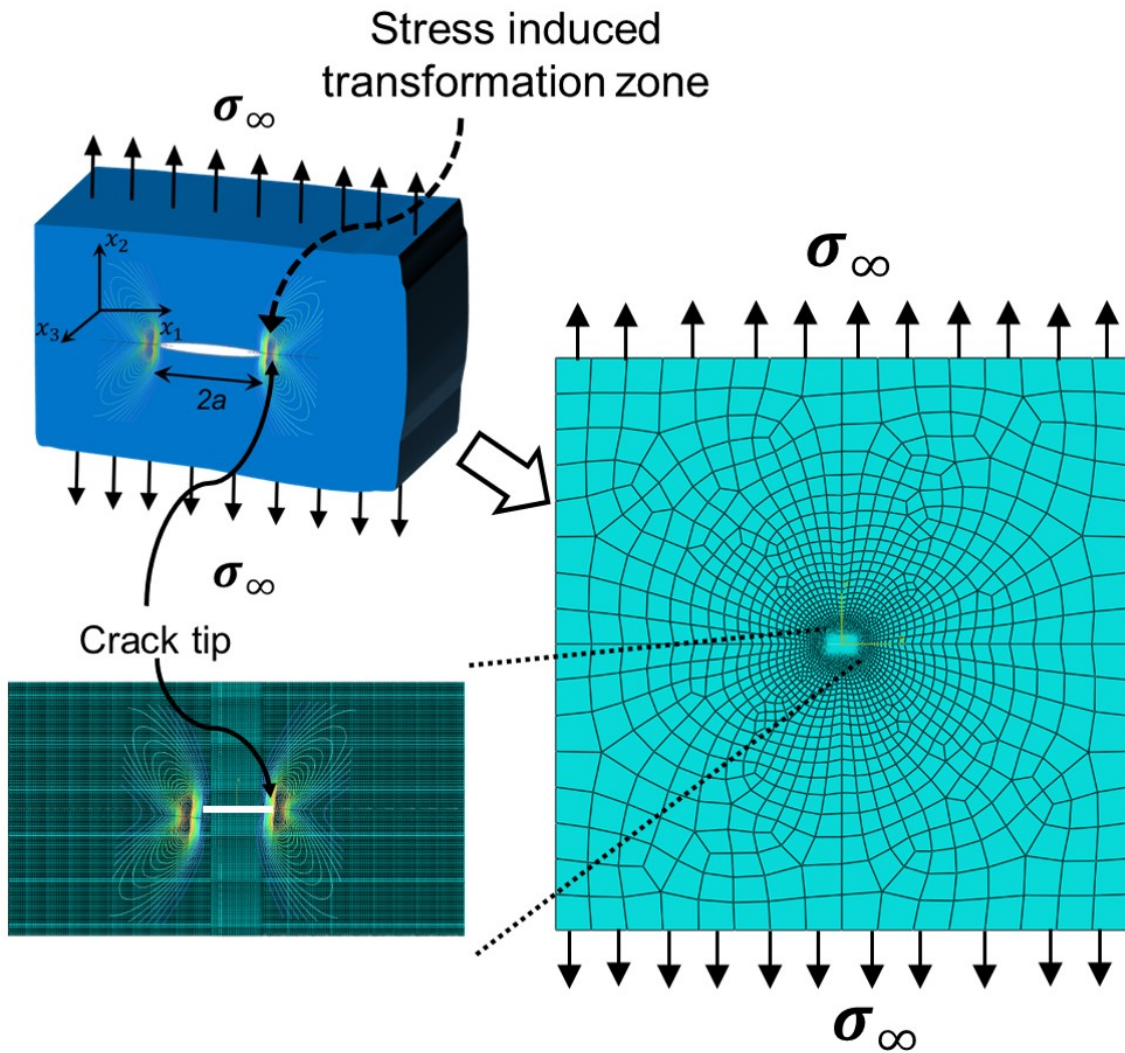
Figure 2.3: Finite element discretization of the infinite medium center-cracked SMA boundary value problem
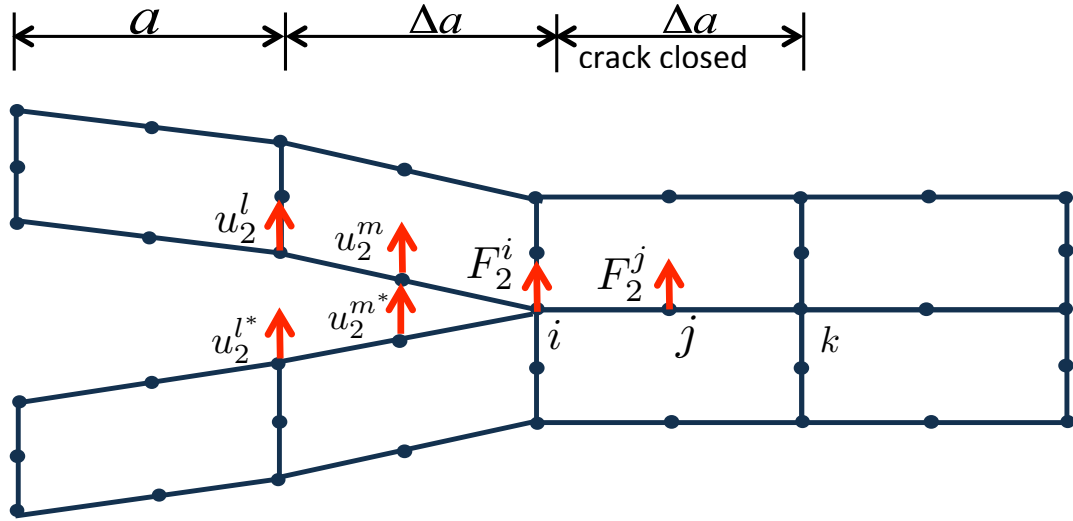
Figure 2.4: VCCT for eight-node quadratic elements

2.4 Numerical Results

Before presenting results pertaining to crack advance, a brief description of the numerical findings regarding the mechanical fields near the crack tip and the driving force for crack growth in static cracks, obtained in [11, 8], is given.

2.4.1 Brief review of the mechanical fields and driving force for crack growth prior to crack advance

As shown in Baxevanis *et al.* [11, 8], prior to crack growth, the incremental response of the material inside the fully transformed zone surrounding the crack tip is linear elastic at all times, and the fields are characterized by a crack-tip energy release rate, G_I. During cooling, the thermomechanically-induced "global" scale phase transformation, *i.e.*, transformation extending to infinity, results in stress redistribution near the crack that substantially increases the crack-tip energy release rate, an order of magnitude for some material systems. The evolution of normalized crack-tip energy release rate, G_I/G_∞, during a thermal cycle is shown in Fig. 2.5

for the parameter values given in Table 2.1 under the assumption that the critical crack-tip energy release rate value required for crack growth is never reached, where G_∞ represents the energy release rate resulting from the applied mechanical load prior to thermal cycling. G_I/G_∞ first increases during cooling, reaches a peak, and then decreases before attaining a constant value at temperature $T = M_f$, at which the entire SMA specimen has fully transformed into martensite. During heating, the energy release rate starts increasing at $T = A_s$, which marks the beginning of reverse phase transformation behind the crack tip, reaches a peak, and decreases before attaining a constant value. As discussed [11, 8], the increase of the energy release rate during cooling should be attributed to "global" phase transformation occurring in a fan ahead of the crack tip where the transformation strains have an anti-shielding effect, whereas, the subsequent decrease once the peak is reached is attributed to phase transformation occurring in regions behind the crack tip. Similar arguments can explain the evolution of energy release rate during heating.
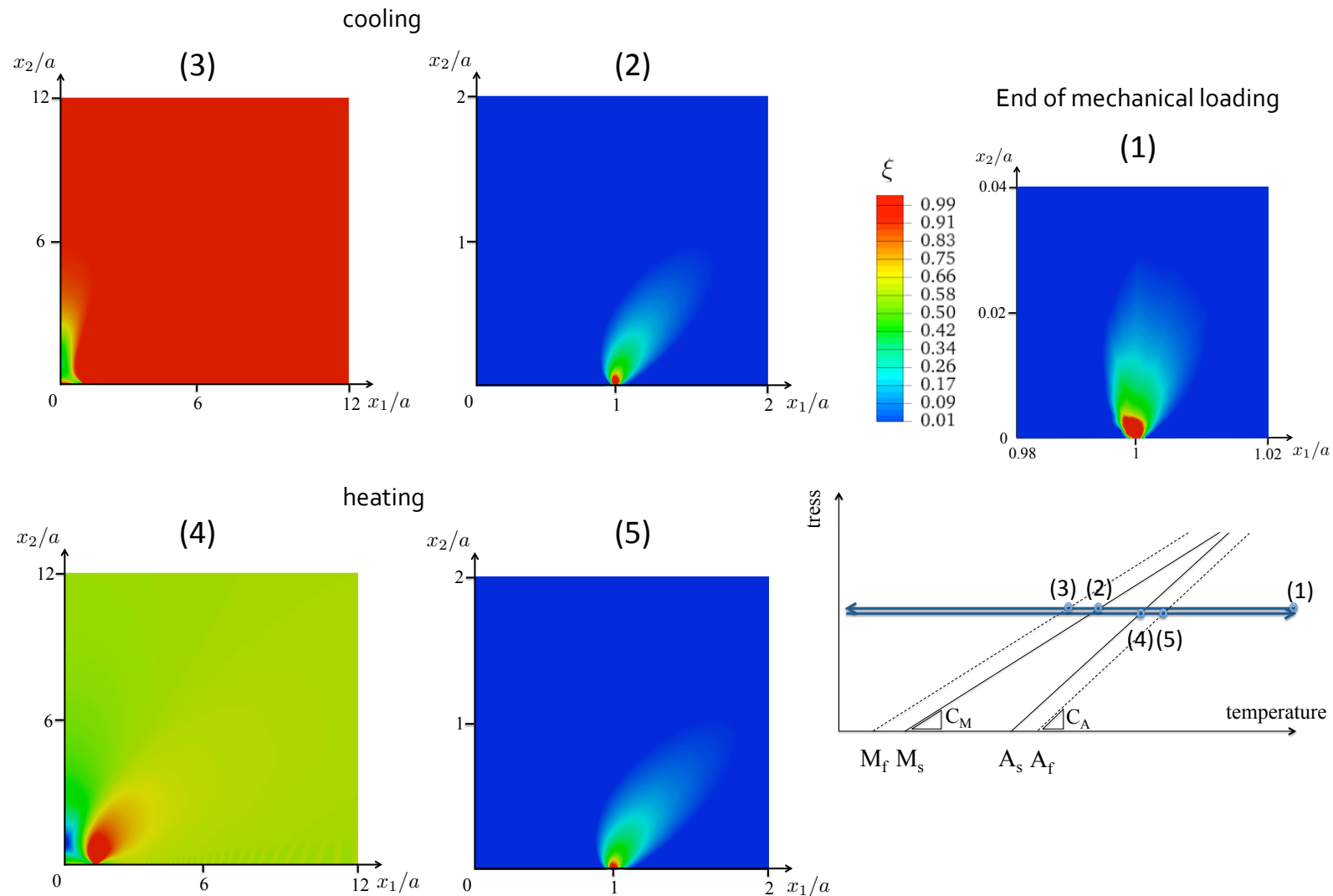
Figure 2.5: Normalized energy release rate, G_I/G_∞, versus normalized temperature, $C_M(T - M_s)/\sigma_\infty$, and martensite volume fraction, ξ, during cooling. The martensite volume fraction distribution during heating is similar to the one during cooling for the same values of G_I/G_∞(from Figure 3 of [11], © 2016 Elsevier, with permission of Elsevier, http://dx.doi.org/10.1016/j.jmps.2015.12.011).

Table 2.1: Dimensionless parameter values used for the numerical results except if stated otherwise.

parameter	value	parameter	value
$E_A H_{sat}/\sigma_\infty$	4	C_M/C_A	1
$C_M(A_s - M_s)/\sigma_\infty$	1	$k\sigma_\infty$	6.25
$C_M(M_s - M_f)/\sigma_\infty$	1	E_M/E_A	0.75
$C_M(A_f - A_s)/\sigma_\infty$	1	ν	0.33

Table 2.2: Parameter values used for the numerical results presented. These values correspond to $Ni_{60}Ti_{40}$ (wt%) [44].

parameter	value	parameter	value
E_A [MPa]	75150	H_{sat}	0.0135
E_M [MPa]	51000	k [MPa^{-1}]	0.0022
$\nu_A = \nu_M$	0.33	M_f [K]	268
		M_s [K]	357
		A_s [K]	293
		A_f [K]	372
		C_A [MPa K^{-1}]	22.16
		C_M [MPa K^{-1}]	23.55
		n_1, n_2, n_3, n_4	0.18, 0.25, 0.18, 0.18
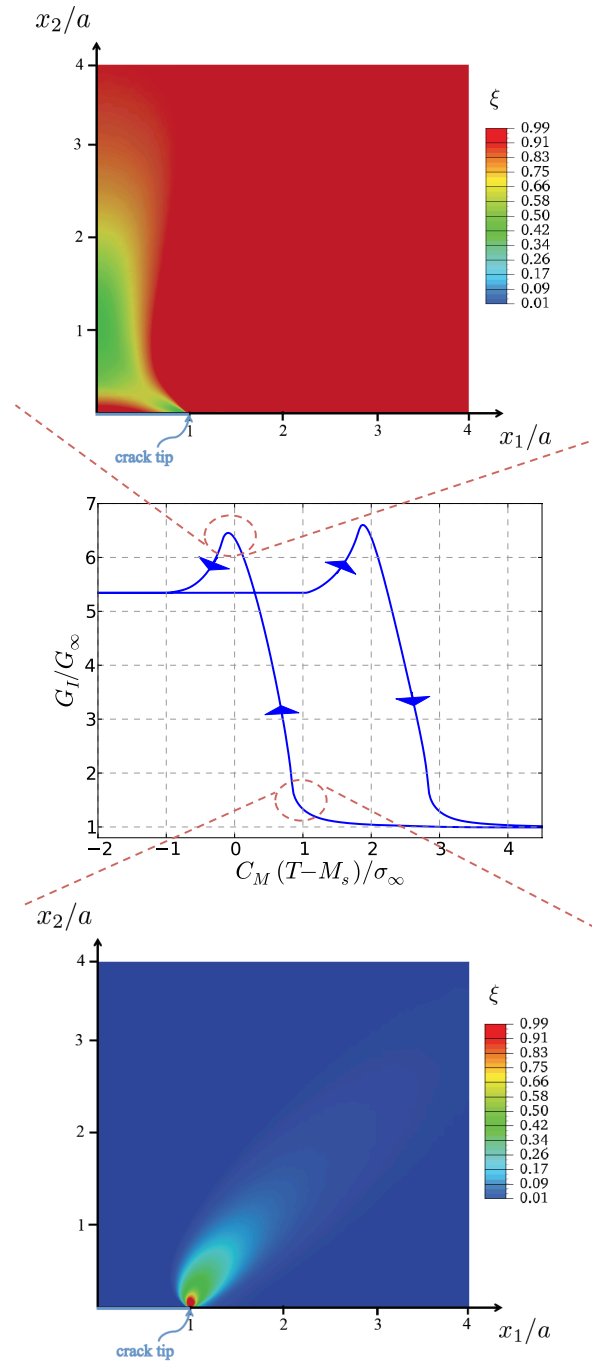
Figure 2.6: Normalized energy release rate, G_I/G_∞, versus normalized temperature, $C_M(T - M_s)/\sigma_\infty$, and martensite volume fraction, ξ, during cooling. The martensite volume fraction distribution during heating is similar to the one during cooling for the same values of G_I/G_∞ (from Figure 6 of [11], © 2016 Elsevier, with permission of Elsevier, http://dx.doi.org/10.1016/j.jmps.2015.12.011).
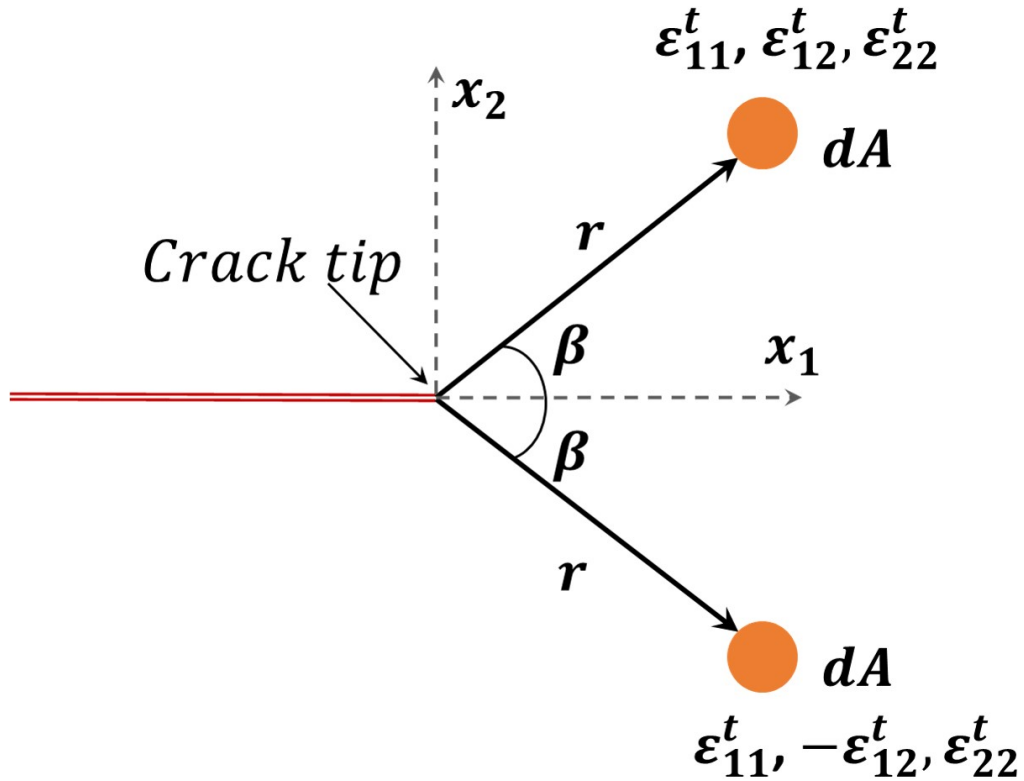
Figure 2.7: Two symmetrically placed circular differential elements of material undergoing simultaneous transformation and plastic strains ($E_{\gamma\delta}^t$) in the presence of a semi-infinite crack in an infinite domain.

The effect of large scale transformation strain on the crack-tip energy release rate G_I, or equivalently on the crack-tip stress intensity factor K_I, can be explained by the enhancement/reduction in the near-tip intensity under plane strain mode I conditions due to two differential elements of equal areas dA placed symmetrically about the crack tip and undergoing transformation straining (Figure 2.7). In the polar co-

ordinate system with crack tip as origin, the first differential element is located at (r, β) and is characterized by uniform stress-free strains $(\varepsilon_{11}^t, \varepsilon_{12}^t, \varepsilon_{22}^t)$, whereas the second is located at $(r, -\beta)$ and undergoes equivalent strains given by $(\varepsilon_{11}^t, -\varepsilon_{12}^t, \varepsilon_{22}^t)$, symmetric due to mode I loading conditions [22, 65]. The enhancement/reduction in the near-tip intensity, dK_I, is given by

$$dK_I = \frac{1}{\sqrt{8\pi}} \frac{EdA}{1 - \nu^2} r^{-3/2} M(\varepsilon_{\gamma\delta}^t, \beta), \tag{2.12}$$

where

$$M\left(\varepsilon_{\gamma\delta}^t, \beta\right) = \varepsilon_{\alpha\alpha}^t \cos\frac{3\beta}{2} + 3\varepsilon_{12}^t \cos\frac{5\beta}{2} \sin\beta + \frac{3}{2}\left(\varepsilon_{22}^t - \varepsilon_{11}^t\right) \sin\frac{5\beta}{2} \sin\beta, \tag{2.13}$$

and $\varepsilon_{\gamma\delta}^t = \varepsilon_{\gamma\delta}^t + \varepsilon_{\gamma\delta}^p$, $\varepsilon_{\gamma\delta}^t$ and $\varepsilon_{\gamma\delta}^p$ being the transformation strain components, and E and ν are the elastic modulus and Poisson ratio of martensite. Greek indices take values 1, 2 and repeated index indicates sum over 1 and 2 in the above expressions.

Expressions (2.12) and (2.13) show that any transforming material contained within a fan at an angle β in front of the crack increases near-tip intensity and thus the energy release rate whereas any material behind this fan reduces it. For a material undergoing purely dilatational transformation $\beta = 60^o$ whereas for a purely shear transformation $\beta = 36^o$. Although this analysis is quantitatively valid only for sufficiently small distances from the crack tip and that the present crack configuration results in intense shearing at planes 45° angles from the tensile direction, global scale phase transformation in front of the crack tip during cooling can plausibly result in similar enhancement in the crack tip energy release rate. Transformation occurring behind the crack tip can similarly reduce the near-tip intensity or crack tip energy

48

release rate and shield the crack. During heating, reverse phase transformation first occurs behind the crack and leads to loss of shielding from the strains intensifying G_I. As regions in front of the crack reverse transform, transformation strains are recovered and the resulting enhancement in G_I is lost, leading to a decrease in G_I. The observed enhancement in near-tip intensity and thereby in the normalized driving force for crack growth G_I/G_∞, can thus be attributed to global phase transformation caused by thermal actuation in the center-cracked infinite medium SMAs.

2.4.3   Stable crack growth

In what follows, the ratio G_{crit}/G_∞ is chosen such that during cooling the crack-tip energy release rate, G_I, reaches the critical value, G_{crit}, and initiates crack growth. The most important result, explained in detail below, is that *stable crack growth* is observed, *i.e.*, further cooling is needed to maintain crack growth.

2.4.3.1   Martensitic transformation and near-tip stress field during crack growth

Prior to presenting results for the toughness enhancement associated with stable crack growth, some features of the crack-tip mechanical fields are now presented.

The transformation region depicted by the martensitic volume fraction close to the crack tip at initiation of crack growth and during crack advance are shown in Figure 2.8 for an applied load level such that $G_{crit}/G_\infty = 2$. The chosen system of co-ordinates (x_1, x_2) is normalized with the initial half crack length, a, where origin represents the center of the crack and $(x_1, 0) = (1, 0)$ represents the initial location of the crack tip. Figure 2.8(a) shows the region of stress induced martensite (red color) at the initiation of crack growth, surrounded by a region of partially transformed material and the rest of the specimen in untransformed austenitic phase (blue color). As the crack advances, unloading takes place in the wake of the growing crack, however, no reverse phase transformation is observed due to further cooling required

49

to drive crack growth (Figure 2.8(b)) (see the phase diagram in Figure 2.1).

The material points in front of of the crack tip experience non-proportional loading due to the "global" transformation interfering with the boundary conditions, as depicted in Figure 2.10, in which the stress triaxiality ratio $T = \bar{\sigma}/\sigma_m$ (σ_m denotes the mean normal stress) distribution is plotted at the initiation of crack growth and during crack advance. However, at the vicinity of the crack-tip, inside the region of fully-transformed material, the stress field at all times is equivalent to the asymptotic K-field of an isotropic elastic material. During crack advance, the stress intensity factor $K = K_{crit}$ is related to the critical crack-tip energy release rate through $G_{crit} = (1 - \nu_M^2)K_{crit}^2/E_M$, as it can be seen in Figure 2.11, in which the angular dependence of the SMA stress field close to the crack tip during crack growth is compared to the angular dependence of the stress field for an isotropic linear elastic solid. Moreover, the numerical results suggest that close to the crack tip the stresses have a $1/\sqrt{r}$ radial asymptotic behavior during thermal cycling. Normalized von Mises stress field during crack growth shown in Figure 2.9, on the other hand, does not show any significant variation in magnitude. The region of high equivalent stresses simply follows the advancing crack tip and is a direct result of the crack growth being driven by stress distribution due to forward phase transformation in front of the tip. These results, apart from justifying the assumption of a single parameter being capable of describing the mechanical fields close to the crack tip, validate the VCCT in calculating that parameter.
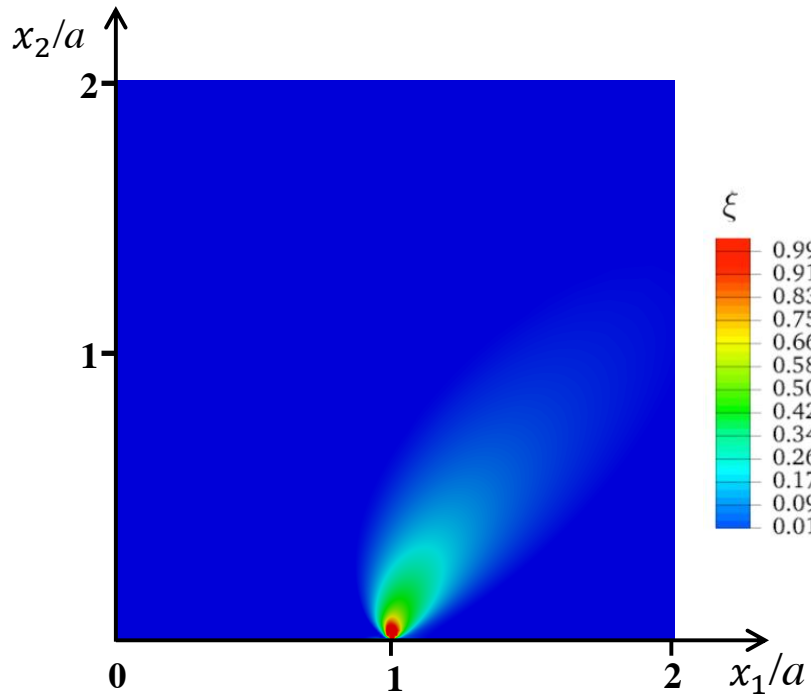
(a) at initiation of crack growth
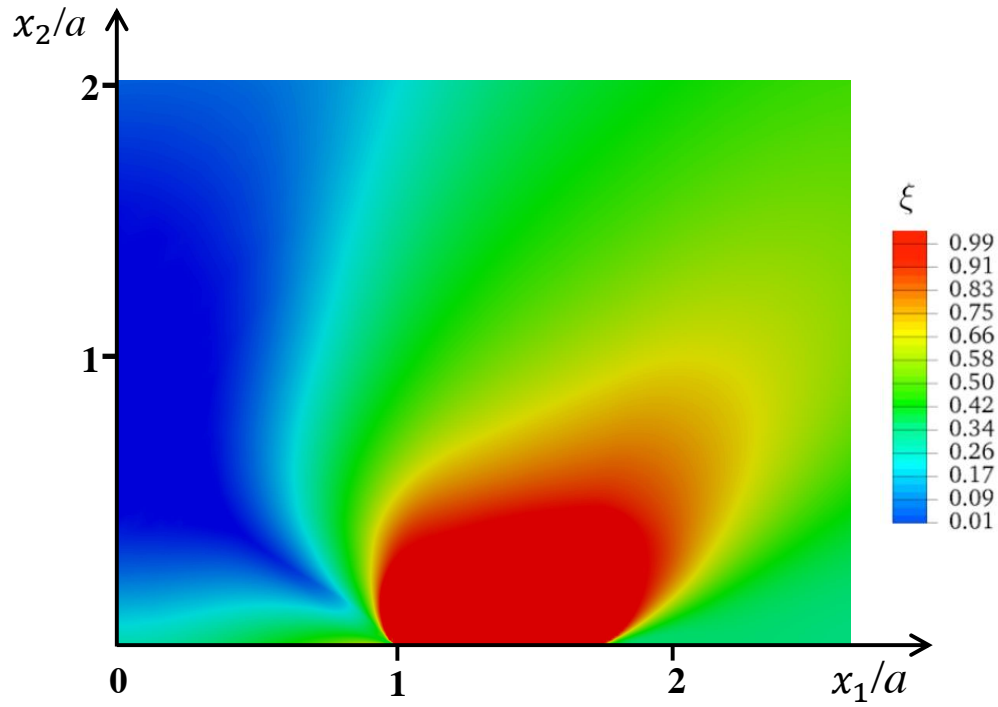
(b) during crack growth

Figure 2.8: Martensite volume fraction distribution, ξ, near the crack tip.
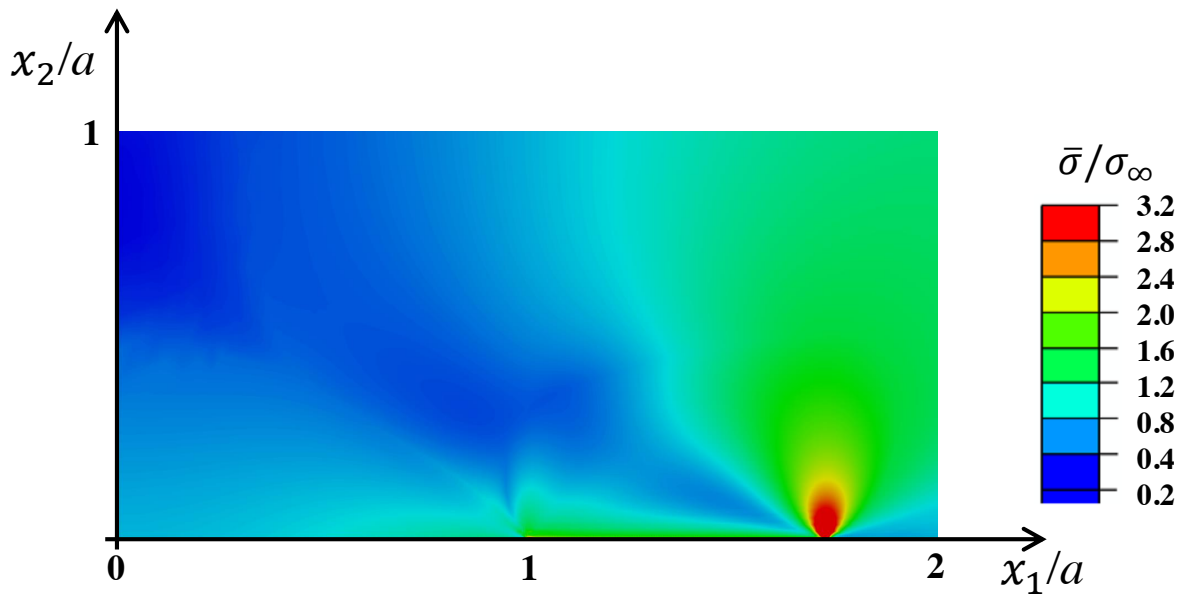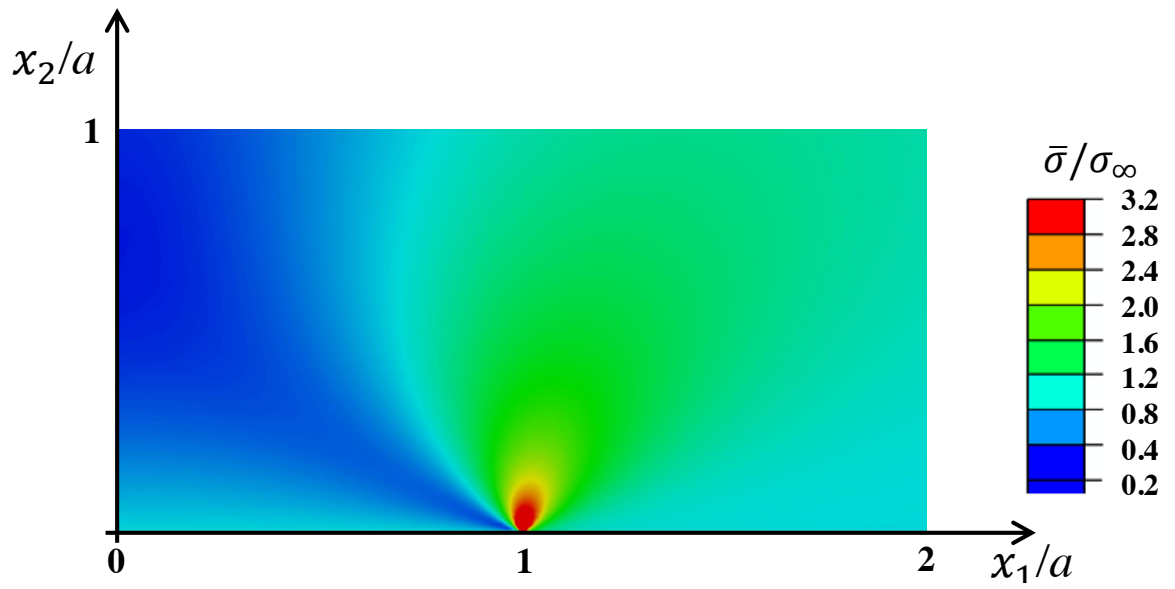
(b) von Mises equivalent stress, $\bar{\sigma}/\sigma_\infty$, during crack growth

Figure 2.9: von Mises equivalent stress normalized with the applied bias stress, $\bar{\sigma}/\sigma_\infty$, where $\bar{\sigma}$ is the von Mises stress and σ_∞ is the applied stress.
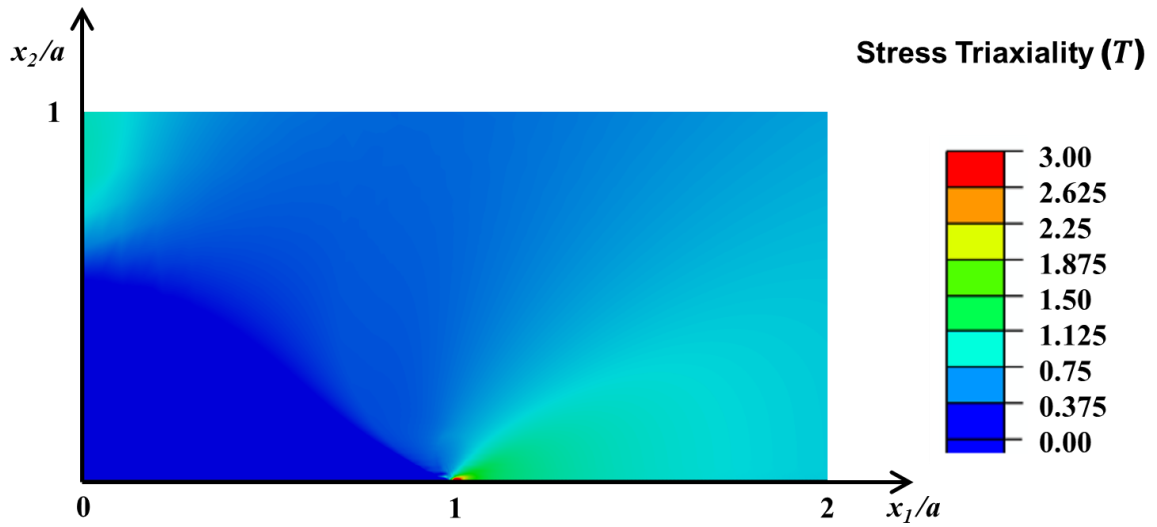
(a) Stress triaxiality ratio, T, at the initiation of crack growth
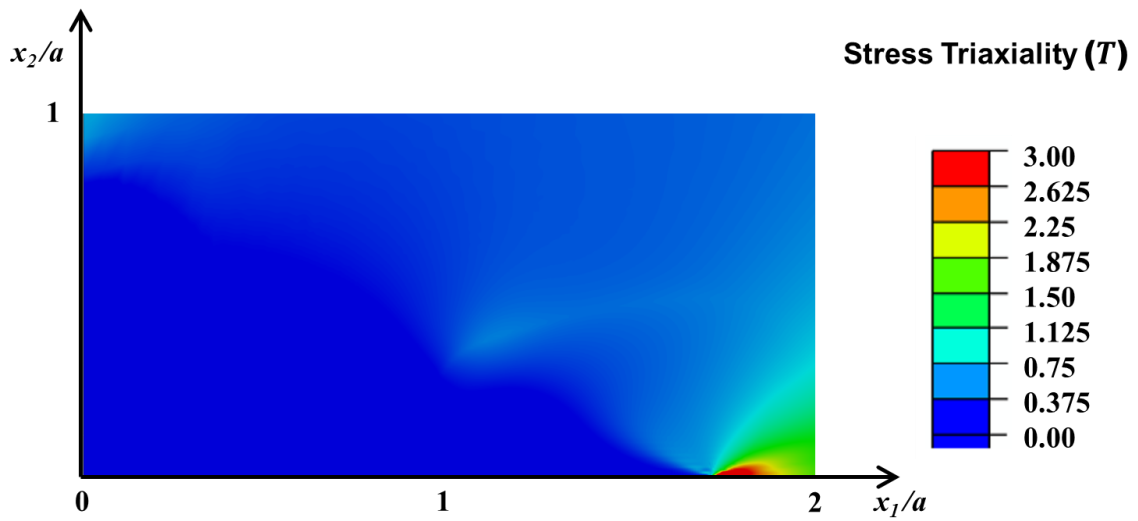
(b) Stress triaxiality ratio, T, during crack growth

Figure 2.10: Stress triaxiality ratio, $T = \bar{\sigma}/\sigma_m$, where $\bar{\sigma}$ is the von Mises stress and σ_m is the mean normal stress.
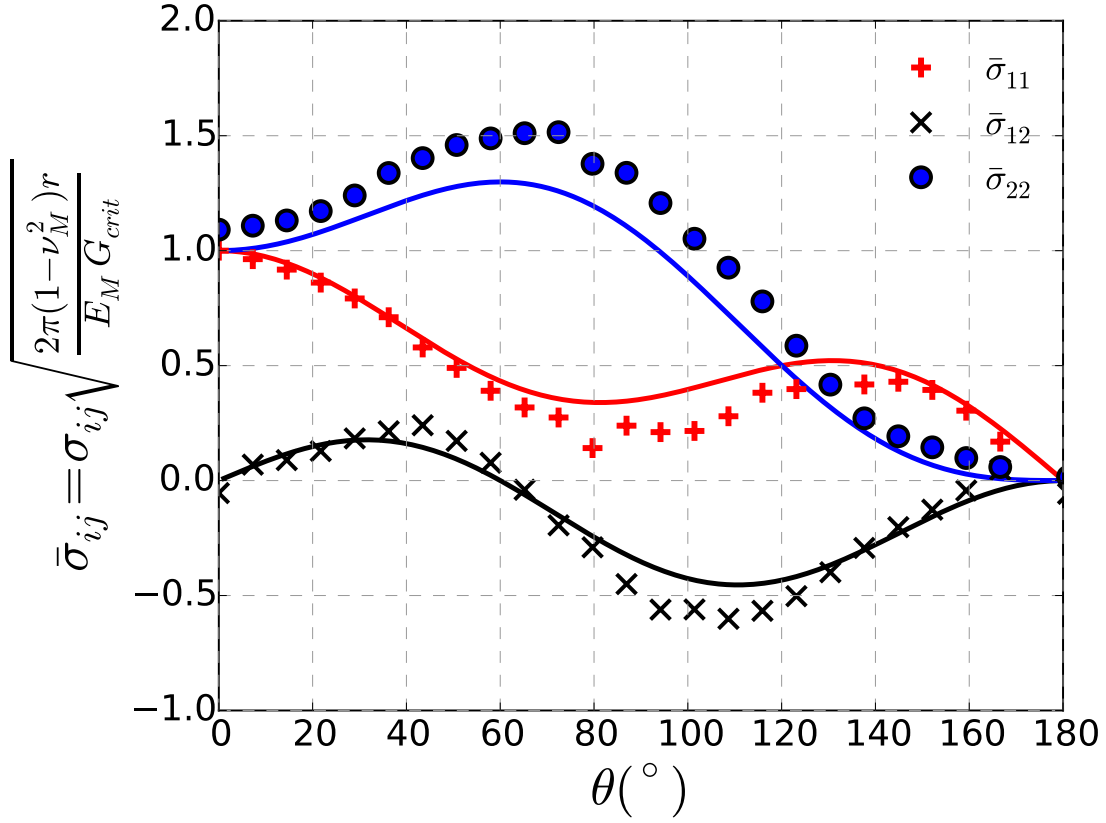
Figure 2.11: Angular distribution of stresses close to the crack tip during crack growth. The markers are the numerical results for the SMA material and the solid lines are numerical results for an elastic material with the properties of martensite. The $1/\sqrt{r}$ radial dependence has been accounted for within the normalization.

2.4.3.2 Toughness enhancement associated with crack advance

Stable crack growth arises due to stress redistribution caused by the transformation deformations left in the wake of the growing crack that shields the crack [11, 8] and it is therefore necessary to continue cooling the material in order to maintain a critical stress field at the advancing crack tip. Eventually, once the crack advances a distance comparable to its initial length, the increment of the loading parameter, *i.e.*, temperature, needed to achieve a given increment of growth diminishes

and the crack approaches nominally steady-state growth at a constant temperature (Fig. 2.12). This transformation toughening response is quite similar to the one observed in pseudoelastic SMAs or other dissipative materials in which cracks grow in an initially stable manner under increasing mechanical load (or, depending on the loading arrangement, load-point displacement) until critical conditions are attained. The normalized temperature–crack advance response in Fig. 2.12 should therefore be considered indicative of toughness enhancement for the loading paths considered here, similarly to the R-curve response of dissipative materials under isothermal loading.
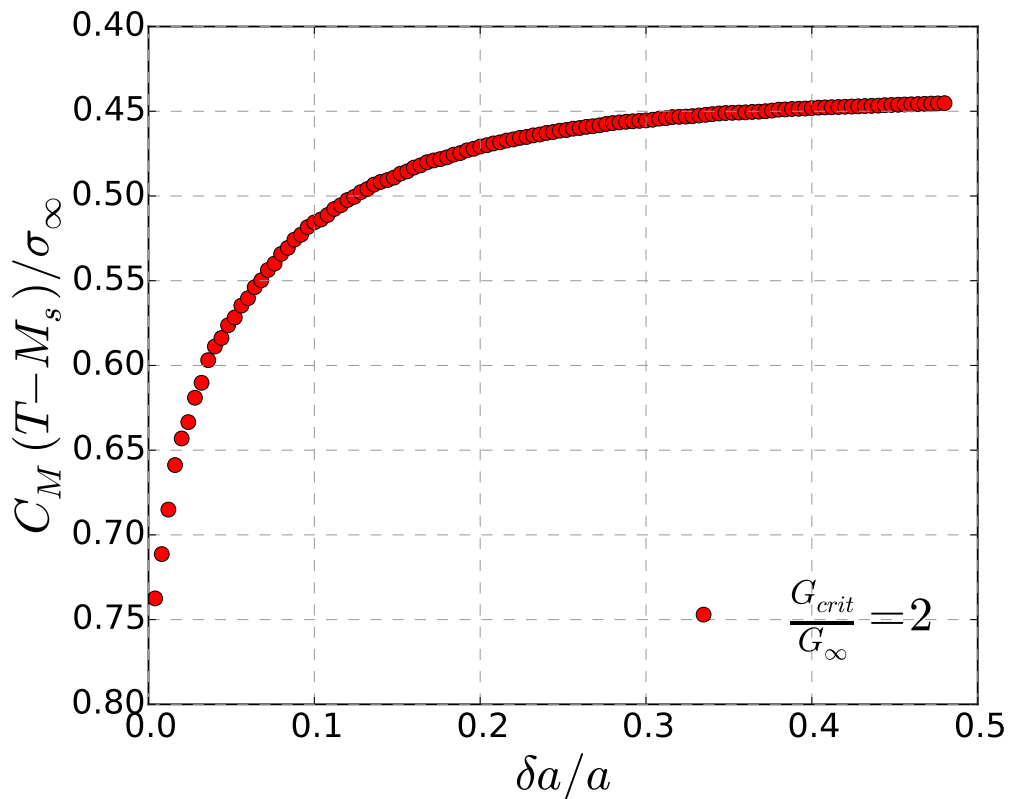
Figure 2.12: Normalized temperature, $C_M(T - M_S)/\sigma_\infty$, vs. normalized crack growth, $\delta a/a$, for $G_{crit}/G_\infty = 2$.

2.4.3.3 Influence of phase transformation metrics and bias load on crack growth

Next, the dependence of actuation-induced transformation toughening on non-dimensional transformations metrics, defined in Eq. (2.11), and bias load is presented.

In Fig. 2.13(a), the normalized temperature, $C_M(T - M_s)/\sigma_\infty$, is plotted against normalized crack growth, $\delta a/a$, for a range of values for the relative maximum transformation strain $E_A H_{sat}/\sigma_\infty$. Larger relative transformation strains implies larger transformation strains left in the wake of the growing crack and more energy being dissipated by the transformed material, which in turn implies that more cooling is required from the initiation of crack growth for steady state conditions to be met. The effect of $C_M(M_s - M_f)/\sigma_\infty$ on the transformation toughening is presented in Fig. 2.13(b). Higher $C_M(M_s - M_f)/\sigma_\infty$-values require higher temperature differentials to reach given levels of martensite volume fraction during forward transformation (which is interpreted as transformation hardening) and result in lower crack-tip energy release rate values in static cracks during thermal cycling [11]. Therefore, for higher $C_M(M_s - M_f)/\sigma_\infty$-values more cooling is required for attaining steady-state growth conditions.
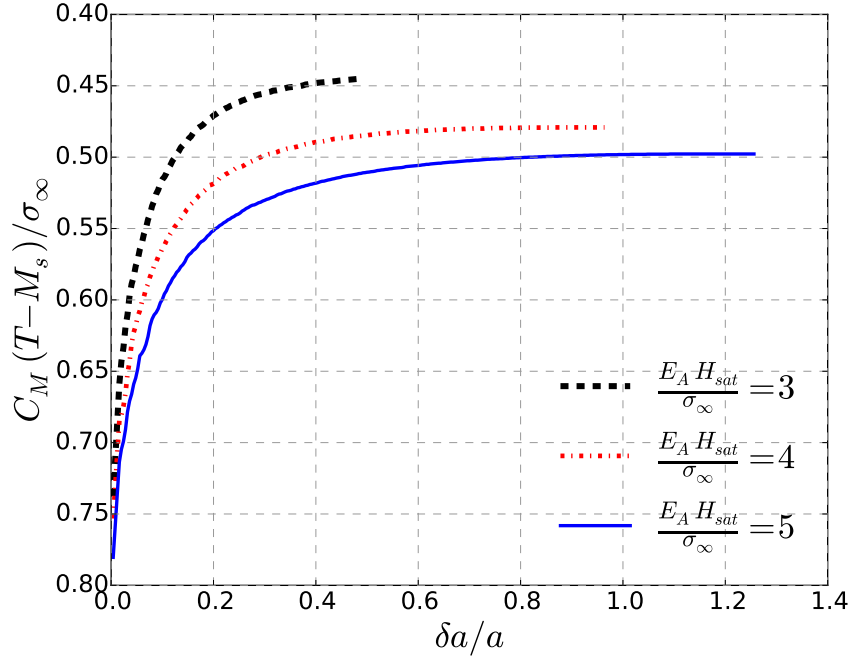
(a) Effect of relative maximum transformation strain $E_A H_{sat}/\sigma_\infty$
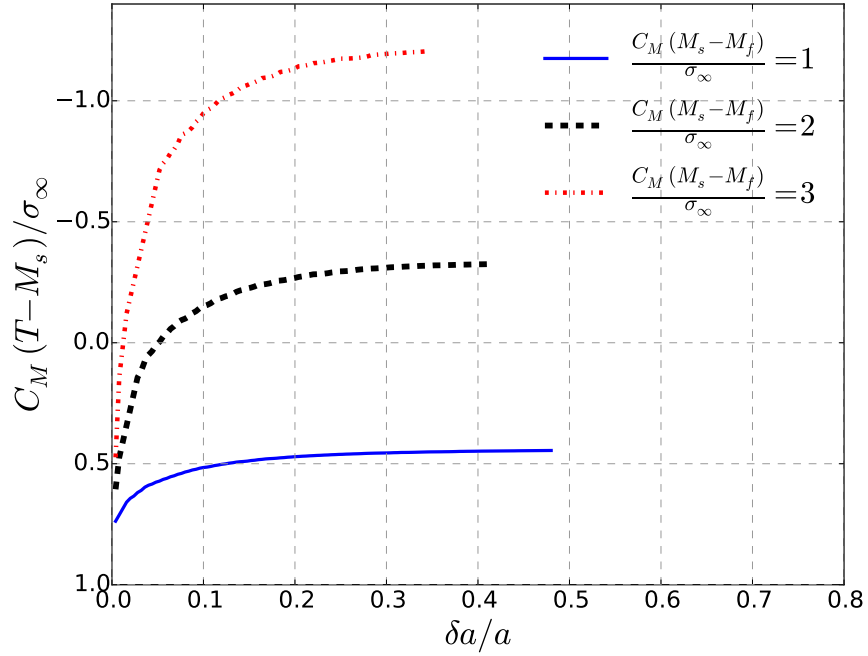
(b) Effect of "transformation hardening" $C_M(M_s - M_f)/\sigma_\infty$

Figure 2.13: Normalized temperature, $C_M(T-M_s)/\sigma_\infty$, vs normalized crack growth, $\delta a/a$.

57

Table 2.3: Parameter values used for the numerical results presented and used for normalization. These values correspond to $Ni_{60}Ti_{40}$ (wt%) [44].

parameter	value	parameter	value
E_A [MPa]	75150	H_{sat}	0.0135
E_M [MPa]	51000	k [MPa^{-1}]	0.0022
$\nu_A = \nu_M$	0.33	M_f [K]	268
		M_s [K]	357
		A_s [K]	293
		A_f [K]	372
		C_A [MPa K^{-1}]	22.16
		C_M [MPa K^{-1}]	23.55
		n_1, n_2, n_3, n_4	1.0, 1.0, 1.0, 1.0
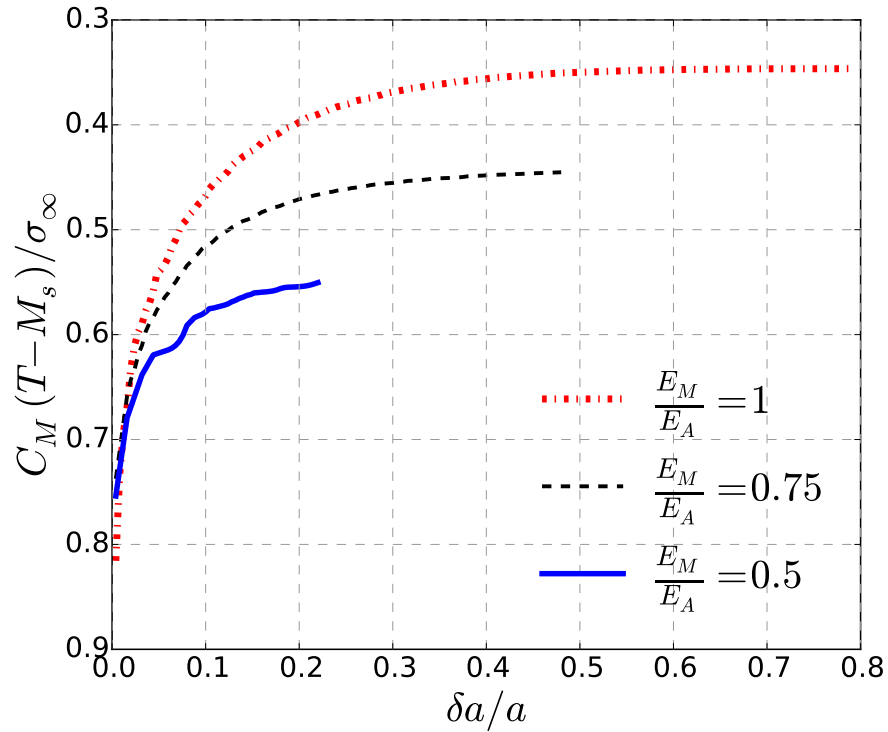
Figure 2.14: Normalized temperature, $C_M(T - M_s)/\sigma_\infty$, vs normalized crack growth, $\delta a/a$ showing the effect of "elastic mismatch" E_M/E_A.

Since most of the non-dimensional parameters listed in Eq. 2.11 depend on the in-plane uniform uniaxial tensile stress at infinity, σ_∞, and therefore are not material parameters, the influence of the bias load on the crack growth kinetics is examined for dimensional parameters chosen so as to conform with those of $Ni_{60}Ti_{40}$ (wt%) and yield quantitative results on the crack growth response expected for this specific material during actuation.
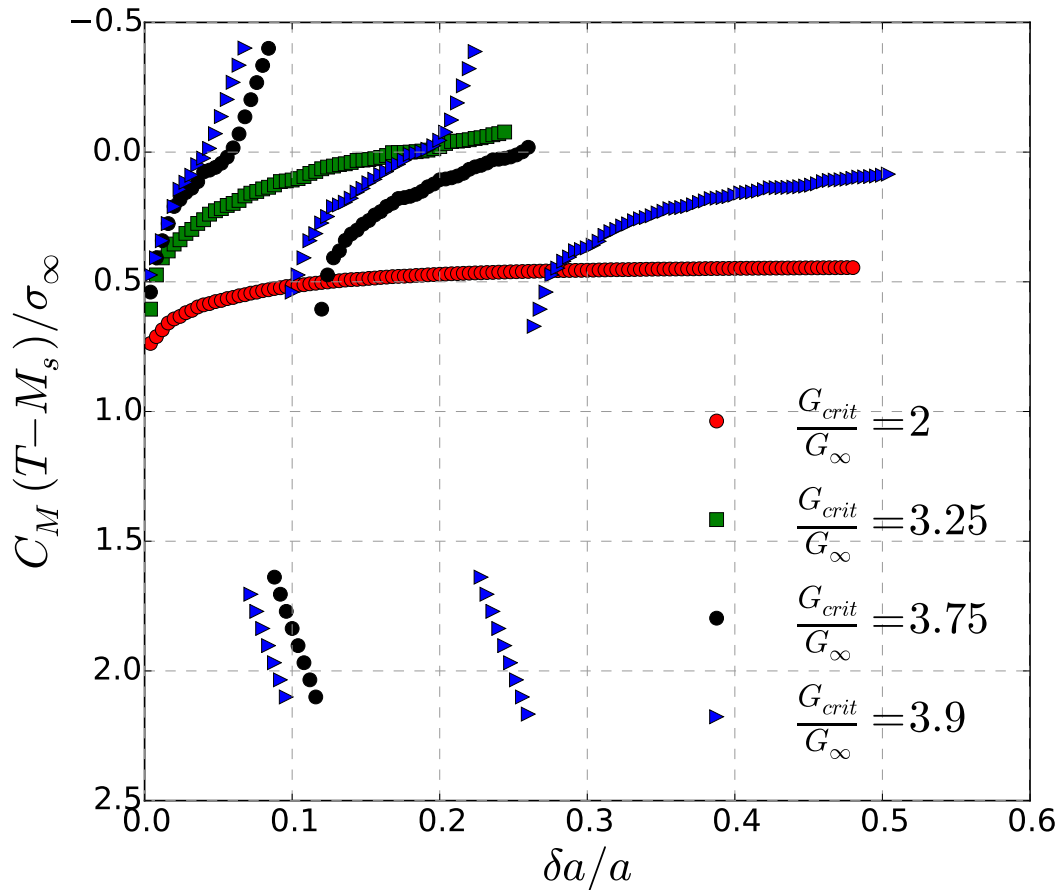
Figure 2.15: Normalized temperature, $C_M(T - M_S)/\sigma_\infty$, vs. normalized crack growth, $\delta a/a$, for varying G_{crit}/G_∞. The parameters values used are those of Table 3.1.

The influence of the stable crack growth response is depicted in Fig. 2.15 for different values of applied load, σ_∞, indirectly resulting in G_{crit}/G_∞ equal to 3.25, 3.75, and 3.9. For $G_{crit}/G_\infty = 3.25$, the response is similar to that of Fig. 2.12, in the sense that steady-state crack growth conditions are met during cooling in the first thermal cycle. For sufficiently high values of G_{crit}/G_∞ (= 3.75 and 3.9), $i.e.$, sufficiently small bias loads, however, the material is capable of sustaining multiple cooling/heating cycles before crack growth reaches nominally steady state conditions. In these cases, the increment of temperature needed to attain a given increment of crack advance initially gets smaller, until transformation starts taking place in a fan behind the crack tip shielding the crack and increasing the required temperature change for attaining a given increment of crack advance. Once the whole material is transformed, crack growth ceases. During heating, $i.e.$, increasing values of $C_M(T - M_S)/\sigma_\infty$, the crack also advances as the shielding effect of transformation behind the crack tip is lost (note that the peak in the energy release rate during heating is usually higher than the corresponding peak during cooling for stationary cracks (Fig. 2.5)). Crack growth in subsequent cycles results from the increase in crack length from the previous cycles since for larger cracks the crack-tip energy release rate is closer to the critical value.
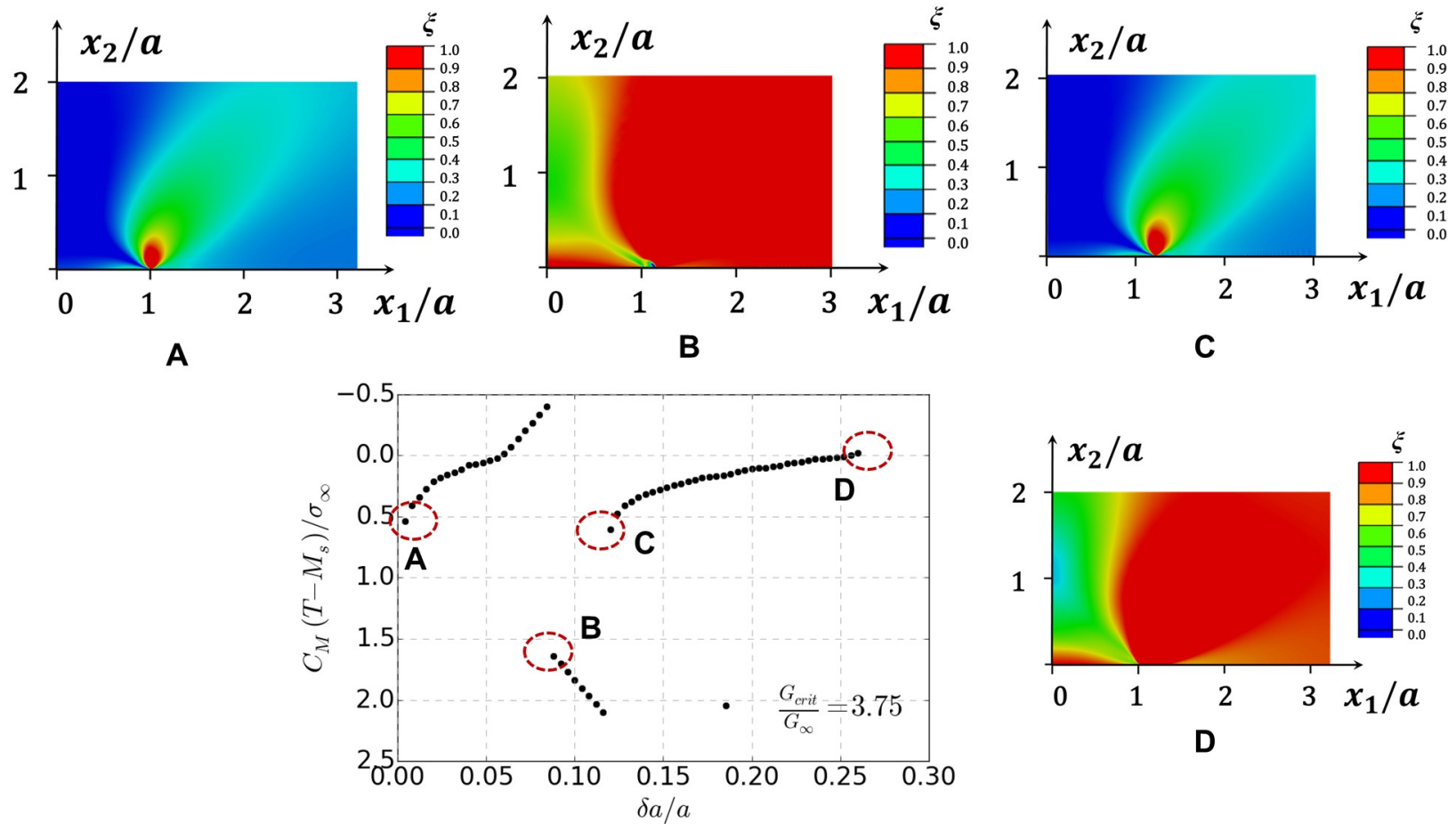
Figure 2.16: Normalized temperature, $C_M(T - M_S)/\sigma_\infty$, vs. normalized crack growth, $\delta a/a$, for $G_{crit}/G_\infty = 3.75$. The near-tip martensite volume fraction contours are shown at different stages of the crack growth: beginning of crack growth in the first cooling cycle, first heating cycle, second cooling cycle and before steady state is achieved.
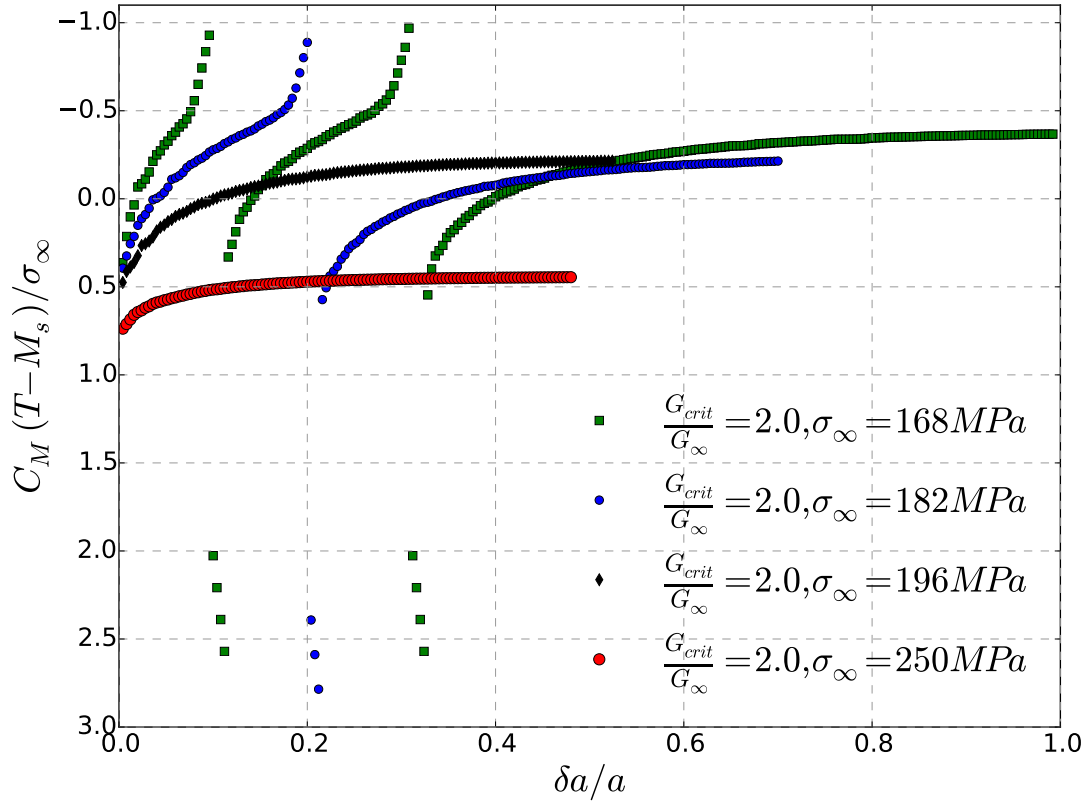
Figure 2.17: Normalized temperature, $C_M(T - M_S)/\sigma_\infty$, vs. normalized crack growth, $\delta a/a$, for varying bias loads, G_{crit}/G_∞. The parameters values used are those of Table 3.1.

To further elucidate the phenomenon of stable crack growth through multiple cycles, contours of near-tip martensite volume fraction during crack growth through two thermal cycles is shown for the case $G_{crit}/G_\infty = 3.75$ in Figure 2.16. Different states of the crack tip fields can be seen: when crack growth is triggered during (A) the first cooling cycle, (B) the first heating cycle and (C) third cooling cycle, and (D) at the end of steady state crack growth. Small region of crack tip martensite can be seen at A, when crack growth begins in the first cooling cycle $G_{crit}/G_\infty = 3.75$, and grows by about 10% of its initial length. After cooling is completed, during heating

the material starts to reverse transforms behind the crack and leads to an increase in the crack tip energy release rate, causing crack to again grow during heating as shown in B. In second cycle, crack tip has moved further ahead as shown in C and the effective initial crack length is larger than original, causing extension at a higher temperature as shown. Finally, steady state is reached when a bulk of the material forward transforms as shown in D and the driving force produced due to thermal variations is enough to sustain crack growth till material failure.

Identical behavior is observed when the critical value of material specific crack tip energy release rate is kept constant at $G_{crit}/G_\infty = 2.0$, and the bias load σ_∞ is actually varied at different levels as shown in Figure ??, where $\sigma_\infty = 250, 196, 182, 168 MPa$. These load levels are chosen such that the crack tip energy release rate generated at the end of mechanical load in each case is equal. Here, the loading case with $\sigma_\infty = 250 MPa$ is the same as that presented in the beginning. Lower applied bias load leads to decreased transformation strains (due to the dependence of transformation strain magnitude on stress levels), and increasing amount of cooling is required to produce the same driving force for crack growth. Reduced transformation toughening in the wake of the crack also occurs due to lower transformation strain. Figure ?? shows that as the bias load is decreased to 196 MPa, crack growth starts at a lower temperature due to the modified crack tip energy release rate. Stable crack growth is seen to require greater temperature decrease or cooling and extends to more than half its original length. With decreasing bias load levels, crack growth occurs through multiple thermal cycles as shown in the figure. For 182 MPa, crack growth is triggered at a lower temperature and transformation in the global sense is completed before steady state of crack growth is reached, leading to crack arrest. In the second cooling cycle, crack growth is triggered at a higher temperature due to increase initial crack length, and reaches steady state when equilibrium

between material critical fracture toughness is equal to that resulting from thermomechanical loading. Similarly, for 168 MPa, stable crack growth occurs through three thermal cycles. Decreasing load levels also results in reduced transformation toughening as seen from the increasing temperature differential required to sustain stable crack growth.

2.4.4   Effect of crack configuration
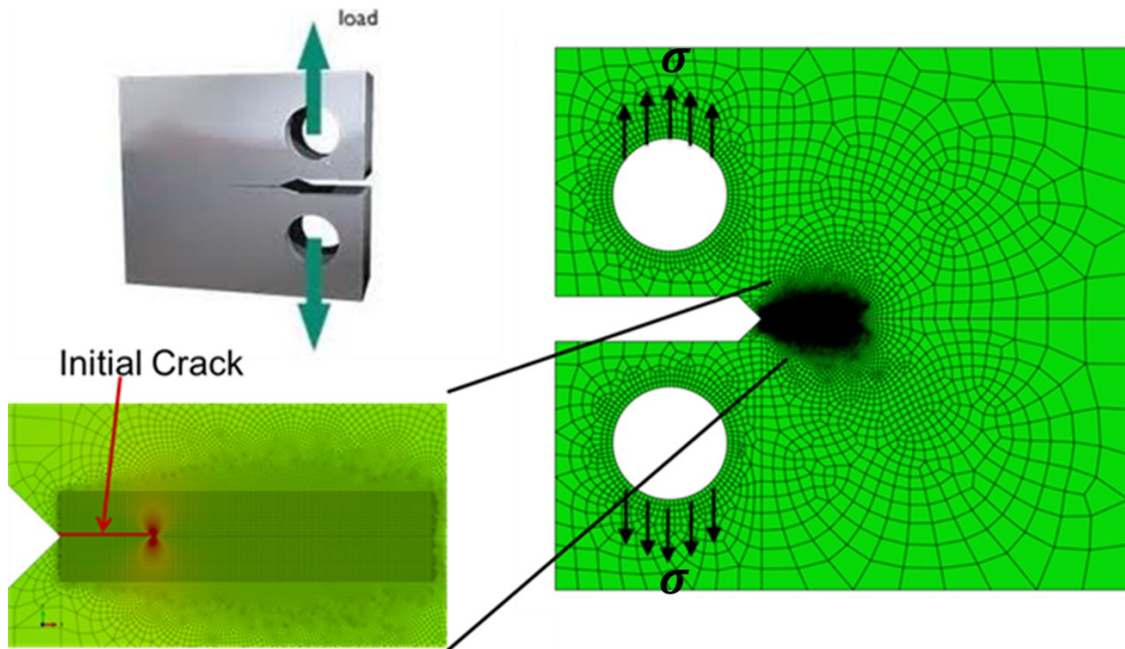
Figure 2.18: Compact tensile specimen - problem formulation and finite element mesh (from Figure 8 of [56], © 2008 Springer US, with permission of Springer-Verlag US, DOI: $10.1007/978 - 3 - 319 - 48766 - 3_17$).

In this section, numerical analysis pertaining to the effect of different crack configurations on fracture toughness of a static crack and toughness enhancement in a
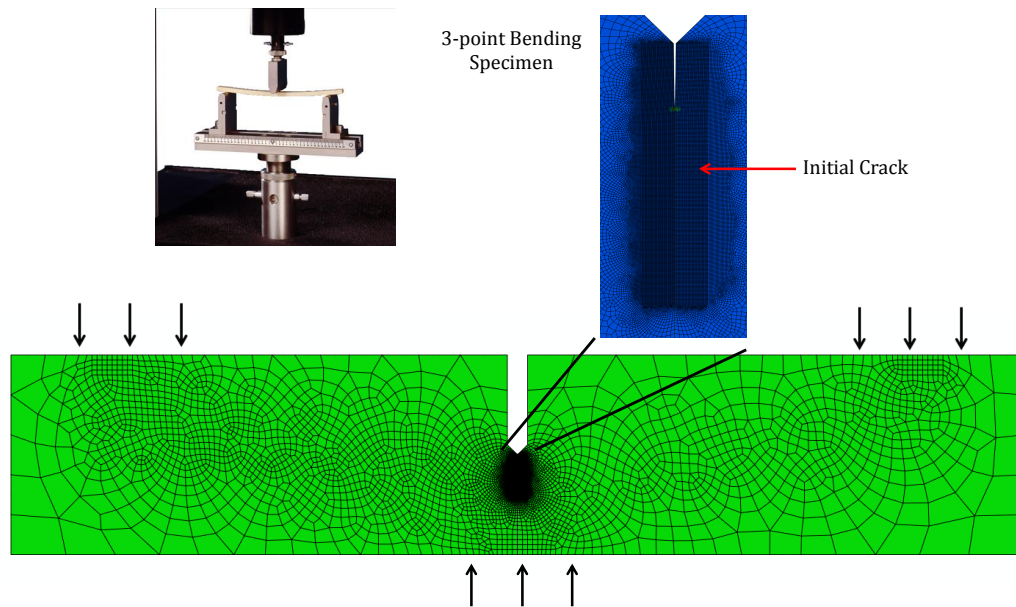
Figure 2.19: 3-point bend or single edge notched bend (SE(B)) specimen - problem formulation and finite element mesh (from Figure 9 of [56], © 2008 Springer US, with permission of Springer-Verlag US, DOI: $10.1007/978 - 3 - 319 - 48766 - 3_17$).

growing crack in thermally actuated SMAs is presented (Figure 2.18 and 2.19). To this end, following crack configurations are selected: (i) compact tension CT specimen, and (ii) three-point bend or single edge notched bend SE(B) specimen, with previously mentioned center cracked infinite domain for comparison. Vast majority of fracture toughness testing in metals is carried out on CT or SE(B) specimens and are hence chosen here. During standard fracture toughness experiments, fatigue pre-cracks are initiated in the specimens at the notch root and fracture toughness tests are then carried out. In the finite element analysis, both specimens contain pre-cracks and are then subjected to a uniaxial tensile load as shown in Figure 2.18 and Figure 2.19 at a high temperature, followed by thermal cycling such that the entire material transforms between austenite and martensite. Crack growth is initially not allowed, and crack tip energy release rate at the stationary crack is plotted in Figure

2.20.
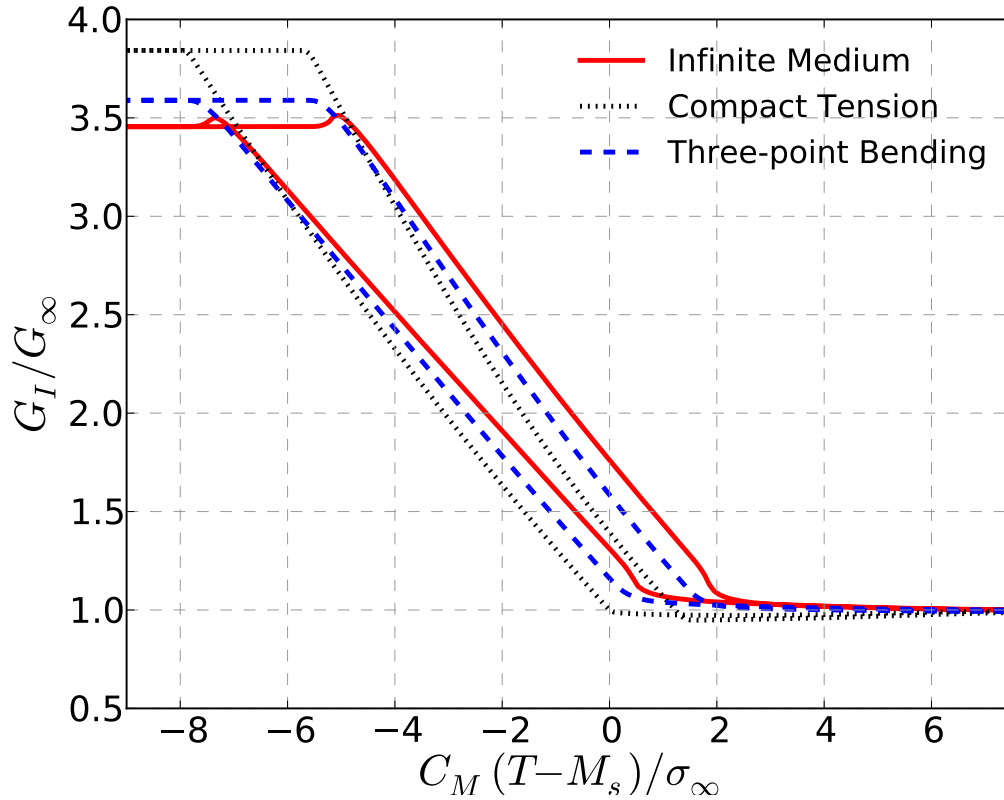
Figure 2.20: Variation of crack-tip energy release rate during thermal actuation for the following crack configurations: (a) infinite medium (b) compact tension and, (c) three-point bending (from Figure 10 of [56], © 2008 Springer US, with permission of Springer-Verlag US, DOI: $10.1007/978 - 3 - 319 - 48766 - 3_17$)..

For the thermo-mechanical parameters listed in Table 3.1, the variation of normalized crack-tip energy release rate (G_I/G_∞) with respect to the normalized temperature $C_M(T - M_s)/\sigma_\infty$ during thermal actuation is calculated for all three crack-configurations and is shown in Fig. 2.20. Bias loads are chosen such that the crack-tip energy release rate due to mechanical loading alone is maintained constant for all

configurations. The overall variation of G_I/G_∞ in CT and SE(B) is similar to that in the infinite medium: constant value before forward transformation, increase during cooling due to global phase transformation followed by plateau at the end, decrease due to reverse transformation during heating, and final constant value when material becomes fully austenite. Increase in crack-tip energy release rate during cooling is highest for the CT specimen followed by SE(B) and infinite medium, in that order. Under constant load followed by cooling, since CT configuration is more deeply cracked than SE(B), energy release rate at the stationary crack in CT rises higher due to larger stresses developed at the crack tip, than that in SE(B) or infinite medium. Towards the end of cooling, since forward transformation reaches the wake of the crack last, there is a dip in G_I/G_∞ in infinite medium. However, since forward transformation in the crack wake in CT and SE(B) specimens occurs earlier, the slight decrease in G_I/G_∞ is absent. Similarly, during heating, slight increase in G_I/G_∞ is absent in CT and SE(B), and it simply decreases back to its original value. The crack tip is closest to the specimen boundaries in CT followed by SE(B), which results in different slopes of the driving force G_I/G_∞ vs. normalized temperature $C_M(T - M_s)/\sigma_\infty$ curves.
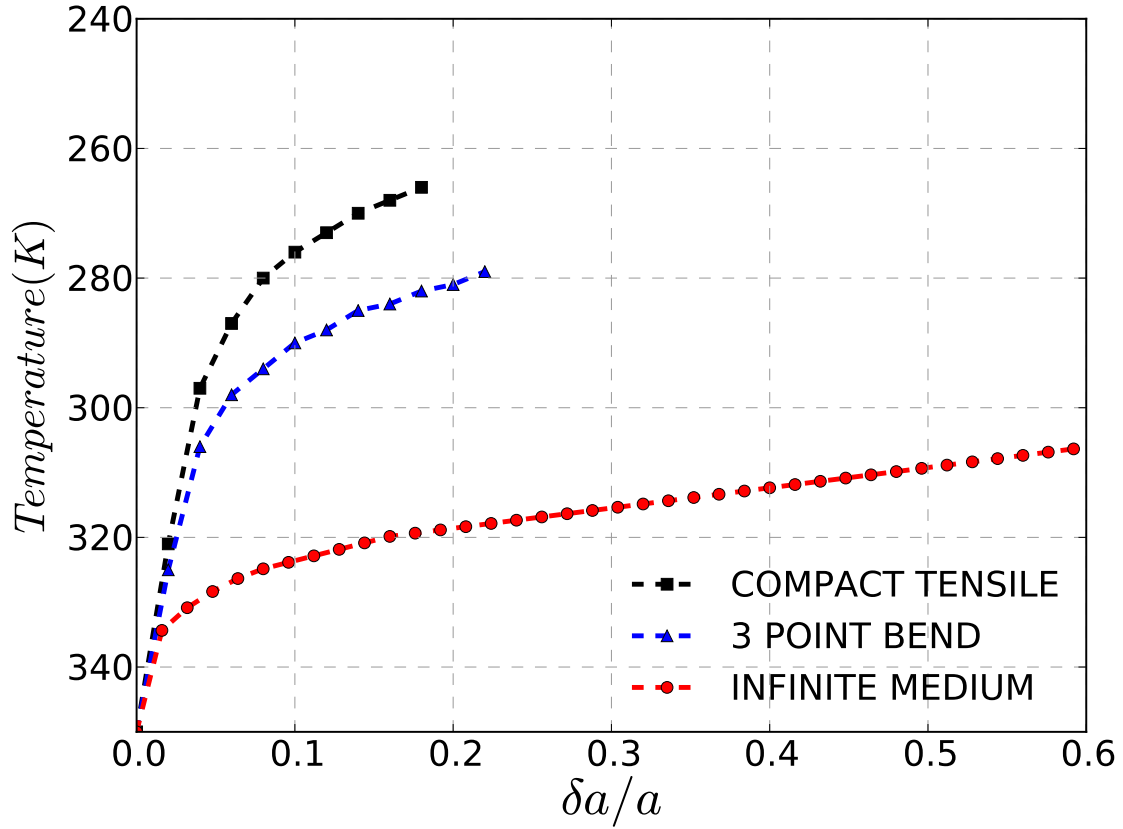
Figure 2.21: Crack resistance R-curves showing temperature vs. normalized crack extension for the following crack configurations: (a) infinite medium (b) compact tension and, (c) three-point bending.

Crack advance is triggered when the driving force for crack growth reaches its critical value in Figure 2.20, i.e., $G_I/G_\infty = G_{crit}/G_\infty = 2.0$. Due to the difference in variation of crack tip energy release rates for stationary crack during thermal actuation in the three configurations, crack growth behavior varies and is plotted in Figure 2.21. Crack advances at a higher temperature in infinite medium than in SE(B) and CT due to the aforementioned effects the boundaries have on crack tip stress fields. The amount of transformation toughening produced in each case is

dependent on the transformation strains generated behind the moving crack tip as well as the geometry of the specimen. As such, the lowest amount of toughening is observed in the infinite medium geometries, where the boundaries are far away and do not interact with state of the crack tip. On the other hand, CT specimen which is more deeply cracked than SE(B), results in higher transformation toughening of the moving crack. This is seen in the increasing temperature differential which is required to advance the crack stably as one goes from infinite medium to SE(B) and CT configurations.

2.4.5 Effect of displacement control

In realistic engineering applications, the constraints and boundary conditions imposed upon an SMA actuator can be a combination of fixed applied traction and fixed displacements. The infinite medium SMA material with a center crack can be subjected to a fixed displacement or a "fixed-grip" boundary condition in order to explore the effects of fixed grip conditions on crack tip mechanical fields in a transforming SMA under actuation loading conditions.

As shown in Figure 2.22, the variation of normalized crack-tip energy release rate G_{crit}/G_∞ with respect to normalized temperature $C_M(T - M_S)/\sigma_\infty$ in the infinite medium material when subjected to a specified displacement followed by cooling and heating of the entire material domain is shown. After application of mechanical load at the boundaries in the form of a specified displacement, a small region of stress induced martensite is formed at the crack tip. Following cooling, the region of fully transformed material initially increases in size in front of the crack tip giving rise to an increasing G_{crit}/G_∞ in the initial part. As global forward phase transformation reaches the boundaries and material behind the crack tip starts to forward transform and produce strains, owing to constraint on the displacement at domain boundaries,

69
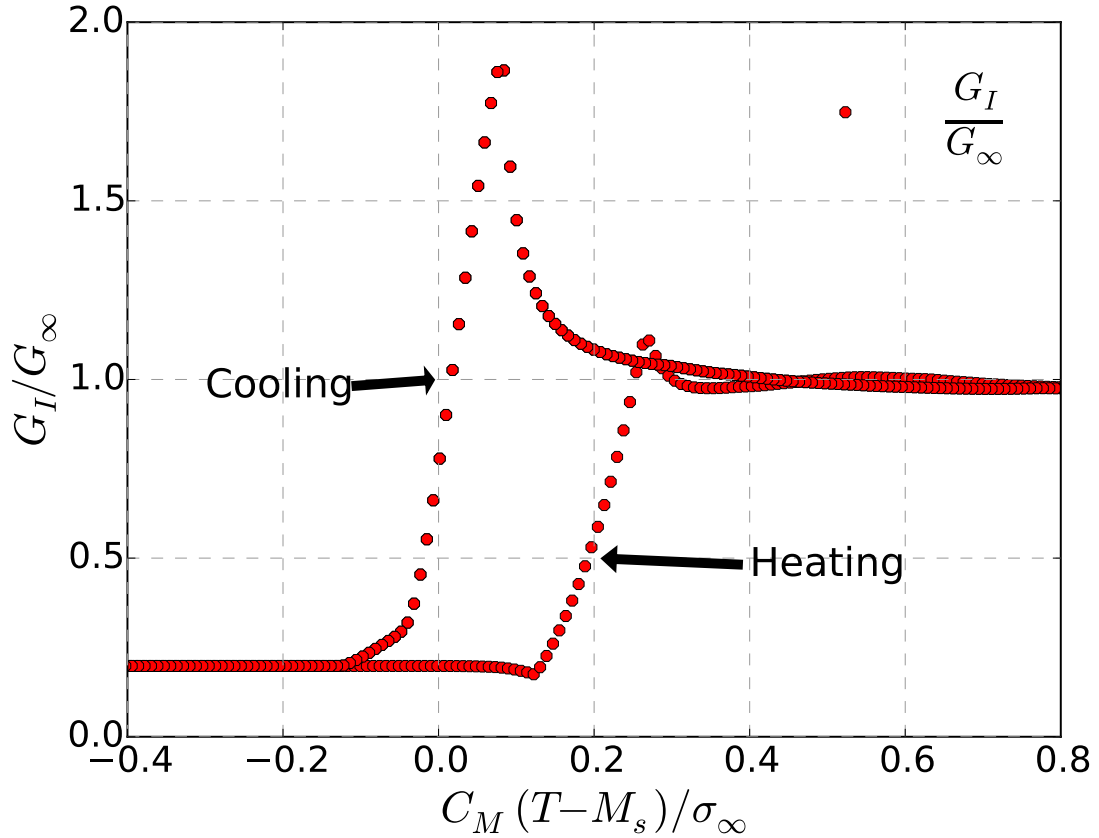
Figure 2.22: Variation of normalized crack-tip energy release rate G_{crit}/G_∞ with respect to normalized temperature $C_M(T - M_S)/\sigma_\infty$ during thermal actuation in an infinite medium SMA material under fixed displacement at the boundaries followed by thermal cycling.

the material behind the crack tip starts to expand and close the crack faces behind the crack tip. As a result of this apparent crack closure, stress intensity at the crack tip reduces and leads to a decrease in the G_{crit}/G_∞, as seen in Figure 2.22. Decrease in the crack tip energy release rate continues as long as forward phase transformation occurs and reaches a constant value when the entire material has transformed.

With subsequent heating, regions behind the crack tip reverse transforms first, losing the crack shielding effect produced by crack closure due to aforementioned for-
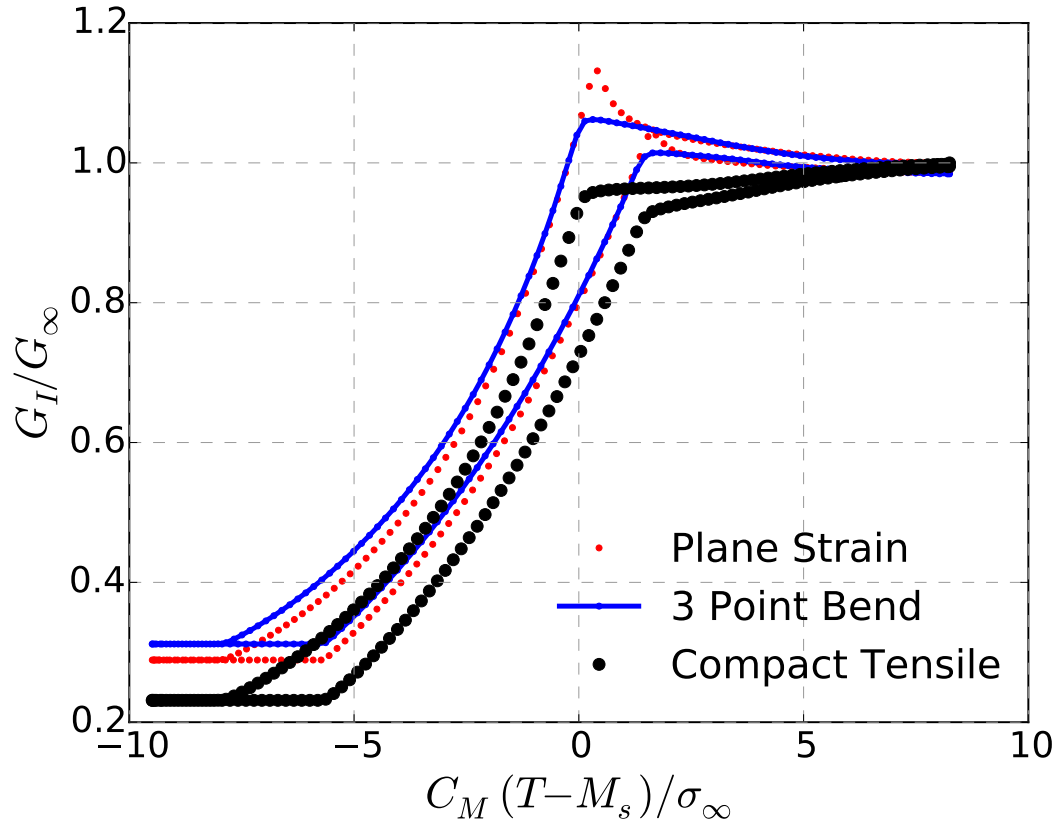
Figure 2.23: Variation of normalized crack-tip energy release rate G_{crit}/G_∞ with respect to normalized temperature $C_M(T - M_S)/\sigma_\infty$ during thermal actuation in SMA material under fixed displacement at the boundaries followed by thermal cycling for infinite medium, compact tensile and 3-point bend crack configurations.

ward transformation combined with fixed grip conditions during cooling, and leads to enhancement in G_{crit}/G_∞. By the end of heating, the entire material transforms to austenite and the value of G_{crit}/G_∞ reaches a constant value. Thus, subjected to fixed grip boundary conditions, cracked infinite medium SMAs respond in a substantially different manner with regards to the crack tip energy release rate, as compared to when subjected to dead load or constant traction boundary conditions.

When fixed grips boundary conditions are applied to realistic crack configura-

tions that are utilized in fracture toughness tests followed by actuation loading, the variation of crack tip G_{crit}/G_∞ is as shown in 2.23. Real material properties as mentioned in Table 1 have been used and the crack tip energy release rate is plotted throughout the thermal cycling. Compact tensile specimens are more deeply cracked than 3-point bend specimens, which are in turn more deeply cracked than the infinite medium configuration. As a result, the intensity of crack tip energy release rates in the deeply cracked specimens changes more substantially than that in the infinite medium configuration. Compact tensile and 3-point bend specimens produce forward transformation fields that rapidly start to result in apparent crack closure as soon as cooling begins, resulting in reduction in near-tip stress intensity and hence in G_{crit}/G_∞. Thus under compact tensile and 3-point bend specimens, owing to monotonously decreasing crack tip energy release rate, displacement control with fixed grip conditions would result in decreasing possibility of crack growth during cooling.

2.5 Summary

Finite element calculations are carried out in an attempt to understand crack growth in SMA actuators. The prototype problem of an infinite center-cracked SMA plate subjected to thermal cycling under plane strain, mode I, constant applied loading is employed in the analysis. The crack is assumed to propagate when the crack-tip energy release rate reaches a material specific critical value. In all cases the applied loads are sufficiently low so that the crack-tip energy release rate prior to thermal cycling is less than the critical value but sufficiently high so that the critical value is reached during the first thermal cycle. Stable crack growth is observed associated with the crack shielding effect of the transformed material left in the wake of the growing crack. This toughening effect is sensitive to the transformation

metrics and applied load levels. The smaller the bias load levels are, more thermal cycles are required for the crack to attain steady-state growth conditions.

A geometry dependence of crack growth resistance is expected as the outer boundaries exert an influence on the crack-tip deformation state whenever they are reached by the transformation zone at sufficiently low temperatures. Crack configurations beyond that of the infinite center-crack problem, such as compact tension and three-point bend specimens are also analyzed using the same numerical approach. Static and advancing cracks in these configurations are compared to the prototype infinite medium problem and a dependence of toughening response with the stress triaxiality at the crack-tip is shown to be possible. Additionally, the effect of fixed grips boundary conditions (as opposed to dead load) are applied to different crack configurations under actuation loading and the variation of crack tip G_{crit}/G_∞ is calculated. Real material properties as mentioned in Table 1 have been used and the crack tip energy release rate is plotted throughout the thermal cycling. Compact tensile specimens are more deeply cracked than 3-point bend specimens, which are in turn more deeply cracked than the infinite medium configuration. The present analysis should also be extended to actuation loading paths beyond the isobaric ones in an effort to fill the gap between the test and working conditions.

3. FRACTURE TOUGHNESS AND STABLE CRACK GROWTH IN SHAPE MEMORY ALLOY ACTUATORS IN THE PRESENCE OF TRANSFORMATION INDUCED PLASTICITY

3.1 Introduction

Solid-state SMA actuators are a potential alternative to traditional electromagnetic actuators in applications where a small envelope volume and/or large actuation force is required and thermodynamic efficiency is not a priority ([43, 108, 80]). When utilized as solid-state actuators, SMAs are generally subjected to hundreds of thousands of combined thermomechanical (actuation) loading cycles where the repeatable nature of phase transformation becomes a crucial factor. It has been experimentally observed that SMAs subjected to multiple actuation loading cycles, even under normal operating loads, develop significant permanent plastic deformations in the form of TRIP ([14]). Cyclic actuation loading also leads to fatigue induced microcracks, the underlying mechanisms of which are governed by various thermomechanical, environmental and microstructural factors. The effective design of high-performing and durable solid-state SMA actuators thus requires a detailed analytical and experimental study of the fracture properties of SMA. Such a study should entail the implementation of fracture mechanics concepts to produce criteria that will connect nucleation and growth of cracks with measurable thermomechanical and microstructural features of SMAs, *viz.* TRIP.

Experiments over the past two decades have shown that generation and accumulation of TRIP [88, 69, 24, 34, 103] is a direct result of permanent changes to the underlying microstructure of the alloy due to incompatibility at the martensite/austenite interfaces during phase transformation [14, 16]. These microstructural

changes also have other significant effects on the macroscopic thermomechanical behavior of SMAs, thereby modifying the transformation hysteresis loop. During thermomechanical loading, these effects on the behavior of SMAs manifest in the following form: the amount of critical stress required for phase transformation, width of the hysteresis loop and maximum transformation strain decrease while transformation hardening increases. Accumulated plastic strains due to cyclic phase transformations thus play a significant role in determining the thermomechanical response of solid-state SMA actuators and are also expected to affect the fracture response of SMA actuators.

Due to their unusual thermomechanical properties, fracture in SMAs is influenced by thermomechanical coupling, reversibility of martensitic transformations, reorientation and detwinning of martensite variants and the presence of dislocation and transformation induced plastic strains, thus making the phenomenon more complex than traditional dissipative metals. In the past decade, a considerable amount of experimental and theoretical research has been dedicated towards addressing the problem of fracture and crack growth in SMAs under mechanical loading at nominally isothermal conditions [13, 38, 114, 118, 29, 96, 28, 27, 30, 73, 74, 66, 46, 3]. At constant ambient temperatures, it has been observed that formation of stress-induced martensite precedes plastic yielding at the crack-tip [38, 41], and various traditional fracture mechanics based approaches have been employed to estimate the resulting fracture toughness [96, 41]. Nevertheless, there is virtually no research that addresses the specific problem of fracture in SMAs when employed as solid state actuators, where cyclic thermomechanical inputs induce phase transformation and plastic strains in the material.

Th problem of static and advancing cracks in SMAs subjected to combined cyclic thermomechanical loading, in the absence of accumulated plastic strains has been

addressed numerically [57, 56, 11, 58]. In case of a stationary/static crack, it has been demonstrated that the crack tip energy release rate (G_I), chosen as a fracture toughness parameter, increases substantially during the cooling portion of thermo-mechanical cycling, and to a lesser degree during heating [11]. Enhancement in the fracture toughness parameter (G_I) for the stationary crack results from stress redistribution caused by global scale transformation in front of the crack [22, 65]. When G_I reaches its material specific *critical* value, the numerics show stable crack growth which is attributed to stress redistribution caused by transformed material left in the wake of the advancing crack [58]. A steady decrease in the specimen temperature is thus needed to grow the crack by about 50% its initial length until steady state is attained. This transformation toughening resulting in stable crack growth is similar to that observed in certain quasi-brittle ceramic materials, (e.g. Mg-PSZ) containing zirconia (ZrO_2) particles, that undergo a tetragonal-to-monoclinic stress-induced shear and volumetric transformation [78, 22] which provide toughening to a growing crack. It has also been observed in SMAs subjected to purely mechanical loads and in other dissipative materials, where incremental mechanical loading is required to further extend the crack once crack growth has been triggered.

In this paper, the aforementioned finite element analysis is extended to a plane strain infinite-medium center-cracked polycrystalline SMA material system with TRIP subjected to constant load and varying temperature. A modified material constitutive law developed by Bo & Lagoudas [14, 15, 16, 17, 33] which incorporates additional internal variables related to the magnitude of irreversible TRIP strain into the classical SMA constitutive model developed by Boyd & Lagoudas [18, 19] is used. Numerical studies similar to those in previous publications delve into the details of the evolution of mechanical fields close to the crack tip using strain energy release rate as a single fracture toughness parameter. The dependence of G_I

on the magnitude and orientation of accumulated plastic strains is studied and the phenomenon of stable crack growth along with the associated transformation toughening is investigated for material specific critical energy release rate and plastic strain parameters.

The section is organized in the following manner: Section 3.2 describes the SMA material behavior used in this analysis which includes a phenomenological constitutive model that is developed within the framework of continuum thermodynamics and is applicable to polycrystalline SMAs with evolving plastic strains. In section 3.3, the boundary value problem of an infinite-medium center-cracked SMA panel subjected to combined cyclic thermomechanical loading with the small scale transformation assumption, is formulated. In section 3.4, numerical results for static and advancing cracks are presented, followed by a summary of the key findings in section 3.5.

3.2 Material Constitutive Model

The matrix material is described using the model proposed by Bo and Lagoudas [14, 16, 18, 19], which is an extension of the constitutive model for polycrystalline SMAs undergoing solid-state diffusionless phase transformation developed by Boyd and Lagoudas [18]. Additive decomposition of the total strain tensor in an elastic, a transformation, and a plastic part is assumed and the classical rate-independent small-strain flow theory framework for the evolution of transformation strains is adopted. The increments of the strain tensor components $d\varepsilon_{ij}$ are thus given as

$$d\varepsilon_{ij} = S_{ijkl}d\sigma_{kl} + dS_{ijkl}\sigma_{kl} + d\varepsilon_{ij}^{t} + d\varepsilon_{ij}^{p}, \qquad (3.1)$$

where σ_{ij}, ε_{ij}^{t}, ε_{ij}^{p} are the Cartesian components of the stress tensor, transformation strain tensor, and plastic strain tensor, respectively, and S_{ijkl} are the components of

the "current" compliance tensor. Throughout this paper, standard Einstein notation is used with summation over repeated indices assumed. The current compliance tensor varies with the martensitic volume fraction ξ as $S_{ijkl} = (1-\xi)S_{ijkl}^A + \xi S_{ijkl}^M$, where S_{ijkl}^A and S_{ijkl}^M are the components of the compliance tensor of austenite and martensite, respectively. In this paper, it is assumed that both austenite and martensite are isotropic and thus $S_{ijkl}^\alpha = \frac{1+\nu_\alpha}{2E_\alpha}(\delta_{il}\delta_{jk} + \delta_{ik}\delta_{jl}) - \frac{\nu_\alpha}{E_\alpha}\delta_{ij}\delta_{kl}$, where the index α stands for A in the case of austenite and for M in the case of martensite. E_α, ν_α denote the Young's modulus and Poisson's ratio, respectively, of the two phases and δ_{ij} is Kronecker's delta.

The plastic strain considered here is different from conventional plasticity in metals. Due to the misfit between the austenite–martensite interfaces, significant distortion is created. In addition, in a polycrystalline SMA, different grains transform in different manners, which causes additional distortion at the grain boundaries. These two phenomena act in concert and the final result is an observable macroscopic plastic strain, which occurs at effective stress levels much lower than the plastic yield limit of the material without phase transformation. This model does not address the plastic strain evolution initiated when pure austenite or martensite is subjected to effective stresses that exceed the critical stress for slip, but is focused on plasticity caused by cyclic transformation only.

3.2.1   Evolution of transformation strain

Evolution equation of the transformation strain is defined so that it is related to the evolution of martensite volume fraction, ξ,

$$
d\varepsilon_{ij}^t = \Lambda_{ij}d\xi, \quad \Lambda_{ij} =
\begin{cases}
\dfrac{3}{2}\dfrac{H^{cur}(\bar{\sigma})}{\bar{\sigma}}s_{ij}, & d\xi > 0, \\[2ex]
\dfrac{\varepsilon_{ij}^t}{\xi}, & d\xi < 0,
\end{cases}
\tag{3.2}
$$

where Λ_{ij} are the components of the direction tensor. Here, $H^{cur}(\bar{\sigma})$ is the uniaxial transformation strain magnitude for complete transformation, $\bar{\sigma} = \sqrt{\frac{3}{2}s_{ij}s_{ij}}$ is the Mises equivalent stress and $s_{ij} = \sigma_{ij} - \sigma_{kk}\delta_{ij}/3$ are the stress deviator components. During forward transformation, the transformation strain is oriented by the direction of the deviatoric stress, which motivates the selected J_2 form of the direction tensor. During reverse phase transformation, it is assumed that the direction and magnitude of the transformation strain recovery is governed by the average orientation of the martensite at transformation reversal (the cessation of forward transformation, be it partial or full). This definition allows to return to a zero transformation strain for every state with a null martensite volume fraction.

$H^{cur}(\bar{\sigma})$ is a function of the stress state since most SMA materials do not exhibit a constant maximum attainable transformation strain at all stress levels. A saturated value of maximum attainable transformation strain, H^{max}, is reached at a high stress level, which is dependent on the SMA material as well as the processing conditions for a polycrystalline material, resulting in different crystallographic and morphological textures, for example. Following this observation, the maximum transformation strain $H^{cur}(\bar{\sigma})$ is represented by the following decaying exponential function

$$H^{cur}(\bar{\sigma}) = H^{max}\left(1 - e^{-k\bar{\sigma}}\right), \tag{3.3}$$

where the parameter k controls the rate at which $H^{cur}(\bar{\sigma})$ exponentially evolves from 0 to H^{max}. As the saturation value of the maximum transformation strain evolves with the number of cycles, its evolution is assumed to obey the following equation

$$H^{max} = (H)^{fin} + \left[(H)^{init} - (H)^{fin}\right]e^{-\lambda_1\zeta^d}, \tag{3.4}$$

79

where $(H)^{fin}$ and $(H)^{init}$ are the final and initial values, and λ_1 is a positive material constant the governs the increasing rate of H^{max}.

3.2.2 Evolution of plastic strain

Similar to the evolution of transformation strain, the direction of plastic strain is determined by the direction of the applied stress. The development of the plastic strain is connected to the detwinned martensitic volume fraction, $\xi^d = \dfrac{H^{cur}(\bar{\sigma})}{H^{max}}\xi$, as

$$d\varepsilon_{ij}^p = \Lambda_{ij}^p d\xi, \quad \Lambda_{ij}^p = \begin{cases} \dfrac{3}{2}C_1^p \dfrac{H^{cur}(\bar{\sigma})}{H^{max}} \dfrac{s_{ij}^{eff}}{\bar{\sigma}^{eff}} e^{-\frac{\zeta^d}{C_2^p}}, & d\xi > 0 \\[4ex] C_1^p \dfrac{H^{cur}(\bar{\sigma})}{H^{max}} \dfrac{\varepsilon_{ij}^t}{\xi} e^{-\frac{\zeta^d}{C_2^p}}, & d\xi < 0. \end{cases} \tag{3.5}$$

where Λ_{ij}^p are the components of the direction tensor,

$$\zeta^d = \int_0^t \frac{H^{cur}(\bar{\sigma})}{H^{max}}|\dot{\xi}|d\tau, \tag{3.6}$$

is the accumulated detwinned martensite volume fraction, s_{ij}^{eff} are the components of the deviatoric part of the effective stress tensor, which is defined as $\sigma_{ij}^{eff} = \sigma_{ij} + \beta_{ij}$, β_{ij} are the components of the back stress that is introduced below, and the material parameters C_1^p and C_2^p govern the saturation value of the plastic strain as well as the number of cycles necessary for its saturation.

The components of the back stress β_{ij}, which control the kinematic portion of the plastic hardening, are assumed to have the following polynomial functional representation

$$\beta_{ij} = \frac{\varepsilon_{ij}^t}{\bar{\varepsilon}^t} \sum_{i=1}^{N^b} D_i^b \left[H^{cur}(\bar{\sigma})\xi\right]^{(i)}, \tag{3.7}$$

where N^b is the degree of the polynomial and D_i^b are the coefficients associated with

80

the back stress. The latter coefficients are assumed to change with the evolution of the accumulated detwinned martensitic volume fraction ζ^d as

$$D_i^b = \left(D_i^b\right)^{fin} + \left[\left(D_i^b\right)^{init} - \left(D_i^b\right)^{fin}\right] e^{-\lambda_1 \zeta^d}, \tag{3.8}$$

where $\left(D_i^b\right)^{fin}$ and $\left(D_i^b\right)^{init}$ are the final and initial values of D_i^b, and λ_1 is a positive material constant the governs the increasing rate of D_i^b. Note, that in the present model, the change of H^{max} is assumed to obey the same governing equation as the change of D_i^d.

3.2.3   Evolution of martensitic volume fraction

The evolution of the martensitic volume fraction can be inferred from the transformation surface

$$\Phi = 0, \quad \Phi = \begin{cases} \pi - Y, & d\xi > 0, \\[2ex] -\pi - Y, & d\xi < 0, \end{cases} \tag{3.9}$$

where

$$\pi = \sigma_{ij}^{eff}\Lambda_{ij} + \sigma_{ij}\Lambda_{ij}^p + \frac{1}{2}\Delta S_{ijkl}\sigma_{ij}\sigma_{kl} + \eta(\xi) + \rho\Delta s_0\left(T - M^{0s}\right) + Y. \tag{3.10}$$

In the above equation

$$M^{0s} = T_0 + \frac{1}{\rho\Delta s_0}\left(Y + \rho\Delta u_0\right), \tag{3.11}$$

is the initial martensitic-start temperature, s_0 and u_0 are the specific entropy and internal energy, respectively, ρ is the density, Δ denotes the difference in property between the martensitic and the austenitic states, Y is a material constant representing

81

a measure of the internal dissipation during phase transformation, and

$$\eta = -D_1^d \left[-\ln(1-\xi) \right]^{\frac{1}{m_1}} + D_2^d \xi, \tag{3.12}$$

is the drag stress that accounts for the isotropic hardening. The latter coefficients are assumed to change with the evolution of the accumulated detwinned martensitic volume fraction ζ^d as

$$D_i^d = \left(D_i^d\right)^{fin} + \left[\left(D_i^d\right)^{init} - \left(D_i^d\right)^{fin} \right] e^{-\lambda_2 \zeta^d}, \tag{3.13}$$

where $\left(D_i^d\right)^{fin}$ and $\left(D_i^d\right)^{init}$ are the final and initial values of the parameter, and λ_2 is a positive material constant governing the evolution of D_i^d. As see above, evolution of the drag stress parameters is governed by the total accumulated martensitic volume fraction ζ and not its detwinned portion ζ^d. This is due to the fact that microstructural changes can be induced by cyclic self-accommodating phase transformation [15]. The equations governing the change of Y, M^{0s}, and $\rho\Delta s_0$ are assumed similar to (3.13)

$$Y = (Y)^{fin} + \left[(Y)^{init} - (Y)^{fin} \right] e^{-\lambda_2 \zeta^d}, \tag{3.14}$$

$$M^{0s} = \left(M^{0s}\right)^{fin} + \left[\left(M^{0s}\right)^{init} - \left(M^{0s}\right)^{fin} \right] e^{-\lambda_2 \zeta^d}, \tag{3.15}$$

$$\rho\Delta s_0 = (\rho\Delta s_0)^{fin} + \left[(\rho\Delta s_0)^{init} - (\rho\Delta s_0)^{fin} \right] e^{-\lambda_2 \zeta^d}. \tag{3.16}$$

Constraints on the evolution of ξ are expressed in terms of the Kuhn-Tucker conditions given for forward and reverse phase transformation as

$$d\xi \geq 0, \quad \Phi \leq 0, \quad \Phi d\xi = 0 \tag{3.17}$$

$$d\xi \leq 0, \quad \Phi \leq 0, \quad \Phi d\xi = 0. \tag{3.18}$$

As evident in Figure 3.1, in which simulations of the matrix stress–strain response under uniaxial cyclic loading are plotted, the constitutive law can reproduce several characteristic changes of the progressive evolution of the hysteresis loop in addition to the evolution of the TRIP strain, *i.e.*, (i) decrease of the stress level required for the onset of transformation, (ii) increase of the transformation hardening, (iii) decrease of the width of the hysteresis loop, and (iv) decrease of the maximum transformation strain. Parameter values for the SMA matrix material used in the present analysis are given in Table 3.1.
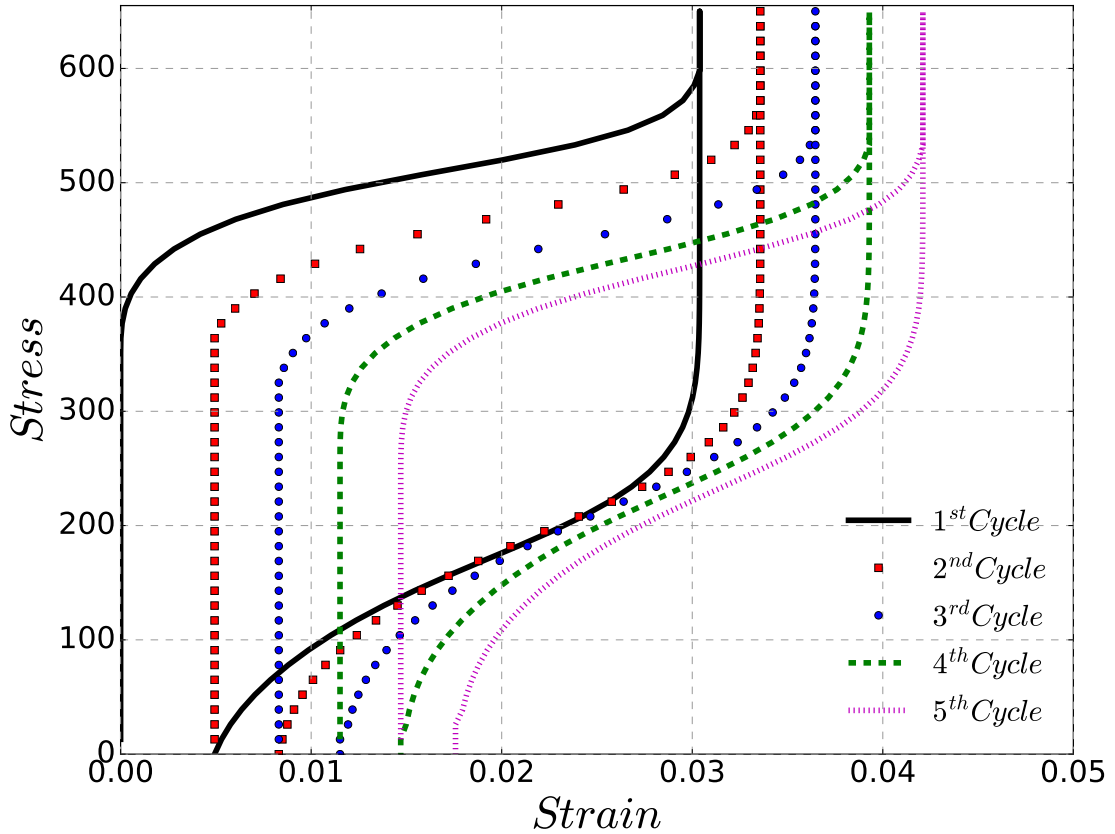
Figure 3.1: Plastic strain accumulation during mechanical loading cycles up to a constant bias load.
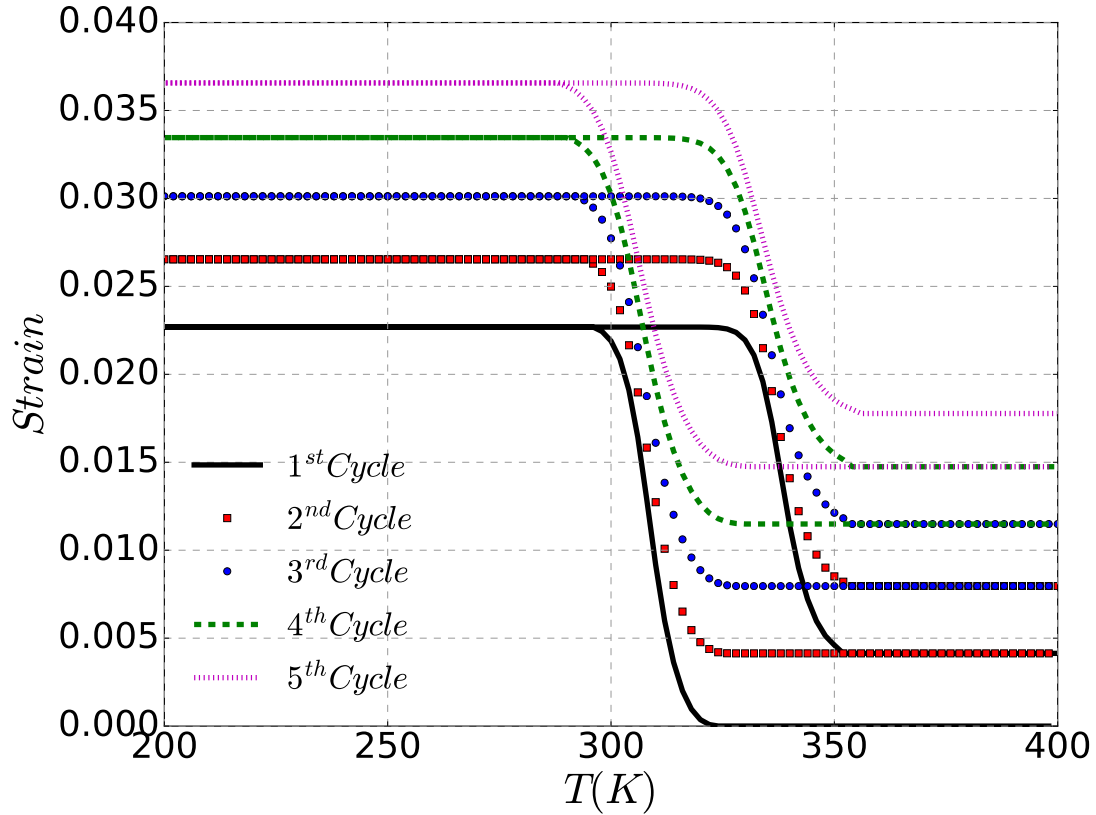
Figure 3.2: Plastic strain accumulation during actuation cycles under a constant bias load.

3.3 Formulation of the Boundary Value Problem

In this section, a brief description of the boundary value problem of an infinite-medium center-cracked SMA panel subjected to constant and uniaxial mode-I tensile load at the far-field boundaries and cyclic thermal loading (Figure 3.3) is given. A system of co-ordinates (x_1, x_2, x_3) is chosen with origin at the center of the crack, x_1-axis extending parallel to the crack faces, x_2 parallel to the direction of loading and x_3 along the thickness of the specimen. The SMA panel is considered to be thick enough so that plane strain conditions hold and analysis is performed in the (x_1, x_2) plane. It is important to note that the material constitutive model takes into account the

Table 3.1: Parameter values for the SMA matrix material. [33]

(a) Physical constants

parameter	value	parameter	value
E_A [MPa]	70000	ν_A	0.33
E_M [MPa]	30000	ν_M	0.33
$\rho c^A [MJ/(m^3 K)]$	2.12	α_A	$11.0 \times 10^{-6} K^{-1}$
$\rho c^M [MJ/(m^3 K)]$	2.12	α_A	$6.6 \times 10^{-6} K^{-1}$

(b) Material parameters characterizing transformation and plastic deformation during cyclic loading

parameter	initial value	final value
M^{0s}	$311.0K$	$311.0K$
H^{max}	0.069	0.069
$\rho \Delta s_0$ [MJ/(m^3 K)]	-0.422	-0.422
D_1^b [MPa]	3.4×10^3	3.4×10^3
D_2^b [MPa]	-2.23×10^5	-2.23×10^5
D_3^b [MPa]	8.32×10^6	8.32×10^6
D_4^b [MPa]	-1.50×10^8	-1.50×10^8
D_5^b [MPa]	1.03×10^9	1.03×10^9
D_1^d [MPa]	3.4×10^3	3.4×10^3
D_2^d [MPa]	3.4×10^3	3.4×10^3
m_1	3.5	3.5
γ	3.0	3.0
Parameters for saturation level plastic strain, $\quad C_1^p = 0.0036$		$C_2^p = 18.0$
Minor loop parameter, $\lambda_1 = 0.25$		

generation of TRIP due to thermomechanical cycling and the subsequent evolution of transformation parameters governing material response. These parameters include the austenite and martensite start and finish temperatures (A_s, A_f, M_s, M_f), which evolve with each thermal cycle. Mechanical load is applied at a temperature $(T = T_h)$ that is higher than the initial austenite finish temperature (A_f) of the material, to ensure that entirety of the SMA material is in austenite phase. At the crack-tip fracture process zone, a small region of fully-transformed stress-induced martensite

is formed due to high stress concentration. As one moves away from the crack-tip, first a region of partially transformed martensite is encountered which is surrounded by untransformed pure austenite close to the boundaries. The size of the initial transformation zone is significantly smaller than the initial crack length $2a$ as the resulting stress produced at boundaries at infinity due to the applied load, σ_∞, is much smaller than the stress required for initiation of martensitic transformation, σ^{Ms}. Small-scale transformation conditions prevail throughout the material. The plate is then subjected to multiple cooling and heating cycles between $T = T_h$ which the tensile load is applied and a low temperature $(T = T_c)$ that is smaller than initial martensite finish (M_f), to ensure that the bulk of the specimen transforms between fully austenitic and martensitic phases. The analysis is quasi-static and the cooling and heating rates are assumed to be small enough to discard any effects of temperature gradients arising out of the generation or absorption of latent heat due to phase transformation.

A co-ordinate system where the center lies at the center of the crack, the x-axis extends along the crack line and the y-axis parallel to the loading direction is chosen. Only right half of the domain is analyzed due to symmetry of the problem and only the top-right quarter is plotted due to symmetry of stress and transformation fields across the crack line. Incremental stress-strain response of the fully transformed martensite in the near-tip region is assumed to be linear elastic for the entirety of analysis. ABAQUS finite element suite is employed and the finite element mesh consists of 4-node bilinear plane strain quadrilateral elements with reduced integration (CPE4R in Abaqus), hourglass control and finer mesh density in the crack growth region in front of the crack tip. In this study, because of evolving plastic strains during the analysis, each integration point in the finite element has a higher number of state dependent variables than the case when plastic strain is absent. As such,
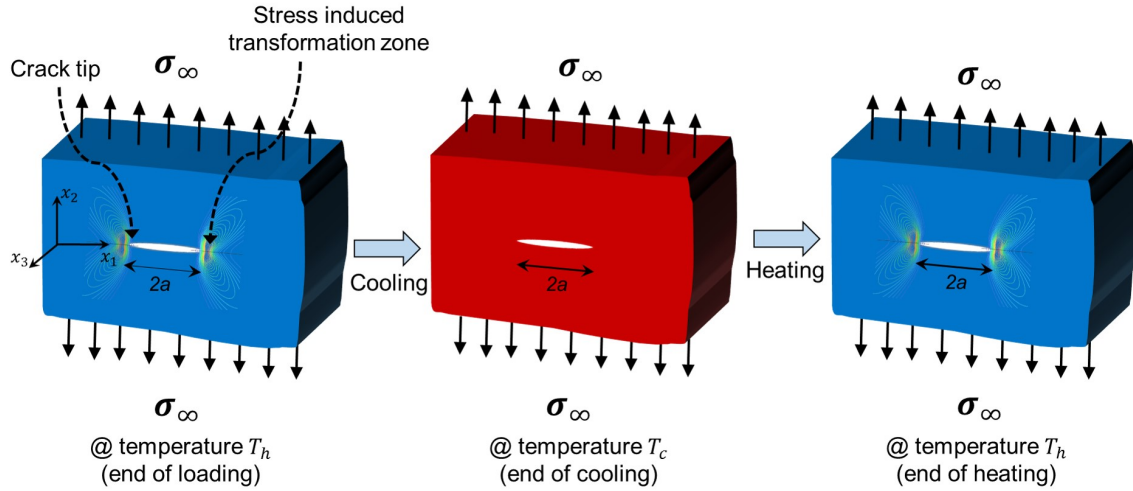
Figure 3.3: Boundary value problem for an infinite-medium center-cracked SMA plate in initial austenite phase subjected to a constant far-field uniaxial tensile loading and thermal cycling and plane strain conditions. Martensite regions are shown in red color and austenite ones in blue.

to help with numerical convergence and reduce computational cost, linear finite elements (unlike quadratic elements in the previous section) have been utilized. Virtual Crack Closure Technique (VCCT) in ABAQUS ([1]), which is based on Irwin's crack closure integral [54, 99, 60, 115], is used to calculate the chosen fracture toughness parameter, $viz.$, crack tip energy release rate (G_I) which characterizes the near-tip mechanical fields. VCCT is based on the assumption that strain energy released when a crack is extended by small increment is the same as that required to close the crack by the same amount, and that state of the crack-tip does not get significantly altered during incremental crack extension. The validity of this method has been established for the constitutive material behavior used for the current analysis which contains linear isotropic elastic martensite at the crack tip [11, 58]. In case of two-dimensional 4-node linear elements placed in front of the crack tip, the method yields

$$G_I = -\frac{1}{2\Delta}F_2^i(u_2^l - u_2^{l*}) \qquad (3.19)$$

where F_2^i indicates the nodal force perpendicular to the crack plane, u_2^l and u_2^{l*} represent the nodal displacements the upper and lower crack faces (Figure 3.4)
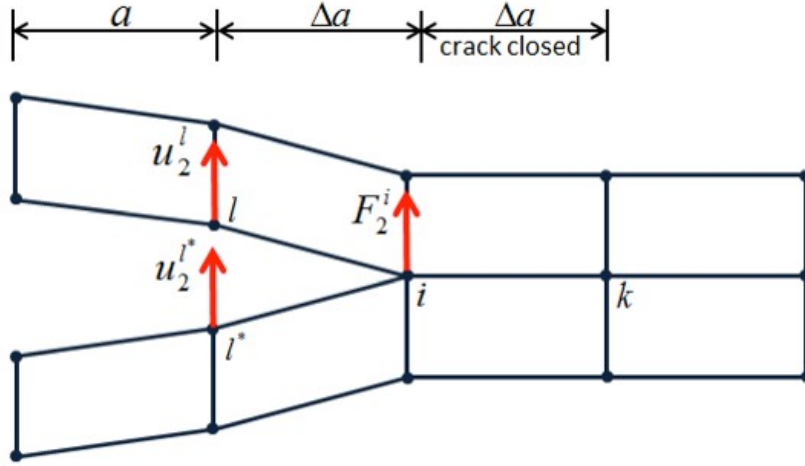
Figure 3.4: VCCT for four-node linear elements

3.4   Results

3.4.1   Mechanical fields close to stationary crack

Numerical results pertaining to mechanical fields close to stationary cracks in an infinite-medium center cracked SMA panel with TRIP under combined thermomechanical loading and plane-strain conditions are now presented. Material properties for a NiTi SMA material with a stable transformation cycle as shown in Table 3.1 are used. Application of uniform far-field mechanical load at the boundary with

material in an initial austenite phase at a constant temperature $(T = T_h)$ results in a small region of fully transformed elastic martensite at the crack tip. Size of transformation zone is approximately 50 times smaller than the crack length, in accordance with the small scale transformation condition. Barring the region of fully-transformed stress-induced martensite near the crack-tip and partially transformed region surrounding it, rest of the material is at a stress level equal to the applied far-field loading (σ_∞). Mechanical load is followed by multiple thermal cycling of the entire SMA material between T_h (fully austenitic state) and T_c (fully martensitic state). The thermomechanically-induced phase transformation and TRIP strains result in a stress redistribution that changes the crack-tip stress field, as shown in Figure 3.5 and Figure 3.6, in which the von Mises stress and mean normal stress, $\sigma_m = 1/3 \cdot (\sigma_{11} + \sigma_{22} + \sigma_{33})$, distributions at the crack tip are presented prior to thermal cycling (*i.e.*, at $T = T_h$) and at the end of cooling (*i.e.*, at $T = T_c$).
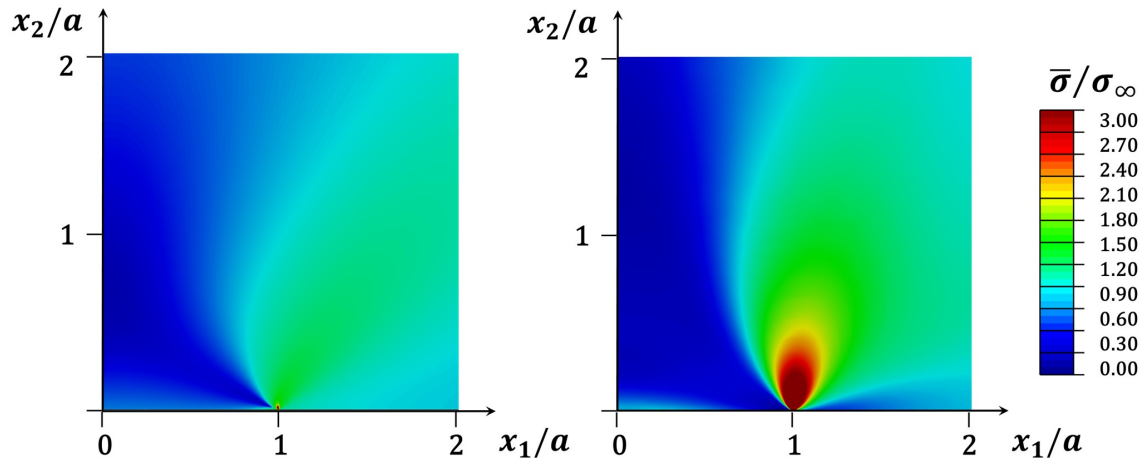
Figure 3.5: von Mises stress distribution (normalized) near the crack tip at $T = T_h$ prior to thermal cycling and $T = T_c$ at the end of cooling.

During cooling, forward phase transformation occurs in a fan in front of the crack tip and gradually expands to region behind the crack, whereas during heating, reverse transformation begins in a zone behind the crack due to lower stresses, and ultimately reaches to the region in front of the crack tip. Evolution of crack tip energy release rate due to thermomechanical loading, normalized by its value at the end of mechanical loading, is plotted with respect to the uniform normalized temperature in the infinite-medium for three thermomechanical cycles (Figure 3.7). Specifically, G_I represents the energy release rate at the crack-tip resulting from the global thermal variations whereas G_∞ represents the energy release rate due to mechanical load alone. The ratio G_I/G_∞ is the normalized value of the driving force for crack growth which is utilized as a single parameter to probe fracture toughness of the static crack. The normalization of uniform temperature in the material is carried out using phase transformation and TRIP parameters in the following manner:
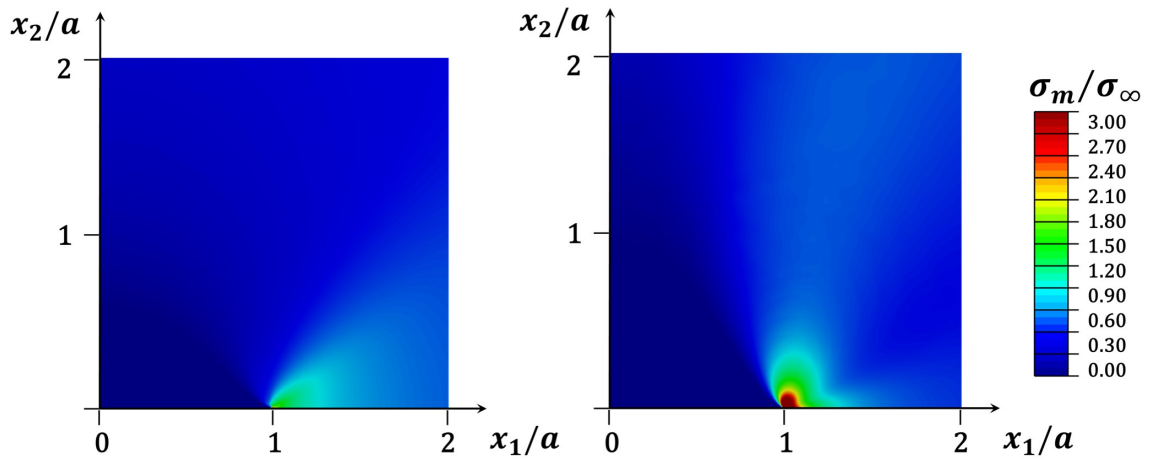
Figure 3.6: Mean stress distribution (normalized) near the crack tip at $T = T_h$ prior to thermal cycling and $T = T_c$ at the end of cooling.
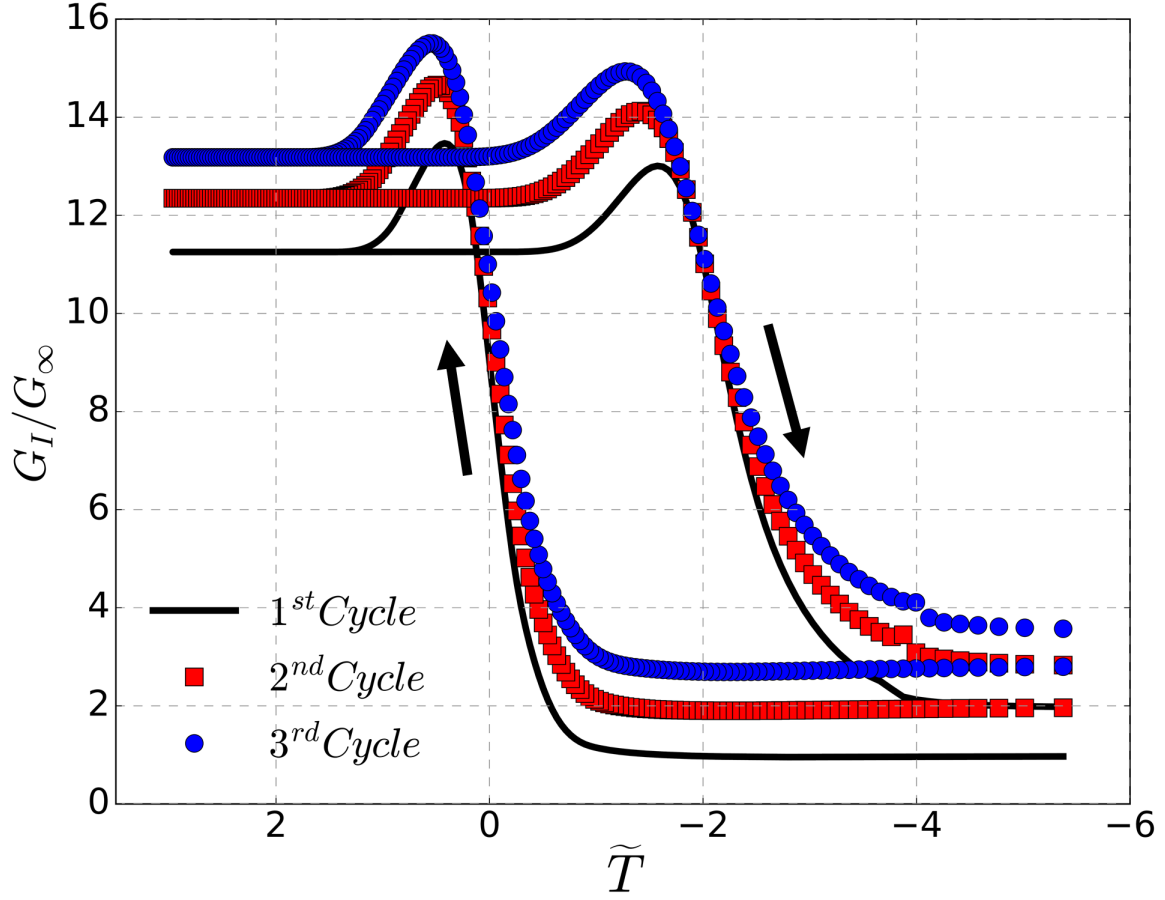
Figure 3.7: Evolution of the normalized crack-tip energy release rate, G_I/G_∞, versus uniform temperature T, over three thermal cycles.

$$\widetilde{T} = \frac{\sqrt{H^{cur\,2} - 2\Delta S \rho \Delta s_o (T - M_s^o)} - H^{cur}}{\Delta S \sigma_\infty} \tag{3.20}$$

where $\widetilde{T}$ is the normalized temperature and T is the absolute temperature in the material; other material parameters are described in the SMA constitutive model.

In the first thermal cycle, G_I/G_∞ remains close to its initial value of 1 ($G_I = G_\infty$), when temperature is higher than that required for martensitic transformation at a given stress (M_s^σ) and forward phase transformation is limited to a small region

near the crack tip. During cooling, once the uniform temperature becomes equal to corresponding M_s^σ, far-field material points start to transform. Large-scale or "global" forward phase transformation occurs in a fan in front of the crack resulting in stress-redistribution altering the near-tip stress fields. Transformation strains in a fan in front of the crack have an anti-shielding effect on the stationary crack and try to open the crack [22, 65, 11, 58]. This is reflected in a significant enhancement in G_I/G_∞, about an order of magnitude, with progressive cooling. Simultaneously, plastic strain which evolves with phase transformation also accumulates in front of the crack tip and contributes to the aforementioned anti-shielding of the crack, and thereby in the enhancement in G_I/G_∞. It is important to note that *(i)* enhancement in the driving force is not merely resulting from variation in the stress field due to elastic moduli mismatch between austenite (E_A) and martensite (E_M), and needs to be understood in the context of large scale phase transformation and plastic strains, and *(ii)* G_I/G_∞ is independent of the crack length *2a* which is an expected result since the crack length is the only length-scale defined in the infinite medium plate ([11]).

The effect of TRIP strains and the change in material properties due to modifications in the underlying microstructure can be decoupled in the material model employed here. Variation of G_I/G_∞ during three thermal cycles when TRIP accumulates in the material but SMA material parameters do not alter is shown (Figure 3.8) as well as when TRIP does not accumulate but material properties change (Figure 3.9). Figure 3.8 shows that with each cycle, G_I/G_∞ varies in a similar manner as described in earlier section: enhancement during cooling followed by decrease towards the end of cooling, and slight increase during heating followed by reduction. By the end of each cycle, G_I/G_∞ accumulates due to the permanent plastic straining in the material and the final value is higher than the initial value. However, since the

transformation temperatures (M_s, M_f, A_s, A_f) do not evolve with thermal cycling, the points in temperature where G_I/G_∞ increases rapidly and reaches peak values during cooling and heating remains constant.
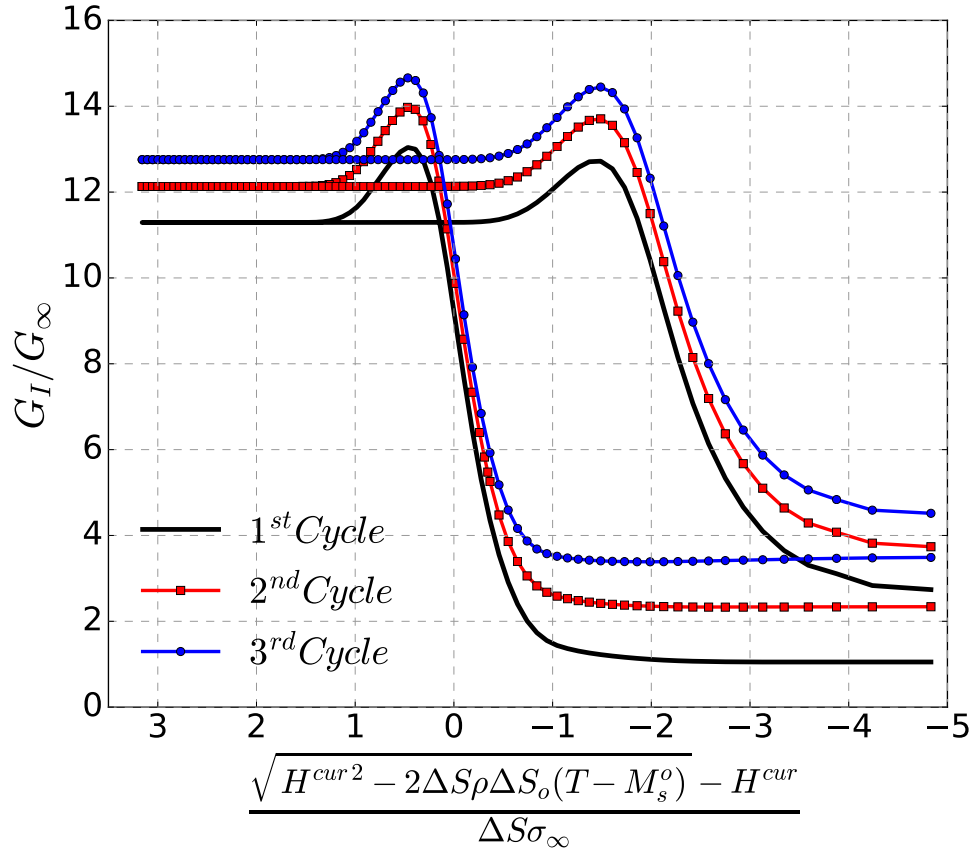
Figure 3.8: Evolution of the normalized crack-tip energy release rate, G_I/G_∞, versus uniform normalized temperature $\widetilde{T}$, over three thermal cycles in the presence of TRIP when material properties do not evolve.

When TRIP strain is maintained to be zero but material properties are allowed to alter, variation of G_I/G_∞ can be seen to closely follow the same trend as described for a material without any TRIP. The value of G_I/G_∞ at the end of each thermal cycle

is equal to its value at the beginning of that cycle, due to the absence of permanent plastic strains. However, since the shift in SMA transformation temperatures, the points in temperature where G_I/G_∞ shows rapid increase or decrease and peak values during cooling/heating can be seen to steadily shift with each thermal cycle. Both plastic strains and shift in transformation temperatures in the SMA material can thus modify the crack tip energy release rate and hence have an effect on the driving force for crack growth.
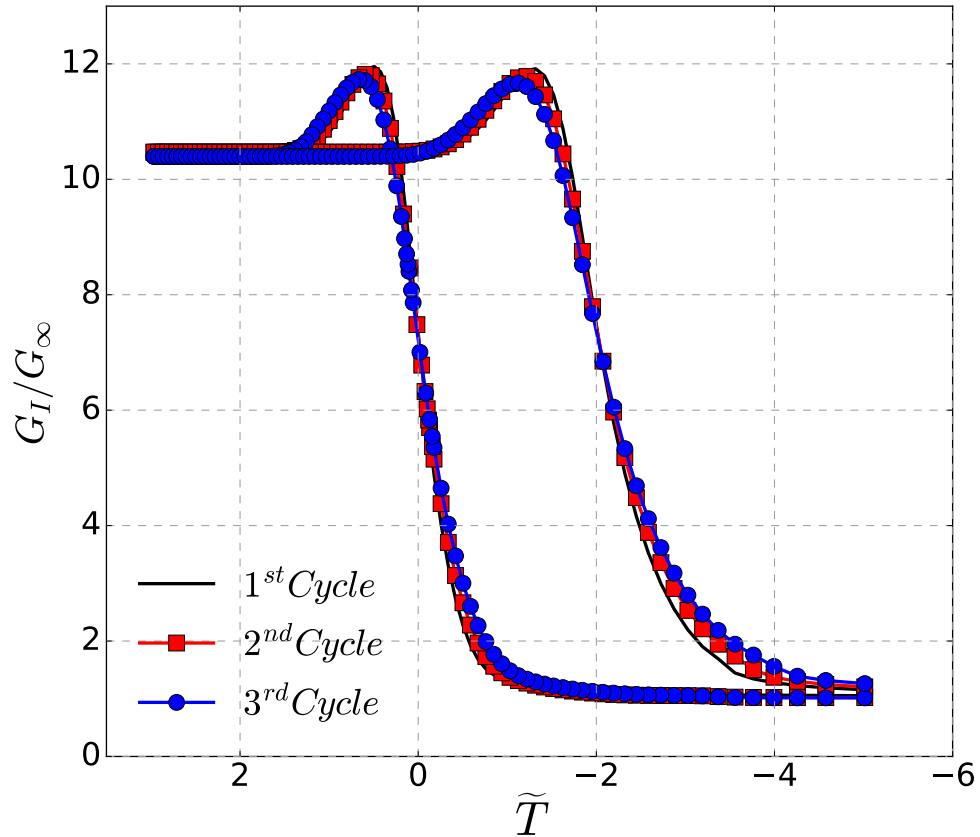
Figure 3.9: Evolution of the normalized crack-tip energy release rate, G_I/G_∞, versus uniform normalized temperature $\widetilde{T}$, over three thermal cycles in the absence of TRIP when material properties evolve cyclically.

A brief description of the enhancement in driving force for crack growth due to stress redistribution at the stationary crack caused by large scale transformation and plastic strain fields is now discussed.

3.4.2 Enhancement/reduction in near-tip stress intensity due to large scale transformations

The effect of large scale transformation strain on the crack-tip energy release rate G_I, or equivalently on the crack-tip stress intensity factor K_I, has been explained in the previous section. Recall that the enhancement/reduction in the near-tip intensity under plane strain mode I conditions is due to two differential elements of equal areas dA placed symmetrically about the crack tip and undergoing simultaneous transformation and plastic straining. In the polar co-ordinate system with crack tip as origin, the first differential element is located at (r, β) and is characterized by uniform stress-free strains $(E_{11}^t, E_{12}^t, E_{22}^t)$, whereas the second is located at $(r, -\beta)$ and undergoes equivalent strains given by $(E_{11}^t, -E_{12}^t, E_{22}^t)$, symmetric due to mode I loading conditions [22, 65]. Restating the equations from section 2, the enhancement/reduction in the near-tip intensity, dK_I, is given by

$$dK_I = \frac{1}{\sqrt{8\pi}} \frac{E dA}{1 - \nu^2} r^{-3/2} M(E_{\gamma\delta}^t, \beta), \tag{3.21}$$

where

$$M\left(E_{\gamma\delta}^t, \beta\right) = E_{\alpha\alpha}^t \cos\frac{3\beta}{2} + 3E_{12}^t \cos\frac{5\beta}{2} \sin\beta + \frac{3}{2}\left(E_{22}^t - E_{11}^t\right)\sin\frac{5\beta}{2} \sin\beta, \tag{3.22}$$

and $E_{\gamma\delta}^t = \varepsilon_{\gamma\delta}^t + \varepsilon_{\gamma\delta}^p$, $\varepsilon_{\gamma\delta}^t$ and $\varepsilon_{\gamma\delta}^p$ being the transformation and plastic strain components, and E and ν are the elastic modulus and Poisson ratio of martensite. Greek

indices take values 1, 2 and repeated index indicates sum over 1 and 2 in the above expressions. Expressions (3.21) and (3.22) show that any transforming material contained within a fan at an angle β in front of the crack increases near-tip intensity and thus the energy release rate whereas any material behind this fan reduces it. Global scale phase transformation and *TRIP* in front of the crack tip during cooling can plausibly result in similar enhancement in the crack tip energy release rate. Transformation and TRIP strains occurring behind the crack tip can similarly reduce the near-tip intensity or crack tip energy release rate and shield the crack. During heating, reverse phase transformation first occurs behind the crack and leads to loss of shielding from the strains, intensifying G_I. However, TRIP strains are not recovered but are in fact accumulated during heating, countering the effect from transformation strains. As regions in front of the crack reverse transform, transformation strains are recovered and the resulting enhancement in G_I is lost, leading to a decrease in G_I. However, the simultaneous accumulation of TRIP strains during recovery of transformation strain leads to a resultant G_I that reaches a value higher than that at the beginning. The observed enhancement in near-tip intensity and thereby in the normalized driving force for crack growth G_I/G_∞, can thus be attributed to global phase transformation and plastic strains caused by thermal actuation in the center-cracked infinite medium SMAs.

3.4.3 Evolution of transformation and plastic strain fields

Evolution of near tip martensite fields in simultaneity with accumulating plastic strains during cyclic phase transformation from isobaric actuation loading is now discussed. Contours of martensite volume fraction (ξ) and equivalent plastic strain ($\widetilde{\varepsilon^p}$) during cooling are shown in Figure3.10 and Figure 3.11. At the beginning of cooling, a small region of fully transformed material ($\xi = 1$) is surrounded by partial

transformation and $\widetilde{\varepsilon^p}$ for the corresponding point is concentrated in a small region similar to that for ξ. Evolution of plastic strain closely follows that of transformation strain (ε^t) and in turn, ξ, due to their dependence on the deviatoric part of the Cauchy stress tensor (Section 3.2). *Global* forward phase transformation *and* plastic strains in front of the crack during cooling leads to stress redistribution at the crack tip via anti-shielding and a significant enhancement in the driving force for crack growth. Driving force G_I/G_∞ reaches a peak when temperature in the specimen is close to martensite finish at the applied load, and is about an order of magnitude higher than that at the beginning of thermal cycling. With further cooling, material in the wake of the crack forward transforms last, owing to lower stresses due to traction free crack faces. Development of transformation and plastic strains behind the crack leads to shielding of the crack resulting in decreasing G_I/G_∞, until a final constant value is reached by the end of cooling (T_c).

In the second part of the thermal cycle, *i.e.* heating, the variation of G_I/G_∞ is opposite to that during cooling. Since stress levels are lower behind the crack tip, reverse phase transformation occurs first behind the crack tip leading to the recovery of transformation strains and loss of crack shielding whereas $\widetilde{\varepsilon^p}$, which has a smaller magnitude than the transformation strain, develops in wake of the crack and provides shielding. Further heating of the specimen extends reverse phase transformation to regions in front of the crack and large scale transformation strain is recovered completely, leading to a reduction in near-tip intensity and hence G_I/G_∞. At the end of the heating cycle (T_h), final value of G_I/G_∞ is higher than that at the beginning of cooling, and this residual crack tip energy release rate is a result of permanent stress intensity enhancement due to irreversible plastic strains during thermal actuation. Effects of accumulated plastic strain and recovered transformation strains during heating compete against each other and result in an elevated value of G_I/G_∞ by

97

the end of a thermal cycle. TRIP strain thus permanently alters the mechanical stress fields surrounding the crack tip during actuation loading and with multiple cooling/heating cycles between T_c and T_h. G_I/G_∞ at the crack tip follows above mentioned trends resulting in a permanent enhancement by the end of each actuation cycle. Compared to previous studies [58, 11] where crack tip energy release rate at the end of thermal cycle becomes equal to its corresponding value at the beginning, this analysis shows that the introduction of TRIP has a direct and significant effect on the driving force for crack growth during thermal actuation.
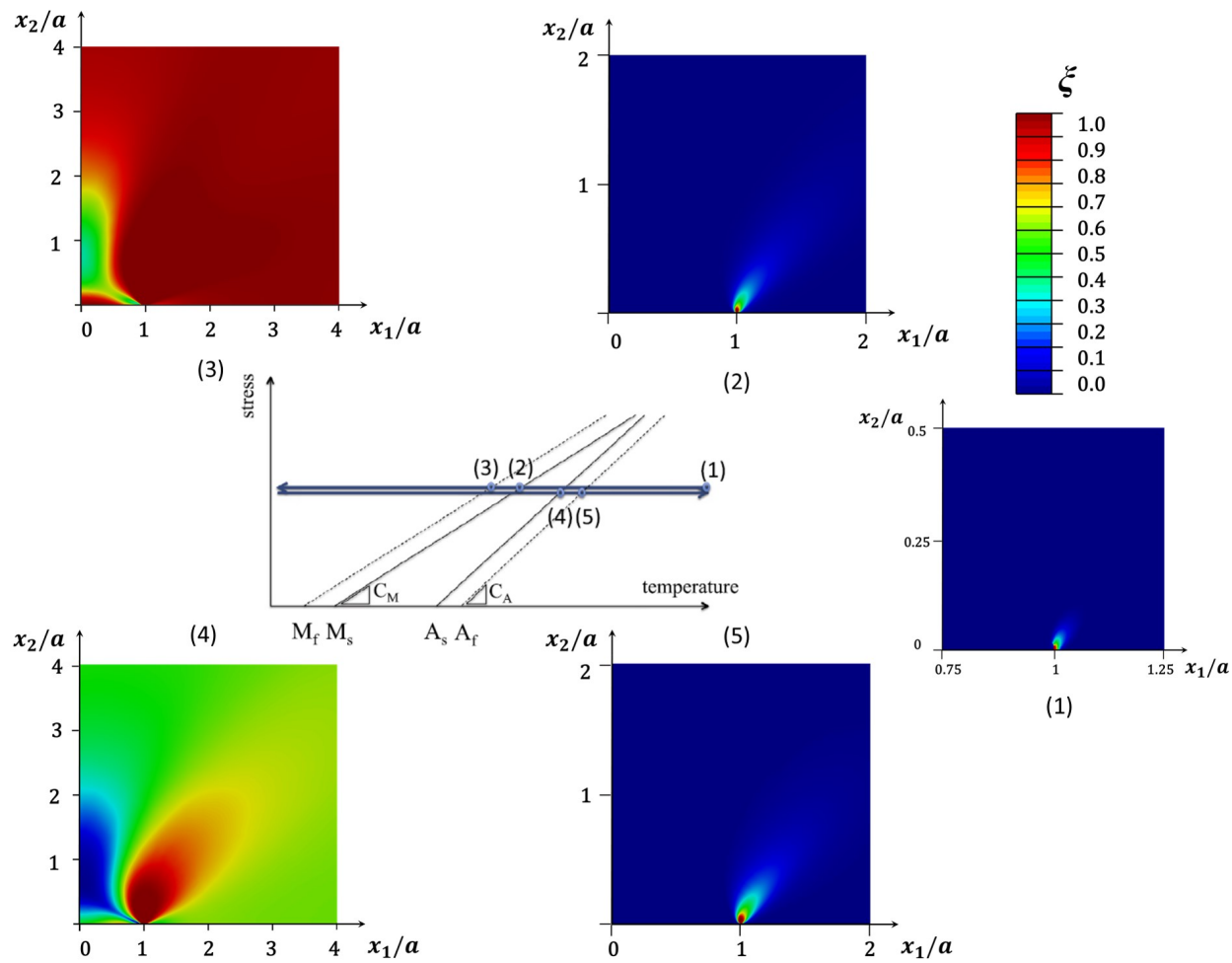
Figure 3.10: Contours of martensite volume fraction ξ at different temperatures numbered on the stress-temperature phase diagram during the actuation loading. Note that the near-tip regions in which martensite volume fraction is depicted are of different sizes.
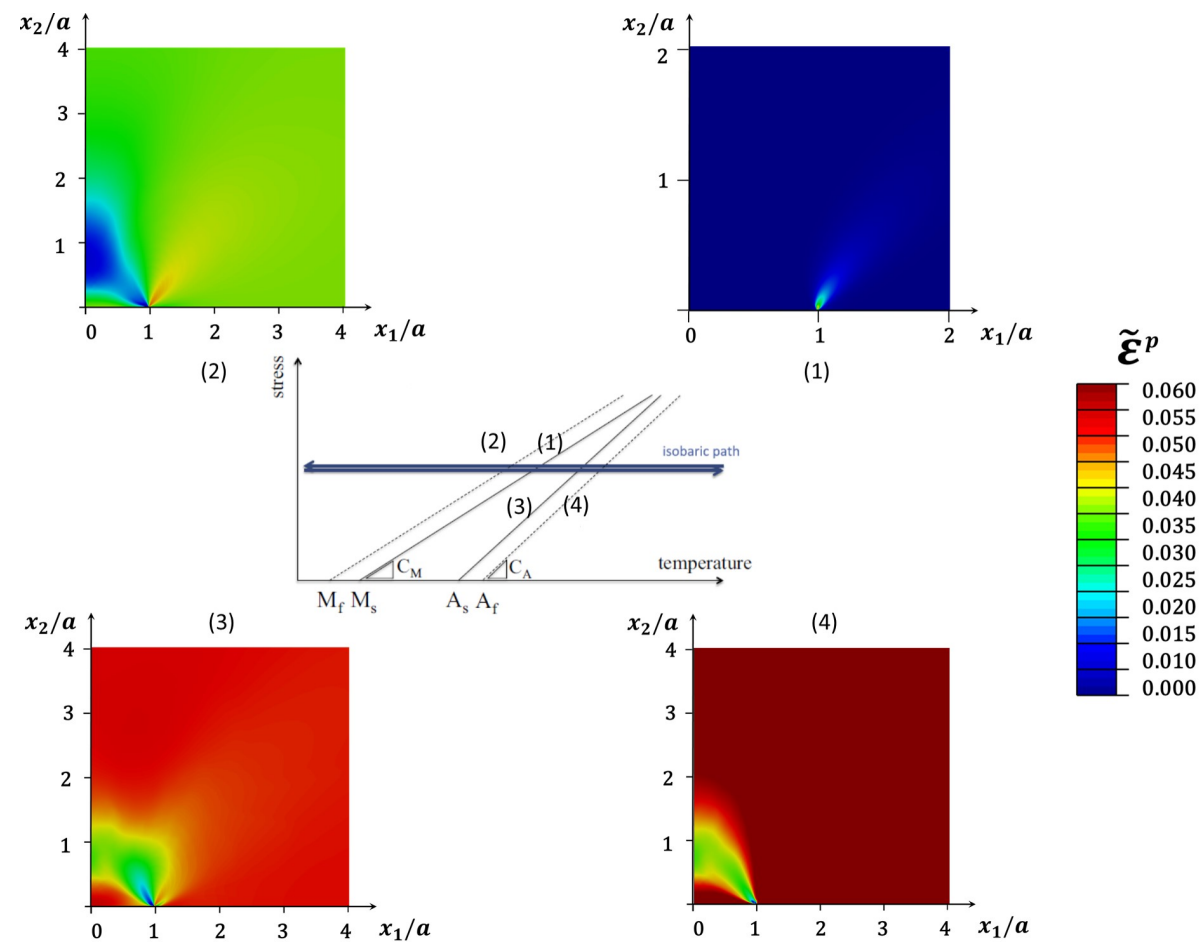
Figure 3.11: Contours of equivalent plastic strain, ε^p, at different temperatures numbered on the stress-temperature phase diagram during the actuation loading. Note that the near-tip regions in which ε^p is depicted are of different sizes.

Evolution of driving force through multiple thermal cycles also shows that the peaks during cooling and heating are at different levels, and is a result of the competition between transformation and plastic strains. During heating, crack shielding from reverse phase transformation is partially canceled by anti-shielding due to plasticity in front of the crack. As a result, peak G_I/G_∞ value during cooling, when transformation and plastic strain act in concert, is slightly higher than that during heating. Plastic straining with each thermal cycle alters the material's thermomechanical properties, including its phase transformation temperatures (M_s, M_f, A_s, A_f). The normalized driving force reaches peak values during cooling/heating, correlated with beginning of forward and reverse transformation behind and in front of the crack, respectively. This leads to another feature of the driving force during multiple thermal cycling, *viz.*, shift in the peak driving force during cooling and heating with respect to temperature. The shift in peaks of G_I/G_∞ during cooling and heating is thus proportional to the thermal cycling induced gradual change in the phase transformation temperatures of the SMA material and occurs through multiple thermal cycles.

3.4.4   Varying saturation level of TRIP strain

In this section, stationary cracks are studied for varying levels of the saturation plastic strain ε_{ij}^p, as described in Section 3.2. The evolution equation of plastic strain as given in Section 2.0.2 is restated here:

$$d\varepsilon_{ij}^p = \Lambda_{ij}^p d\xi, \quad \Lambda_{ij}^p = \begin{cases} \dfrac{3}{2} C_1^p \dfrac{H^{cur}\left(\bar{\sigma}\right)}{H^{max}} \dfrac{s_{ij}^{eff}}{\bar{\sigma}^{eff}} e^{-\frac{\zeta^d}{C_2^p}}, & d\xi > 0 \\[2em] C_1^p \dfrac{H^{cur}\left(\bar{\sigma}\right)}{H^{max}} \dfrac{\varepsilon_{ij}^t}{\xi} e^{-\frac{\zeta^d}{C_2^p}}, & d\xi < 0. \end{cases} \tag{3.23}$$

Here, material parameters C_1^p and C_2^p govern the magnitude and the number of cycles necessary for the attainment of the saturation level plastic strain. For a

multiaxial loading case, such as present, the product $C_1^p * C_2^p$ is interpreted as a measure of saturation level of the total equivalent plastic strain produced as a result of cyclic phase transformation. The physical meaning of these parameters can be better understood with a simple 1-D uniaxial loading case ([62]). The evolution equation for the plastic strain can be written as

$$\dot{\varepsilon}^p = \Lambda^p \dot{\zeta}^d, \tag{3.24}$$

and the TRIP tensor Λ^p is given by

$$\Lambda^p = \Lambda_{11}^p = \begin{cases} C_1^p \dfrac{\sigma^{eff}}{|\sigma^{eff}|} e^{-\frac{\zeta^d}{C_2^p}}, & \dot{\xi} > 0 \\ C_1^p \dfrac{\varepsilon_{max}^t}{|\varepsilon_{max}^t|} e^{-\frac{\zeta^d}{C_2^p}}, & \dot{\xi} < 0. \end{cases} \tag{3.25}$$

Integrating (21) yields the following expression for plastic strain ε^p as a function of the detwinned martensite volume fraction ζ^d:

$$\varepsilon^p = C_1^p C_2^p (1 - e^{-\frac{\zeta^d}{C_2^p}}) = \varepsilon_{sat}^p (1 - e^{-\frac{\zeta^d}{C_2^p}}) \tag{3.26}$$

where the maximum (saturation) level of plastic strain is given as $\varepsilon_{sat}^p = C_1^p C_2^p$.

In the present analysis, $C_1^p C_2^p$ is varied at different levels in order to study the effect of varying saturation plastic strains. Since these parameters control two separate aspects of the evolution of the TRIP, *viz.* C_1^p represents the final values of saturation TRIP strain whereas C_2^p is the number of cycles that are required to reach that strain level. ε_{sat}^p can thus be controlled by varying the values of C_1^p and C_2^p, from negligibly low ($\varepsilon_{sat}^p = 0.5\%$ *i.e.* $C_1^p = 0.00028$, $C_2^p = 18$) to intermediate ($\varepsilon_{sat}^p = 5\%$ *i.e.* $C_1^p = 0.0028$, $C_2^p = 18$), and significantly high ($\varepsilon_{sat}^p = 20\%$ *i.e.* $C_1^p = 0.011$, $C_2^p = 18$). The number of cycles for TRIP strain saturation is kept constant at 18, in

order to correctly identify the effect of magnitude of the irreversible strain values on the crack-tip mechanical fields, for both static and advancing cracks. Moreover, the saturation value of the transformation strain (H^{max}) is kept constant for these cases. The numerical results for these three cases is compared in this section.

Variation of driving force for crack growth in the form of normalized crack-tip energy release rate G_I/G_∞ during the first thermal cycle for two saturation plastic strain levels is plotted (Figure 3.12(a)). During cooling, G_I/G_∞ varies in a similar manner for both ε_{sat}^p strain levels: initial plateau before global forward phase transformation begins in crack front, steep increase due to anti-shielding effect from transformation and plastic strains in crack front, final decrease when transformation strains in the wake shield the crack. During heating, the driving force shows initial plateau before global reverse phase transformation sets in, followed by slight increase due to anti-shielding from recovered transformation strain behind the crack tip followed by steep decrease due to shielding effect from recovered transformation strains in front of the crack. With increasing ε_{sat}^p magnitude, the contribution to crack anti-shielding and thereby to the crack tip energy release rate due to plastic strain increases, leading to an increase in the peak driving force during both cooling and heating; the peak during cooling is slightly higher than that during heating due to aforementioned difference in the role of plastic strain *vis-a-vis* transformation strain. ε_{sat}^p magnitude also influences the rate of change of crack tip energy release rate with respect to temperature; higher magnitude leading to a steeper G_I/G_∞ vs. temperature slope during cooling due to corresponding higher anti-shielding (Figure 3.12(a)).

Moreover, for negligible ε_{sat}^p (0.5%), the variation of driving force follows similar trend as that in a material without any plastic strain, and since plastic strain plays an insignificant role in shielding and anti-shielding of the crack, G_I/G_∞ at the end

103
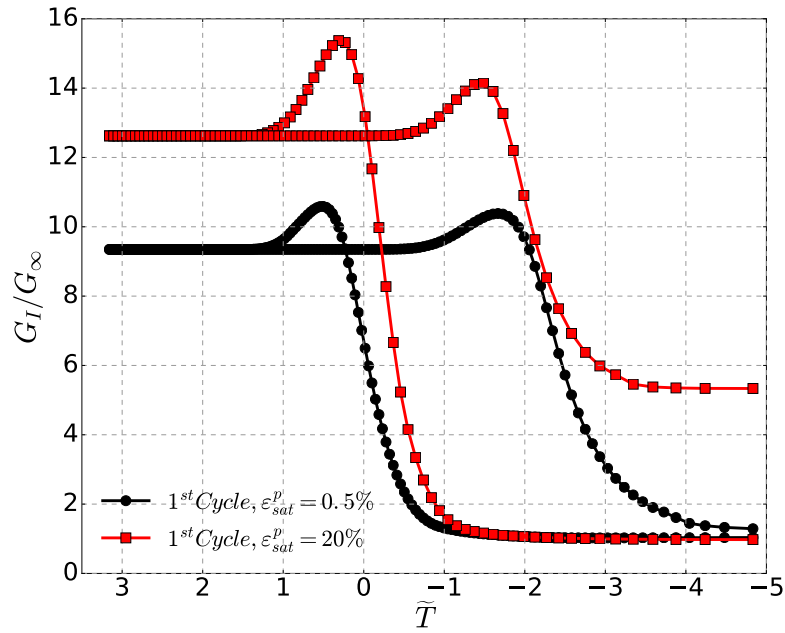
(a) during first thermal cycle
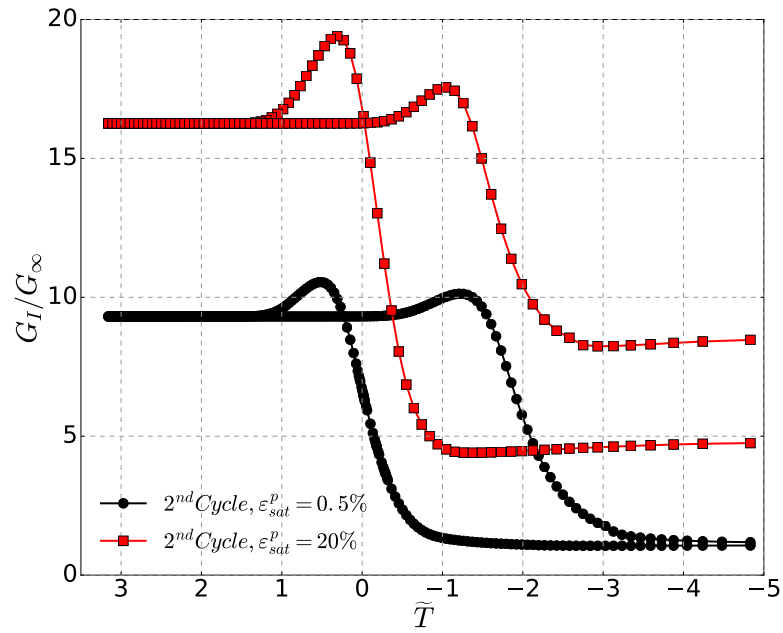
(b) during second thermal cycle

Figure 3.12: Evolution of the normalized energy release rate, G_I/G_∞, versus normalized temperature $\widetilde{T}$, during the first and second thermal cycles for two levels of TRIP. Black curves show the case where the saturation level of the plastic strain is low enough to be negligible (0.5%); red curves show the case where saturation plastic strain has a significant value (20%).

of heating is approximately equal to that at the beginning of cooling. With high ε_{sat}^p (20%), the crack driving force is affected to a greater extent by shielding from plastic strain behind the crack and anti-shielding from plastic strain ahead of the crack leading to a residual G_I/G_∞ that is increasingly higher at the end of thermal cycle. Crack driving force curves during the second thermal cycle (Figure 3.12(b)) diverge significantly from their initial values during the first thermal cycle. A substantial difference in the maximum driving force during cooling and heating during second cycle exists for high ε_{sat}^p, but is practically absent in the case of negligibly small ε_{sat}^p, since the material does not undergo any significant irreversible microstructural changes. A general trend can thus be identified to be an overall monotonic increase in crack driving force magnitude with greater saturation TRIP levels under cyclic thermal loading.

3.4.5 Advancing cracks

For a material specific "critical" crack-tip energy release rate (G_{crit}), the crack can be assumed to propagate when $G_I = G_{crit}$. Consequently, monotonic increase in the magnitude of G_I/G_∞ with increasing saturation TRIP strains and progressive thermal cycling can eventually lead to triggering of crack growth (when $G_I = G_{crit}$), even if initial thermal cycles do not produce enough crack driving force and $G_I <<$ G_{crit}. In an SMA material with TRIP and relatively high critical energy release rate, the possibility of crack growth from an initial crack thus depends not only on the number of thermal cycles but also the saturation level of the TRIP strain magnitude. Notably, as observed in Figure 3.12, the difference between the initial and final values of the driving force do not show any considerable change with cyclic thermal loading, since this difference is only proportional to the saturation TRIP strain magnitude, and thus remains nearly constant for a fixed ε_{sat}^p. In this section,

these ideas are explored in greater detail by studying advancing cracks in SMA materials with varying levels of saturation TRIP strains and a constant critical energy release rate, G_{crit}.

3.4.5.1 Stable crack growth

In this section, some aspects of the near-tip distribution of transformation and plastic strain fields during stable crack growth for the material properties in Table 3.1 are discussed. Crack growth is triggered in the first thermal cycle when the plane strain driving force for crack growth *i.e.* crack-tip energy release rate G_I becomes equal to a material specific "critical" energy release rate G_{crit}. A particular case when $G_I = G_{crit} = 2G_\infty$ is presented first. Figure 3.13 shows contours of martensite volume fraction in vicinity of the crack-tip for a quarter of the infinite medium; red color represents material elements that have undergone complete austenite-to-martensite phase transformation, blue color represents non-transformed austenite, whereas colors in between correspond to partially transformed regions. Horizontal axis (x_1) shows the direction of crack growth and vertical axis (x_2) is the direction of applied load, where the abscissas and ordinates are normalized with the initial half-crack length "a". With decreasing temperature, when $G_I = G_{crit} = 2G_\infty$, crack grows in mode-I along the x_1 direction. The region around the crack tip progressively transforms into martensite and the region of transformation grows in size (Figure 3.13(a),(b)).

As discussed by the authors in a previous publication ([58]), global phase transformation interacting with the material's boundaries results in non-proportional loading in region surrounding the moving crack-tip. Normalized von Mises stress field during crack growth shown in Figure 3.14, on the other hand, does show significant variation in magnitude. The region of high equivalent stresses follows the advancing

106
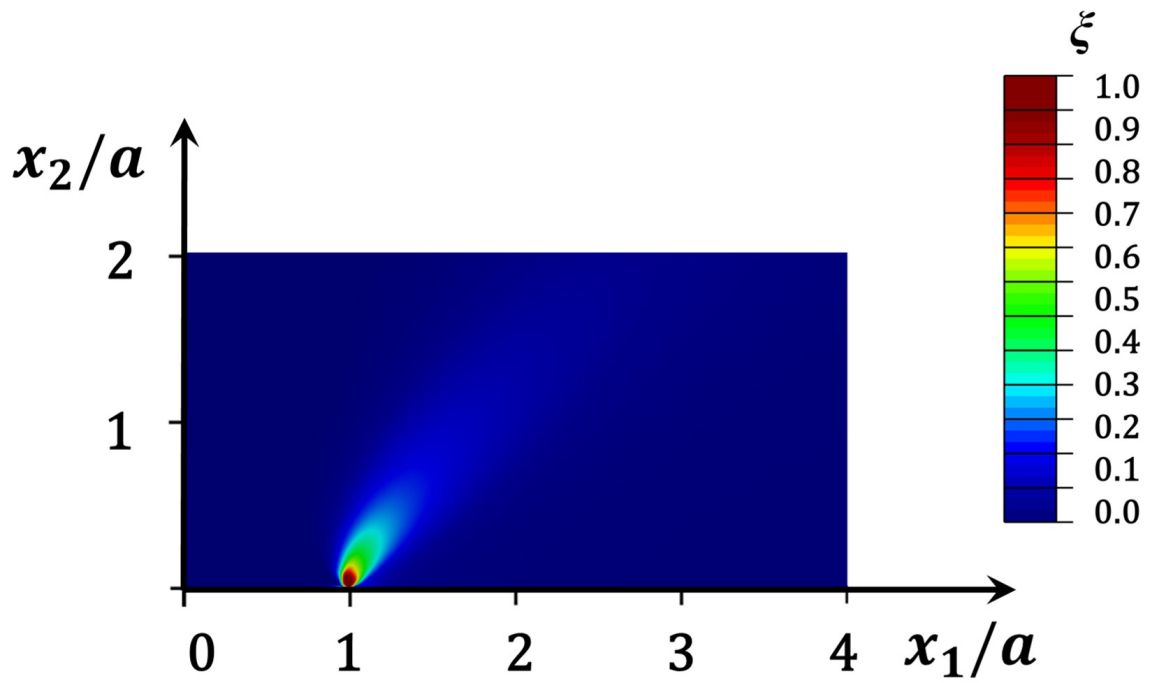
(a) at initiation of crack growth
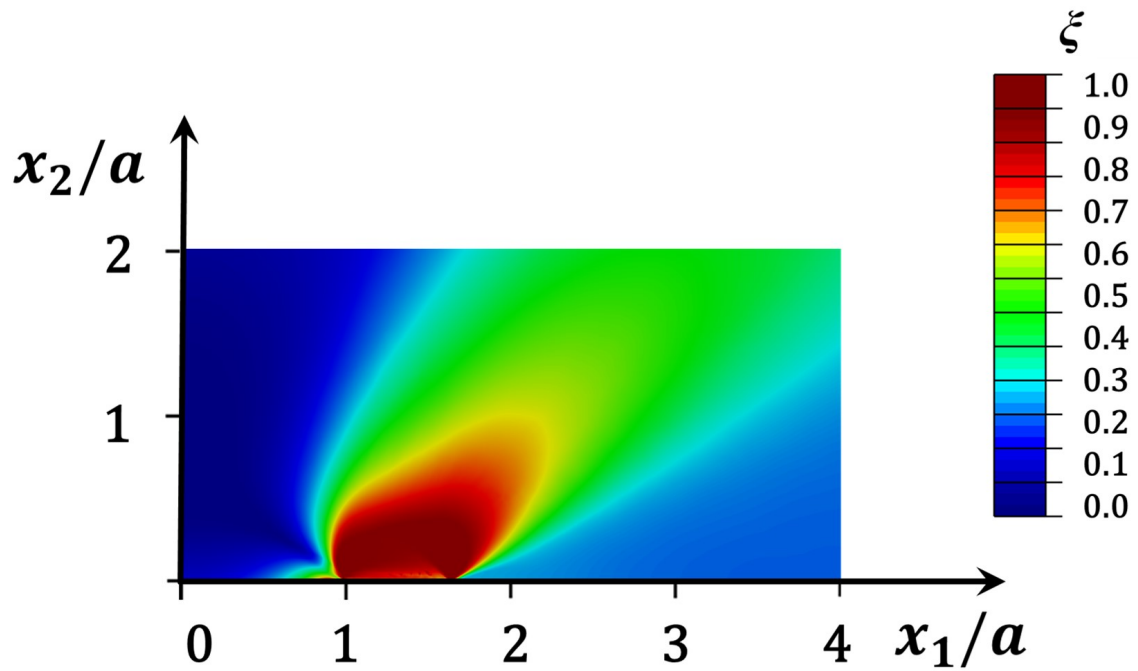
(b) during crack growth

Figure 3.13: Martensite volume fraction, ξ, in the vicinity of the crack tip during stable crack growth.
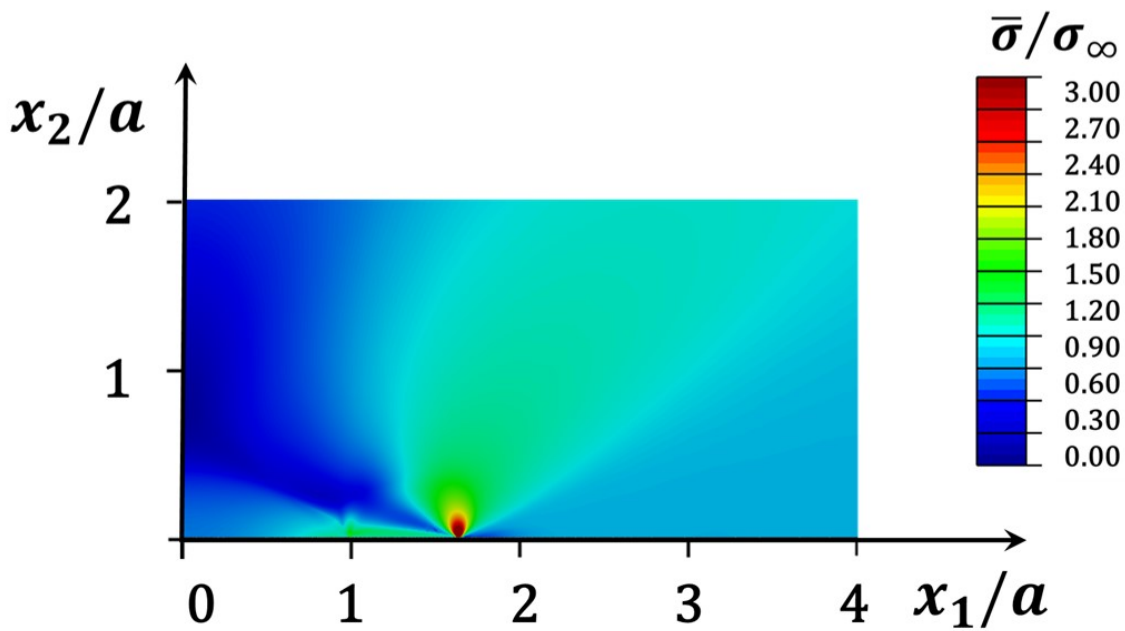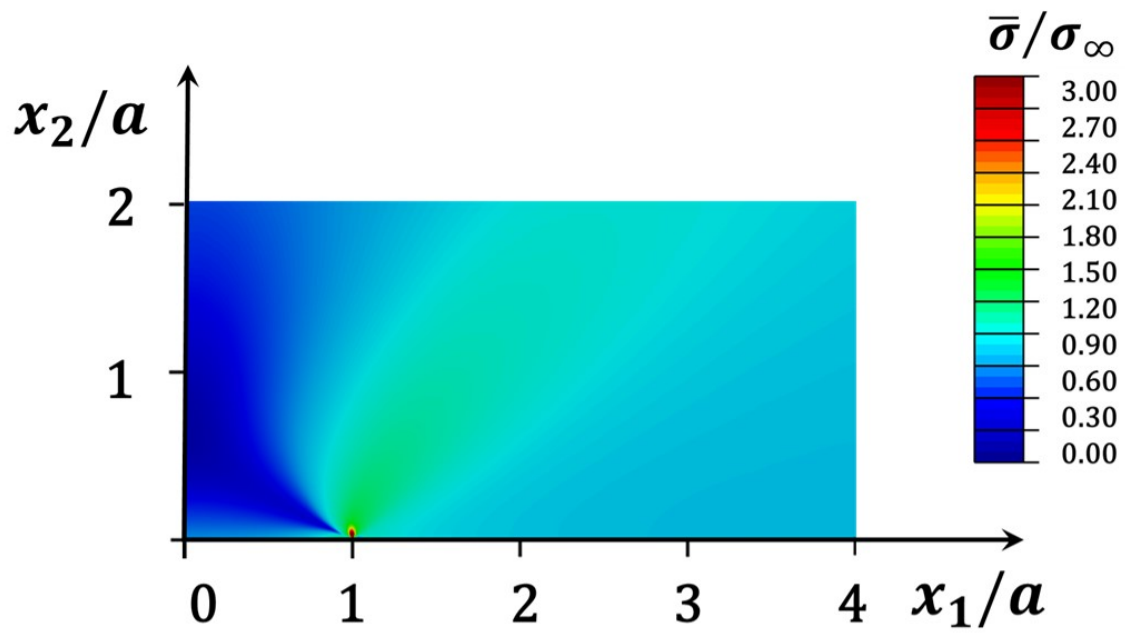
Figure 3.14: Normalized Mises equivalent stresses, $\overline{\sigma}/\sigma_\infty$, in the vicinity of the crack tip during stable crack growth.
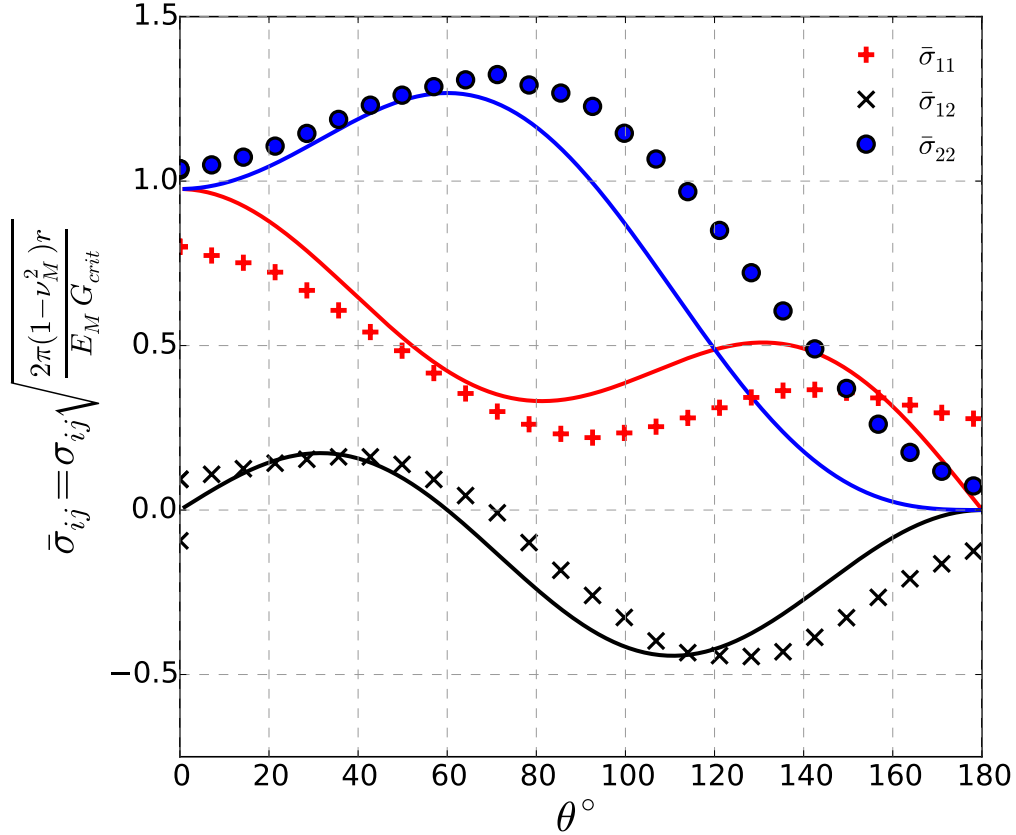
Figure 3.15: Angular distribution of stresses close to the crack tip during stable crack growth. The markers are numerical results for the SMA material with TRIP and solid lines represent analytical results for an elastic material with the properties of martensite. The $1/\sqrt{r}$ radial dependence has been accounted for within the normalization.

crack tip and is a direct result of the crack growth being driven by stress distribution due to forward phase transformation in front of the tip. However, increasing magnitude of TRIP during crack growth increases the overall equivalent stresses in the region surrounding the advancing crack tip. Inside the fully transformed domain in the vicinity of crack-tip, stress field is equivalent to the asymptotic K-field of an isotropic elastic material with the properties of martensite. During crack growth,

stress intensity factor ($K = K_{crit}$, K_{crit} being the critical fracture toughness for crack growth) is related to the critical crack-tip energy release rate (G_{crit}) as follows: $G_{crit} = (1 - \varepsilon_M^2)K_{crit}/E_M$. The angular distribution of normalized stress components in the vicinity of the crack tip during crack growth is shown in Figure 3.15, and is equivalent to the stress distribution in a purely elastic material with properties of martensite where the stresses have a $1/\sqrt{r}$ radial asymptotic behavior. These plots provide further justification for the usage of a single fracture toughness parameter (crack-tip energy release rate, in this case) to fully characterize the near-tip mechanical fields and the validity of VCCT to numerically calculate that parameter.

As the crack grows incrementally, fully transformed region is left in the wake of the crack, as shown in Figure 3.13(b). Owing to the continually decreasing temperature, material left in wake of the traveling crack tip does not reverse transform, despite reduction in stresses due to unloading at the crack faces. As a result, only elastic unloading occurs in the transformed material behind the tip of the moving crack. The constraint of the surrounding far-field elastic austenite on the fully transformed martensite in the wake, along with the accumulation of transformation and plastic strains in the transformed martensite, results in an apparent reduction in the crack opening displacement, and hence crack driving force, required for stable crack growth [111]. Further decrease in temperature (cooling) compensates for this reduction in driving force by intensification of near-tip stresses due to further phase transformation in front of the crack and results in the crack-resistance "R-curve" or transformation toughening behavior. The "R-curve", where temperature is plotted on vertical axis against the normalized crack growth on horizontal axis, is shown in Figure 3.16. It can be seen that a gradual decrease in temperature (from about 316K to 310K), which corresponds to stress redistribution due to forward phase transformation, is required to stably extend the crack. Stable crack growth is seen until

110
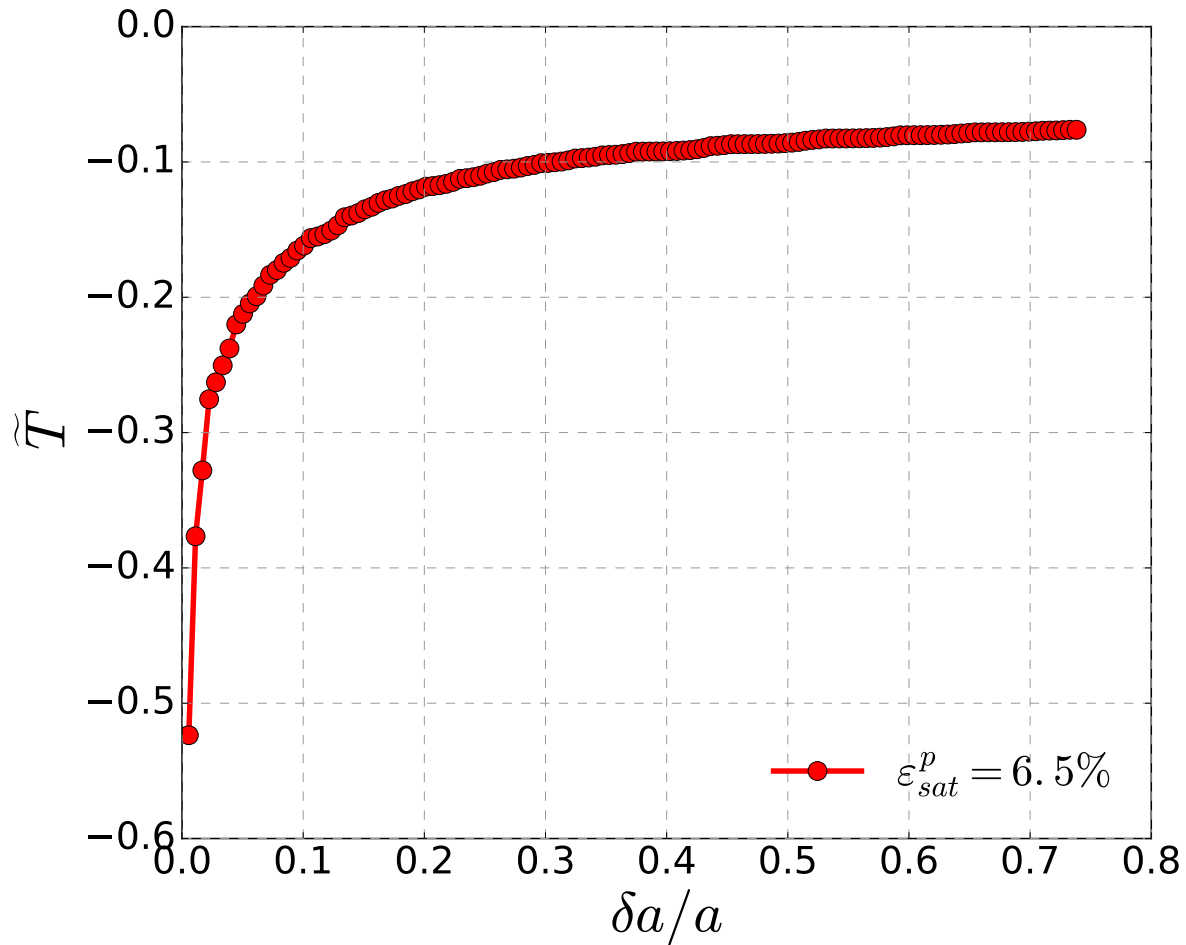
Figure 3.16: Normalized temperature $\widetilde{T}$ versus normalized crack growth, da/a, for $\frac{G_{crit}}{G_\infty} = 2$.

the crack extends by roughly 75% of its original length, at which point the global forward phase transformation is enough to sustain steady state crack growth.

Accumulation of plastic strains follows the same trend as phase transformation and occurs mainly in front of the crack during cooling part of thermal cycle. Figure 3.17 shows the near-tip contours of equivalent plastic strain($\tilde{\varepsilon}^p$), during stable crack growth. Relatively higher values of this normalized equivalent plastic strain

(about 0.04) are in region closer to the crack tip and decreasing plastic strain is found as one moves away from the crack tip. As the crack grows in a stable manner, the region of plastic strain in front of the crack expands providing further driving force for crack extension, whereas the region in wake of the crack shows accumulated irrecoverable plastic strain. Plastic strain coupled with forward phase transformation ahead of the crack tip results in anti-shielding effect and increases the driving force for crack growth via stress redistribution, whereas accumulated martensite and irreversible plastic strain in transformed material behind the crack provides transformation toughening which results in stable crack growth shown in Figure 3.16. TRIP strain in an SMA under actuation loading, thus, aids the process of crack extension as well as assists in the transformation toughening process ultimately resulting in stable crack growth until steady state is reached.

As mentioned earlier, due to monotonously accumulating TRIP in the material, crack tip energy release may become equal to the critical value in a subsequent thermal cycle. As shown in Figure 3.18, the critical crack tip energy release rate is considered to be high enough such that crack growth is not observed in the first thermal cycle. The evolution of G_I/G_∞ in the first thermal cycle, as a result, follows the same trend as described before. In the second thermal cycle, however, crack growth is triggered, when $G_I/G_\infty = G_I/G_{crit} = 13$. Once triggered, stable crack growth is observed through multiple cycles due to transformation and TRIP strain that are left in the wake of the moving crack. In subsequent cycles, transformation and TRIP strains providing the increase in driving force start to overcome the shielding produced by strains in the crack wake (which takes a few cycles, without much crack extension however) as seen in Figure 3.19, where the region of fully transformed material is much larger compared to the cases discussed earlier. After several thermal cycles, the stress intensity enhancement provided by global phase transformation and
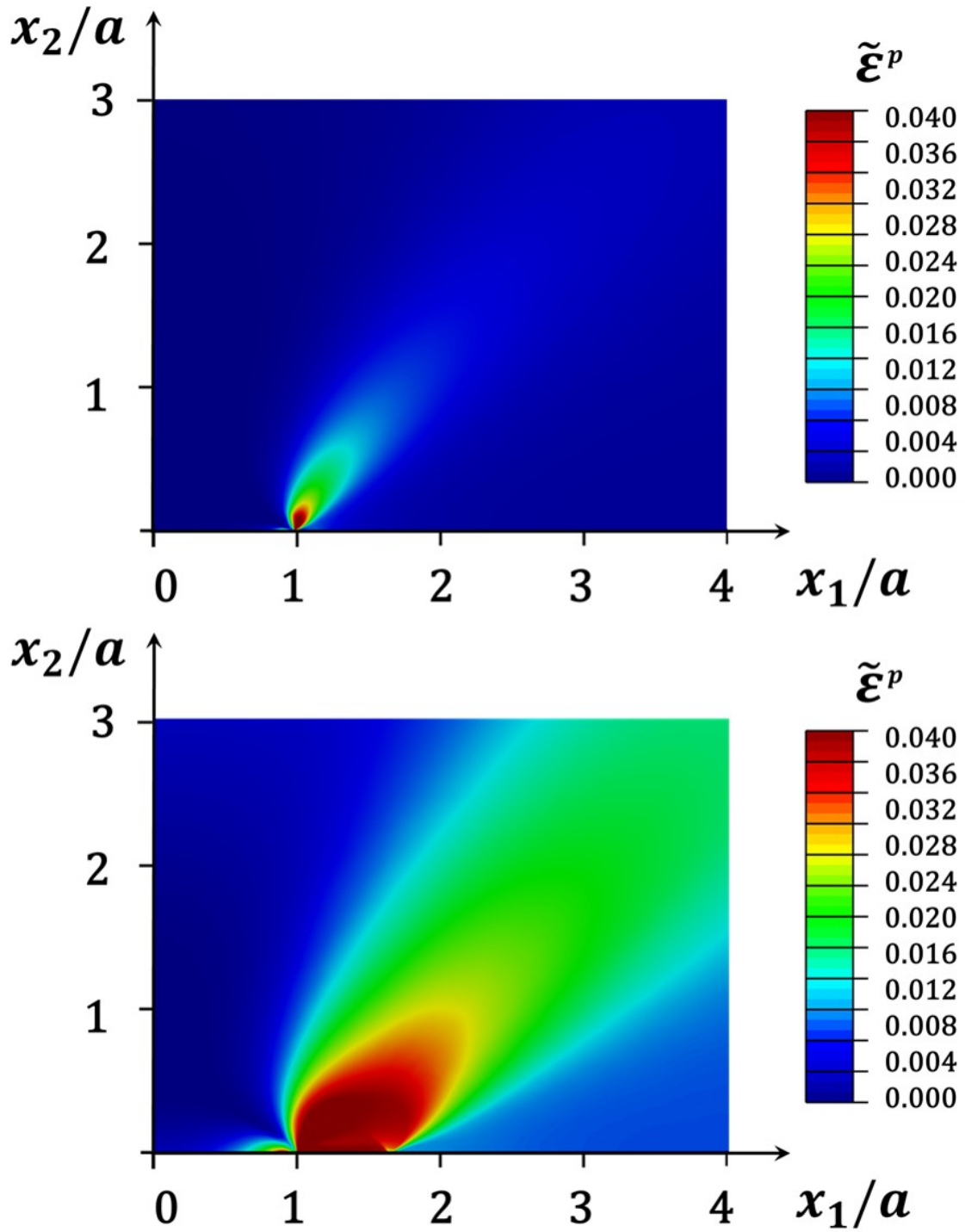
Figure 3.17: Equivalent transformation induced plastic strain, $\tilde{\varepsilon}^p$, in the vicinity of the crack tip during stable crack growth.

TRIP is enough to overcome toughness enhancement resulting from transformation and TRIP strains left in the crack wake and steady state crack growth is attained.
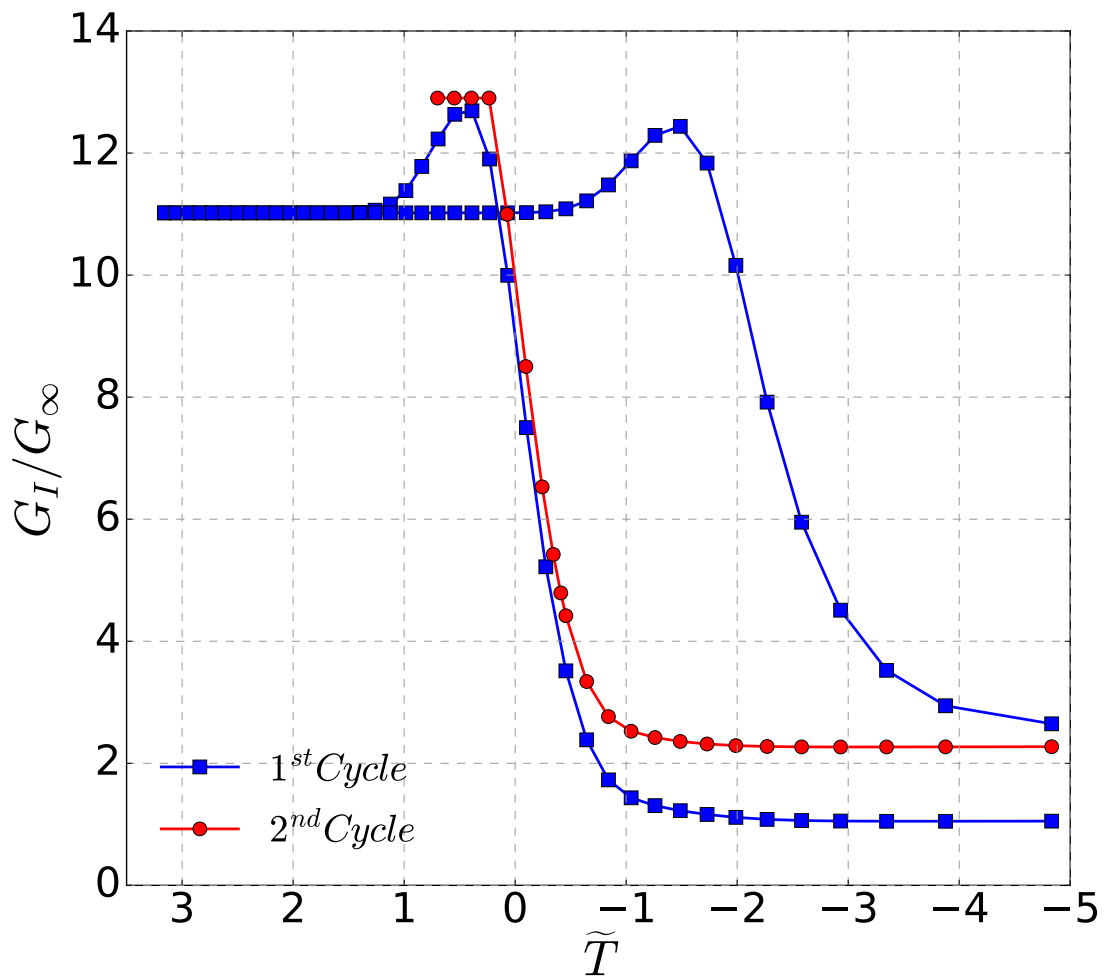
Figure 3.18: Evolution of the normalized crack-tip energy release rate, G_I/G_∞, versus uniform normalized temperature $\widetilde{T}$, over two thermal cycles, where crack growth is triggered in the second cycle when $G_I/G_\infty = 13$.
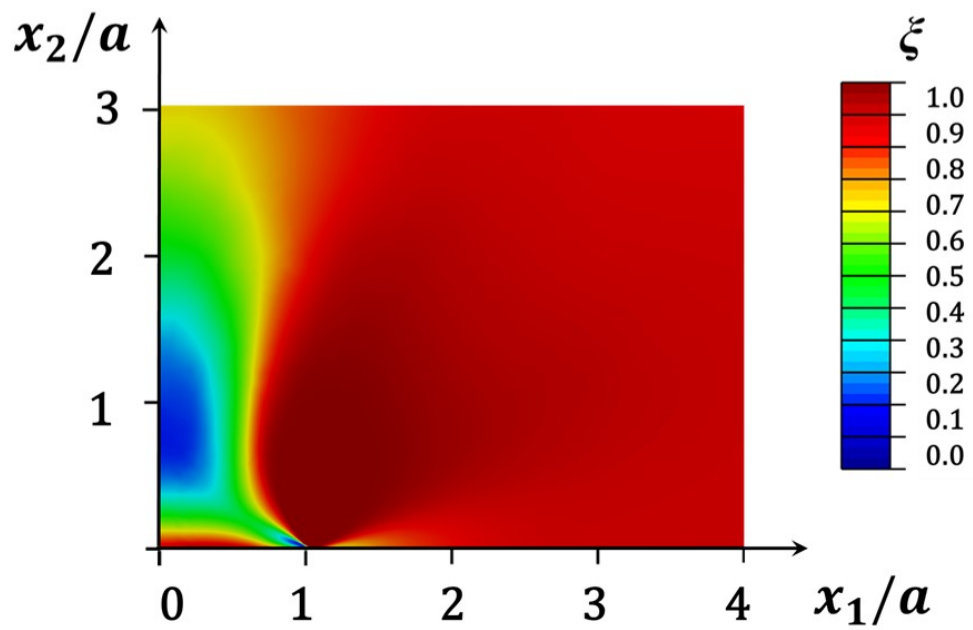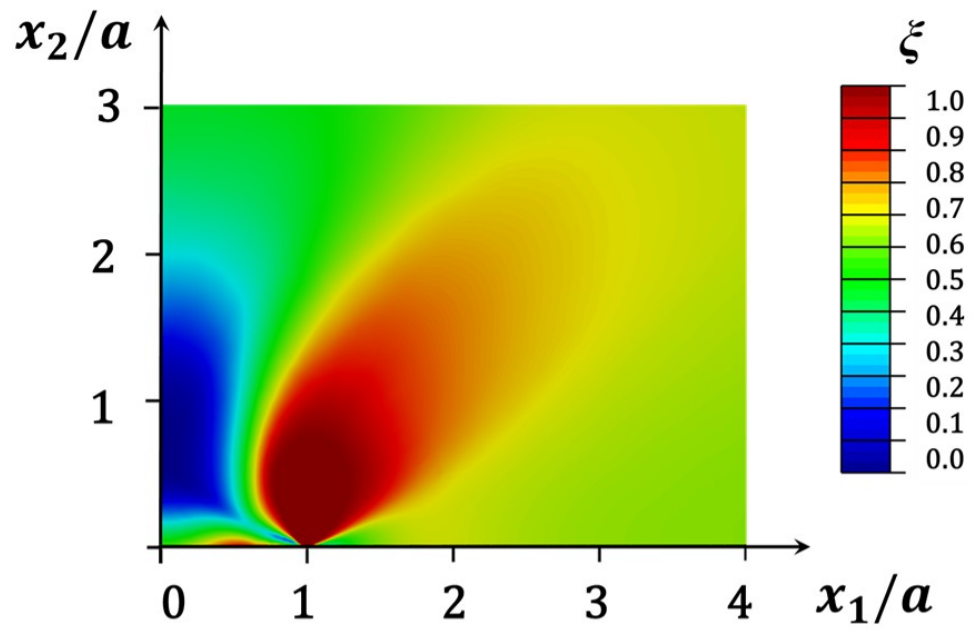
Figure 3.19: Contours of martensite volume fraction ξ at the initiation of crack growth and during stable crack growth.

3.4.5.2 Varying saturation levels of TRIP strain

Advancing cracks in SMA materials with a constant material specific critical energy release rate G_{crit}, and varying saturation level of TRIP strains are numerically analyzed. Crack growth is assumed to trigger during cooling when the crack tip energy release rate G_I resulting from global phase transformation and TRIP strains due to thermomechanical loading becomes equal to G_{crit}, *i.e.* when $G_I = G_{crit} = 2G_\infty$.

Crack-resistance "R-curves" with normalized temperature $\widetilde{T}$ on the vertical axis plotted against normalized crack extension da/a on the horizontal axis for three magnitudes, $\varepsilon^p_{sat} = 0.5\%, 5\%, 20\%$. Crack growth is triggered at increasingly higher points with respect to the uniform normalized temperature (*i.e.* higher absolute temperatures) in the SMA material, with larger TRIP strain magnitudes. The role of temperature in initiating crack advance with respect to ε^p_{sat} strain is related to the increasing *driving force-versus-temperature* slopes observed in Figure 3.12, where higher temperature results in the same level of *crack* tip energy release rate for greater ε^p_{sat} magnitude during cooling. Stable crack growth is observed for all cases and once crack growth is triggered, further incremental cooling is required to maintain crack advance, until crack growth reaches a steady-state leading to eventual uncontrolled material failure.

Crack resistance curves in Figure 3.20 show that with increasing ε^p_{sat} magnitudes, the stable crack growth response diminishes monotonically. Steady state conditions are attained when the crack has extended by about 1.25, 1.4 and 1.5 times that of its original length for $\varepsilon^p_{sat} = 20\%$, 5% and 0.5% respectively. The amount of cooling in the form of decrease in temperature responsible for stable crack growth is higher for larger magnitude $\varepsilon^p_{sat} = 20\%$ ($\approx 6.84^oK$, from 322^oK to 315.16^oK) than that re-
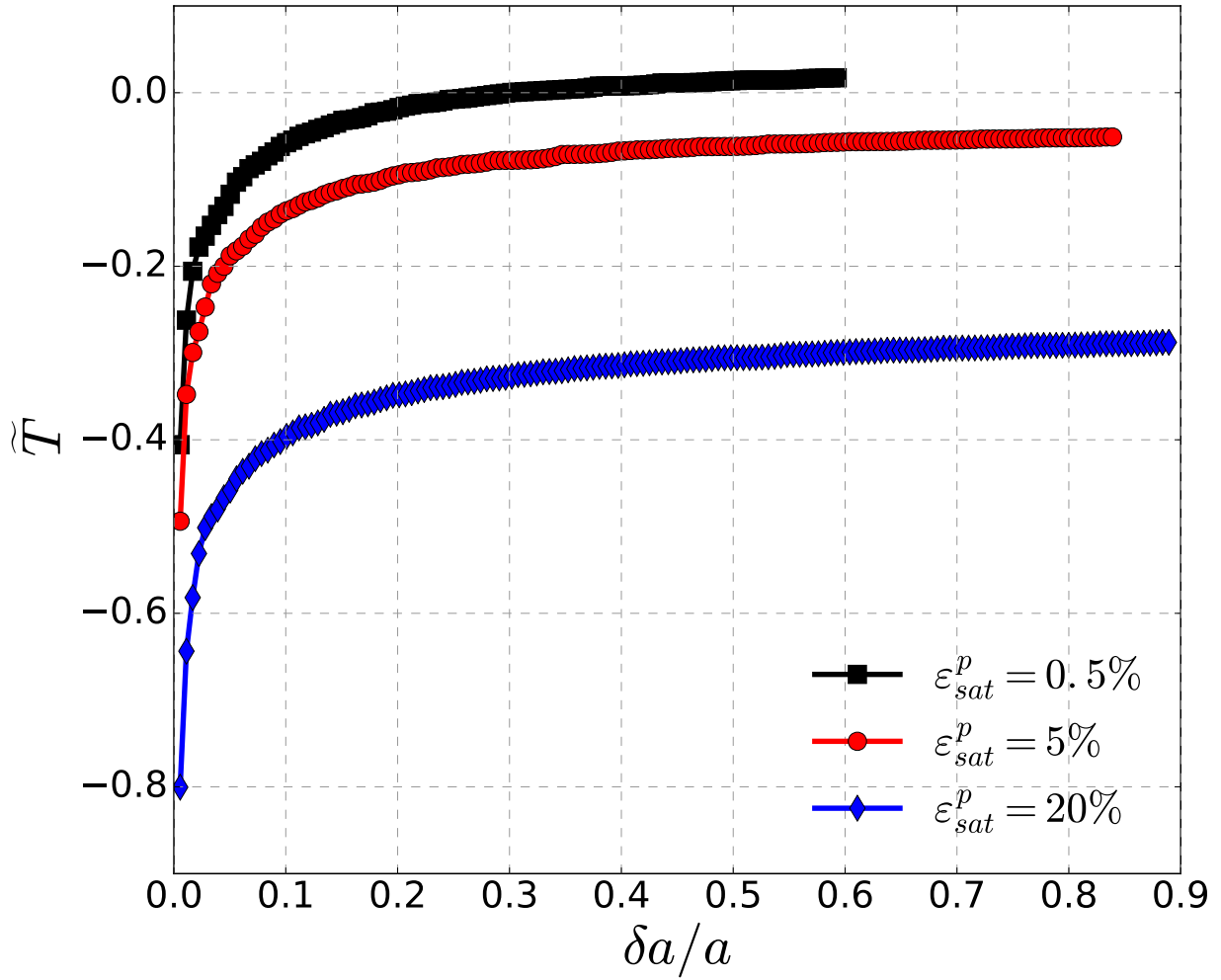
Figure 3.20: Normalized temperature, $\widetilde{T}$ versus normalized crack growth, da/a, for $G_{crit}/G_I = 2$ showing the crack resistance "R-curve" behavior. Black curve shows the case where the saturation level of the plastic strain is low enough to be negligible (0.5%); red curve shows the case where saturation plastic strain has a significant value (20%), whereas blue curve shows a case with intermediate level of saturation plastic strain(5%).
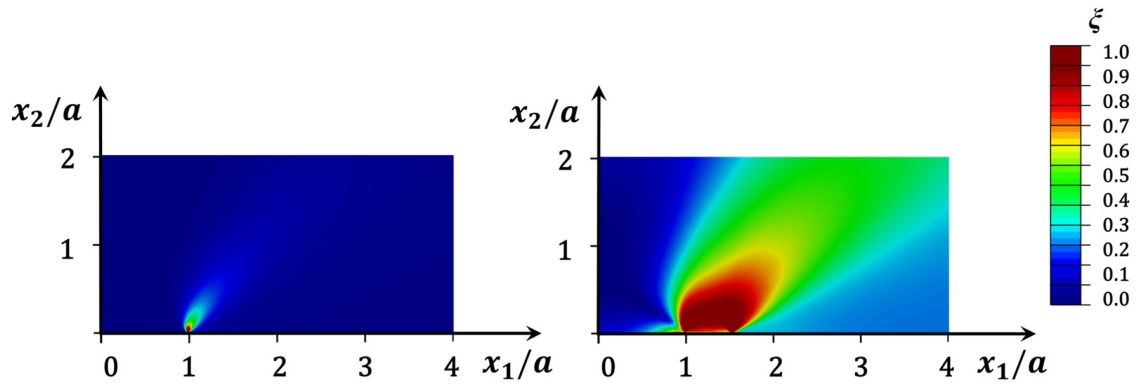
(a) $\varepsilon_{sat}^{p} = 0.5\%$: at initiation of crack growth and during stable crack growth
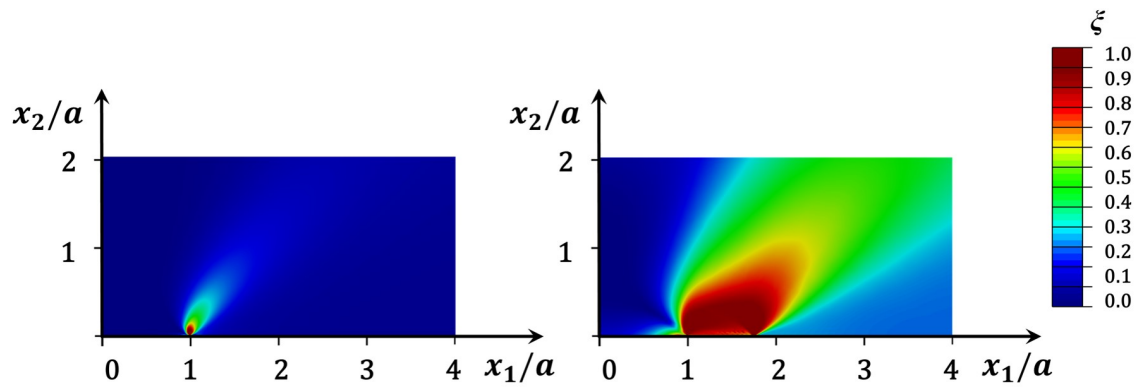
(b) $\varepsilon_{sat}^{p} = 5\%$: at initiation of crack growth and during stable crack growth
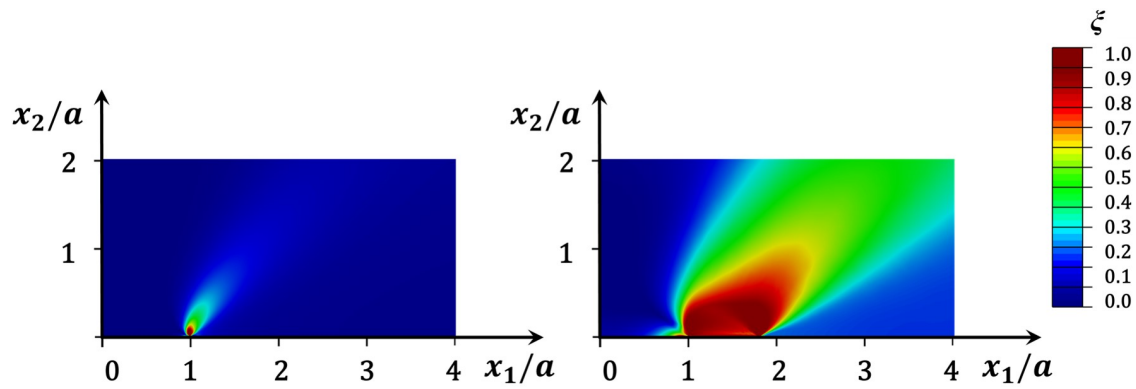
(c) $\varepsilon_{sat}^{p} = 20\%$: at initiation of crack growth and during stable crack growth

Figure 3.21: Martensite volume fraction, ξ, in the vicinity of the crack tip during crack initiation and stable crack growth for varying levels of saturation TRIP strain (ε_{sat}^{p}).

quired in cases with smaller magnitudes $\varepsilon_{sat}^{p} = 0.5\%$, 5% ($\approx 6.05^{o}K$ and $\approx 6.25^{o}K$), and is directly related to the influence of plastic strains on enhancement of the crack driving force. Although the temperature differentials are small, it is necessary to note that stable crack growth itself occurs in a short window of temperature change during cooling. Higher plastic strains provide a greater degree of crack-tip shielding in addition to that arising from transformation strains leading to greater enhancement in the apparent fracture toughness of the material. For negligibly low plastic strains, the contribution of shielding from plastic strains and the resulting toughness enhancement is relatively smaller. Anti-shielding due to global-scale plastic strain (when $\varepsilon_{sat}^{p} = 20\%$), which tends to enhance near-tip intensity and open up the crack due to conditions in the mechanical fields *ahead* of the crack tip is less dominant compared to the crack shielding due to apparent reduction in driving force from accumulated plastic strain *behind* the crack tip. As such, higher shielding due to accumulated strains in wake of the moving crack tip leads the crack to reach steady state at a relatively slower rate. This produces a more stable crack-growth response compared to that in low ε_{sat}^{p} strain, as seen in 3.20, and is further elaborated using the near-tip distribution of transformation and plastic strain fields next.

Martensite volume fraction (ξ), which denotes the regions that have completely or partially transformed into martensite, in regions close to the crack tip at the initiation of crack growth and during stable crack growth is plotted in Figure 3.21. Three cases for $\varepsilon_{sat}^{p} = 0.5\%$, 5% and 20% are shown, to compare the dependence of crack-tip phase transformation in a moving crack on the saturation level plastic strain in the material. The degree of stable crack growth is seen to be directly proportional to the magnitude of plastic strain in the material, and is evident from the size of fully transformed region which is considerably larger when $\varepsilon_{sat}^{p} = 20\%$ than when $\varepsilon_{sat}^{p} = 0.5\%$. With advancing crack, region in the wake of the tip which has forward

119
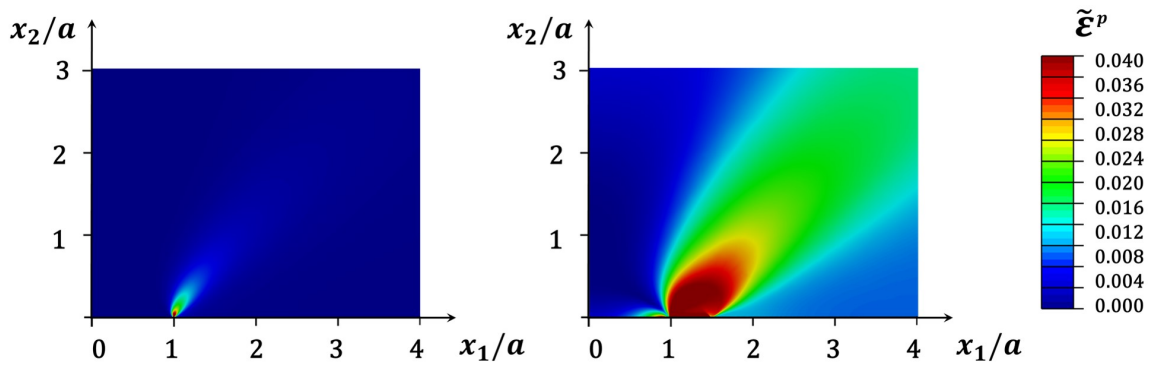
(a) $\widetilde{\varepsilon^p}$ distribution for $\varepsilon_{sat}^p = 0.5\%$: at initiation of crack growth and during crack growth.
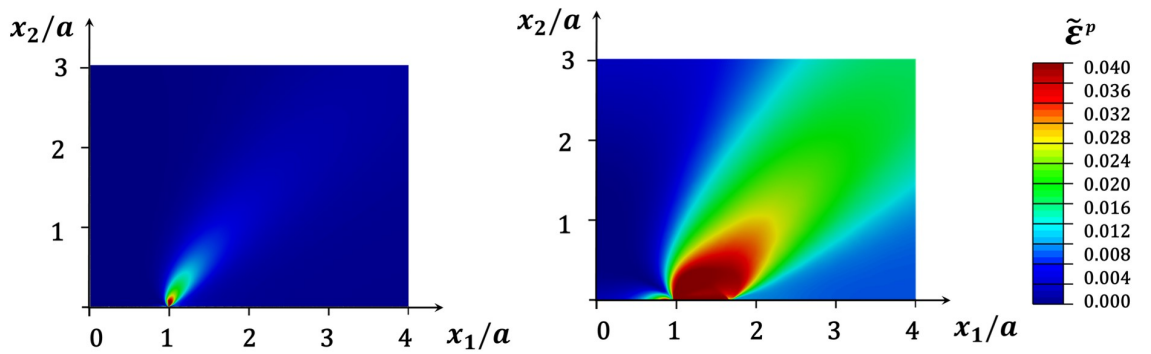
(b) $\widetilde{\varepsilon^p}$ distribution for $\varepsilon_{sat}^p = 5\%$: at initiation of crack growth and during crack growth.
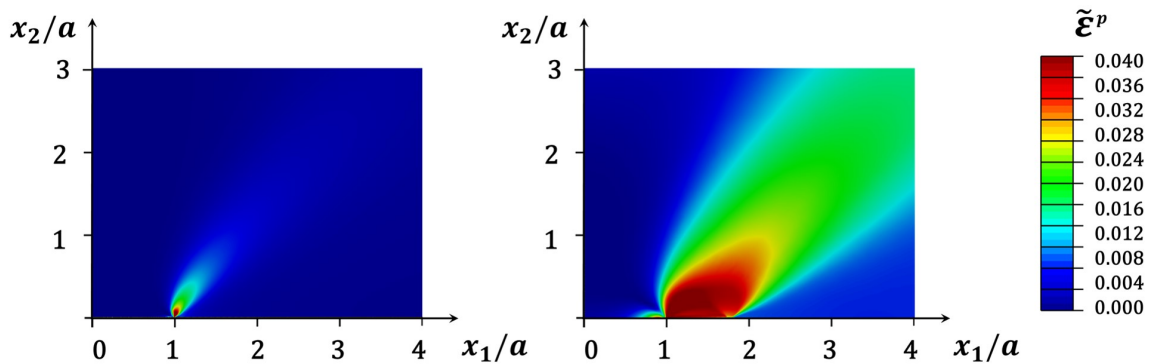
(c) $\widetilde{\varepsilon^p}$ distribution for $\varepsilon_{sat}^p = 20\%$: at initiation of crack growth and during crack growth.

Figure 3.22: Transformation induced plastic strain in the direction of applied load, $\widetilde{\varepsilon^p}$, in the vicinity of the crack tip during crack initiation and stable crack growth for varying levels of saturation TRIP strain (ε_{sat}^p).

transformed remains in martensitic state and also contains TRIP strains. When the crack advances into a larger transformation zone in the absence of reverse phase transformation, a greater reduction in the near-tip stress intensity occurs leading to an apparent increase in the material's fracture toughness. As such, toughness enhancement seen in these three cases is seen to vary according to the amount of TRIP strain generated during crack growth.

Distribution of the normalized equivalent plastic strain, $(\widetilde{\varepsilon^p})$, in the region close to the moving crack tip is plotted in Figure 3.22. The extent of the region of relatively high plastic strains in the wake of the crack tip aids in transformation toughening resulting in stable crack growth seen in crack resistance plots. However, with incremental crack growth during cooling, magnitude of $\widetilde{\varepsilon^p}$ also increases in a fan in front of the crack tip. The highest magnitude of plastic strain $\widetilde{\varepsilon^p}$ in front of the crack tip is observed towards the end of stable crack growth and has values approximately 0.1% and 0.4% respectively with increasing magnitudes of the saturation TRIP strains. Global scale plastic strain in front of the growing crack increases the driving force for crack growth and acts against the toughening effect produced by transformation and plastic strains in the zone behind the crack tip. As a result, the crack grows stably as long as stress intensity reduction due to strains in the crack wake is equivalent to stress intensity enhancement due to strains in front of the crack and the resultant near-tip intensity or energy release rate G_I stays incrementally lower than the material specific critical G_{crit}. During progressive cooling in case of ε_{sat}^p =20%, larger plastic strains in front of the crack result in accelerated crack growth to reach steady state. When ε_{sat}^p =0.5% plastic strains in front of the crack are relatively smaller in magnitude and transformation toughening stays dominant leading to comparatively more stable crack growth. Magnitude of the saturation level TRIP strain in an SMA, when other material parameters are maintained constant, thus has a crucial effect

on the crack-tip mechanical fields for stationary as well as advancing cracks and also influences the stable crack growth response.

3.5   Summary

In this work, finite element calculations are carried out to investigate mechanical fields near stationary and advancing cracks in SMAs with different levels of irreversible transformation induced plasticity subjected to thermal actuation loading. The prototype problem of an infinite-medium center-cracked shape memory alloy plate subjected to multiple thermal cycles under plane strain mode-I constant applied load is investigated. Crack tip energy release rate is calculated using VCCT in ABAQUS and its normalized form, G_I/G_∞, is utilized as a fracture toughness parameter and as the driving force for crack growth.

Following observations are made for stationary cracks when the driving force G_I/G_∞ is plotted against the uniform temperature in the material: *(i)* G_I/G_∞ is independent of the crack length, an expected result since the crack length is the only length scale in the considered fracture problem. *(ii)* G_I/G_∞ at the end of heating is greater than that at the beginning of cooling and this mismatch depends on the magnitude of saturation level TRIP strain in the material (ε_{sat}^p). *(iii)* The peak value of G_I/G_∞ during cooling is higher than the peak value during heating and the difference is directly proportional to ε_{sat}^p. *(iv)* There is a shift towards lower temperature in peak G_I/G_∞ - values during multiple thermal cycles, which is a result of evolution of the material's phase transformation temperatures due to permanent microstructural changes. *(v)* ε_{sat}^p affects the rate of change of crack tip energy release rate with respect to temperature; higher magnitude leading to a steeper G_I/G_∞ vs. temperature slope during cooling due to higher anti-shielding produced by plastic strain. Presence of plastic strains thus alters the evolution of crack driving force with

thermal cycling and makes crack growth more likely with increasing value of G_I/G_∞ with each thermal cycle. It can thus be concluded that an SMA material may not fail in the initial thermomechanical cycles but undergo crack growth as cyclic phase transformation generates TRIP, raising the crack tip energy release rate above the material specific critical value.

With regard to growing cracks, crack growth is triggered when $G_I/G_\infty = G_{crit}/G_\infty$ during cooling. Contours of martensite volume fraction and components of plastic strain in crack tip vicinity illustrate that the driving force for crack growth arises from phase transformation and plastic strain in front of the crack. Transformation toughening and resulting stable growth occurs due to transformed material with irrecoverable plastic strains left in wake of the crack. TRIP strain thus assists in providing driving force for crack growth and also contributes to stable crack growth by transformation toughening until steady state is reached. Crack opening due to anti-shielding coming from plastic strains in front of the crack counter-acts and dominates the crack shielding produced by plastic strains in the transformed material behind the crack and results in the amount of toughening to be inversely proportional to the magnitude of ε_{sat}^p.

4. EFFECT OF THERMOMECHANICAL COUPLING AND LATENT HEAT ON THE FRACTURE TOUGHNESS OF SHAPE MEMORY ALLOY ACTUATORS

4.1 Introduction

High, seemingly permanent, reversible strains render shape memory alloys desirable in a wide range of actuation, energy absorption, and vibration damping applications, as discussed in previous sections. SMAs exhibit reversible diffusionless solid-to-solid transformation from cubic austenite to monoclinic martensite phases, which entails the generation of entropy and latent heat of transformation during forward transformation from austenite to martensite, and absorption of latent heat during reverse transformation from martensite to austenite. Latent heat of transformation can influence the temperature of the material and, as a result, also the phase transition stress-values, resulting in a strong "thermomechanical coupling". Incorporation of this coupling between the stress and temperature of the SMA due to presence of latent heat into the material constitutive model of SMA is thus an important aspect of SMA modeling in order to accurately mimic their behavior.

Thermomechanical coupling in SMAs under mechanical loading has been demonstrated in numerous experiments on SMA wires, strips, and tubes by studying the dependence of SMA response on mechanical loading rates [62]. The latent heat of transformation and associated temperatures for the start and end of forward/reverse martensitic transformation is generally determined using differential scanning calorimetery (DSC). Experiments have also shown that the stress–strain diagrams and the microstructural details of pseudoelastic response depends strongly on the loading rates, the types of heat bath, and sample geometries [104, 25, 105, 26].

Loading rates are seen to affect the rate of formation of martensite/austenite during forward/reverse transformation and thereby the amount of latent heat released/absorbed, changing the temperature fields. On the other hand, types of heat bath or cooling methods influence the conduction/convection of heat energy within the specimen, and from specimen to the environment, thereby affecting the temperature distribution. Size and shape of the SMA samples also govern the conduction/convection of heat and has a similar effect on the temperature distribution. Spatial evolution of temperature fields is also related to the nucleation and growth processes of stress-induced martensite and depends on the microstructure. Stress hysteresis is seen ([121]) to depend non-monotonically on the applied strain rate and such a rate dependence is governed by the competition between phase-transition time (latent-heat release/absorption time) and the time of heat exchange of SMA with environment. Whilst the hysteresis peak is achieved when these two time scales become comparable. Thus, heat transfer theory dictates that temperature variation is governed by both the rate of latent-heat release/absorption and the rate of heat exchange (convection or sometimes conduction) between the SMA and its environment.

Modeling of thermomechanical coupling in SMAs has been focused on incorporating the effect of mechanical strain rates during loading-unloading under quasi-static non-isothermal conditions. In these analyses, the area under stress-strain hysteresis, which depends on the entropy flux i.e. heat flux divided by ambient temperature is considered as the indicator for energy dissipation (important for applications in seismic sensors and vibration control) and thermodynamic irreversibility. Strain rates do not have an effect when latent heat of transformation is neglected and the analysis becomes essentially isothermal [117]. In isothermal processes (when the ambient temperature is constant), larger heat fluxes lead to greater entropy production, which

125

in turn leads to a larger area of stress-strain hysteresis. However, when latent heat and the resultant coupling is considered in SMA specimen geometries (such as wires, tubes, plates, etc.), varying strain rates cause nonuniform temperature distribution in the SMA leading to a nonlinear effect on the entropy production. Since transformation stresses in SMAs are strongly dependent on the temperature, the stress-strain hysteresis varies significantly with strain rates showing a peak at intermediate loading rates ([121]). For polycrystalline SMAs, the local change of temperature during forward/reverse transformation due to latent heat is specified by a set of coupled equations and depends on many variables, such as stress and martensitic volume fraction. Already important in case of SMA used in mechanical pseudoelastic applications, thermomechanical coupling plays an even greater role when SMAs are used as solid-state actuators and are subjected to cyclic thermomechanical loading. As such, consideration of stress-temperature coupling in its full form is crucial to analyze thermomechanical behavior and fracture response of SMA actuators.

As seen in previous sections and literature review, crack-tip stress-induced phase transformation is primarily responsible for the phenomenon of stable crack growth in SMAs under monotonically increasing load or displacement conditions, see also [8]. On the other hand, stress redistribution due to global phase transformation is shown to be responsible for driving force for crack growth under combined thermo-mechanical loading [11, 58]. The transformation toughening effect during cooling is associated with the energy dissipated by the transformed material left behind the advancing crack tip. In case of both pure mechanical and combined thermomechanical loading, once the crack has advanced to a length which is few times the maximum height of the transformation zone, increment of the loading parameter needed to achieve a given amount of crack growth diminishes, leading to the steady-state crack growth kinetics seen in R-curves. The effect of various transformation metrics, crack-

126

configurations, stress-states and the presence of irreversible TRIP strains in the SMA material has also been discussed in the previous sections. However, in all the aforementioned analyses, the rate of change of temperature (during cooling/heating) in the material was assumed to be small enough so that at each point in the analysis, thermal equilibrium was established and temperature was considered uniform everywhere in the material. Under these nominally isothermal conditions, the effect of latent heat generation/absorption due to phase transformation and the resulting thermomechanical coupling between the temperature and stress in the material, was neglected.

In previous studies, two extreme loading cases have been considered with respect to quasi-static loading conditions, *viz.* isothermal and adiabatic processes ([9]). Finite element analysis of mode-I plane strain polycrystalline center-cracked infinite domain SMAs were conducted to calculate the steady-state fracture toughness enhancement under adiabatic and isothermal conditions. Computations showed that the levels of fracture toughness enhancement associated with the energy dissipated by the transformed material in the wake of growing crack were *lower* under adiabatic conditions than under isothermal conditions. In real SMA applications the thermomechanical conditions are usually not ideal, and hence analysis under adiabatic/isothermal conditions provides a lower/upper bound on the toughening enhancement. However, to the best of our knowledge, no study that analyzes the effect of thermomechanical coupling on fracture response of SMAs under actuation loading conditions has been conducted. It is thus important to better understand and model the thermomechanical fracture behavior of SMAs subjected to varying cooling/heating rates, the development of non-uniform temperature fields as a result of latent heat generation/absorption, and exchange of heat with the environment, when subjected to actuation loading.

In this section, an SMA material constitutive model that includes full thermo-mechanical coupling is utilized to study the effect of cooling rates, and latent heat of phase transformation on fracture toughness and toughness enhancement of SMAs under actuation loading. Finite element method is employed for the analysis of static cracks in an infinite medium center cracked SMA material under plane strain, mode I loading, and subjected to convective cooling at the crack surfaces simultaneously. Various cooling rates are utilized to probe the interplay between different time scales: phase transformation and resulting latent heat generation/absorption, and conduction of the heat energy through the material. The constitutive response of the material is assumed to be that of a polycrystalline SMA and the constitutive law can account for the thermomechanical interactions. Numerical results on the crack-tip mechanical fields and fracture toughness are given for a range of the key material parameters and cooling rates.

4.2   Material Model

In this section the SMA material unified model for polycrystalline SMAs proposed by [18] and already discussed in section 2 is extended for thermomechanical coupling. As mentioned earlier, it is developed within the framework of continuum thermodynamics and adopts the classical rate-independent small-strain flow theory for the evolution equations of the transformation strains. To aid the present analysis of boundary value problem, consider an arbitrary body Ω and its bounding surfaces $\partial\Omega$.

For this arbitrary body Ω, first and second laws of thermodynamics or the law of

128

conservation of energy and the entropy inequality principle can be written as

$$\rho \dot{u} = \boldsymbol{\sigma} : \dot{\boldsymbol{\varepsilon}} - \nabla \cdot \boldsymbol{q} + \rho r \quad \text{in } \Omega, \tag{4.1}$$

$$\rho \dot{s} + \frac{1}{T} \nabla \cdot \boldsymbol{q} - \frac{1}{T^2} \boldsymbol{q} \cdot \nabla - \frac{\rho r}{T} \geq 0 \quad \text{in } \Omega, \tag{4.2}$$

where $\dot{u}$ is the material time derivative of the specific internal energy, $\boldsymbol{\sigma}$ is the Cauchy stress tensor, T is the absolute temperature, $\boldsymbol{q}$ the heat flux vector, r internal heat source/sink, and s is the entropy.

The constitutive laws required to describe the thermomechanical response of SMAs has been stated in section 2 using a postulated Gibbs free energy potential whose form has been described in Equation 2.1.

The transformation surface Φ is assumed of the form

$$\Phi(\boldsymbol{\sigma}, p, -1) = \begin{cases} \boldsymbol{\sigma} : \boldsymbol{\Lambda}^{fwd} + p - f^{fwd} - Y & \text{for forward transformation,} \\ \\ -\boldsymbol{\sigma} : \boldsymbol{\Lambda}^{rev} - p + f^{rev} - Y & \text{for reverse transformation,} \end{cases} \tag{4.3}$$

where Y is the critical value for activation of transformation. Evolution equations for the transformation strains are given by

$$\dot{\boldsymbol{\varepsilon}}^t = \begin{cases} \boldsymbol{\Lambda}^{fwd} \dot{\xi}, & \dot{\xi} > 0 \\ \\ \boldsymbol{\Lambda}^{rev} \dot{\xi}, & \dot{\xi} < 0 \end{cases}, \tag{4.4}$$

and the direction tensors are defined as

$$\boldsymbol{\Lambda}^{fwd} = \frac{3}{2} \frac{H}{\bar{\sigma}} \boldsymbol{\sigma}', \qquad \boldsymbol{\Lambda}^{rev} = \frac{\boldsymbol{\varepsilon}^t}{\xi}, \tag{4.5}$$

where H is the transformation strain magnitude for complete transformation, $\bar{\sigma} =$

$\sqrt{\frac{3}{2}\boldsymbol{\sigma}':\boldsymbol{\sigma}'}$ is the Mises equivalent stress, $\boldsymbol{\sigma}' = \boldsymbol{\sigma} - \text{tr}(\boldsymbol{\sigma})\boldsymbol{\delta}/3$ is the deviatoric stress tensor, and $\boldsymbol{\delta}$ is Kronecker's delta with components $\delta_{ij} = 1$ if $i = j$ and $\delta_{ij} = 0$ if $i \neq j$.

The first law of thermodynamics (4.1), can thus be written for the constitutive equations presented in terms of the rate of the martensite volume fraction, $\dot{\xi}$, as

$$\rho T \dot{s} = \pi \dot{\xi} - \nabla \cdot \boldsymbol{q} + \rho r, \tag{4.6}$$

where

$$\dot{s} = -\frac{\partial \dot{G}}{\partial T} = \frac{1}{\rho}\boldsymbol{\alpha} : \dot{\boldsymbol{\sigma}} + c\frac{\dot{T}}{T} + \left[\frac{1}{\rho}\Delta\boldsymbol{\alpha}:\boldsymbol{\sigma} - \Delta c \ln\left(\frac{T}{T_{ref}}\right) + \Delta s_0\right]\dot{\xi}, \tag{4.7}$$

and

$$\pi = \begin{cases} \boldsymbol{\sigma} : \boldsymbol{\Lambda}^{fwd} + p - f^{fwd}, & \dot{\xi} > 0, \\ \boldsymbol{\sigma} : \boldsymbol{\Lambda}^{rev} + p - f^{rev}, & \dot{\xi} < 0, \end{cases} \tag{4.8}$$

is the total thermodynamic force conjugate to ξ. Note that invoking the assumption that all internal variable evolutions are linked to changes in ξ as formulated in (4.4), the second law can be written as $\pi \dot{\xi} \geq 0$.

Combining (4.6) and (4.7) yields

$$T\boldsymbol{\alpha} : \dot{\boldsymbol{\sigma}} + \rho c \dot{T}$$
$$- \left[\pi - T\Delta\boldsymbol{\alpha}:\boldsymbol{\sigma} + \rho\Delta cT \ln\left(\frac{T}{T_{ref}}\right) - \rho\Delta s_0 T\right]\dot{\xi}$$
$$= -\nabla \cdot \boldsymbol{q} + \rho r \quad (4.9)$$

which is the three-dimensional form of the fully thermomechanical coupled energy

130

balance equation for shape memory alloys. In the above heat equation, The first term of the left hand $T\boldsymbol{\alpha} : \dot{\boldsymbol{\sigma}}$ represents the thermoelastic heat change attributed to the change of volume of a material under elastic load, *i.e.* how the temperature changes due to a change in the stress state of the material. $\rho c \dot{T}$ is the energy change associated with the specific heat capacity, and the contents of the bracket in (4.9) represent the heat given up or absorbed during phase transition and expresses how the temperature of the SMA changes due to a variation of the martensitic volume fraction. The first and second terms of the right-hand side of (4.9) are related to the heat transfer processes by the heat flux, q, and heat sources, ρr.

Given these constitutive relations and neglecting the effects of Δc, which is a common engineering assumption, neglecting the thermoelastic coefficients ($\boldsymbol{\alpha} = 0$) for martensite and austenite which are usually infinitesimally small, and assuming that heat transfer of the SMA material with environment only occurs through heat flux $\boldsymbol{q}$ and any heat sources/sinks are absent ($r = 0$) Equation 4.9 can be rewritten as,

$$\rho c \dot{T} - [\pi - \rho \Delta s_0 T]\dot{\xi} = -\nabla \cdot \boldsymbol{q} \tag{4.10}$$

In the following section, boundary value problem of a center-cracked infinite medium SMA specimen under constant remote tensile loading followed by cooling via surface heat flux at the crack faces, is formulated.
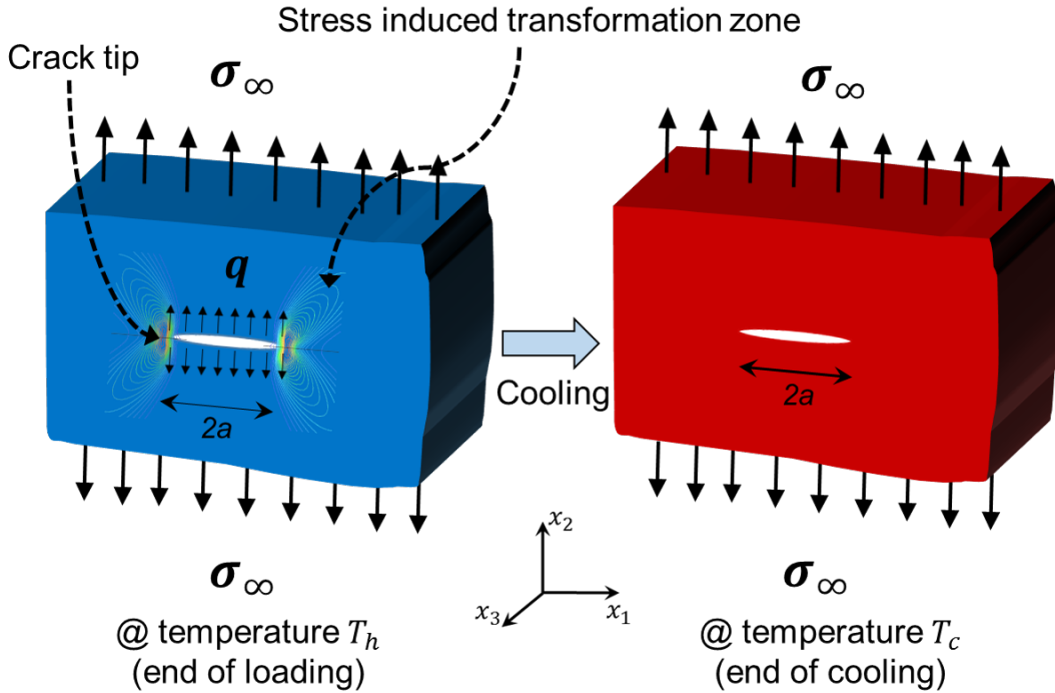
Figure 4.1: Boundary value problem for an infinite-medium center-cracked SMA plate in initial austenite phase subjected to a constant far-field uniaxial tensile loading followed by convective cooling at the crack surfaces under plane strain conditions. Martensite regions are shown in red color and austenite ones in blue.

In this section, the boundary value problem of mode-I crack growth in an infinite center-cracked SMA plate subjected to cooling under plane strain constant applied loading is described. Unlike previous sections, cooling on the SMA material is non-uniform and applied as a specified heat flux at the crack surfaces. The SMA plate is subjected to far-field in-plane uniform uniaxial tensile load, in the direction normal the crack line as shown in Fig. 4.1. The load is applied at a nominal temperature higher than the austenitic-finish, A_f, and a region of transformed material is formed

near the crack tip. Small scale transformation conditions prevail, according to which the size of the transformation zone is small compared to the crack length $2a$, by applying a load resulting in uniaxial tensile stress at infinity, σ_∞, that is sufficiently smaller than the stress required for initiation of martensitic transformation, σ^{M_s}, at the given temperature. Maintaining the tensile load at the boundary constant, the entire cracked SMA specimen is then subjected to cooling, $i.e.$, via a specified distributed surface heat flux directed outwards at the crack surface, until a low temperature is reached that is smaller than M_f (to ensure that the bulk of the specimen completely transforms between pure austenite and martensite). The cooling rates are assumed to be at varying degrees with respect to the time rate of heat transfer by conduction, and any effects of local temperature gradients arising from latent heat of phase transformation throughout the specimen are captured by coupling the SMA model.

Due to symmetry of the problem, the analysis is restricted to one quarter of the plate. A system of co-ordinates (x_1, x_2) is chosen such that the origin lies at the center of the crack and the x_1-axis is extending along the line of the crack while the x_2-axis is aligned in the direction of loading. A finite element mesh of 4-node, isoparametric reduced-integration coupled temperature-displacement ($CPE4RT$) bilinear quadrilateral elements is constructed in ABAQUS to represent the center-cracked SMA specimen with a finer mesh density in the crack growth path in front of the the crack-tip. In ABAQUS, a fully coupled thermal-stress analysis is performed when the mechanical and thermal solutions affect each other strongly and, therefore, must be obtained simultaneously; and solution requires the existence of elements with both temperature and displacement degrees of freedom in the model [1]. Analysis is transient and conducted for real time, and usage of coupled temperature-displacement finite elements ensures that temperature is a nodal degree of freedom along with

nodal displacements and rotations. VCCT capability of ABAQUS, which is an extension of the classical crack-closure technique based on Irwin's crack closure integral [54, 99, 60, 115], is employed to calculate the crack-tip energy release rate.

Recalling Equation 4.10, and invoking Fourier's law which gives the relationship between the heat flux and temperature gradient in a material with uniform thermal conductivity K, it can be rewritten as,

$$\rho c \dot{T} - [\pi - \rho \Delta s_0 T]\dot{\xi} = -\nabla \cdot (-K\nabla T) = K\Delta T \tag{4.11}$$

where Δ is the Laplacian operator and is given as following for a 2-D analysis (as present case) in cartesian co-ordinates: $\Delta = \nabla^2 = \dfrac{\partial^2}{\partial x^2} + \dfrac{\partial^2}{\partial y^2}$. Dividing both sides of the equation by C_M, we get the form,

$$\frac{\rho c}{C_M}\dot{T} - \frac{1}{C_M}[\pi - \rho \Delta s_0 T]\dot{\xi} = \frac{K}{C_M}\Delta T \tag{4.12}$$

From this equation and some further operations, we get two dimensionless parameters,

$$\widetilde{\rho} = \frac{\rho c}{C_M}, \qquad \widetilde{t} = \frac{Kt}{\rho c a^2} \tag{4.13}$$

where $\widetilde{\rho}$ is the dimensionless density and $\widetilde{t}$ is the dimensionless (nondimensionalized) time which is used to plot numerical results. The parameter $\widetilde{t}$ is used to plot crack tip energy release rate for varying rates of heat fluxes, where the effect of real time is normalized by known material parameters.

In the following section, stationary cracks and mechanical fields close to the crack tip are studied using finite element analysis of center-cracked infinite medium SMA material, when it is cooled at varying rates using different levels of applied surface heat fluxes.

4.4.1   Stationary cracks
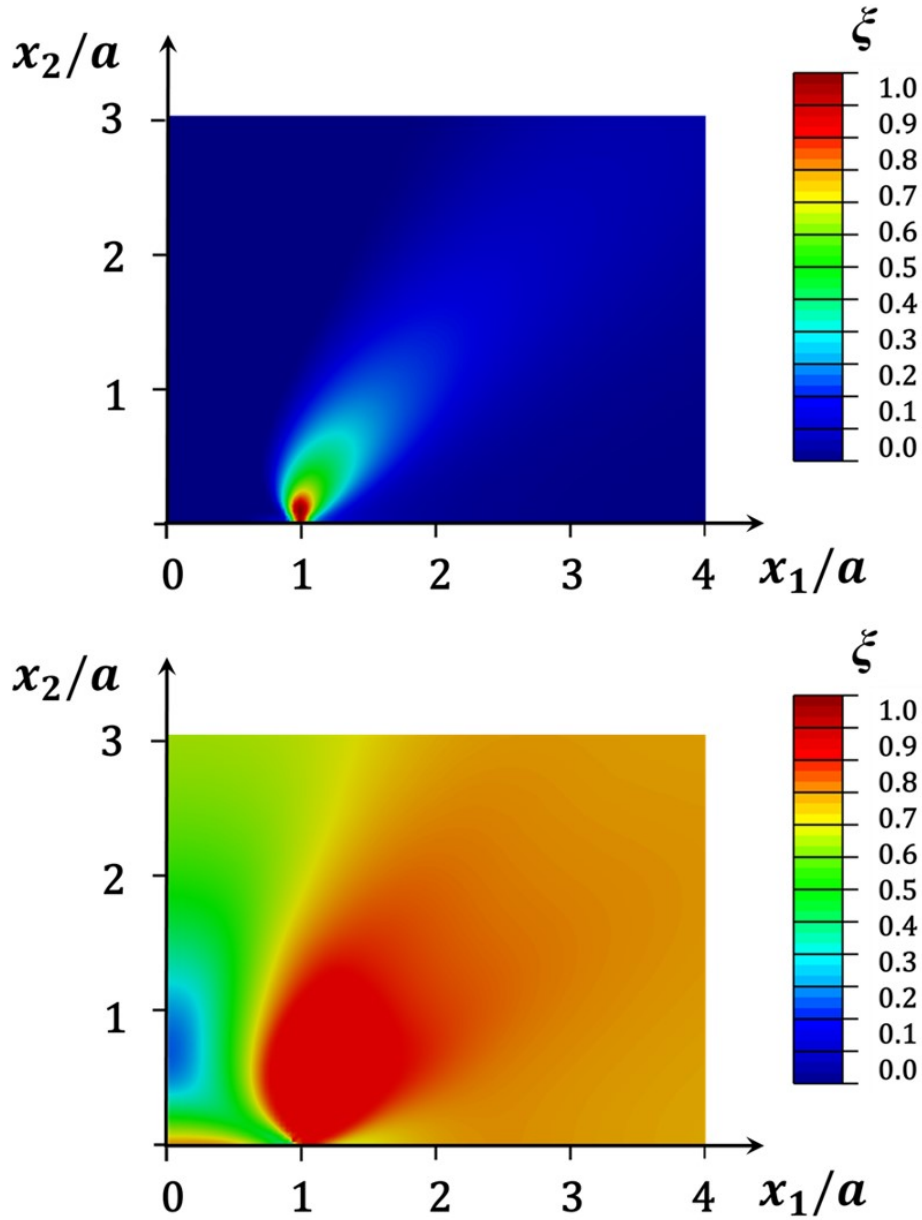
Figure 4.2: Contours of near-tip martensite volume fraction ξ at different temperatures during cooling when heat flux $\boldsymbol{q} = 25 \times 10^3 \, J/m^2/s$: at the beginning of cooling and towards the end of cooling.
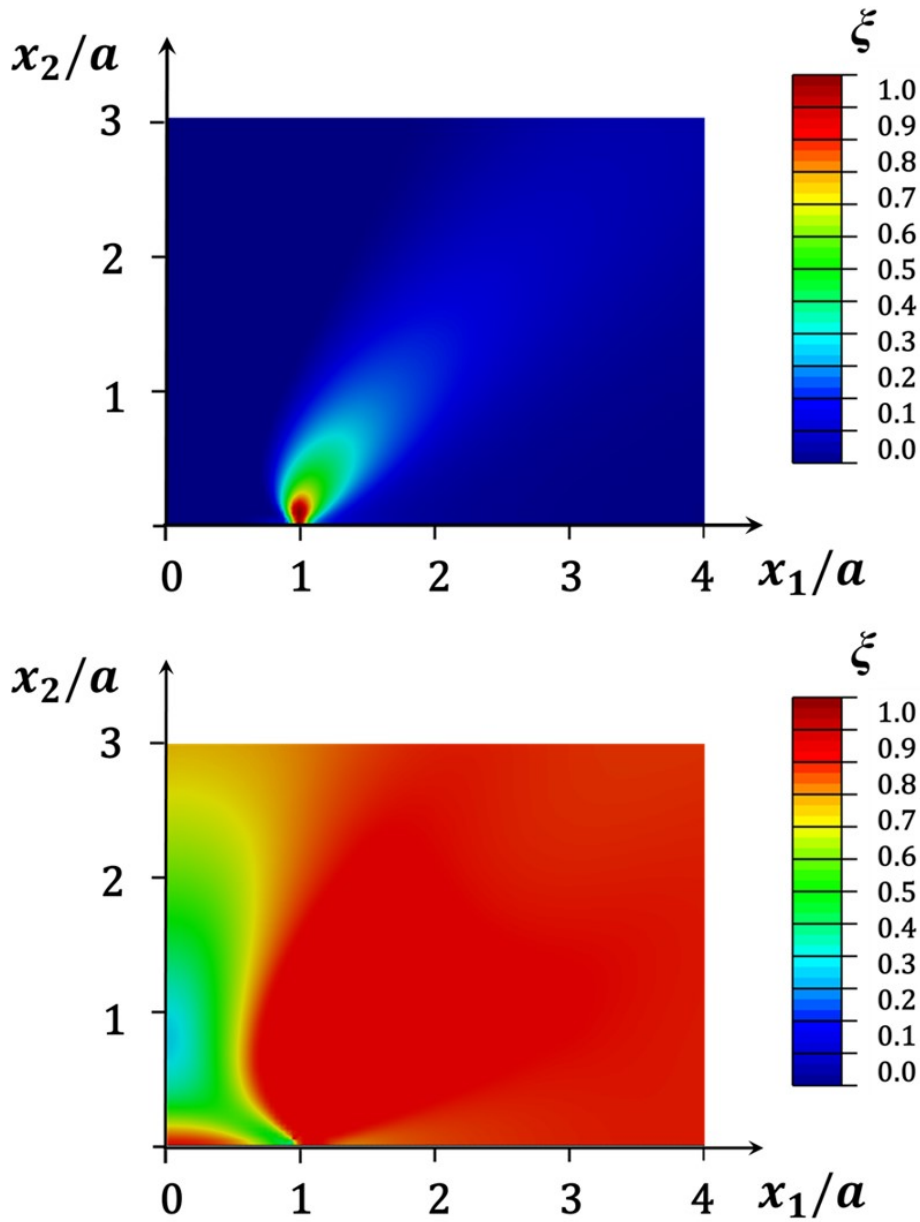
Figure 4.3: Contours of near-tip martensite volume fraction ξ at different temperatures during cooling when heat flux $\boldsymbol{q} = 1 \times 10^3 \, J/m^2/s$: at the beginning of cooling and towards the end of cooling.

Evolution of near-tip martensite fields during cooling of infinite medium cracked SMA with thermomechanical coupling and varying heat fluxes is now presented. Contours of martensite volume fraction (ξ) during cooling are shown in Figure 4.3 and

Figure 4.2, for two levels of applied surface heat fluxes (1×10^3 and $25 \times 10^3 J/m^2/s$). Size of transformation zone is approximately 50 times smaller than the crack length, in accordance with the small scale transformation condition. After the application of remote uniaxial loading σ_∞, the outward heat flux starts cooling the material in the vicinity of the crack tip first. At the beginning of cooling, a small region of fully transformed material ($\xi = 1$) due to applied stress, is surrounded by partial transformation. Barring the region of fully-transformed stress-induced martensite near the crack-tip and partially transformed region surrounding it, rest of the material is at a stress level equal to the applied far-field loading (σ_∞). The thermomechanically-induced phase transformation strains result in a stress redistribution that changes the crack-tip fields.

Variation of crack tip energy release rate, normalized with its value at the end of mechanical loading, *i.e.* G_I/G_∞ is plotted with nondimensionalized time ($\tilde{t}$) in Figure 4.4, for constant specified surface heat fluxes applied at the crack face, $\boldsymbol{q} = 1 \times 10^3, 2.5 \times 10^3, 5 \times 10^3, 10 \times 10^3, 25 \times 10^3, 50 \times 10^3 J/m^2/s, 100 \times 10^3 J/m^2/s$. As cooling is applied, forward phase transformation region grows in front of the crack tip and results in stress redistribution at the crack tip via anti-shielding. Global phase transformation strains as a result of global cooling leads to anti-shielding effect on the crack and is seen as a significant enhancement in the driving force for crack growth. The rate of enhancement of driving force with respect to time is directly proportional to the magnitude of applied surface heat flux. The slope of G_I/G_∞ vs. nondimensionalized time is highest for $\boldsymbol{q} = 100 \times 10^3$ and lowest for $\boldsymbol{q} = 1 \times 10^3 J/m^2/s$. The peak value of G_I/G_∞ during cooling is also dependent on the cooling rate and is seen to vary in a non-monotonic manner. In the following section, the variation of G_I/G_∞ with respect to time is explained further.
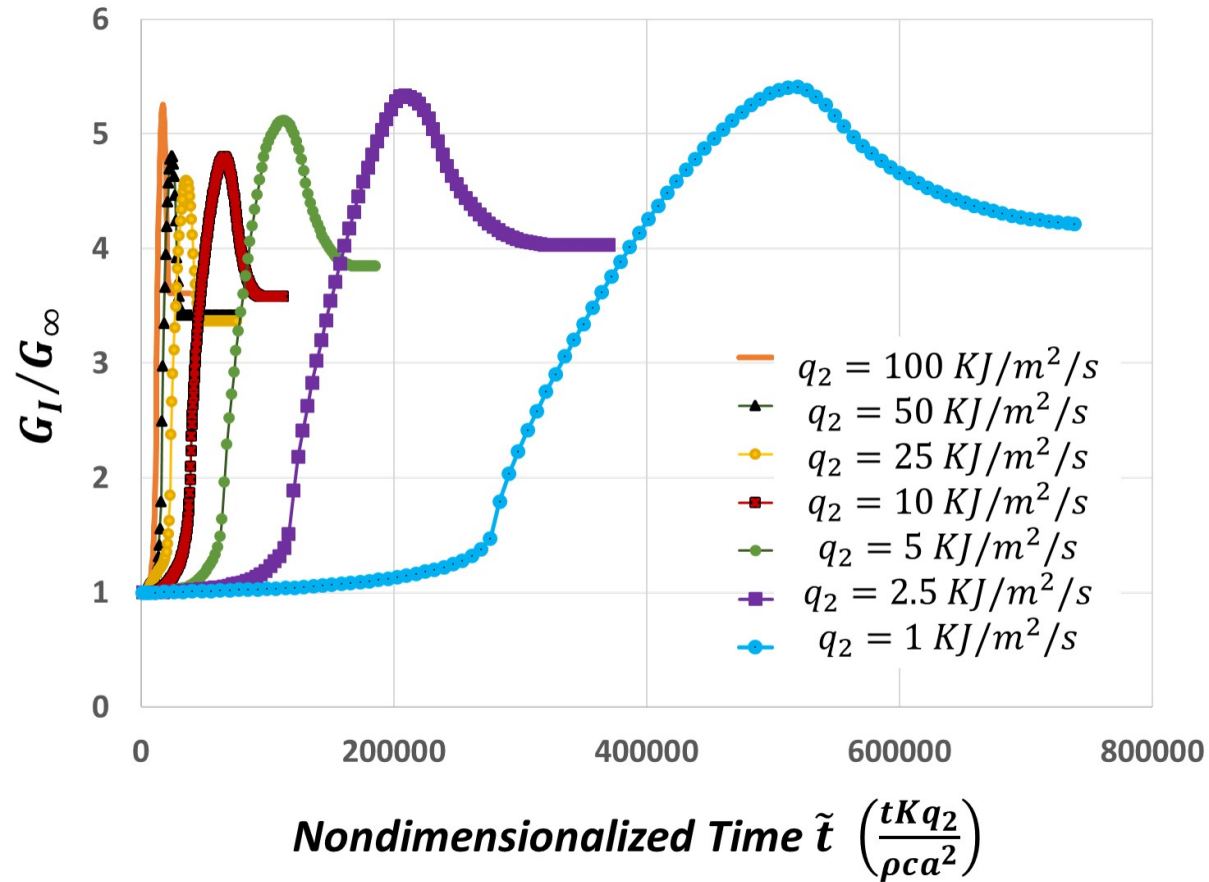
Figure 4.4: Evolution of the normalized crack-tip energy release rate, G_I/G_∞, versus nondimensionalized time $(\tilde{t})$, during cooling for different values of surface heat flux (qqq) applied at the crack surface.

When the surface heat flux has a *high* magnitude ($\boldsymbol{q} = 100 \times 10^3 J/m^2/s = 100KJ/m^2/s$), material in vicinity of crack tip is cooled faster and forward transforms into martensite relatively earlier. Forward phase transformation from austenite to martensite thus leads to generation of latent heat in accordance with energy balance as described in Equation (4.10) and leads to increase in the local temperature. However, relatively fast cooling due to high $\boldsymbol{q}$ results in further forward transformation negating the effect of localized heating due to latent heat. Thus with higher cooling rates, temperature decrease from cooling dominates the increase due to latent heat. Driving force reaches a peak when bulk of the material has transformed in front of the crack and stress redistribution leads to enhancement of crack tip stress intensity. When surface heat flux has *low* magnitude (e.g. $\boldsymbol{q} = 1 \times 10^3 J/m^2/s = 1KJ/m^2/s$), martensitic transformation takes place relatively slow. When material in the vicinity of crack tip transforms, latent heat is released raising the temperature locally. However, due to the relatively low magnitude of applied heat flux the temperature increased from latent heat generation takes longer to decrease in order for forward transformation to proceed. With lower cooling rates, temperature increase due to latent heat dominates temperature decrease from cooling. This is evident in Figure 4.4, where the variation of driving force is proportional to phase transformation in front of the crack. Moreover, compared to the case with high surface heat flux, the peak value of driving force G_I/G_∞ reaches a slightly higher value in case of lowest magnitude of heat flux. The variation of crack tip energy release rate thus has a non-monotonic dependence on cooling rates and is governed by the competition of phase-transition time (or latent-heat release/absorption time) and the time of heat exchange with the environment.
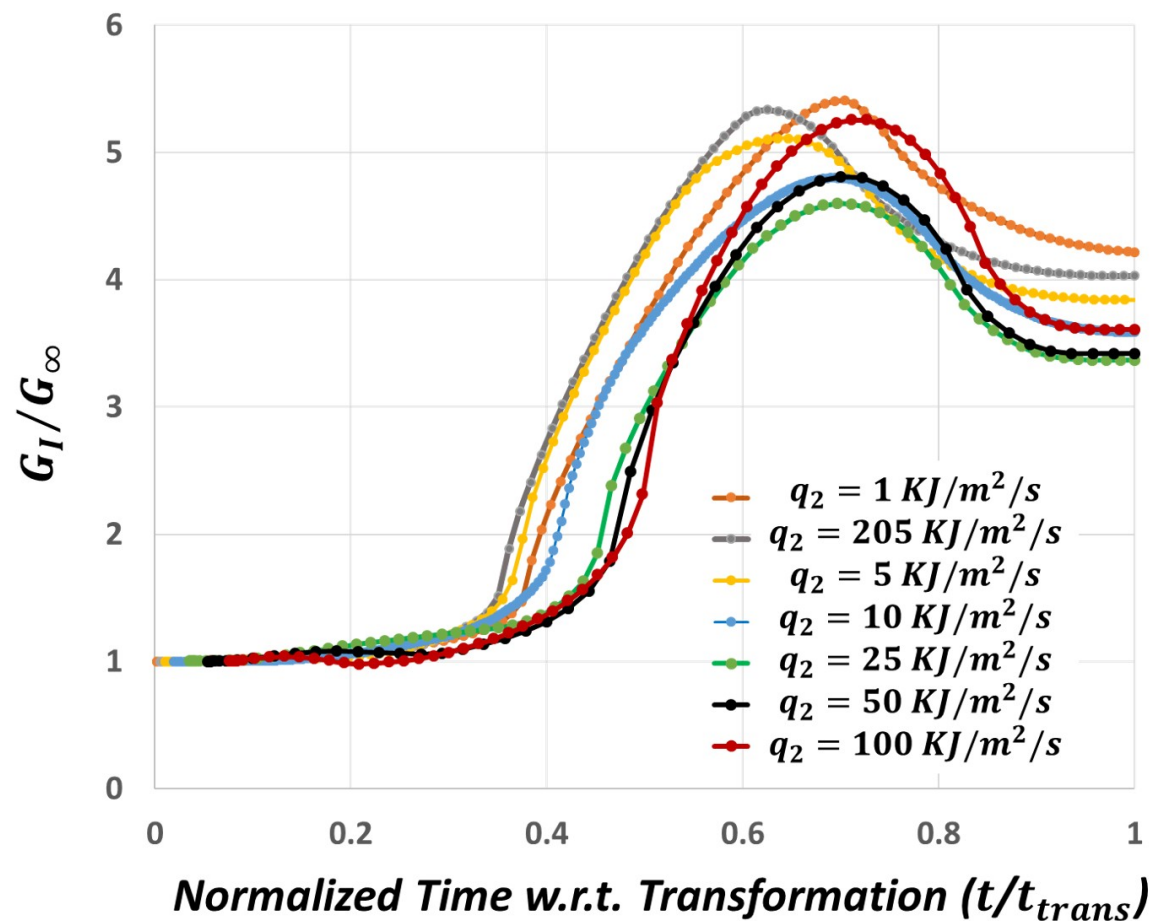
Figure 4.5: Evolution of the normalized crack-tip energy release rate, G_I/G_∞, versus normalized time with respect to transformation, during cooling for different values of surface heat flux (qqq) applied at the crack surface.

The non-monotonic dependence of crack tip energy release rate on cooling rates can be explained as follows: (i) for higher flux magnitude, cooling dominates the temperature increase due to latent heat, and phase transformation proceeds faster leading to a lower peak G_I/G_∞ and (ii) for lower flux magnitude, temperature increase due to latent heat dominates over cooling leading to a slow increase in driving force and a final peak value of G_I/G_∞ that is slightly higher. Intermediate flux magnitudes are seen to have G_I/G_∞ vs. time slopes and peak values that are in between the lowest and highest heat fluxes. To further explain the variation of driving force and its dependence on the cooling rate, real time is modified with a variable t_{trans} which is defined as the total time required for the entire material to fully transform into martensite, at each cooling rate. Real time is normalized by t_{trans} and G_I/G_∞ is plotted until the time when entire material transforms to martensite as shown in Figures 4.5, 4.6, 4.7.

Following forward phase transformation in front of the crack, material behind the crack tip starts to transform last, shielding the crack, and leading to a decrease in G_I/G_∞ as seen in all cases of applied heat fluxes. The drop in driving force for crack growth is seen to be higher for high magnitudes of negative heat fluxes applied for cooling (see Figure 4.5). As material behind the crack starts to forward transforms due to cooling at the crack faces, latent heat is released and is responsible for raising the local temperature. This increase in temperature is quickly dominated by faster cooling provided by higher heat flux, leading to completion of forward transformation at a faster pace. On the other hand, for a lower magnitude of heat flux, local temperature increase due to latent heat is dominant resulting in longer time for complete forward transformation of the material.

Similar to the anti-shielding behavior, dominance of cooling over temperature increase leads to a smaller drop in driving force from its peak values, whereas domi-
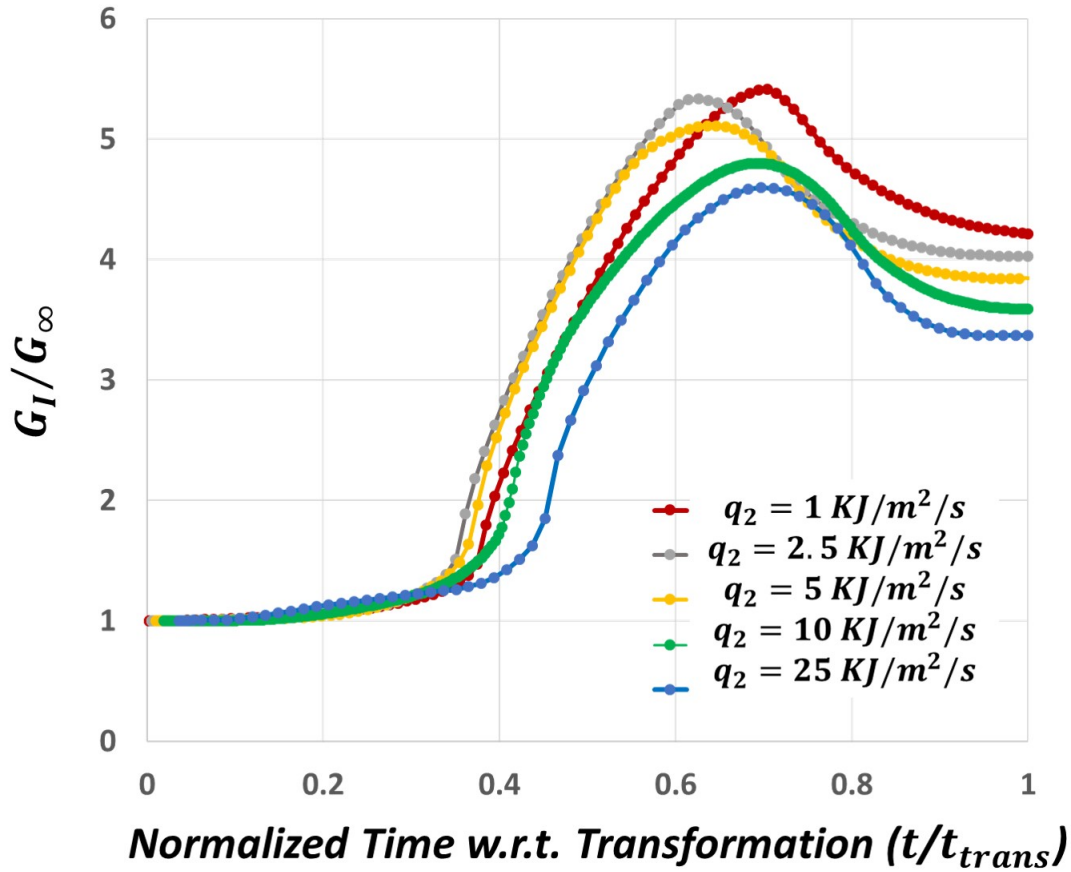
Figure 4.6: Evolution of the normalized crack-tip energy release rate, G_I/G_∞, versus normalized time with respect to transformation, during cooling for surface heat fluxes, $\boldsymbol{q} = 1 \times 10^3, 2.5 \times 10^3, 5 \times 10^3, 10 \times 10^3, 25 \times 10^3 \, J/m^2/s$, applied at the crack surface.

nance of heating due to latent heat over cooling leads to a larger drop in the driving force from the peak value. Driving force G_I/G_∞ reaches a peak and is about 5–6 times higher than that at the beginning of thermal cycling. Lastly, intermediate heat flux magnitudes are seen to produce drop in driving force that is in between the extreme cases. As such, large applied heat flux depicts a case where the effect of latent heat is diminished leading to decrease in driving force enhancement, whereas low magnitude of heat flux depicts the case where effect of latent heat becomes dominant and leads to a higher enhancement of driving force for crack growth. In Figure
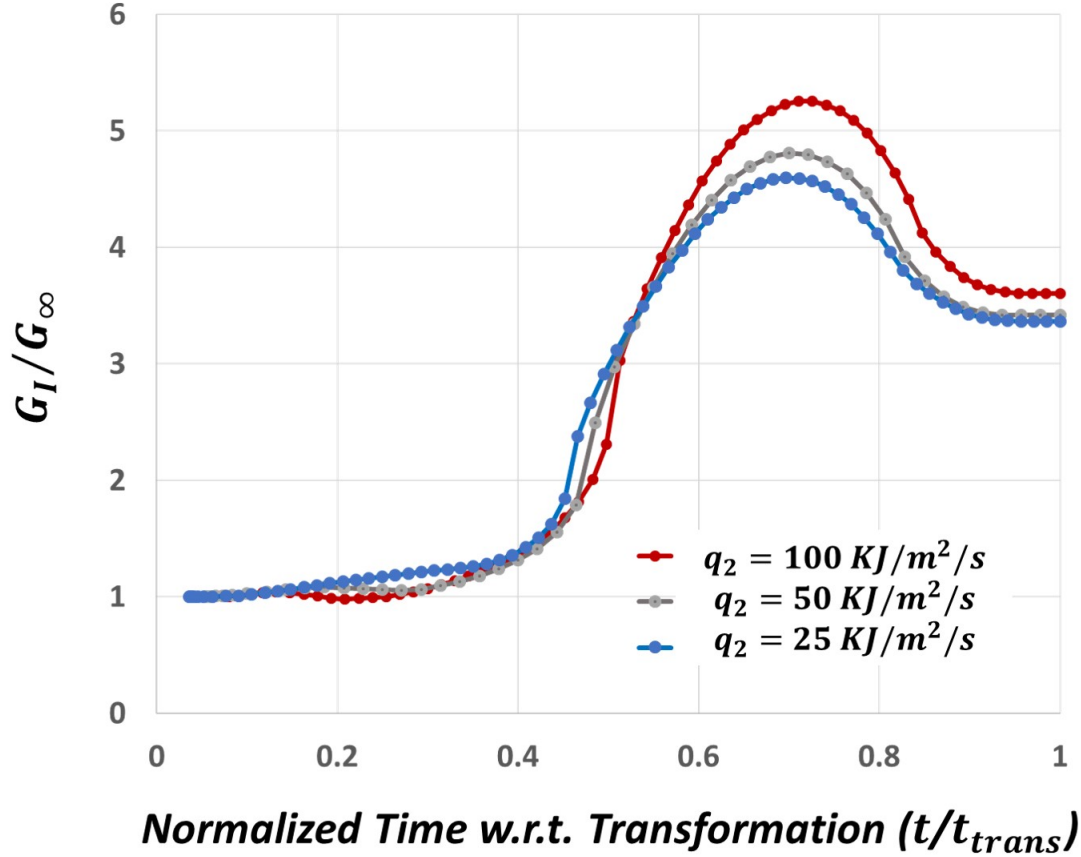
Figure 4.7: Evolution of the normalized crack-tip energy release rate, G_I/G_∞, versus time (s), during cooling for surface heat fluxes, $\boldsymbol{q} = 1 \times 10^5, 5 \times 10^4, 2.5 \times 10^4 J/m^2/s$, applied at the crack surface.

4.6 and 4.7, five curves for the low magnitude of heat flux and three curves for high applied heat fluxes are plotted, in order to emphasize and clearly show the trend in driving force values and its non-monotonic dependence on cooling rates.

Figures 4.3 and 4.2 show the contours of martensite volume fraction during the beginning and towards the end of cooling for two heat flux magnitudes: $\boldsymbol{q} = 1 \times 10^3 J/m^2/s$ and $\boldsymbol{q} = 25 \times 10^3 J/m^2/s$. For the higher flux magnitude, the size of martensite zone when global forward phase transformation is about to begin is equal to that for lower heat flux magnitude. Towards the end of forward phase transformation in front of the crack, region of fully transformed martensite is larger when

143

cooling rate is low, whereas this region is smaller for larger cooling rates. Moreover, forward transformation behind the crack occurs simultaneously with driving force enhancement for low flux magnitude, resulting in a transformation zone that includes less austenite volume fraction when peak value of driving force is reached. These contours plots explain the increasing levels of final driving force G_I/G_∞ with decreasing heat flux magnitudes.

In context of these results for stationary cracks, it is plausible that crack *growth* behavior will be substantially influenced by the magnitude of heat flux responsible for cooling carried out through the crack faces, *i.e.* cooling rates. Crack growth can be triggered during cooling when the crack tip energy release rate becomes equal a material specific *critical* value (G_{crit}). Since cooling via high heat flux magnitude leads to faster forward phase transformation in front of the crack tip, crack growth will be triggered earlier when flux magnitude is higher. For a low magnitude heat flux, growth will thus be triggered at a later instant in time. Moreover, due to the fact that slope of G_I/G_∞ vs. time is directly proportional to cooling rates, after crack growth is triggered, faster cooling can result in the advancing crack to reach steady state faster. Thus, for lower cooling rates, the amount of stable crack growth will be higher as a direct result of delayed forward transformation in front of the crack due to competition between the cooling from external sources and the latent heat generated from forward phase transformation.

At higher cooling rates, on the other hand, cooling from external source dominates the local heating from latent heat release, leading to diminished stable crack growth. In terms of transformation toughening provided by transformed material left in the wake of the crack, similar argument can be made where slower cooling rate leads to a larger region of martensite with higher strains and provides shielding for the growing crack. On the other hand, fast cooling rate leads to a relatively smaller martensitic

144

region and lower strains providing less degree of shielding for the advancing crack.

4.5   Summary

In this section, finite element calculations are carried out on the prototype problem of an infinite center-cracked SMA plate subjected to global cooling using a specified heat flux or cooling rate, under plane strain, mode I, constant applied remote loading and *full thermomechanical coupling*. Varying levels of heat flux directed away from the crack faces are applied using a transient analyses in real time.

Crack tip energy release rate is utilized as a fracture toughness parameter and as driving force for crack growth (G_I/G_∞) and is calculated using VCCT in ABAQUS, under varying cooling rates. Following observations are made for stationary cracks when the driving force G_I/G_∞ is plotted against time: *(i)* G_I/G_∞ is independent of the crack length, an expected result since the crack size is the only length scale in this fracture problem. *(ii)* Slope of G_I/G_∞ with respect to time is observed to be directly proportional to cooling rates. *(iii)* Peak value of G_I/G_∞ during thermal variation has a non-monotonic dependence on cooling rates and the difference can be explained as a result of competition between cooling from a external source at the crack faces, and localized temperature increase due to latent heat from forward phase transformation.

With regard to growing cracks, crack growth is triggered when $G_I/G_\infty = G_{crit}/G_\infty$ during cooling and crack growth under varying cooling rates will thus be significantly affected by the rate of cooling. Further numerical simulations are needed that analyze crack growth and the effect of cooling rates on transformation toughening and resulting stable growth due to transformed material left in wake of the crack.

5.   SUMMARY AND FUTURE WORK

5.1   Conclusions and Summary

Recent fracture toughness experiments on SMA CT specimens with fatigue precracks subjected to constant tensile load followed by thermal cycling between austenitic and martensitic phases have demonstrated very intriguing SMA material response. Experiments showed that crack growth was triggered primarily during cooling when large scale forward phase transformation took place mainly in front of the crack, acting as driving force for growth. Moreover, once triggered, stable crack growth was seen to take place which also depended on the magnitude of initial bias tensile load applied. In this research work, numerical modeling and analysis of fracture and crack growth in SMAs under combined thermomechanical loading is carried out using the finite element method along with the energetics based VCCT approach using ABAQUS FEA suite. The prototype problem of infinite medium center-cracked SMA plate subjected to thermal variations under plane strain, mode I, constant remote applied loading is chosen for the analysis. In order to comprehensively address the complex phenomenon of SMA fracture under thermomechanical loading, SMA nonlinear material response in the form of transformation induced plasticity and thermomechanical coupling was also included via constitutive models.

5.1.1   Crack growth studies and effect of boundary conditions

The first major contribution of this work is the modeling and analysis of stable crack growth in polycrystalline SMAs when subjected to actuation loading. Based on recent findings, crack is assumed to propagate when the crack-tip energy release rate reaches a material specific critical value, driven by global martensitic phase transformation occurring in front of the crack. Stable crack growth is observed in the

form of resistance R-curves and is associated with crack shielding or transformation toughening effect of the transformed material left in the wake of advancing crack, and this toughening effect is shown to be influenced by transformation metrics and applied load levels. Smaller bias load levels result in more thermal cycles required for the crack to attain steady-state growth conditions. Since outer boundaries exert an influence on stress-state and deformation at the crack tip owing to *global* phase transformation, geometry dependence of crack resistance is expected.

Crack configurations beyond that of the infinite center-crack problem, such as compact tension and three-point bend specimens are thus analyzed using the same numerical approach and material constants. Static and advancing cracks in these two configurations compared to infinite medium problem show a dependence of toughening response with the stress triaxiality at the crack-tip. Additionally, when fixed grips boundary conditions (as opposed to "dead load" condition, which is presented before) are applied to these crack configurations followed by actuation loading, the variation of crack tip G_{crit}/G_∞ is seen to be opposite to that in the prototype problem. Due to fixed boundaries, transformation strains generated during cooling tend to compress the entire material domain leading to shielding effect on the crack and hence apparent crack-closure, and is reflected in a decrease in driving force for crack growth. For deeply cracked compact tensile specimens and 3-point bend specimens, this effect is amplified when compared to that in the infinite medium and thus would result in decreasing possibility of crack growth during cooling.

5.1.2 *Transformation induced plasticity*

The second contribution of this work is the incorporation of effect of irreversible TRIP strains on the mechanical fields close to stationary cracks and transformation toughening leading to stable crack growth in polycrystalline SMAs under actuation

loading. The prototype problem chosen is again that of an infinite medium center-cracked thick SMA panel under plane strain conditions and subjected to uniaxial loading and thermal cycling. Evolution of TRIP strains, which is dependent on cyclic transformations, and alterations in material microstructure leading to a shift in thermomechanical SMA properties, is added using appropriate constitutive material model. With regards to stationary cracks, the driving force G_I/G_∞ shows the following trends: (i)G_I/G_∞ at the end of heating is greater than that at the beginning of cooling and depends on the magnitude of TRIP strain in the material, (ii)peak value of G_I/G_∞ during cooling is higher than the peak value during heating, and (iii) shift towards lower temperature in peak G_I/G_∞ - values during multiple thermal cycles, due to evolution of the material's phase transformation temperatures.

Thus, an SMA material may not fail in the initial thermomechanical cycles, but fail later as cyclic transformation generates TRIP raising the crack tip energy release rate above the material specific critical value. Crack growth is triggered during cooling and transformation toughening and resulting stable growth occurs due to transformation as well as irrecoverable plastic strains left in wake of the crack are observed. TRIP strain thus plays a dual role and contributes in driving force for crack growth and stable crack growth by transformation toughening. Higher levels of TRIP are seen to produce more driving force for crack growth due to their global nature, overshadowing the toughening provided by TRIP strains left in the crack wake. As such, amount of stable crack extension and the toughening provided in terms of cooling required to drive growth is dependent on TRIP strain magnitudes generated over multiple cycles.

5.1.3 Thermomechanical coupling

Finally, another contribution of this work is the introduction of full thermomechanical coupling in the boundary value problem introduced in the second section. Finite element calculations are carried out on infinite center-cracked plane strain SMA plate subjected to constant applied remote loading followed by an outward heat flux at the crack faces *i.e.* a specified cooling rate. Varying levels of heat flux directed away from the crack faces are applied using a transient analyses in real time. For stationary cracks when the driving force G_I/G_∞ is plotted against time, following observations are made: *(i)* Slope of G_I/G_∞ with respect to time is observed to be directly proportional to cooling rates. *(ii)* Peak G_I/G_∞ and the drop following phase transformation behind the crack are inversely proportional to cooling rates and the difference can be explained owing to the interplay between temperature decrease due to external cooling and latent heat leading to local temperature increase. Crack growth under varying cooling rates will thus be significantly affected by the rate of cooling and further numerical simulations are needed to analyze crack growth and the effect of cooling rates on transformation toughening and resulting stable growth.

5.2 Recommended Future Research

Some areas of potential future research related to SMA fracture are as follows:

- Thermomechanical coupling effect should be added to numerical analysis of crack growth during thermal variations using varying cooling rates at the crack surfaces. Currently the author is working on modeling a finite element problem where localized cooling via heat fluxes can be applied to growing/changing crack surfaces as result of phase transformation to accurately capture the effect of cooling rates and latent heat release/absorption on the fracture toughness of the SMA material.

149

- Studying stationary and advancing cracks by incorporating large strain effects in the analysis of SMAs via a new constitutive model, especially when TRIP is involved, is another important extension of the work presented in this thesis. Martensite variant reorientation, which becomes important for non-proportional loading cases such as a that in a growing crack, should be incorporated in the constitutive model. Three dimensional effects need to be considered by implementing a full 3D finite element problem with similar boundary conditions to study the effect of specimen thickness and stress-state on growing cracks. Moreover, conducting explicit numerical analysis using appropriate material user subroutines and perhaps incorporating dynamic fracture studies of transforming SMAs is another avenue of potential research work.

- Studies with careful experimentation, fractography and large number of fracture toughness tests of traditional and high-temperature SMA systems subjected to combined thermomechanical loading are necessary to create a broader knowledge base of SMA fracture properties. Single crystal SMA specimens also need to be tested in order to identify the favorable cleavage planes responsible for brittle fracture. Numerical models can then be modified and updated in order to replicate experimental observations and conclusions.

- The micromechanical SMA constitutive model can be improved by considering a more comprehensive crystal plasticity based model that can capture complex microstructural deformation mechanisms such as twinning, dislocation slip and climb, etc., in order to capture the dependence of fracture on crystal anisotropy and texture.

REFERENCES

[1] Abaqus. *Analysis User's Manual*. Dassault Systèmes of America Corp., Woodlands Hills, CA, 2015.

[2] T.L. Anderson. *Fracture Mechanics: Fundamentals and Applications, Third Edition*, pages 25–171. Taylor and Francis Group, Boca Rotan, FL, 2005.

[3] S. Ardakani, A.H. Hatefi, and S. Mohammadi. Thermo-mechanically coupled fracture analysis of shape memory alloys using the extended finite element method. *Smart Mater. Struct.*, 24:045031, 2015.

[4] R. S. Barsoum. On the use of isoparametric finite elements in linear fracture mechanics. *Int. J. Num. Meth. Eng.*, 10:25–37, 1976.

[5] R. S. Barsoum. Triangular quarter-point elements as elastic and perfectly-plastic crack tip elements. *Int. J. Num. Meth. Eng.*, 11:85–98, 1977.

[6] T. Baxevanis, Y. Chemisky, and D. C. Lagoudas. Finite element analysis of the plane-strain crack-tip mechanical fields in pseudoelastic shape memory alloys. *Smart Mater. Struct.*, 21(9):094012, 2012.

[7] T. Baxevanis and D. C. Lagoudas. A mode I fracture analysis of a center-cracked infinite shape memory alloy plate under plane stress. *Int. J. Fract.*, 175(2):151–166, 2012.

[8] T. Baxevanis and D. C. Lagoudas. Fracture mechanics of shape memory alloys: review and perspectives. *Int. J. Fract.*, 191:191–213, 2015.

[9] T. Baxevanis, C.M. Landis, and D. C. Lagoudas. On the effect of latent heat on the fracture toughness of pseudoelastic shape memory alloys. *J. Appl. Mech., Transactions ASME*, 81(10):101006, 2014.

[10] T. Baxevanis, C.M. Landis, and D.C. Lagoudas. On the fracture toughness of

pseudoelastic shape memory alloys. *J. Appl. Mech.*, 81:041005, 2013.

[11] T. Baxevanis, A. Parrinello, and D.C. Lagoudas. On the driving force for crack growth during thermal actuation of shape memory alloys. *J. Mech. Phys. Solids*, 89:255, 2016.

[12] T. Baxevanis, A.F. Parrinello, and D. C. Lagoudas. On the fracture toughness enhancement due to stress-induced phase transformation in shape memory alloys. *Int. J. Plast.*, 50:158–169, 2013.

[13] V. Birman. On mode I fracture of shape memory alloy plates. *Smart Mater. Struct.*, 7:433–437, 1998.

[14] Z. Bo and D.C. Lagoudas. Thermomechanical modeling of polycrystalline SMAs under cyclic loading, part I: Theoretical derivations. *International Journal of Engineering Science*, pages 1089–1140, 1999.

[15] Z. Bo and D.C. Lagoudas. Thermomechanical modeling of polycrystalline SMAs under cyclic loading, part II: Material characterization and experimental results for a stable transformation cycle. *International Journal of Engineering Science*, pages 1141–1173, 1999.

[16] Z. Bo and D.C. Lagoudas. Thermomechanical modeling of polycrystalline SMAs under cyclic loading, part III: Evolution of plastic strains and two-way shape memory effect. *International Journal of Engineering Science*, pages 1175–1203, 1999.

[17] Z. Bo and D.C. Lagoudas. Thermomechanical modeling of polycrystalline SMAs under cyclic loading, part IV: Modeling of minor hysteresis loops. *International Journal of Engineering Science*, pages 1205–1249, 1999.

[18] J. Boyd and D. C. Lagoudas. A thermodynamical constitutive model for shape memory materials. Part I: The monolithic shape memory alloy. *Int. J. Plast.*, 12-6:805–842, 1996.

[19] J. Boyd and D. C. Lagoudas. A thermodynamical constitutive model for shape memory materials. Part II. The SMA composite material. *Int. J. Plast.*, 12-7:843–873, 1996.

[20] W. Brocks, A. Cornec, , and Scheider I. *Comprehensive Structural Integrity*, volume 3, pages 127–209. Elsevier Science Ltd., Amsterdam, Netherlands, 2003.

[21] E. Budiansky and J. R. Rice. Conservation laws and energy release rates. *J. Appl. Mech.*, 40:201–203, 1973.

[22] B. Budniansky, J. W. Hutchinson, and J. C. Lambropoulos. Continuum theory of dilatant transformation toughening in ceramics. *Int. J. Solids Struct.*, 19:337–355, 1983.

[23] G.P. Cherepanov. Crack propagation in continuous media. *Journal of Applied Mathematics and Mechanics*, 31(3):503–512, 1967.

[24] M. Cherkaoui, M. Berveiller, and Sabar H. Micromechanical modeling of martensitic transformation induced plasticity (TRIP) in austenitic single crystals. *International Journal of Plasticity*, 14:597–626, 1998.

[25] C.B. Churchill, J.A. Shaw, and M.A. Iadicola. Tips and tricks for characterizing shape memory alloy wire: part 2-fundamental isothermal responses. *Exp. Tech.*, 33(1):51–62, 2009.

[26] C.B. Churchill, J.A. Shaw, and M.A. Iadicola. Tips and tricks for characterizing shape memory alloy wire: part 1differential scanning calorimetry and basic phenomena. *Exp. Tech.*, 34(2):63–80, 2010.

[27] A. Creuziger, L.J. Bartol, K. Gall, and W.C. Crone. Fracture in single crystal NiTi. *J. Mech. Phys. Solids*, 56:2896–2905, 2008.

[28] S. Daly, A. Miller, G. Ravichandar, and K. Bhattacharya. An experimental investigation of crack initiation in thin sheets of nitinol. *Acta Mater.*, 55:6322–

6330, 2007.

[29] M.R. Daymond, M.L. Young, J.D. Almer, and D.C. Dunand. Strain and texture evolution during mechanical loading of a crack tip in martensitic shape-memory NiTi. *Acta Mat.*, 55:3929–3942, 2007.

[30] S. Desindes and S. Daly. The small-scale yielding of shape memory alloys under mode III fracture. *Int. J. Solids Struct.*, 47:730–737, 2010.

[31] T. Duerig, K. Melton, D. Stockel, and C. Wayman. *Engineering Aspects of Shape Memory Alloys*, pages 170–177. Butterworth-Heinemann, London, 1990.

[32] T. Duerig, A. Pelton, and D. Stöckel. An overview of nitinol medical applications. *Mater. Sci. Eng. A*, 273–275:149–160, 1999.

[33] P. Entchev and D.C. Lagoudas. Modeling of transformation-induced plasticity and its effect on the behavior of porous shape memory alloys. part I: constitutive model for fully dense SMAs. *Mechanics of Materials*, 36:865–892, 2004.

[34] F. Fischer, G. Reisner, K. Werner, E. Tanaka, and T. Cailletaud, G. Antretter. A new view on transformation induced plasticity (TRIP). *International Journal of Plasticity*, 16:723–748, 2000.

[35] Yuval Freed and Leslie Banks-Sills. Crack growth resistance of shape memory alloys by means of a cohesive zone model. *J. Mech. Phys. Solids*, 55(10):2157–2180, 2007.

[36] M. Frotscher, K. Neuking, R. Bockmann, K.-D. Wolff, and G. Eggeler. In situ scanning electron microscopic study of structural fatigue of struts, the characteristic elementary building units of medical stents. *Mater. Sci. Eng.*, A 481482:160–165, 2008.

[37] H. Funakubo. *Shape Memory Alloys*. Gordon and Breach Science, United States, 1987.

[38] K. Gall, N. Yang, H. Sehitoglu, and Y.I. Chumlyakov. Fracture of precipitated

NiTi shape memory alloys. *Int. J. Fract.*, 109:189–207, 2001.

[39] E. Gdoutos. *Fracture Mechanics: An Introduction, Second Edition*, pages 79–116. Springer, AH Dordrecht, The Netherlands, 2005.

[40] S. Gollerthan, Herberg D., A. Baruj, and G. Eggeler. Compact tension testing of martensitic/pseudoplastic niti shape memory alloys. *Mater. Sci. Eng. A*, A481A482:156–159, 2008.

[41] S. Gollerthan, M. L. Young, A. Baruj, J. Frenzel, W. W. Schmahl, and G. Eggeler. Fracture mechanics and microstructure in NiTi shape memory alloys. *Acta Mater.*, 57:1015–1025, 2009.

[42] S. Gollerthan, M.L. Young, K. Neuking, U. Ramamurty, and G. Eggeler. Direct physical evidence for the back-transformation of stress-induced martensite in the vicinity of cracks in pseudoelastic niti shape memory alloys. *Acta Mater.*, 57(19):5892–5897, 2009.

[43] D. J. Hartl and D. C. Lagoudas. Aerospace applications of shape memory alloys. Proceedings of the Institution of Mechanical Engineers, Part G: Journal of Aerospace Engineering, pages 535–552. SAGE, 2007.

[44] D.J. Hartl, D. C. Lagoudas, and F.T. Calkins. Advanced methods for the analysis, design, and optimization of SMA-based aerostructures. *Smart Mater. Struct.*, 20:094006, 2011.

[45] D.J. Hartl, J.T. Mooney, D.C. Lagoudas, F.T. Calkins, and J.H. Mabe. Use of a Ni60Ti shape memory alloy for active jet engine chevron application: II. Experimentally validated numerical analysis. *Smart Mater. Struct.*, 19:015021, 2010.

[46] S. Hazar, W. Zaki, Z. Moumni, and G. Anlas. Modeling of steady-state crack growth in shape memory alloys using a stationary method. *Int. J. Plast.*, 67:26–39, 2015.

[47] T. K. Hellen. On the method of virtual crack extension. *Int. J. Num. Meth. Eng.*, 9:187–207, 1975.

[48] R. D. Henshell and K. G. Shaw. Triangular quarter-point elements as elastic and perfectly-plastic crack tip elements. *Int. J. Num. Meth. Eng.*, 9:495–507, 1975.

[49] R.L. Holtz, K. Sadananda, and M.A. Imam. Fatigue thresholds of NiTi alloy near the shape memory transition temperature. *Int. J. Fatig.*, 21:S137–S145, 1999.

[50] J.W. Hutchinson. Singular behavior at the end of a tensile crack in a hardening material. *J. Mech. Phys. Solids*, 16:13–31, 1968.

[51] J.W. Hutchinson. On steady quasi-static crack growth. (DEAP S-8), 1974.

[52] Wawrzynek P. A. Ingraffea, A.R. *Comprehensive Structural Integrity*, volume 3, pages 25–171. Elsevier Science Ltd., Amsterdam, Netherlands, 2003.

[53] G. R. Irwin. Analysis of stresses and strains near the end of a crack traversing a plate. *J. Appl. Mech.*, 24:361–364, 1957.

[54] G. R. Irwin. *Handbuch der Physik VI*, pages 558–590. Spinger Verlag, Berlin, Germany, 1958.

[55] Raju I.S. Calculation of strain-energy release rates with higher order and singular finite elements. *Eng. Fract. Mech.*, 28:251–274, 1987.

[56] S. Jape, Parrinello A., T. Baxevanis, and D.C. Lagoudas. On the fracture response of shape memory alloy actuators. In Metals The Minerals and Materials Society(TMS), editors, *Middle East - Mediterranean Materials Congress on Energy and Infrastructure Systems (MEMA 2015*, pages 165–180, 2015.

[57] S. Jape, T. Baxevanis, and D.C. Lagoudas. Stable crack growth during actuation in shape memory alloys. In International Society for Optics and Photonics, editors, *SPIE Smart Structures and Materials+ Nondestructive Evaluation and*

Health Monitoring, pages 905802(1–9), 2014.

[58] S. Jape, T. Baxevanis, and D.C. Lagoudas. Stable crack growth during thermal actuation of shape memory alloys. *Shape Memory and Superelasticity*, 2:104–113, 2016.

[59] B. Karihaloo and Q. Z. Xiao. *Comprehensive Structural Integrity*, volume 2, pages 81–212. Elsevier Science Ltd., Amsterdam, Netherlands, 2003.

[60] R. Krueger. Virtual crack closure technique: History, approach, and applications. *Appl. Mech. Rev.*, 57(2):109–143, 2004.

[61] J. Kudva. Overview of the DARPA smart wing project. *J. Int. Mater. Syst. Struct.*, 15:261–67, 2004.

[62] P. K. Kumar and D. C. Lagoudas. *Shape Memory Alloys: Modelling and Enginnering Applications*, pages 1–51. Springer, New-York, 2008.

[63] D. C. Lagoudas, D. Hartl, Y. Chemisky, L. Machado, and P. Popov. Constitutive model for the numerical analysis of phase transformation in polycrystalline shape memory alloys. *Int. J. Plast.*, 32–33:158–183, 2012.

[64] D.C. Lagoudas, O.W. Bertacchini, and E. Patoor. *Surface Crack Development in Transformation Induced Fatigue of SMA Actuators*, pages 1309–1310. Springer Netherlands, Netherlands, 2006.

[65] J. C. Lambropoulos. Shear, shape and orientation effects in transformation toughening. *Int. J. Solids Struct.*, 22:1083–1106, 1986.

[66] C. Lexcellent, M. R. Laydi, and V. Taillebot. Analytical prediction of the phase transformation onset zone at a crack tip of a shape memory alloy exhibiting asymmetry between tension and compression. *Int. J. Fract.*, 169(1):1–13, 2011.

[67] C. Lexcellent and F. Thiebaud. Determination of the phase transformation zone at a crack tip in a shape memory alloy exhibiting asymmetry between tension and compression. *Scripta Mater.*, 59:321–323, 2008.

[68] H. W. Liu. *Discussion in Fracture toughness testing and its applications, ASTM STP 381*. Am. Soc. Testing Mat., Philadelphia, 1965.

[69] Y. Liu and McCormick P. Thermodynamic analysis of the martensitic transformation in NiTi –I. effect of heat treatment on transformation behaviour. *Acta Metallurgica et Materialia*, 42:2401–2406, 1994.

[70] G.M. Loughran, T.W. Shield, and P.H. Leo. Fracture of shape memory CuAlNi single crystals. *Int. J. Solids Struct.*, 40(2):271–294, 2003.

[71] Stankiewicz J. M., S.W. Robertson, and R.O. Ritchie. Fatigue crack growth properties of thin-walled superelastic austenitic nitinol tube for endovascular stents. *J. Biomed. Mater. Res. Part A*, 81A(3):685–691, 2007.

[72] C. Maletta. A novel fracture mechanics approach for shape memory alloys with trilinear stress-strain behavior. *Int. J. Fract.*, 177(1):39–51, 2012.

[73] C. Maletta and F. Furgiuele. Analytical modeling of stress-induced martensitic transformation in the crack tip region of nickel-titanium alloys. *Acta Mater.*, 58:92–101, 2010.

[74] C. Maletta and F. Furgiuele. Fracture control parameters for NiTi based shape memory alloys. *Int. J. Solids Struct.*, 48:1658–1664, 2011.

[75] C. Maletta and M.L. Young. Stress-induced martensite in front of crack tips in NiTi shape memory alloys: Modeling versus experiments. *J. Mater. Engi. Perf.*, 20(4–5):597–604, 2011.

[76] A. McKelvey and R.O. Ritchie. Fatigue-crack propagation in nitinol, a shape-memory and superelastic endovascular stent material. *J. Biomed. Mater. Res. Part A*, 47A(3):301–308, 1999.

[77] A. McKelvey and R.O. Ritchie. Fatigue-crack growth behavior in the superelastic and shape-memory alloy Nitinol. *Metall. Mater. Trans. A*, 32:731–743, 2001.

[78] R. M. McMeeking and A. G. Evans. Mechanics of transformation-toughening in brittle materials. *J. Am. Ceram. Soc.*, 65:242–246, 1982.

[79] Shih C.F. Moran B. Crack tip and associated domain integrals from momentum and energy balance. *Engineering Fracture Mechanics*, 27:615–642, 1987.

[80] A. Nespoli, S. Besseghini, S. Pittaccio, E. Villa, and S. Viscuso. The high potential of shape memory alloys in developing miniature mechanical devices: A review on shape memory alloy mini-actuators. *Sensor Actuat. A-Phys.*, 158(1):149–160, 2010.

[81] H. Okada and T. Kamibeppu. A virtual crack closure-integral method (vccm) for three-dimensional crack problems using linear tetrahedral finite elements. *Applied Mechanics Review*, 10(3):229–338, 2005.

[82] H. Okadaa, H. Kawaib, and Araki K. A virtual crack closure-integral method (vccm) to compute the energy release rates and stress intensity factors based on quadratic tetrahedral finite elements. *Engineering Fracture Mechanics*, 75(15):4466–4485, 2008.

[83] K. Otsuka and C. M. Wayman, editors. *Shape Memory Materials.* Cambridge University Press, Cambridge, 1999.

[84] D. M. Parks. A stiffness derivative finite element technique of crack tip stress intensity factors. *Int. J. Fract.*, 10:487–501, 1974.

[85] D. M. Parks. The virtual crack extension method for nonlinear material behavior. *Comp. Methods Appl. Mech. Eng.*, 12:353–364, 1977.

[86] N. Perez. *Fracture Mechanics*, pages 121–145. Kluwer Academic Publishers, Boston, 2004.

[87] J. Perkins. *Shape Memory Effects in Alloys.* Plenum Press, New York, 1975.

[88] J. Perkins and P. Bobowiec. Microstructural effects of martensitic transformation cycling of a cu-zn-ai alloy: Vestigial structures in the parent phase.

Metallurgical Transactions A, 17A:195–203, 1986.

[89] L. Petrini and F. Migliavacca. Biomedical applications of shape memory alloys. *J. Metall.*, 2011:1–15, 2011.

[90] M. A. Qidwai and D. Lagoudas. Numerical implementation of a shape memory alloy thermomechanical constitutive model using return mapping algorithms. *Int. J. Num. Meth. Eng.*, 47:1123–1168, 2000.

[91] J. R. Rice. A path independent integral and approximate analysis of strain concentration by notches and cracks. *J. Appl. Mech.*, 35:379–386, 1968.

[92] J.R. Rice. Stresses due to a sharp notch in a work-hardening elastic-plastic material loaded by longitudinal shear. *ASME J. Appl. Mech.*, 34:287–298, 1967.

[93] J.R. Rice. Some remarks on elastic crack-tip stress fields. *Int. J. Solids Structures*, 8:751–758, 1972.

[94] J.R. Rice and G.F. Rosengren. Plane strain deformation near a crack tip in a power-law hardening material. *J. Mech. Phys. Solids*, 16:1–12, 1968.

[95] S. Robertson and R. Ritchie. In vitro fatigue-crack growth and fracture toughness behavior of thin-walled superelastic nitinol tube for endovascular stents: A basis for defining the effect of crack-like defects. *Biomaterials*, 28:700–709, 2007.

[96] S. W. Robertson, A. Mehta, A. R. Pelton, and R. O. Ritchie. Evolution of crack-tip transformation zones in superelastic Nitinol subjected to in situ fatigue: A fracture mechanics and synchrotron X-ray micro-diffraction analysis. *Acta Mater.*, 55:6198–6207, 2007.

[97] S. W. Robertson and R. O. Ritchie. A fracture-mechanics-based approach to fracture control in biomedical devices manufactured from superelastic nitinol tube. *J Biomed Mater.Res. B*, 1:26–33, 2008.

[98] S.W. Robertson, A.R. Pelton, and R.O. Ritchie. Mechanical fatigue and fracture of nitinol. *Int. Materi. Rev.*, 57(1):1–36, 2012.

[99] E. Rybicki and M. Kanninen. A finite element calculation of stress intensity factors by a modified crack closure integral. *Eng. Fract. Mech.*, 9:931–938, 1977.

[100] E.F. Rybicki, D.W. Schmueser, and Fox J. An energy release rate approach for stable crack growth in the free-edge delamination problem. *J. Compos. Mater.*, 11:470–487, 1977.

[101] T. Saburi. *Shape Memory Materials*, pages 49–93.

[102] B. Sanders, R. Crowe, and E. Garcia. Defense advanced research projects agency – Smart materials and structures demonstration program overview. *J. Int. Mater. Syst. Struct.*, 15:227–233, 2004.

[103] T. Sawaguchi, L. Bujoreanu, T. Kikuchi, K. Ogawa, M. Koyamaa, and M. Murakamic. Mechanism of reversible transformation-induced plasticity of femnsi shape memory alloys. *Scripta Materialia*, 59:826–829, 2008.

[104] J.A. Shaw, C.B. Churchill, and M.A. Iadicola. Tips and tricks for characterizing shape memory alloy wire: part 1differential scanning calorimetry and basic phenomena. *Exp. Tech.*, 32(5):55–62, 2008.

[105] J.A. Shaw, C.B. Churchill, and M.A. Iadicola. Tips and tricks for characterizing shape memory alloy wire: part 3-localization and propagation phenomena. *Exp. Tech.*, 33(5):70–78, 2009.

[106] C.F. Shih. Relationships between the j-integral and the crack opening displacement for stationary and extending cracks. *J. Mech. Phys. Solids*, 29:305–326, 1981.

[107] K.N. Shivakumar, P.W. Tan, and Newman J.C. A virtual crack-closure technique for calculating stress intensity factors for cracked three dimensional bod-

ies. *Int. J. Fract.*, 36:R43–R50, 1988.

[108] M. Sreekumar, T. Nagarajan, M. Singaperumal, M. Zoppi, and R. Molfino. Critical review of current trends in shape memory alloy actuators for intelligent robots. *Ind. Robot*, 34(4):285–294, 2007.

[109] G. Stam and E. van de Giessen. Effect of reversible phase transformations on crack growth. *Mech. Mater.*, 21:51–71, 1995.

[110] D. Stoeckel, A. Pelton, and T. Duerig. Self-expanding Nitinol stents: Material and design considerations. *European Radiology*, 14(2):292–301, 2004.

[111] S. Suresh. *Fatigue of Materials*, pages 249–251. Cambridge University Press, Cambridge, 1991.

[112] R. Vaidyanathan, D.C. Dunand, and U. Ramamurty. Fatigue crack-growth in shape-memory NiTi and NiTi-TiC composites. *Mater. Sci. Engi. A*, 289(1–2):208–216, 2000.

[113] G.M. Vasko, P.H. Leo, and T.W. Shield. Prediction and observation of crack tip microstructure in shape memory CuAlNi single crystals. *J. Mech. Phys. Solids*, 50(9):1843–1867, 2002.

[114] X. M. Wang, Y. F. Wang, A. Baruj, G. Eggeler, and Z. F. Yue. On the formation of martensite in front of cracks in pseudoelastic shape memory alloys. *Mater. Sci. Engng. A*, 394:393–398, 2005.

[115] D. Xie and S. Biggers. Progressive crack growth analysis using interface element based on the virtual crack closure technique. *Fin. Elem. Anal. Des.*, 42:977–984, 2006.

[116] F. Xiong and Y. Liu. Effect of stress-induced martensitic transformation on the crack tip stress-intensity factor in Ni-Mn-Ga shape memory alloy. *Acta Mater.*, 55:5621–5629, 2007.

[117] Yan Y., Yin H., Sun Q. P., and Huo Y. Rate dependence of temperature

fields and energy dissipations in non-static pseudoelasticity. *Continuum Mech. Thermodyn.*, 24:675–695, 2012.

[118] W. Yan and Y.W. Mai. *Theoretical Consideration on the Fracture of Shape Memory Alloys*, volume 127, pages 217–226. Springer Netherlands, (2006).

[119] S. Yi and S. Gao. Fracture toughening mechanism of shape memory alloys due to martensite transformation. *Int. J. Solids Struct.*, 37:5315–5327, 2000.

[120] S. Yi, S. Gao, and S. Shen. Fracture toughening mechanism of shape memory alloys under mixed-mode loading due to martensite transformation. *Int. J. Solids Struct.*, 38:4463–4476, 2001.

[121] He Y.J. and Sun Q.P. On non-monotonic rate dependence of stress hysteresis of superelastic shape memory alloy bars. *International Journal of Solids and Structures*, 48:1688–1695, 2011.

[122] M.L. Young, S. Gollerthan, A. Baruj, J. Frenzel, W.W. Schmahl, and G. Eggeler. Strain mapping of crack extension in pseudoelastic niti shape memory alloys during static loading. *Acta Mater.*, 61(15):5800–5806, 2013.

[123] X-K Zhu and J.A. Joyce. Review of fracture toughness (g, k, j, ctod, ctoa) testing and standardization. *Eng. Frac. Mech.*, 85:1–46, 2012.

APPENDIX A

FIRST APPENDIX

A.1 Fundamentals of Computational Fracture Mechanics

A.1.1 Fracture Mechanics: An Overview

Fracture mechanics consists of the comprehensive study of fatigue crack propagation and structural life prediction, brittle and ductile fracture, and residual strength estimation of solid bodies under mechanical or thermal stresses. For studying cracked solid bodies under quasi-static mechanical loading, two main approaches have been developed over the past century: linear elastic fracture mechanics (LEFM) which deals with elastic bodies undergoing brittle or quasi-brittle fracture, and elastic-plastic fracture mechanics which includes the study of cracked solids with substantial plastic dissipation. Griffith first introduced his theory of brittle fracture in solid materials based on a global energy based approach, now known as the Griffith theory of brittle fracture. Based on earlier stress analysis of plates with elliptical holes by Inglis, Griffith argues that crack propagation in solids occurred when energy supplied to the crack tip through external loading was greater than a certain *critical* energy required to break atomic bonds and create new fracture surfaces [59, 2]. This energy, per unit crack extension, was termed as the energy release rate (G) and was identified as a global fracture toughness parameter for crack growth, whereas its corresponding critical value was termed as the *critical* energy release rate.

Consider a 2D plate with width w and thickness t with a center crack of length $2a$ such that $a << w$ subjected to remote uniaxial tensile loading σ_∞. In order for the crack to extend, sufficient potential energy must be available in the

164
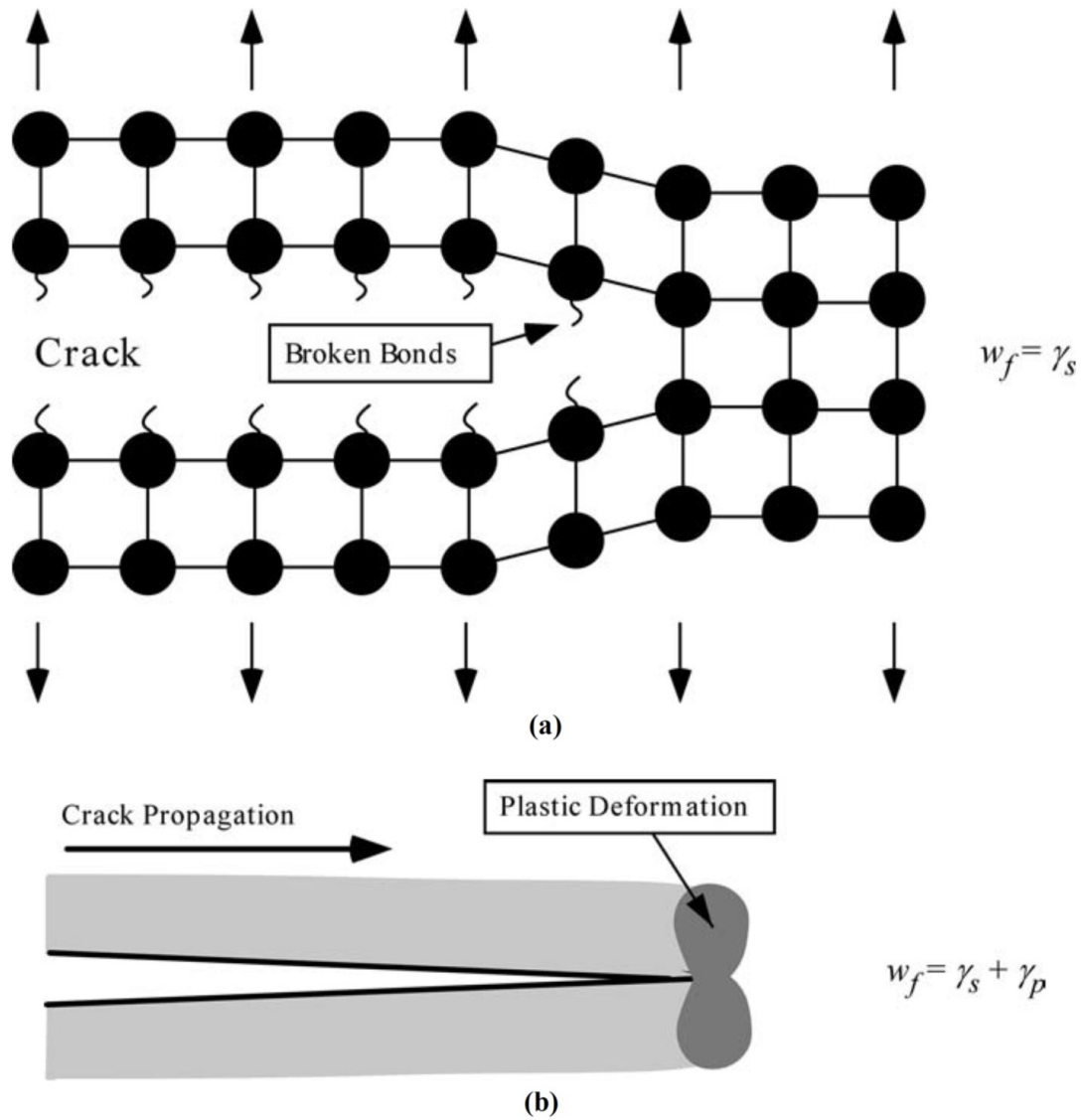
Figure A.1: Crack propagation in various types of materials, with the corresponding fracture energy in (a) ideally brittle material with no plasticity (Griffith criterion), (b) quasi-brittle elastic-plastic material with limited plasticity (Irwin criterion); w_f is the work required to created a new fracture surface, γ_s is and surface energy of the material and γ_p is the plastic work per unit area of surface created (from Figure 2.6 of [2], © 2005 Taylor and Francis, with permission of Taylor and Francis Group LLC Books).

system to be converted into crack surface energy. Let E is the total energy of the system, W_s is the work required to create new surfaces for crack formation, and Π is the potential energy supplied by internal strain energy and external mechanical forces. Provided that there is no other form of energy exchange (thermal, kinetic, or other) with the environment, and if the boundaries are free to move, under mechanical equilibrium the total rate of change of energy E of the system should be zero [86, 39]. The Griffith energy balance can thus be expressed as [2]:

$$\frac{\partial E}{\partial A} = \frac{\partial \Pi}{\partial A} + \frac{\partial W_s}{\partial A} = 0 \qquad \text{or} \qquad \frac{\partial \Pi}{\partial A} = -\frac{\partial W_s}{\partial A}$$

Rate of change of W_s per unit crack extension dA is thus equal to the rate of change in potential energy P of the system. As the crack extends incrementally by a small amount dA at each end (the total crack surface area created is $4dA * t$), energy due to applied mechanical loading flows into the crack tips where it is utilized in the fracture process zone in overcoming the atomic forces in the material. Crack propagation will thus occur as long as energy provided by mechanical loading and stored in the material is equal to that required for crack growth. For the crack to grow in a stable manner, the energy available for crack growth must be equal to the material resistance to crack extension and the Griffith energy balance equation can be rewritten as [2],

$$\frac{\partial}{\partial a}(W + \Gamma) = 0 \qquad \text{or} \qquad -\frac{\partial W}{\partial a} = \frac{\partial \Gamma}{\partial a} \text{ i.e. } G = R$$

where $\quad G = -\dfrac{\partial W}{\partial a} =$ energy release rate or crack driving force
and $R = \dfrac{\partial \Gamma}{\partial a} =$ crack resistance.

166

From Figure A.1, w_f is the fracture energy of the material, which realistically includes plastic, viscoelastic or viscoplastic dissipation effects in the material as well as effects arising from crack branching and meandering. Crack extension occurs when $G = 2w_f$ and it can be approximately assumed that energy required for each increment of crack growth is constant and the crack propagation criterion can be rewritten as $G = G_c$ where G_c is the material specific critical energy release rate ([2, 52]).

The crack resistance or fracture resistance of a material, (which can be interpreted as critical energy release rate or critical stress-intensity factor) when plotted against the crack extension, gives the crack-resistance or crack driving-force curve or simply, the *R-curve* [2]. Depending on whether the material is purely brittle (eg. glass) or quasi-brittle (eg. small-scale plasticity with strain-hardening behavior), the R-curve can be flat with a constant crack resistance or rising with increasing crack resistance required to extend the crack (Figure A.2). Crack growth is understood to be *stable* if incrementally higher levels of external load (mechanical, or otherwise) are required to maintain a steady increase in the crack length. In such cases, cessation or applied load will lead to crack arrest and only further loading will lead to crack growth until the point of failure. Such materials, where the R-curve has a rising shape, cannot be characterized by a single value of critical driving force and are hence characterized using a critical value for the *initiation* of crack growth ([2]). Brittle materials exhibit a flat R-curve owing to their constant critical crack-resistance, whereas quasi-brittle materials or ductile materials show a rising R-curve owing to the increasing resistance to crack growth stemming from relatively small nonlinear mechanical fields near the crack-tip (eg. strain-hardening plasticity, phase-transformation or viscoplasticity). The umbrella term of linear elastic fracture mechanics (LEFM) is used to describe the above phenomena and is considered valid only as long as the nonlinear deformation

167

fields near the crack tip are confined to a small region when compared to the overall dimensions of the domain. In the present work, the ideas of Griffith and Irwin, as described above, with tools from computational fracture mechanics and finite element analysis have been utilized to simulate fracture in shape memory alloys under combined thermomechanical loading.
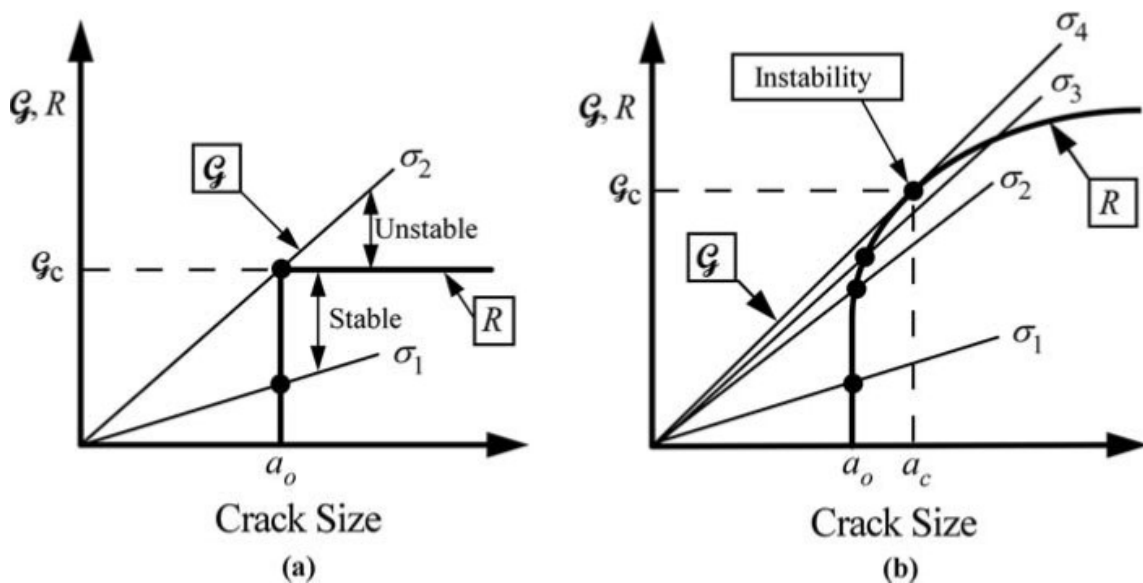
Figure A.2: Schematic for the crack-resistance R-curves showing driving force vs. crack extension for (a) an ideally brittle material where there is no plasticity and the R-curve is flat and (b) a quasi-brittle material with nonlinear effects (eg. plasticity, viscoplasticity etc.) in a limited region at the crack-tip where the R-curve is rising due to changing material fracture resistance (from Figure 2.10 of [2], © 2005 Taylor and Francis, with permission of Taylor and Francis Group LLC Books).

Irwin and Orowan independently modified the Griffith criterion, which was valid only for ideally brittle materials, by adding a term reflecting the plastic work per unit area of crack surface (shown in Figure A.1) making it applicable for quasi-brittle fracture. Irwin also, along with Williams and Westergaard, extended Griffith's analysis by introducing stress-intensity factors (or SIFs, represented by K) and provided

closed-form solutions for mechanical fields in the near-tip region of a sharp crack. They also noted that stress fields in the neighborhood of a sharp crack depend only on the applied load and geometry or configuration of the cracked domain and show a $1/\sqrt{r}$ singular dependence on the distance "r" from the crack-tip. Near-tip region where stresses show a dominant $1/\sqrt{r}$ singular dependence is termed as the K-dominated region where all components of stress, strain and displacements can be calculated from the known K and the William's expansion. This idea provided a local stress-based approach to analyze cracked bodies, and for ideally brittle materials both Griffith and Irwin criteria are identical. In the special case of an infinite elastic medium with a semi-infinite crack, the relationship between G and K is simply $G = \dfrac{K^2}{E'}$, where $E' = E$ for plane stress and $E' = \dfrac{E}{1 - \nu^2}$ for plane strain (E = elastic modulus and ν = Poisson ratio).
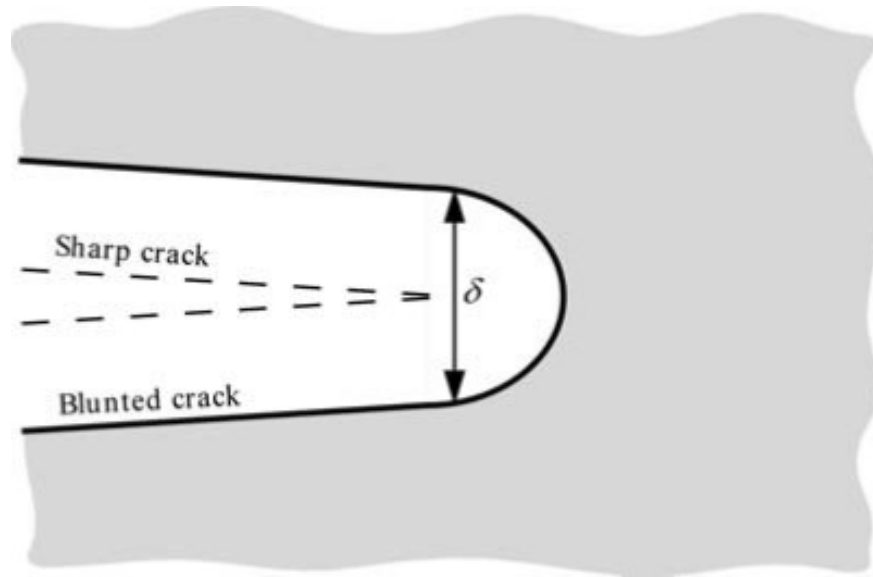
Figure A.3: Schematic for crack-tip opening displacement (CTOD) showing an initially sharp crack blunting due to plastic deformation at the crack tip, resulting in a displacement δ separating the crack faces at the crack tip location (from Figure 3.1 of [2], © 2005 Taylor and Francis, with permission of Taylor and Francis Group LLC Books).

Elastic-plastic fracture mechanics (EPFM) applies to those materials with significant time-dependent nonlinear stress-strain behavior (plasticity or viscoplasticity, for instance) [2, 68] where LEFM analysis is not enough to characterize the material's fracture behavior. Two important quantities, *viz.* crack-tip opening displacement (CTOD, which is an experimental measure) and J-integral [91], are used to characterize fracture toughness of elastic-plastic materials and provide fracture criteria which are less restrictive than those of Griffith and Irwin. CTOD has been shown to provide a much more accurate measure of fracture toughness in case of plastic materials where crack-tip plasticity leads to crack-blunting (the degree of blunting being directly proportional to material toughness) of an initially sharp crack (Figure A.3). Under the conditions of small-scale yielding, CTOD has been shown to be a

linear function of the energy release rate and the stress-intensity factor [106, 21]. Another important and widely successful parameter for fracture toughness calculations is the well-known J-integral, first introduced by Rice in 1968 (and independently by Cherepanov in 1967) [23, 91, 92, 93]. Rice defined a line contour integral in a region close to the crack-tip of a material with deformation plasticity (or nonlinear elasticity), and this J-integral was later shown by Hutchinson, Rice and Rosengran to uniquely characterize the near-tip mechanical fields of a cracked elasto-plastic material well beyond the restrictions of LEFM [94, 51, 50].
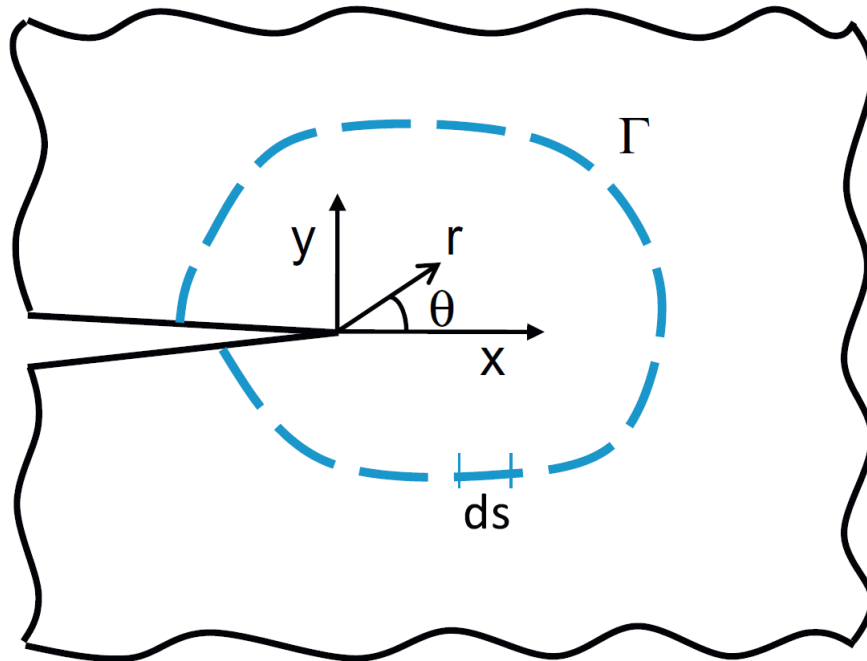

Figure A.4: Schematic for calculating the J contour integral in a homogeneous cracked body with small deformations. Γ is a line contour that begins and ends on the crack faces and contains the crack tip, and n is the normal to this contour. (from Figure 7 of [123], © 2012 Elsevier, with permission of Elsevier, http://dx.doi.org/10.1016/j.engfracmech.2012.02.001).

171

For quasi-static fracture in small deformation problem of nonlinear elastic, or deformation-theory-based elastoplastic material V free of body forces and subjected to traction and displacement boundary conditions (S_σ and S_u), the path-independent J-integral defined on a contour Γ containing the crack faces with normal n, close to the crack tip is given as:

$$J = \int_\Gamma [W(\varepsilon_{ij})dx_2 - \sigma_{ij}n_j \frac{\partial u_i}{\partial x_1}ds] \tag{A.1}$$

Where W_{ij} is the strain energy density, u_i, σ_{ij}, and ε_{ij} are the components of displacement vector, stress and strain tensor respectively. x_1, x_2 are the Cartesian coordinates, ds is the infinitesimal length of the contour Γ surrounding the crack tip. In the limiting case of LEFM or small-scale yielding, G, K and J all can be related to each other via a linear relationships. Budiansky and Rice [21] showed that J-integral is identical with the energy release rate in the following manner:

$$J = G = -\frac{\delta U}{\delta A}$$

for a plane crack extension, where U is the potential energy and A is the area of cracked surface. For mixed-mode fracture in a linear elastic material, J is related to the stress intensity factors by:

$$J = G_I + G_{II} + G_{III} = \frac{1}{E'}(K_I^2 + K_{II}^2) + \frac{1}{2G}(K_{III}^2)$$

where I, II, III denote the three fracture modes. Mode I (or opening mode) refers to a planar symmetric state of deformation where direction of load is in the crack plane and perpendicular to crack edges, which causes a crack to open symmetrically in a tensile mode. Mode II (in-plane shear or sliding mode) is a planar antisymmetric state of stress, with the loading direction is parallel to crack edges causing the crack

faces sliding over one another in an in-plane shear mode. Mode III (the anti-plane shear or tearing mode) is a state of stress where the applied load causes the crack faces to slide out-of-plane of the crack and perpendicular to the crack edges in an anti-plane shear manner ([53, 2]).

A.1.2 Fracture Mechanics using Finite Element Method

Following the developments in fracture mechanics, finite element method (FEM) which is applied using a high performance computing environment, has been widely used to model and analyze the mechanics of solids with cracks or crack-like defects. In such modeling scenarios, cracks can be visualized as mathematical singularities in 2D or 3D solid bodies under mechanical or other type of loading. To simulate stress singularities at the stationary crack-tips, like the $1/\sqrt{r}$ singularity encountered in LEFM with a specific K, singular elements (triangular or quadrilateral) have been developed. The so-called "collapsed" or "quarter-point" quadrilateral isoparametric elements were developed by Henshell and Shaw [48] and Barsoum [4, 5]. These type of finite elements form some of the most popular choices for calculating stress-intensity factors and J-integral in commercial FEM software packages like Abaqus. Different types of singularities, depending on the type of material behavior ($1/\sqrt{r}$ singularity in LEFM or $1/r$ singularity in case of limited plasticity) being investigated, can be modeled using collapsed elements. Quadrilateral and triangular quarter point elements in both 2D and 3D and with linear and quadratic degrees have been developed in order to capture the crack-tip stress intensity and singular stress, strain and displacement fields. Most of these methods and elements are employed for analysis of mechanical fields close to a stationary crack tips, but can also be extended for growing cracks. Methods specifically applied to crack propagation are discussed next.

Some of the methods that can be used to directly or indirectly extract the crack-tip stress intensities in case of growing cracks can be categorized into two types: point matching or direct methods which include displacement and stress intensity correlation (stresses in front of the crack tip or displacements behind the crack tip); energy methods or indirect methods such as virtual crack extension and modified crack closure integral and the J-integral [52] where energy release rates and the J-integral are computed numerically and stress intensity factors are derived from them. Energy methods have certain advantages like their applicability to nonlinear material behavior and are generally more accurate, but show disadvantages where mixed-mode analysis is required due to complexity in the expression for mixed-mode energy release rates. On the other hand, direct or point matching methods are much easier to use and consist of simple expressions that can be used as a check on energy methods. However, in order to obtain accurate results from correlation techniques the mesh near the crack tip region needs to be highly refined and the area of correlation has to completely in the zone that is K-dominant, and aforementioned quarter point methods can be employed to simulate the tip singularity. Ultimately, stress intensity factors are computed using the numerically obtained nodal displacements and matching them with their analytical counterparts [52].

Amongst the energy approaches, virtual crack extension method, also known as stiffness derivative method, is based on evaluation of the change in potential energy of the material with a unit *virtual* crack extension, which is equated to energy release rate in LEFM and was first developed by Parks [84, 85] and Hellen [47]. Although this method is highly accurate it is plagued with complications due to the need to calculate changes in elemental stiffnesses in the finite elements surrounding the virtually moving crack tip and becomes numerically expensive. Apart from that, it also requires the decomposition of the derived energy release rate into its components

when a mixed-mode fracture scenario is encountered. Another numerical method to calculate the global energy release rate for a material with growing crack is via the evaluation of the energy domain integral which yields the classical J-integral and is equal to the energy release rate for a linear elastic fracture analysis [79]. There have been extensions of the original integral to include inertia effects via the addition of body forces and non-mechanical loads (such as thermal, electrical, magnetic, etc.) that are shown to be path-independent. Equivalent domain integral methods can be developed for both linear and nonlinear problems that additionally allows for easy ways for mode separation [60]. Both virtual crack extension and the numerically calculated energy domain integral form of the J-integral have been found to be accurate for calculation of energy release rates for scenarios involving growing cracks. The modified crack closure integral (MCCI) formulated by Irwin and further implemented in the form of virtual crack closure technique (VCCT) is now discussed briefly.

According to Irwin's postulation, in a linear elastic material if the crack extends by a small amount δa, the energy absorbed in the process of crack extension should be equal to the work required to close the crack to its original length [99]. Using a polar co-ordinate system with the crack tip as the origin, r as distance from the crack tip and θ is the angle with the direction of crack extension (horizontal), numerical formulation of the modified crack closure integral (MCCI) can be stated as follows:

$$
G = \lim_{\Delta a \to 0} \frac{1}{2\Delta a} \int_0^{\Delta a} \sigma_y(\Delta c - r, 0)(w)(r, \pi) dr + \lim_{\Delta a \to 0} \frac{1}{2\Delta a} \int_0^{\Delta a} \tau_{xy}(\Delta c - r, 0)(u)(r, \pi) dr
$$

$$(A.2)$$

where G is the energy-release rate, σ_y, and τ_{xy} are the normal and shear stresses near the crack tip, u and w are the relative sliding and opening displacements between

points on the crack faces and Δa is the crack extension at the crack tip. The first and second integrals in Equation A.2 represent the mode-I and mode-II components of the energy release rate and can thus be decomposed into the respective forms as:

$$\begin{cases} G_I = \lim_{\Delta a \to 0} \frac{1}{2\Delta a} \int_0^{\Delta a} \sigma_y(\Delta c - r, 0)(w)(r, \pi)dr \\ G_{II} = \lim_{\Delta a \to 0} \frac{1}{2\Delta a} \int_0^{\Delta a} \tau_{xy}(\Delta c - r, 0)(u)(r, \pi)dr \end{cases} \quad (A.3)$$

where G_I and G_{II} are the energy release rates for mode-I and mode-II fracture.

The integrals in Equation A.2 can be interpreted as the amount of work required to close the crack and the amount of crack extension Δa. When implemented in the finite element method, in a mesh surrounding the crack tip this work translates into one-half of the product of nodal forces required to open or close the respective nodes multiplied by the nodal displacements. More specifically, the *crack closure technique*, is shown in Figure A.5(a), is a two step technique where the above mentioned principle that the work required to open the crack by a unit distance ($= G_I$ and G_{II} for the two modes) is equal to the amount of energy released when the crack is closed by the same amount [59, 20]. In a two dimensional four-node elements as shown, the energy in terms of the nodal forces and displacements is given as:

$$G = \frac{1}{2}[X_{1l}\Delta u_{2l} + Z_{1l}\Delta w_{2l}] \quad (A.4)$$

where X_{1l} and Z_{1l} are the shear and opening nodal forces and Δu_{2l} and Δw_{2l} are the nodal displacements in the sliding and opening modes, at node l. The energy G, according to crack closure method is the same for crack extension and closure and can be calculated from this formula for both linear and quadratic elements, adjusting for forces on the upper and lower surfaces of the closed crack and the corresponding nodes. Crack is then further extended in the second analysis step to the new length
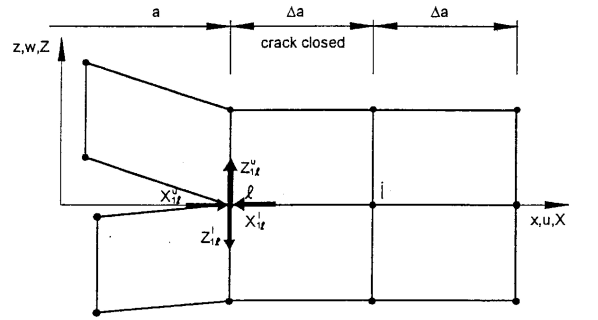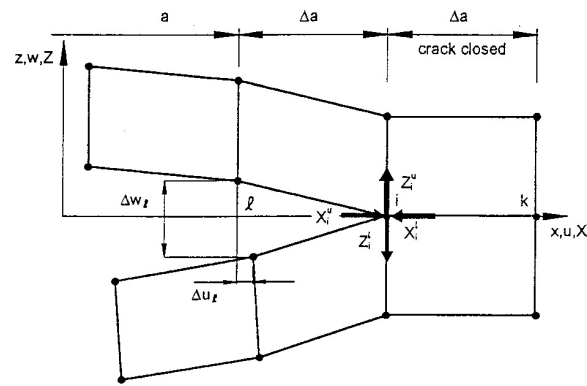
(a). *First Step - Crack closed*
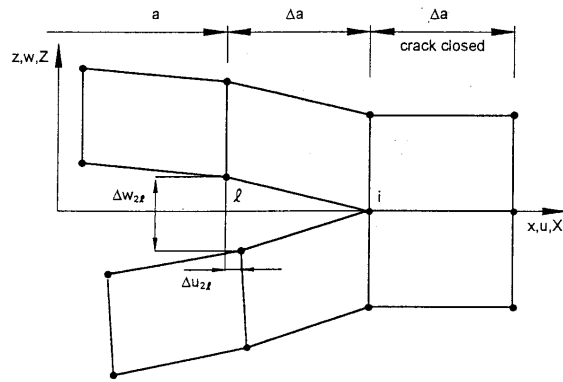
(b). *Second Step - Crack extended*

(a) Two-step crack closure technique based on the modified crack closure integral.

(b) One-step *virtual* crack closure technique based on the modified crack closure integral.

Figure A.5: Application of the crack closure techniques based on modified crack closure integrals to a finite element mesh. Taken from Figure 3, 4 of [60].

177

of a + Δa.

In VCCT (or sometimes referred to as modified crack closure technique), assumptions in the crack closure technique based on MCCI are maintained along with an additional assumption: the crack extension from a to a+Δa does not significantly affect the state of the crack tip. Hence, as shown in Figure A.7 when the crack tip moves to from node i to node k, since the state of the crack tip is maintained, displacements behind the crack tip at k are approximately equal to displacements behind the crack tip at node i when the crack tip was located at node i. Furthermore, the energy released in crack extension between a+Δ a and a+2Δ a, is identical to that required to close the crack between nodes i and k as well as between l and i. In a 2D finite element plane stress or plane strain model, the crack of length a is represented as a 1D discontinuity by a pair of line of nodes, with identical co-ordinates for the individual nodes at the top surface and the bottom surface (often called master and slave surfaces in certain FEA packages, such as Abaqus CAE) of the discontinuity. These nodes are independent and not directly connected to each other, allowing the elements in the top and bottom surfaces of the crack to deform independently and allows the crack to open when nodal forces are enough to separate the identical nodes [55, 60, 115]. In case of 4-node linear elements, the crack propagation by release of nodal forces in a kinematically compatible manner is straightforward due to the fact that with each node opening/closing in a sequential manner is equivalent to separation of the linear elements. However, in case of 8-node 2D quadratic elements, it is difficult to maintain kinematic compatibility when node-by-node release is implemented, and has been addressed by introducing complete element-wise release, where both corner and mid-side nodes are released simultaneously, for an incremental crack advance [55, 81, 82, 107]. When modeled in 2D with linear quadrilateral elements, the total mixed-mode energy release rate and its decompositions into mode-I and

mode-II is given as follows:

$$G = \frac{1}{2}[X_{il}\Delta u_l + Z_{il}\Delta w_l] \tag{A.5}$$

$$\begin{cases} G_I = \dfrac{1}{2\Delta a}[Z_i(w_l - w_{l*})] \\[3mm] G_{II} = \dfrac{1}{2\Delta a}[X_i(u_l - u_{l*})] \end{cases} \tag{A.6}$$

where Δa is the length of elements in the crack front and also the incremental crack growth, X_i and Z_i are the shear and normal forces at the crack tip nodal point i; the relative displacements behind the growing crack are calculated from the difference between opening and shear displacements at the upper and lower crack faces, *viz.* w_l, w_{l*} and u_l, u_{l*}. For an eight node 2D quadratic elemental crack advance, the modal decomposition of the energy release rate in terms of the nodal forces and displacements is given as follows:

$$\begin{cases} G_I = \dfrac{1}{2\Delta a}[Z_i(w_l - w_{l*}) + Z_j(w_m - w_{m*})] \\[3mm] G_{II} = \dfrac{1}{2\Delta a}[X_i(u_l - u_{l*}) + X_j(u_m - u_{m*})] \end{cases} \tag{A.7}$$

where w_m, w_{m*} and u_m, u_{m*} are the opening and shear displacements at the mid-side nodes at upper and lower crack faces; X_j and Z_j are the shear and normal forces at the crack tip mid-side nodal point j. In both type analyses, linear and quadratic, the crack area is given as $\Delta A = \Delta a * 1$, since a unit thickness of 1 is assumed in 2D plane analyses. The energy release rates calculated using this methodology can be easily converted into the respective stress intensity factors, which despite being more accurate than correlation or direct methods are less accurate than those obtained from numerical J-integral calculations. However, the simplicity and computation-

ally inexpensive nature of this method, largely due to the fact that nodal forces and nodal displacements, which are standard outputs in any FE program, are the only relevant quantities needed for calculating G, has resulted in widespread popularity of VCCT being chosen for crack propagation analyses [100]. In this research work, VCCT is applied to simulate crack propagation in SMAs subjected to combined thermomechanical loading in the presence of unique material responses such as transformation induced plasticity and thermomechanical coupling, and is shown to be a robust methodology for solving these problems.